Formation et surfusion de gouttes d'alliage eutectique AuSi sur substrats de Si : étude in situ par rayonnement synchrotron X

Rémi Daudin

UNIVERSITÉ DE GRENOBLE

THÈSE

Pour obtenir le grade de

DOCTEUR DE L'UNIVERSITÉ DE GRENOBLE

Spécialité: **Physique de la Matière Condensée et du Rayonnement**

Arrêté ministériel : 7 août 2006

Présentée par

Rémi DAUDIN

Thèse dirigée par **Gilles RENAUD** et **Alain PASTUREL**
codirigée par **Tobias SCHÜLLI**

préparée au sein du **CEA Grenoble - Service de Physique des Matériaux et des Microstructures**
dans **l'École Doctorale de Physique de Grenoble**

Formation and supercooling of AuSi eutectic droplets on Si substrates: an *in-situ* study using synchrotron radiation

Thèse soutenue publiquement le **10 Février 2012**
devant le jury composé de :

M. Jean-Marie Dubois
Directeur de Recherche CNRS, IJL Ecole des Mines, Nancy, Président
M. A. Lindsay Greer
Professeur, University of Cambridge, MSM, Cambridge, Rapporteur
M. Harald Reichert
Docteur, Max Planck Institut, Stuttgart, Rapporteur
M. Yves Garreau
Professeur, Université Paris-Diderot, LMPQ, Paris-7, Examinateur
M. Joël Chevrier
Professeur, Université Joseph Fourier, Grenoble, Examinateur
M. Gilles Renaud
Docteur, CEA Grenoble, SP2M, Directeur de thèse
M. Alain Pasturel
Directeur de Recherche CNRS, SIMaP, Grenoble, Directeur de thèse
M. Tobias Schülli
Docteur, Responsable scientifique ligne ID01, European Synchrotron Radiation Facility, Grenoble, Co-Directeur de thèse

Contents

Introduction

Nanotechnologies have attracted a lot of attention these past few years. It is mainly due to the explosion of the use of electronic devices such as cell phones or computers. These products are made of integrated circuits with the major part composed of semi-conductor devices such as transistors. The efficiency of an integrated circuit being proportional to the number of transistors, the reduction of their sizes therefore increases their performances and at the same time reduces the production costs. More recently, new interests are emerging in the use of nano-objects in other domains such as nanosensor in biochemistry.

There are two different approaches to build nanostructures. The first one is called the "top-down" approach and consists in sculpting the material in the desired shape and size. This approach is however sometimes limited when one wants to reach very small sizes as the techniques used, even if they are very precise, create defects that affect the properties of the object. The second approach is called "bottom-up" as the object is built almost atom by atom. In this case, the aim is to find some methods which can lead, by using well-controlled experimental conditions driving the processes, to the self-organization of the atoms. In both cases, the new features displayed by these objects are dominated by surface effects at the origin of the new properties.

In this context, semi-conductor nanowires (NWs), which can be seen as one-dimensional objects [i], exhibit unique optical, mechanical or electronic properties. More precisely, Si NWs are one of the most studied one-dimensional semi-conductors and are expected to be unavoidable components in new applications such as solar cells, sensors or new electronic devices.

Even if new ways to produce them have been discovered, the historical and the most studied process remains the one proposed in 1964 by Wagner and Ellis [Wagner and Ellis, 1964]. This process, presented in the first chapter of this work, requires the help of liquid gold which serves as a catalyst to organize the silicon atoms in the form of a NW. Even if such catalytic mechanisms are highly investigated, many fundamental questions in crystal-growth behaviour remain unanswered or/and controversial. As the state of the catalyst is of prime importance to control growth parameters (kinetic, orientation, morphology...) on which will later depend NMs properties, we need to investigate in details this mechanism.

This PhD work has been carried out at the SP2M-NRS [i] laboratory of the CEA Grenoble which is in charge of a beamline dedicated to the characterization of the growth of nano-objects on surfaces at the ESRF [ii]. It is however only recently that the group has been equipped with the required elements to perform the growth of NWs. The work presented in this manuscript does not deal with NWs growth, but results from an unexpected measurement : the existence of the catalyst in its liquid state at unusually low temperatures.

i. Their length is much larger than their diameter.
i. Service de Physique des Matériaux et Microstructures-Nanomatériaux et Rayonnement Synchrotron.
ii. European Synchrotron Radiation Facility.

The existence of an element as a fluid phase in a metastable liquid state below its melting temperature is a phenomenon called supercooling. Despite it is a well-known phenomenon, the understanding of the mechanisms governing it is incomplete. Their are two complementary theories to explain this effect. The first one, which is often reported to be the "classical" one, adopts a macroscopic point of view to describe the supercooling behaviour. Using thermodynamical concepts, cooling down a liquid below its melting point, in order to crystallize it, is necessary as it enables the formation of a stable solid nucleus. This nucleus serves as a seed for the atoms still in the liquid phase that attach to it and allow the growth of the solid phase. As the size of the stable nucleus is inversely proportional to the degree of supercooling, the more the liquid is supercooled the easier it solidifies. This description is widely used in material science to predict and control solidification processes.

The second theory adopts a more atomistic point of view. It explains the supercooling behaviour by the fact that the liquid atoms locally form clusters displaying structures incompatible with those of solid crystals. As a consequence, the liquid-solid transition is slowed down because the atoms are already ordered, presenting a stable configuration of low energy, and thus have to deeply reorganize their arrangement to adopt the crystal structure. These special clusters are assumed to present a five-fold symmetry, such as icosahedra, that prevents the formation of an ordered crystal [i]. This kind of ordering in liquids has already been observed but remains very difficult to characterize experimentally [ii]. It is even more difficult to make the link between the development of a five-fold ordering in liquids and their supercooling behaviour. However, the improvement of the characterization techniques now allows to study in more details this still unclear organization which is at the heart of an intense research in the field of condensed matter.

The complexity of supercooling phenomena is increased when it concerns the solidification of alloys. This is however the case in this work into which the Au-Si system is investigated. Moreover, the Au-Si liquid alloy forms a eutectic liquid which means that for a certain composition, the AuSi liquid phase is already stabilize down to low temperatures. Below this eutectic temperature, the eutectic liquids are expected to undergo very small supercooling and to crystallize after the separation of the different components. In the present work this is therefore the observation of the AuSi eutectic liquid well below its eutectic temperature (under the form of nano-droplets in contact with a Si substrate) that led us to investigate its atomic structure using surface X-ray diffraction. The understanding of the interactions between the AuSi liquid and its substrate are of prime importance as they are the bases of the different parameters that govern the growth of nanowires.

i. A crystal presenting an order at long distances adopts a three, four or six-fold symmetry.
ii. Evidences of this kind of ordering has been demonstrated by simulations.

The different aspects of this work concerning the formation and the supercooling behaviour of the AuSi eutectic droplets are presented as follows in the manuscript :

- **Chapter I : State of the art.** In this part are presented the physical concepts required to understand the following results. Some particular features concerning surface science are described, the materials used in this work and the process in which they are used for the growth of nanowires are presented. As this process is based on solidification, a large part of this chapter is dedicated to the structure of the liquids and the liquid-solid transitions. We briefly recall some general concepts on solidification processes but linger on the specific alloys studied in this work. Some features concerning these liquid alloys brought to the nanoscale and the specific cases of nanowires growth are described.

- **Chapter II : Methods and experimental set up.** Our experiments consist in an *in-situ* study of substrates' surfaces, in Ultra High Vacuum, by the use of synchrotron radiation. In this chapter are therefore recalled some bases concerning surface X-ray diffraction and the properties of the synchrotron light. We present in details how the measurements are performed as well as the experimental set up for a good understanding of the results.

- **Chapter III : Growth of Au on Si(111).** Before investigating the liquid droplets, we focus on how they form on the substrates via the deposit of a thin gold film that turns into islands and then into droplets by increasing the temperature. This chapter aims to measure the morphological parameters of the islands as well as the evolution of atomic structure of the gold-silicon interface with annealing.

- **Chapter IV : Au-induced reconstructions of Si(111) : (6×6) and ($\sqrt{3}\times\sqrt{3}$)R30°** . The formation of the gold islands and the droplets takes place in the presence of a gold wetting layer inducing a surface reconstruction with a very peculiar structure. In this chapter we present our experimental results concerning the formation of this reconstruction and the determination of its atomic structure.

- **Chapter V : Supercooling in AuSi droplets.** In this PhD work, particular supercooling effects have been observed in the AuSi eutectic droplets in interaction with different structures of the Si substrates. This chapter is dedicated to the presentation of the results dealing with the solidification processes and the structure of the liquid.

- **Chapter VI : Case of other systems and inert substrates.** The major part of

this work consists in the investigation of the Au-Si system. However, some experiments in other systems that are used for the growth of semi-conductor nanowires have been studied using the same experimental conditions. The results obtained on the Au-Ge and Al-Si systems are presented in this chapter.

- **Chapter VII : Discussion and synthesis.** Although this PhD work is in line with the very intense research dealing with the Au-Si system, the concepts tackled here concern some specific questions raised in the last decade due to the appearance of new experimental conditions and new means of characterization. In this last chapter, we compare our results to the recent literature and propose an overview of the different concepts that are still under debate.

Chapter I

State of the art

Contents

This chapter presents the general concepts that have been encountered during this work. This overview contains the bases on the growth of nanowires, the description of the materials used in this study as well as specific features concerning the physics of surfaces. A consequent part is dedicated to the liquid state, the solidification processes and the problems linked to the presence of interfaces.

I.1 Nanowires production

The topic of this section is a short introduction to the Vapour-Liquid-Solid (VLS) process as well as some considerations concerning epitaxial growth. In this study, attention was paid on the physical interactions of the deposited metal with the underlying substrate to understand the very first events arising in this process. The studied systems were not exposed to vapour flux and no nanowire has been formed. The VLS process is however presented here because it is at the heart of nanowire growth and highlights the different physical parameters arising in this field of nanoscience. Some particular features concerning growth will also be introduced in this chapter to get a clear understanding of the purpose of this work. For rather complete descriptions concerning the growth of nanowires, the reader is advised to refer to recent reviews of Wang *et al.* [Wang *et al.*, 2008], Schmidt *et al.* [Schmidt *et al.*, 2010] and Ross *et al.* [Ross, 2010] as well as references therein.

I.1.1 The Vapour-Liquid-Solid process

Figure I.1 illustrates the successive steps describing the VLS mechanism :

- First, the metal catalyst is deposited on the substrate, for instance at room temperature (RT), in the form of a thin film.
- Then, the sample is annealed, the film dewets (see section I.3.3) and liquid droplets form at the eutectic temperature T_e of the given system (see section I.3.1)
- Finally, the catalyst droplet is exposed to a semiconductor (SC) vapour flux. The incoming SC atoms diffuse inside or at the surface of the droplet due to concentration gradients. A typical VLS growth experiment is performed between 700 K and 900 K. With respect to the phase diagram of the concerned system, the SC atoms crystallize at the droplet-substrate interface and nanowires start to grow. The growth is thus performed by a constant arrival of new SC atoms at the interface between the droplet and the newly-formed nanowires, its diameter depending on the lateral size of the droplet.

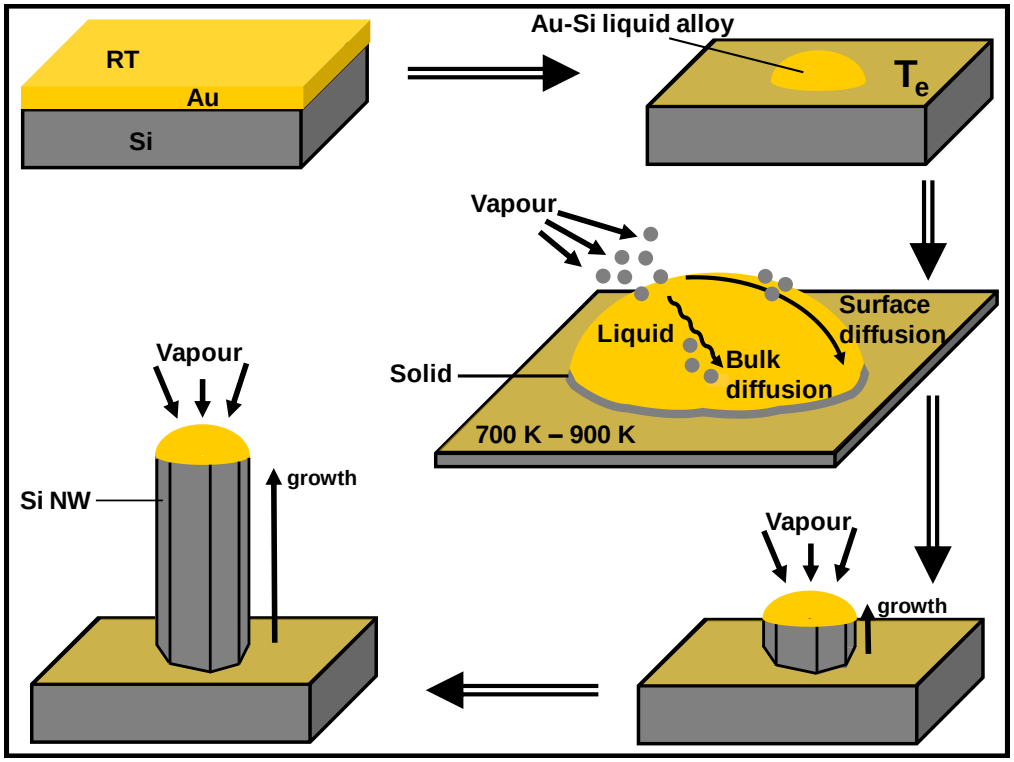

Figure I.1 – Scheme of the Vapour-Liquid-Solid process in the case of Si nanowires growth catalyzed by Au islands.

I.1.2 Molecular Beam Epitaxy (MBE) and growth modes

As we have just seen, the deposit of the catalyst on the substrate is a prerequisite to VLS experiments. Epitaxial[i] growth is a very common field of surface science, beyond the field of nanowires studies. For example, the growth of Ge on Si substrates has been extensively studied [Voigtländer, 2001; Zhou *et al.*, 2011; Gossmann *et al.*, 1985; Köhler *et al.*, 1991]. Typical epitaxial growths are performed by Molecular Beam Epitaxy which consists in heating a material source which provides a flux of atoms orientated towards the desired substrate. Depending on experimental parameters[ii] many atomic processes can take place at the surface, as represented in Figure I.2. Controlling the flux as well as the deposition time makes possible the formation of thin films of several Angströms.

The crystalline growth performed through MBE creates a solid-solid interface. At the thermodynamical equilibrium there exists three different growth modes (see Figure I.3) :

- the Frank-Van der Merwe mode, corresponding to a complete wetting of the successive deposited layers. The growth mode is thus achieved layer by layer.
- the Stranski-Krastanow mode for solids presenting a lower wettability with respect to

i. The word "Epitaxy" comes from a combination of Greek words : "$\epsilon\pi\iota$" and "$\tau\alpha\xi\iota$" which mean "on" and "arrangement", respectively.

ii. such as nature of materials, temperature, flux, etc...

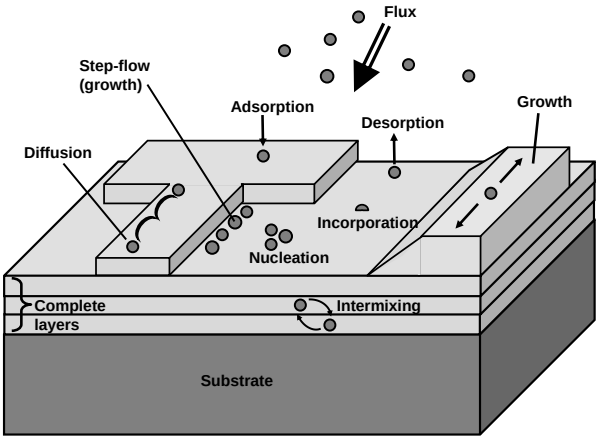

Figure I.2 – Illustration of the different physical process that can arise during Molecular Beam Epitaxy.

the substrate. In this case a few atomic layers can wet the substrate (called wetting layers (WL)), the following atoms form solid islands on top of it.

– the Volmer-Weber mode for which no wetting layer can form. The growth consists in the formation of islands directly on the substrate.

Basically, these different growth modes depend on the difference between the surface energies of the two materials. For example, metal atoms deposited on a ceramic would very likely grow following the Volmer-Weber growth mode. However if the surface energies are of the same order, it is quite difficult to predict the growth mode, the difference between two modes being sometimes very small and the equilibrium conditions rarely achieved. A more detailed discussion on growth mode is presented in Chapter III in the case of Au on Si(111). Precisions will also be given concerning surface energies when dealing with wetting properties (see section I.3.4).

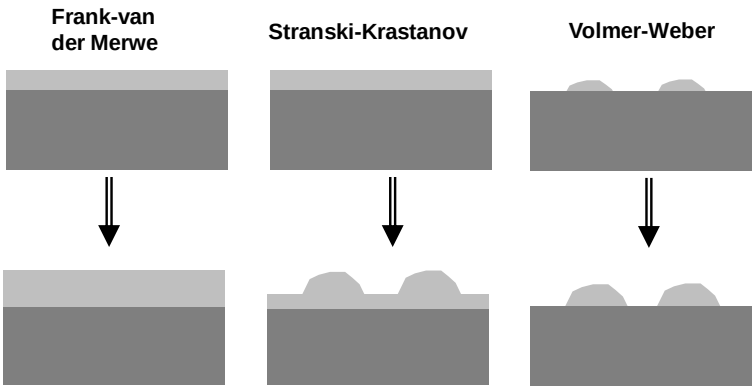

Figure I.3 – Presentation of the three typical growth modes. The Frank-van der Merve mode consisting in a layer by layer growth, the Stranski-Krastanow mode for which 3D objects form on a wetting-layer and the Volmer-Weber mode displaying direct island nucleation.

I.2 Semi-conductor substrates and metal catalysts

In this work, we have studied mostly the Au-Si system as well as the Au-Ge and Al-Si systems. A quick introduction to these materials is given in this section.

I.2.1 Substrates and surfaces : Silicon and Germanium

Silicon [iii] (Z=14) is the second most abundant element in the earth's crust (the first one being oxygen) and is found naturally under the form of oxides but also in minerals. Pure silicon, easily available commercially, is extracted from its oxide form by reaction with graphite [iv]. It belongs to the semi-conductor class (narrow gap between the valence and conduction bands) and its photoabsorption properties are used in everyday life, for example in solar panels.

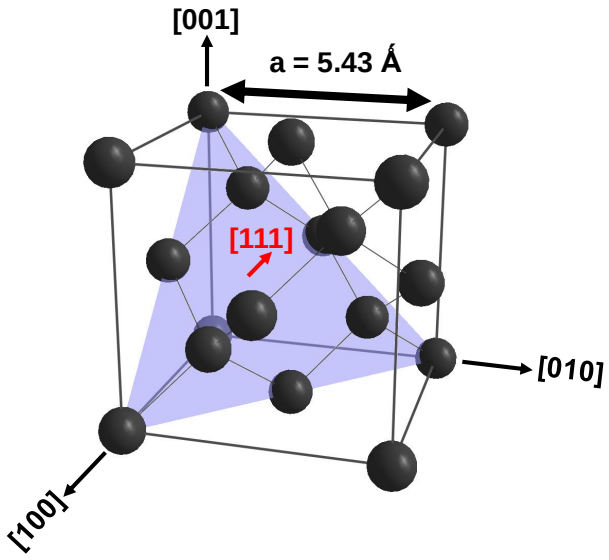

Figure I.4 – Silicon crystal in its diamond-type structure consisting in two face centered cubic (fcc) crystals translated by a $(1/4, 1/4, 1/4)$ vector. In transparency is printed the (111) plane which corresponds to the orientation of substrates studied in this work.

It crystallizes in a diamond structure [v] (see Figure I.4), with a lattice parameter of 5.4309 Å, into which each atom is located in the center of a tetrahedral site and shares four bonds with the nearest neighbours.

Germanium (Z=32) [vi] is also a semi-conductor with properties very similar to the ones

iii. The discovery of silicon is generally attributed to Jöns Jacob Berzelius (in 1824), its name coming from the Latin word "silicis" which means "flint".

iv. SiO_2+2C→Si+2CO

v. Groupe number : 227 ; Space groupe : $Fd\bar{3}m$

vi. The Germanium element was predicted by Mendeleev in 1871 and discovered by Clemens Alexander Winkler in 1886. Its name comes from "Germania" meaning "Germany" in Latin.

of silicon. It crystallizes in the same structure, with a lattice parameter slightly larger : 5.6575 Å(+4% compared to Si). It is however much rarer.

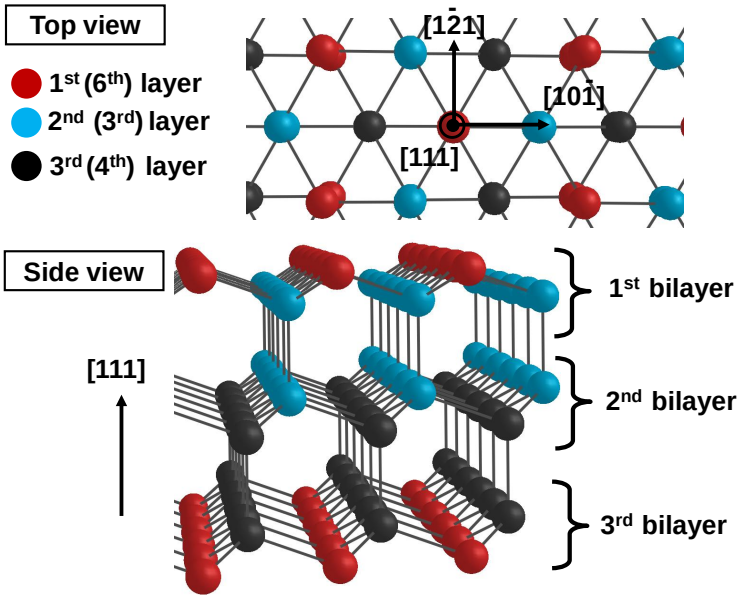

Figure I.5 – Top view and side view of a silicon (111) orientated substrate.

In surface science, the interesting features do not really concern the bulk behaviour of the material. It is therefore more relevant to present some surface properties encountered in this field and particularly in this work. One of the most relevant property of surfaces is their possibility to rearrange their atomic surface structure to reduce their surface energy. The resulting structure is called surface reconstruction.

The Si(111)-(7×7) reconstruction is a nice example to understand how surface atoms change their configuration to create an energetically favourable surface order. It is the first reconstruction that has been imaged by Scanning Tunneling Microscopy (STM) [Binnig *et al.*, 1983]. A detailed description can be found in [Takayanagi *et al.*, 1985] and [Voigtländer, 2001].

The Si(111) surface reconstruction arises because under pure conditions[vii], the surface atoms of the bulk-terminated (111) crystal present a lack of neighbours and therefore display dangling bonds. The more dangling bonds, the higher the surface energy, therefore surface atoms try to reduce the number of dangling bonds. How do they achieve this ?

Figure I.5 shows that Si atoms in (111) planes are arranged in bi-layers. If the surface is composed of the lower part of the first bi-layer (blue atoms in first bi-layer), it is clear that the surface presents three dangling bonds per surface atom. However, if the crystal is terminated by the higher part of the bi-layer (red atoms), the surface dangling bonds are reduced to one

vii. In the case of Si(111), the sample must be outgased for several hour around 900 K and then flashed at about 1500 K under Ultra High Vacuum.

per surface atom. This explains why, experimentally, a Si(111) surface is always terminated by a bi-layer.

In addition, atoms of the first layer also lower the number of dangling bonds by changing their configuration. This is achieved by the creation of new bonds with surface neighbours and leads to a new surface unit cell which is seven times larger than the one of the bulk-terminated (111) crystal (see Figure I.6).

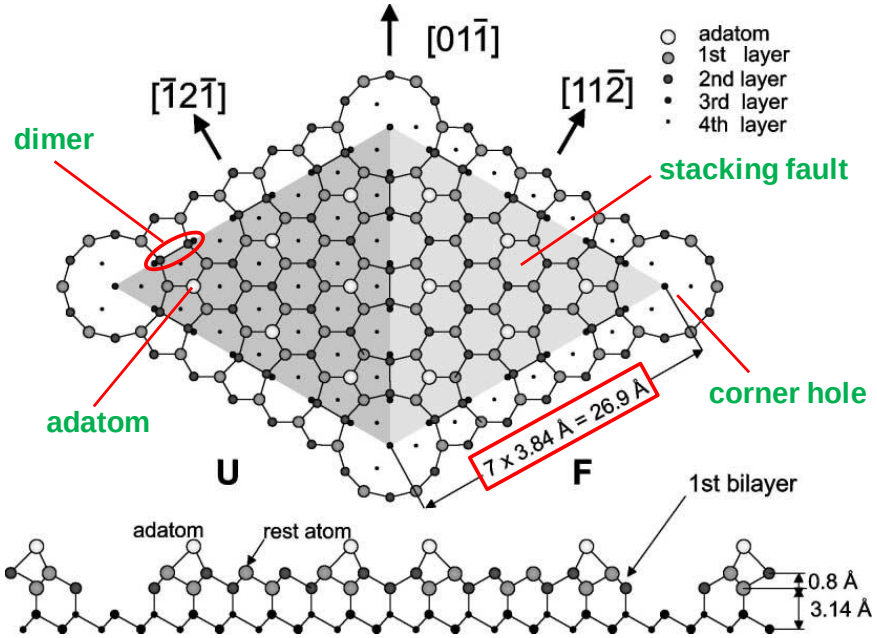

Figure I.6 – Top-view and side-view of the Si(111)-(7x7) reconstruction structure [Voigtländer, 2001]. The rearrangement of atoms creates a surface unit cell seven times larger than the theoretical one.

The rearrangement of surface atoms leads to the appearance of :

- adatoms, sharing three dangling bonds with underlying rest atoms and
- dimers, which form around adatom regions (at the edges of the half unit cell) and also reduce the number of dangling bonds.

The formation of dimers creates stacking faults and yields one half of the unit cell that is faulted (F) and the other half that is unfaulted (U), with respect to the bulk stacking sequence. It also creates empty sites where six (7×7) unit cells meet, which are called corner holes [viii]. This arrangement allows the structure to reduce its number of dangling bonds from 49 to 19 and therefore to reduce its surface energy [Stich *et al.*, 1992]. As a reconstruction is a consequence of local electronic density adjustment, it highly depends on the crystallographic orientation. For example, the Si(001) surface atoms form a (2×1) surface reconstruction and

viii. The complete transformation process from the unreconstructed Si(111) surface to Si(111)-(7×7) structure can be seen via the nice animation performed by Yan Liang from the Department of Chemical Engineering and Materials Science, University of Minnesota : http ://vimeo.com/1086112 .

its energy is higher than the one of the Si(111) surface.

Following the same philosophy, a non polluted Ge(111) surface is also reconstructed. Surprisingly, although Si and Ge are very similar materials, they do not present the same surface reconstruction : the most stable surface structure of Ge(111) is the c(2×8) reconstruction presenting adatoms and restatoms without dimers, corner-holes or stacking faults [Becker *et al.*, 1989].

I.2.2 Catalysts : Gold and Aluminum

Gold (Z=79) is certainly the first metal studied in human history. Nobody knows who discovered it first but the reason might be that it was shiny [ix].

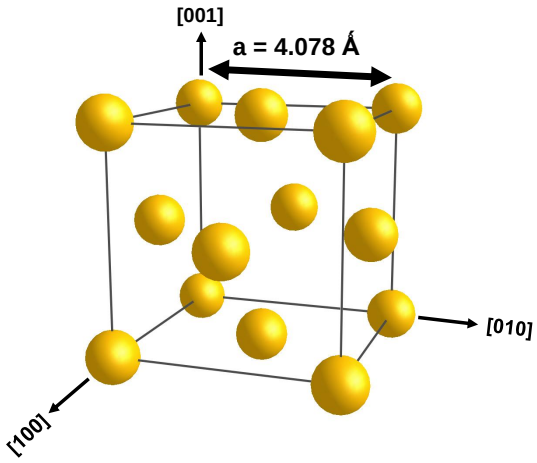

Figure I.7 – Gold crystal unit cell illustrating its fcc structure.

Gold is a soft, ductile metal ; a good conductor of heat and electricity and is inert to air and most reagents. It is historically widely used in jewelery for its color. Its bio-compatibility (malleability and corrosion resistance for instance) makes it relevant for its use in dentistry. More recently, with strong advancements made in the field of nanomaterials, gold nanoparticles were found to be valuable candidates in diverse medical applications [Boisselier and Astruc, 2009]. Its crystal structure is face centered cubic (fcc) [x] with a lattice parameter of 4.0782 Å, as represented in Figure I.7.

Aluminum (Z=13) and almost all the possible Al-based alloys were also prone to studies. However aluminum was isolated only in 1825 and is a nonmagnetic and nonsparking metal. It is not found pure in nature but has to be extracted from bauxite. It can easily be cast and is used, mostly under the form of alloys, in a wide range of applications (from cans or foil

ix. The first traces of gold manipulations go back to about 3600 BC in Egypt.
x. Group number : 225 Space group : $Fm\bar{3}m$

to aerospace industry). Like gold, its crystal structure is fcc with a lattice parameter slightly smaller : 4.0495 Å.

I.3 Interactions

In the previous section (I.2), we have briefly presented the general properties of the materials studied in this work. In this section we focus on several phenomena that arise from potential interactions between the deposited metal and the SC substrate.

I.3.1 Phase diagrams

A thermodynamical phase diagram displays the different domains (phases) into which the binary alloy, or the pure elements, form a specific structure in the solid state. It also shows the domains where the alloy is liquid or where the liquid phase is in equilibrium with a solid phase. The different domains depend on the concentration as well as on the temperature[xi].

Figure I.8 displays the equilibrium phase diagram of the Au-Si system which is at the heart of the present work. It is rather simple, with only 5 different phases : the homogeneous liquid phase (■), the two domains into which pure solid Au (■) or Si (■) coexist with a liquid alloy and the two solid Au-FCC and Si-Diamond structures.

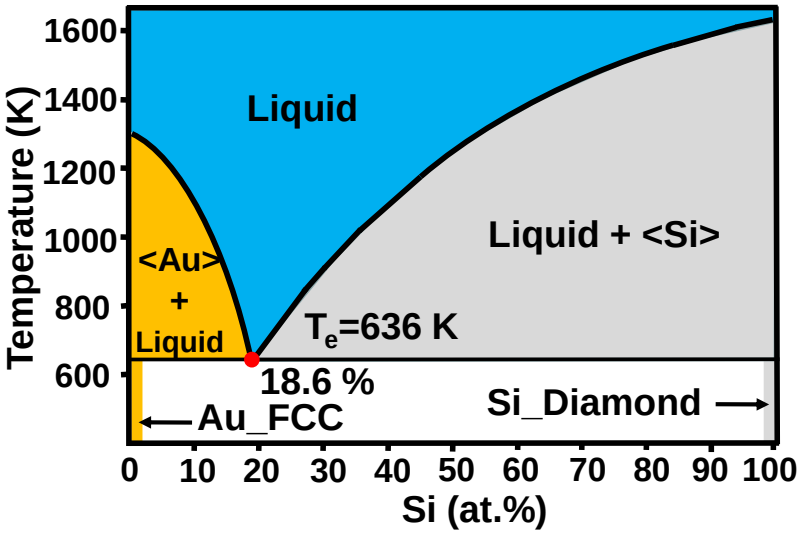

Figure I.8 – Gold-Silicon phase diagram.

Two remarkable features can be pointed out :

– the presence of a very low eutectic point (x_{Si}=∼19 at.%, T_e=636 K) which shows that for a given composition, the alloy can stay in its liquid state at a very low temperature

xi. [ ], ( ) and < > stand for gas, liquid and solid phases, respectively.

compared to the melting temperatures of each component taken seperately.

– the absence of stable bulk crystalline alloy : silicon is not soluble in the Au solid phase (and inversely).

The study of the Au-Si phase diagram allows us to give here some precisions on the VLS process presented in section I.1.1. At the eutectic temperature the system is composed of a droplet which is assumed to be at the eutectic composition. If one wants to perform the growth of nanowires at 700 K, annealing the system to the desired temperature leads to dissolution of the substrate Si atoms into the droplet following the Si liquidus line. At 700 K the Si concentration in the droplet is about 21 at.% and is almost tantamount to the eutectic one due to the very steep liquidus line. Then, when the droplet is exposed to the Si vapour flux, the Si atoms enter the liquid phase and diffuse to the interface. Following the phase diagram, the droplet concentration is shifted to the right hand side of the liquidus line and the system enters the grey area corresponding to the two-phases <Si>+(AuSi) domain. Following the Shell-Gulliver rules, the silicon in excess (compared to the liquidus composition at 700 K) crystallizes to form the solid phase. The solidification arises at the droplet-substrate interface because it offers perfect nucleation sites to the Si atoms. Ideally, the nanowire can keep growing as long as the Si vapour flux is maintained. Note here that the system is out of equilibrium but remains in a stationnary process consisting in incorporation, diffusion and solidification of the Si atoms.

The Au-Ge and Al-Si phase diagrams, represented in Figure I.9(a) and I.9(b), respectively, also display eutectic points which differ in composition and temperature. The VLS growth can also be performed using these systems (as well as many others [Schmidt *et al.*, 2010]). However, for these two systems, a small fraction of the SC phase is soluble in the solid structure of the respective metal. This is illustrated by a small domain at the left hand side of the diagram, often noted α in literature.

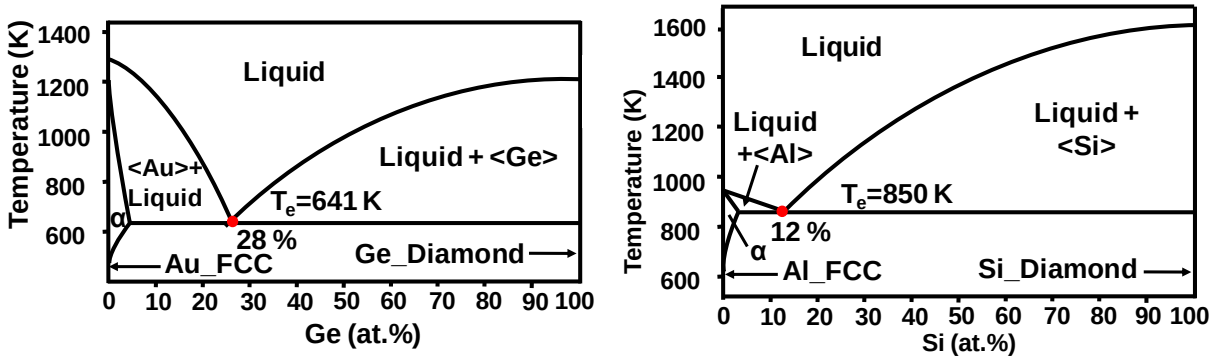

(a) (b)

Figure I.9 – (a) Gold-Germanium phase diagram.(b) Aluminum-Silicon phase diagram. The α phase corresponds to the metal-SC bulk solid phase in both cases.

The phase diagrams presented above are consistent when considering the given systems in their bulk structure, which consists in neglecting surface effects. As it will be presented later (see section I.7), some considerable gaps from the bulk behaviour can arise when systems are brought to the nanoscale [xii].

In the field of surface science, a specific feature that has been intensely studied is the reconstruction of a substrate's surface upon deposition of a small amount of metal.

I.3.2 Deposit-induced surface reconstructions

We have seen in section I.2.1, that the atoms at the surface of the Si(111) substrate rearranged themselves because of the lack of neighbours. This reorganization being a mean of decreasing the energy per surface atom. A similar process takes place at the very early stages of metal deposit. The deposited material induces rearrangement of the surface atoms in a surface structure that has a periodicity larger than the bare surface.

Figure I.10 is an arbitrary example of a (2×2) reconstruction. The deposited atoms form a surface unit cell which is twice larger than the surface unit cell of the substrate. Moreover, some specific reconstructions periodicities can sometimes require to be turned with respect to the substrate surface lattice. The angle is therefore added to the notation : for example, a $(\sqrt{3}\times\sqrt{3})$R30° reconstruction would refer to a surface unit cell $\sqrt{3}$ times larger with a mesh turned by 30° with respect to the substrate one.

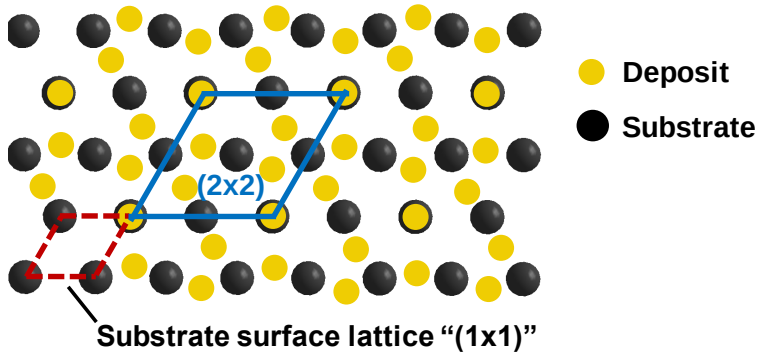

Figure I.10 – Illustration of a (2×2) reconstruction. The surface unit cell displayed by the deposited atoms (yellow) contains in this case 5 atoms ($4 \times 1/4 + 4$) and is twice as large as the surface unit cell of the underlying substrate (black).

For the metal-SC systems presented in this work, several reconstructions are known to exist. For deposited Au atoms on a Si(111) substrate, the most commonly observed reconstructions are the (5×2), the $(\sqrt{3}\times\sqrt{3})$R30° and the (6×6) reconstruction. A more detailed description of these reconstructions is given in Chapter III . Other less studied reconstructions

xii. This is perfectly illustrated in the case of the carbon element : the physical properties of a single sheet of graphite (under the form of graphene or nanotube, or even fullerene) differ a lot from the ones of bulk.

of gold on Si(111) such as (2×2) [Seifert *et al.*, 2001], ($2\sqrt{3}\times2\sqrt{3}$) or ($2\sqrt{21}\times2\sqrt{21}$)R±10.9° [Sakai *et al.*, 1998] have so been reported.

In the same way, Au forms a ($\sqrt{3}\times\sqrt{3}$)R30° reconstruction on the Ge(111) substrate which is supposed to be similar to the one on Si(111) [Howes *et al.*, 1993]. Note here that no (6×6) reconstruction is known to form in the Au-Ge(111) system. As far as Al is concerned, pioneering work of Lander and Morrison revealed the formation of surface reconstruction of Al on Si(111) for submonolayer range and at high temperatures [Lander and Morrison, 1964]. The Si(111)-($\sqrt{3}\times\sqrt{3}$) -Al reconstruction was subsequently studied in more details by several techniques [Northrup, 1984; Yamada *et al.*, 1984; Huang *et al.*, 1990; Horio, 1999]

Surface reconstructions are therefore most of the times two-dimensional structures and are studied for coverages of the order of one monolayer [xiii]. For higher coverages, typically above 2 ML, the formation of thin crystalline films (or islands depending on the growth mode, see section I.1.2) starts to be favoured. These thin epitaxial solid films can undergo morphological transformations that turn them into islands. This is the topic of the next section (I.3.3).

I.3.3 Dewetting of thin films : formation of islands

Throughout the literature, it is often mentioned that the liquid catalyst droplets are obtained by increasing the temperature, which induces the dewetting of the solid film previously deposited at RT by MBE. This precision is useful because the droplets could have been obtained using other methods. For instance, a deposit performed at higher temperature can lead to direct islanding according to the Wolmer-Weber or the Stranski-Krastanow growth modes. It is even possible to directly lay down Au microdroplets on the substrate [Ferralis *et al.*, 2008]. If the dewetting process is often used, it is rarely described in details. Before the Au deposit transforms into liquid catalyst droplets that can be used for the growth of nanowires, the solid film first dewets in the solid state, *i. e.* it undergoes structural changes upon annealing leading to the creation of solid islands. We give here a brief description of this process to introduce the results presented in Chapter III.

Pioneering work of Rayleigh [Rayleigh, 1878], as well as following studies of Mullins [Mullins, 1957] allowed more recent authors to derive models concerning the dewetting process through the study of the stability of thin solid films [Srolovitz and Safran, 1986a; 1986b; Jiran and Thompson, 1992]. These solid films present a high surface-to-volume ratio so that the system tries to reduce its surface area. This reduction can be achieved via diffusion of atoms which tend to agglomerate. Obviously, the agglomeration is easier at high temperature

xiii. The case of Ge-(2×N) reconstruction on Si(001), with N depending on the coverage (1-3 ML) has been reported [Zhou *et al.*, 2011].

as atomic diffusion is enhanced. The dewetting is therefore a consequence of annealing but annealing is not the driving force (which is the reduction of the surface energy). Figure I.11 illustrates the dewetting process which occurs in two steps : the creation of voids in the film ((a), (b)) and their subsequent growth ((c), (d)).

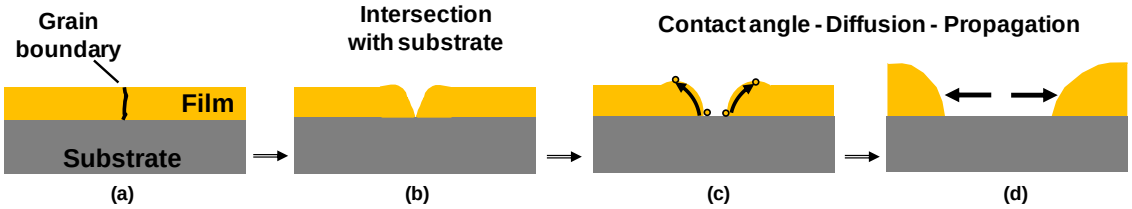

Figure I.11 – Side view illustrating the two steps dewetting process. (a) The polycrystalline film is flat with the presence of a grain boundary. (b) Fluctuation due to thermal activation sets in at the position of the grain boundary (c) The created voids is large enough to create a contact angle (d) The void starts to grow.

If a stable thin solid film is annealed, small amplitude fluctuations appear :*i. e.* the film gets rougher. The creation of voids is the consequence of fluctuations large enough to create a deep groove that can reach the substrate. In polycrystalline films, it is reasonably assumed to arise at grain boundaries (Figure I.11(a), (b)). A contact angle is created between the substrate and the solid if the groove intersects the surface. Then, mass transfers occur via surface diffusion to reduce the curvature of the film edge resulting in the growth of the voids (Figure I.11(c), (d)). Due to an inhomogeneous repartition of the removed atoms (see Figure I.12), some regions are thicker (A) than others (B). As a consequence, the void grows faster in front of B areas and the result is a non-planar propagation of the voids. At some point the thick area of type A detaches from the film and a solid island remains.

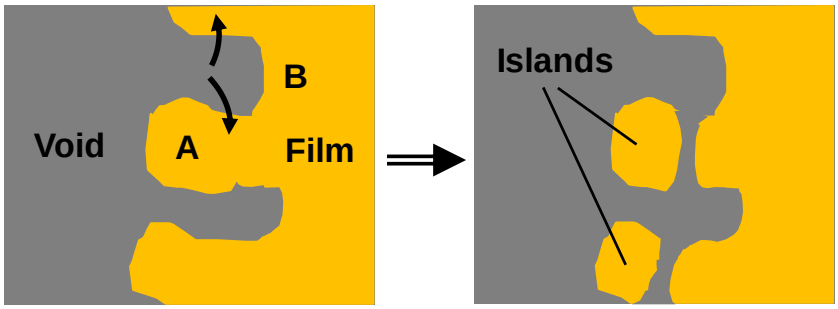

Figure I.12 – Top view showing the non-planar propagation of the void. This results in the presence of thicker areas (A) which detach from the solid film and become islands.

This simple model well describes the general trends concerning the dewetting of solid films. A nice example concerning the dewetting of Au films can be found in [Shaffir *et al.*, 2009]. However for the description of more complex phenomena, more precise models have been derived [Wang and Schaaf, 2011; Pierre-Louis *et al.*, 2009] (and references therein).

I.3.4 Wetting droplet on a solid surface

Because of the dewetting process, thin metal solid films form solid islands on the underlying SC substrate. When the system temperature is increased up to the eutectic one, the solid-liquid transition takes place and a liquid droplet remains. The morphological equilibrium linking the droplet to the substrate can be expressed using the Young's equation presented hereafter.

a Young's equation

The wetting properties of a liquid droplet (*i. e.* its shape) in interaction with a solid substrate depends on an energetic equilibrium described by the well-known Young's equation proposed in 1805 [Young, 1805] :

$$\gamma_{liq-vap}\cos(\theta) = \gamma_{sol-vap} - \gamma_{sol-liq} \tag{I.1}$$

with $\gamma_{liq-vap}$, $\gamma_{sol-vap}$ and $\gamma_{sol-liq}$ the liquid-vapour, solid-vapour and solid-liquid surface tensions, respectively and θ the contact angle (measured in the liquid phase), as represented in Figure I.13. However, although a contact angle is quite easy to measure, the three surface energy terms, which are fundamental parameters in material science as they are related to the binding force between atoms, are difficult to obtain experimentally. The study of surface energies is a scientific field dealing with many facets of material science and can not be introduced here. However, several specific features concerning the present work are presented briefly hereafter.

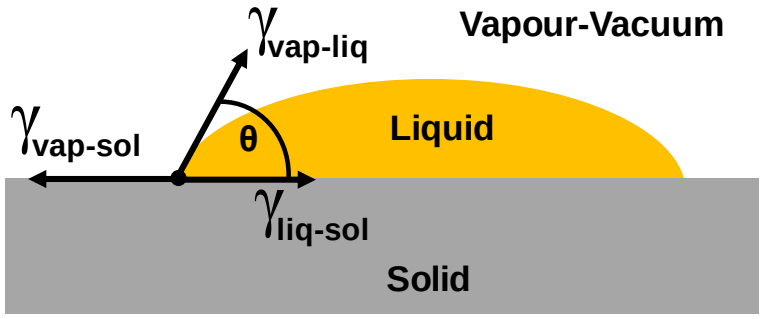

Figure I.13 – Scheme representing the wetting of a liquid droplet in interaction with a solid substrate.

b Precisions relative to surface energies

A first remark has to be made here on the definitions used for the surface energies that are surface stress, surface free energy or surface tension. For clarity, we only remind here that

surface stress is a quantity described by a tensor and is related to the work needed to deform a solid surface elastically, whereas surface energy is related to the work needed to create a new surface area (in J.m^{-2}). The surface tension term is the liquid analogue of the surface energy for solid. In material science it is common to use the surface tension or the surface energy term equally for both phases.

In this study, attention was paid on the wetting behaviour of AuSi droplets on Si substrates. It is therefore important to have an idea of the different surface energy values concerning this system for which the surface energy of solid Si needs to be known as well as the different surface tension terms of gold.

Si substrate surface energy

Using experimental cleavage techniques [Jaccodine, 1963] or, more recently, indentation techniques coupled to molecular dynamic simulations [Tanaka *et al.*, 2006] as well as theoretical calculation using the Modified Embedded Atom Method (MEAM) [Zhang *et al.*, 2003] it is possible to evaluate the Si crystal surface energy. The surface energy of solid silicon depends on its crystallographic orientation with the low index planes presenting the lowest energies and :

$$\gamma_{Si(111)} \sim 1.2 \text{ J.m}^{-2} < \gamma_{Si(110)} \sim 1.5 \text{ J.m}^{-2} < \gamma_{Si(100)} \sim 1.9 \text{ J.m}^{-2} \tag{I.2}$$

Gold surface energies

The case of gold seems to be a bit more complex, as illustrated by Table I.1 which gathers the different γ values encountered in literature. It reveals that for the liquid-vapour and solid-liquid energies, the comparison between the different papers are in good agreement and provides the commonly used values :

- $\gamma_{liq-vap} \sim 1.2$ J.m^{-2} and
- $\gamma_{sol-liq} \sim 0.13$ J.m^{-2}.

For the value of the solid-vapour surface energy $\gamma_{sol-vap}$, the dispersion is larger and must arise from the different assumptions used in the simulation techniques as well as the experimental uncertainties.

In addition, $\gamma_{sol-vap}$ is temperature dependent and, as for Si, crystallographic orientations also influence the result. However, in most metal, the difference in $\gamma_{sol-vap}$ between 0 K and the melting temperature T_m do not exceed 10 % [Tyson and Miller, 1977], the error thus remains quite low.

The mean value of all the $\gamma_{sol-vap}$ of Table I.1 is 1.54 $\pm$ 0.19 J.m^{-2}. It compares well with the value of the studies that do not take into account crystallographic orientations effects [Tyson and Miller, 1977; Mezey and Giber, 1982]. One can also note here that, as for

Table I.1 – Surface energy values found in literature for pure gold. The temperature and the method are indicated when explicitly mentioned.

$\gamma(Au)$	Energy (J.m^{-2})	Technique	Reference
$\gamma_{Au(111)}$ $\gamma_{Au(001)}$ $\gamma_{Au(110)}$	1.28 (0 K) 1.63 (0 K) 1.70 (0 K)	DFT	[Vitos *et al.*, 1998]
$\gamma_{Au(111)}$ $\gamma_{Au(001)}$ $\gamma_{Au(110)}$	1.38 (0 K) 1.49 (0 K) 1.85 (0 K)	Tight binding total-energy method	[Mehl and Papaconstantopoulos, 1996]
$\gamma_{Au(111)}$ $\gamma_{Au(001)}$ $\gamma_{Au(110)}$	1.61 (0 K) 1.71 (0 K) 1.79 (0 K)	*Ab-initio*	[Skriver and Rosengaard, 1992]
$\gamma_{sol-vap}$	1.25 (0 K)	Pseudopotential energy method	[Needs and Mansfield, 1989]
$\gamma_{sol-vap}$	1.5 (0 K) $\sim$1.35 (1336 K)	Surface entropy estimation	[Tyson and Miller, 1977]
$\gamma_{sol-vap}$	1.62 (300 K) 1.36 (900 K)	Calculation from enthalpy of atomization	[Mezey and Giber, 1982]
$\gamma_{liq-vap}$	1.15	Thermodynamic model	[Vinet *et al.*, 2002]
$\gamma_{liq-vap}$	1.18		[han, 2010]
$\gamma_{liq-vap}$	1.3 (300 K)	Levitated droplet	[Egry *et al.*, 1995]
$\gamma_{sol-liq}$	0.13	Thermodynamic model	[Vinet *et al.*, 2002]
$\gamma_{sol-liq}$	0.13	Droplets on glass	[Turnbull, 1950a]

all fcc metals, close packed surfaces (low indexes planes) of the crystal are the most stable : $\gamma_{Au(111)} < \gamma_{Au(001)} < \gamma_{Au(110)}$.

Beyond pure gold, the interest of this work lies in the Au-Si alloy. As it has been shown above, surface energies of pure elements are already difficult to evaluate. Obviously, it is even harder in the case of alloys and very few studies deal with them. As pointed out by Schmidt *et al.* in their recent review on nanowires, the wetting properties of the catalyst strongly influence the shape of the nanowires. It is therefore relevant to attempt an evaluation of the different energy terms in the case of the AuSi alloy.

Taking $\gamma_{sol-vap} = 1.25$ J.m^{-2} for the Si(111) surface energy, $\gamma_{liq-vap} = 0.85$ J.m^{-2} for the AuSi liquid alloy [Naidich *et al.*, 1975], and 43° as a contact angle [Ressel *et al.*, 2003], the Young's equation provides an evaluation of the interface energy between the droplet and the substrate ($\gamma_{<Si>-(AuSi)}$) of 0.62 J.m^{-2} [Schmidt *et al.*, 2010].

In the case of a droplet at the tip of a nanowire and for which wetting properties are different, the thermodynamical process proposed by Roper *et al.* yields $\gamma_{liq-vap} = 0.91$ J.m^{-2}

and $\gamma_{sol-liq} = 0.8$ J.m^{-2} [Roper *et al.*, 2007]. This agrees well with the proposed values of $\gamma_{sol-liq} = 0.75$ J.m^{-2} by Nebol'sin *et al.* [Nebolsin and Shchetinin, 2003].

Moreover, the observation of the melting process of pure gold by incorporation of Si atoms allowed Kim *et al.* to calculate the interface energy between the solid Au and the AuSi liquid alloy : $\gamma_{<Au>-(AuSi)} = 0.3$ J.m^{-2}, at 800 K [Kim *et al.*, 2009].

I.4 Description of the liquid state : the pair-correlation function

The study of liquids requires to devise mathematical concepts in order to describe the atoms behaviour in this state of matter. The first picture that comes in mind is that in a liquid, the atoms are distributed randomly. However some statistics can be derived to picture the arrangement at a given time. This static description can be done through the use of the pair correlation function which describes the variation of the atomic density as a function of the distance from a distinct particle. This function is important in the studies of liquids as it can be determined using X-ray or neutron scattering techniques.

This function, usually noted $g(r)$, is plotted on the graph in Figure I.14. In this case is represented the radial correlation function which measures the independence between the positions of the particles. The function equals zero at the origin (where an atom is placed) because of electronic repulsions and then presents several maxima corresponding to the different groups of atoms defined as first, second, third, etc... neighbours. For large values of r, the function tends to unity as the liquid is disordered at long range : the position of the atom located at large r is not influenced by the position of the reference atom.

Using a simple idea, the correlation function can be seen as the probability of finding an atom in a ring of finite thickness Δr centered on the reference particle. It is given by :

$$g(r) = \frac{V}{N}\frac{n(r)}{4\pi r^2 \Delta r} \tag{I.3}$$

with N the number of identical particles located in a space of volume V and $n(r)$ the number of atoms located between r and $r + \Delta r$.

It therefore allows one to calculate the mean number of atoms present at a distance R around the atom at the origin, which is called the coordination number $\mathcal{N}$:

$$\mathcal{N} = 4\pi\rho \int_{R_1}^{R_2} r^2 g(r) \mathrm{d}r\,, \quad \text{for } r \text{ limited to the shell of first nearest-neighbours} \tag{I.4}$$

$\mathcal{N}$ corresponds to the red area under the curve of $g(r \in [R_1, R_2])$ and is of the order of

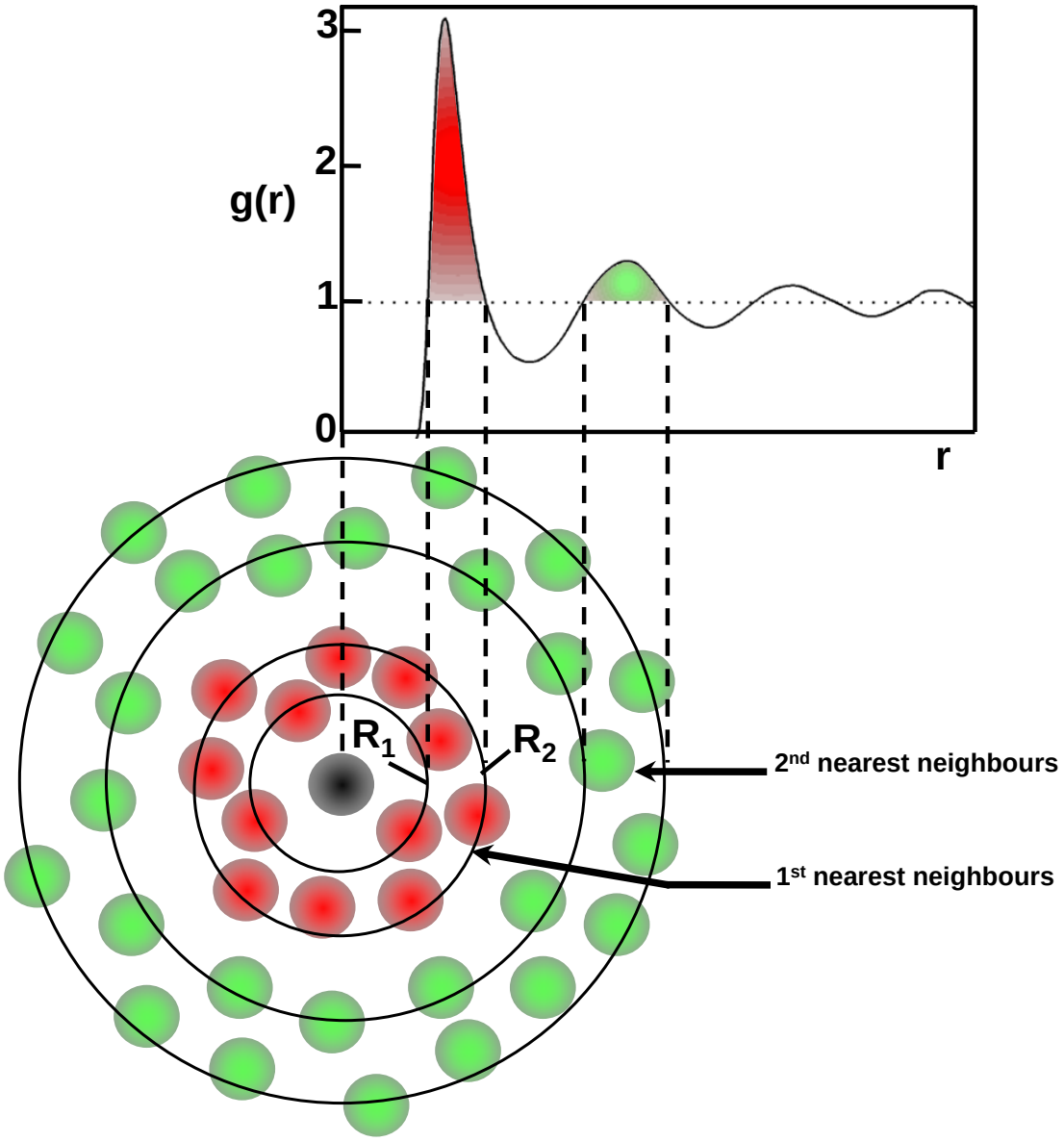

Figure I.14 – Pair correlation function g(r) and the corresponding groups of nearest neighbours responsible for the different peaks.

12 for most liquids, which is compatible with a compact arrangement.

During an X-ray or neutron experiment for characterizing liquids, the measured quantity is the structure factor S(Q) (with Q the momentum transfer defined in section II.1.2), which is related to $g(r)$ by :

$$S(Q) = 1 + \rho \int_0^\infty (g(r) - 1) e^{i\boldsymbol{Q}\cdot\boldsymbol{r}} \, \mathrm{d}\boldsymbol{r} \tag{I.5}$$

A simple Fourier transform of S(Q) therefore allows us to deduce the experimental pair correlation function.

I.5 Liquid-solid phase transition

Now that we have seen what is a liquid and how it is possible to describe it, we will discuss some theoretical aspects of the solidification process, *i. e.* the creation of a solid phase from a liquid phase. An important concept in the study of liquid-solid transitions is the fact that a liquid does not transform into a solid as soon as the melting point is reached. A liquid needs to be cooled below its melting point in order to form a stable aggregate. This phenomenon is called supercooling or undercooling. This behaviour was pointed out by Fahrenheit in 1724 who recorded the first supercooling experiment on liquid water[xiv] [Fahrenheit, 1724]. It has been clearly shown that a liquid needs to overcome an energetic barrier to transform into a solid phase. This is described within the classical nucleation theory briefly presented hereafter. This theory, based on early works of Becker [Becker and Doring, 1935; Becker, 1938], has been developed further by Turnbull [Turnbull and Fisher, 1949; Turnbull, 1950d] in the case of metals by describing the conditions of formation of solid clusters from the melt and how the size of these clusters evolves with time.

I.5.1 Supercooling : thermodynamic and classical model

A phase transition, solidification for instance, of a pure element is driven by the variation of the free enthalpy G given by[xv] :

$$\Delta G_s = \Delta H_s - T\Delta S_s \tag{I.6}$$

with T the temperature (K), ΔH the enthalpy variation (related to the energy of the chemical bonds) and ΔS the entropy variation (related to the structural organization). At the melting temperature T_m, the continuity of the function G implies that $G_{solid} = G_{liquid}$ and it comes :

$$\Delta G_s = 0 \;\Rightarrow\; \Delta S_s = \frac{\Delta H_s}{T_m} \tag{I.7}$$

So, the equation (I.6) becomes for $T \neq T_m$:

$$\Delta G_s = T_m\frac{\Delta H_s}{T_m} - T\frac{\Delta H_s}{T_m} \;\Rightarrow\; \Delta G_s = \Delta T\frac{\Delta H_s}{T_m}\,, \quad \text{with } \Delta T \text{ the supercooling value.} \tag{I.8}$$

xiv. It is worth mentioning here that even for water, the most common liquid, the solidification process in not completely understood.

xv. the index 's' stands for "solidification"

A quick look at the sign of ΔG_s allows us to know whether or not the transition can be achieved. With ΔS_s negative for a solidification process (creation of order) :

$$\begin{cases} T > T_m \;\Rightarrow\; \Delta T < 0 \;\Rightarrow\; \Delta G_s > 0 \;\Rightarrow\; \text{solidification impossible} \\ T < T_m \;\Rightarrow\; \Delta T > 0 \;\Rightarrow\; \Delta G_s < 0 \;\Rightarrow\; \text{solidification possible} \end{cases} \tag{I.9}$$

The first thing to note here, is that the liquid must be supercooled to have a chance to solidify. Nevertheless, the thermodynamic only acquaints the possible existence of the solid phase but does not explain how this latter is created from a microscopic point of view. For $T < T_m$, the variation of free enthalpy ΔG of a group of atom which is about to form a spherical solid nucleus of radius r depends on the energetic competition between the creation of a solid/liquid interface $\gamma_{sol-liq}$ and the variation of free enthalpy per volume unit $\Delta g_V (= \Delta T\, \Delta H_s / T_m)$:

$$\Delta G_{nucleus} = \overbrace{\frac{4}{3}\pi r^3 \Delta g_V}^{\Delta G_{volume}} + \overbrace{4\pi r^2 \gamma_{sol-liq}}^{\Delta G_{surface}} \tag{I.10}$$

This equation shows the different forces driving the solidification process.

We now present the results deriving from this statement, which concern the potential formation and the stability of a created nucleus in two different cases : homogeneous and heterogeneous nucleation.

a Homogeneous nucleation

Thermodynamics of nucleation :

The process of homogeneous nucleation consists in the creation of a stable nucleus by aggregation of atoms somewhere in the liquid phase. Equation (I.10) shows that the stability of this nucleus depends on its size r.

In Figure I.15(a) are plotted the surface and the bulk part of the free enthalpy as a function of the radius r to highlight their respective contribution to the total variation. This latter presents a maximum at r^*, called the critical radius, corresponding to the energetic barrier that has to be overcome to create a stable nucleus. If $r < r^*$, the r^2 surface term dominates ("creating surface costs too much") and the solid returns in the liquid state. If $r > r^*$ the bulk term is preponderant, the nucleus is stable and the solid can start to grow. This process is illustrated in Figure I.15(b) for the case $r = r^*$. In this configuration, there are equal chances for the nucleus to be stable or not.

The calculation of the value of r^* is done for :

$$\frac{\mathrm{d}\Delta G}{\mathrm{d}r^*} = 0 \quad \text{so it comes :} \; r^* = \frac{-2\gamma_{sol-liq}}{\Delta g_V} = \frac{-2\gamma_{sol-liq}\, T_m}{\Delta T\, \Delta H_s} = \frac{2\Gamma}{\Delta T}\,, \tag{I.11}$$

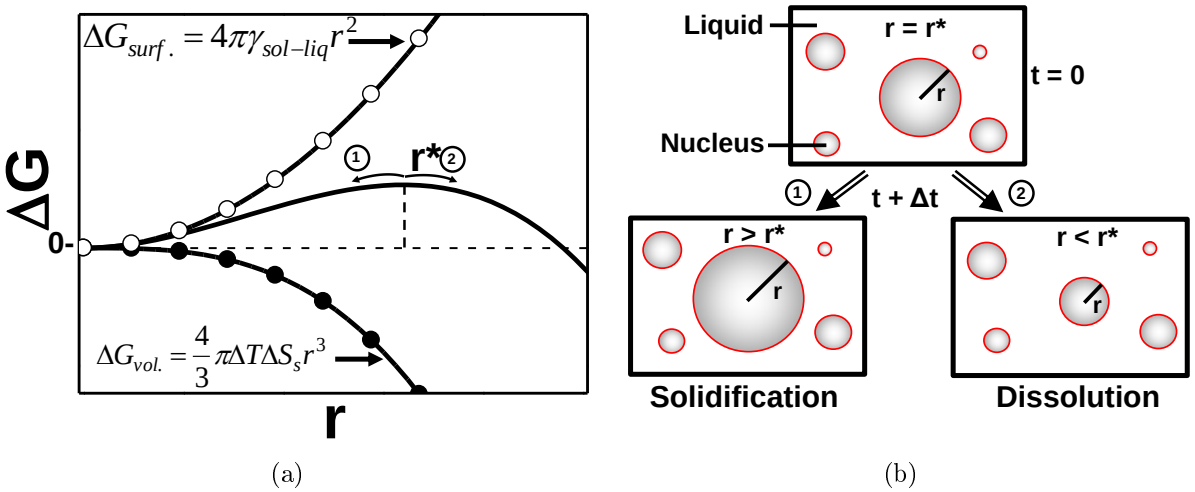

(a) (b)

Figure I.15 – (a) Plot of ΔG_{volume} and $\Delta G_{surface}$ as well as their sum ($\Delta G_{nucleus}$) as a function of r. The maximum of the $\Delta G_{nucleus}$ function is obtain for a nucleus of size r^*. (b) Illustration of two scenarios 1 (starting growth) and 2 (returning to liquid state) that can follow when a nucleus reaches a size of r^* (at t=0).

with $\Gamma = -\gamma_{sol-liq}\, T_m/\Delta H_s$ being the Gibbs parameter. In the case of pure gold, with $\gamma_{sol-liq} = 0.13$ J.m^{-2} (see section I.3.4), ΔH_s=-12.5 kJ.mol^{-1}=-1.22 10^9 J.m^{-3} and T_m=1336 K, the Gibbs parameter Γ is 1.45 10^{-7} K.m [xvi]. Therefore the more the liquid is supercooled (large ΔT), the smaller the critical radius is hence the easier it is for the liquid to solidify. The critical radius as a function of the supercooling value is plotted on the graph in Figure I.16.

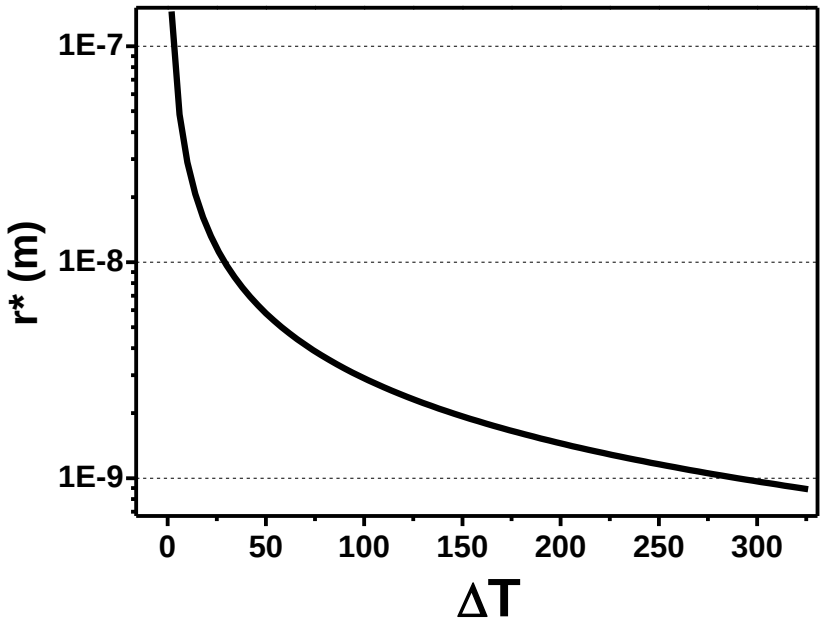

Figure I.16 – Supercooling dependence of the critical size of a forming nucleus for pure Au.

xvi. $\Gamma \sim 10^{-7}$ K.m for most metals.

Kinetics of nucleation

In the case of a cluster of critical size r^* (*i. e.* containing n^* atoms), the addition of another structural unit will lower its free energy (see previous section). It is however reasonable to assume that there exists an energetic barrier that has to be overcome due to the incorporation process (ΔG_{inc}), as illustrated in Figure I.17.

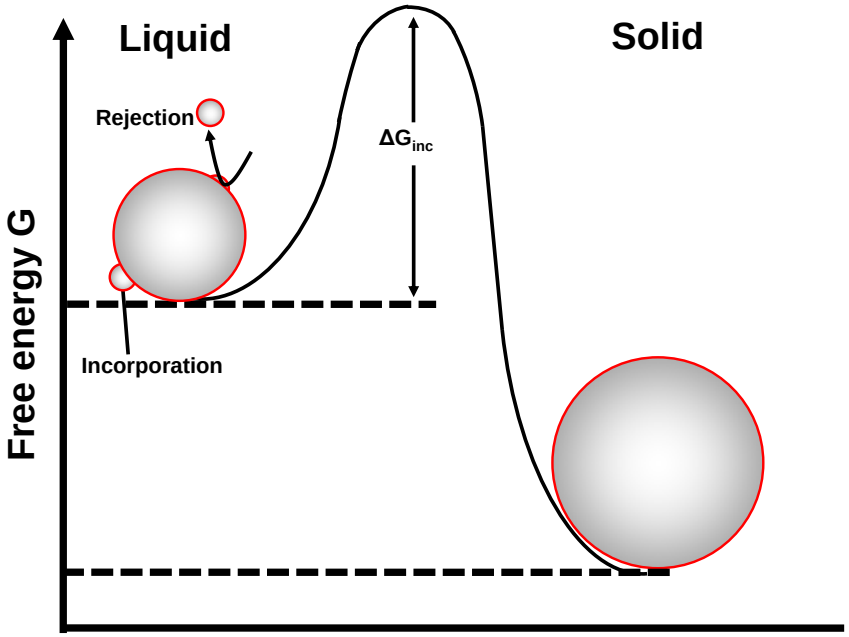

Figure I.17 – Plot of the free energy variation undergone by a solid which grows by addition of a structural unit. An energetic barrier has to be overcome for each new addition.

The nucleation rate corresponding to the incorporation of new atoms in the solid cluster is thus :

$$J = Ae^{-\frac{\Delta G^* + \Delta G_{inc}}{k_B T}} \tag{I.12}$$

with A a term encompassing the shape factor of the nucleus, the number of available nucleation sites at the liquid-solid interface and the vibrational frequency of the particles that try to overcome the barrier.

The conditions of formation of a stable nucleus as well as its capacity to grow in the liquid therefore depend on thermodynamical conditions but also on diffusion processes. This is why for example, it is possible to form solids presenting no crystalline structure (glasses) by quenching them. The cooling rate being very high, the atoms do not have enough time to diffuse and form a crystal : these particular solids can be seen as a frozen picture of the liquid state in a first approximation.

Until the 1950s, no large supercooling tendency had been observed in monoatomic liquid metals, most of them presenting a solidification temperature T_s reduced by 15 to 20% com-

paring to T_m [Turnbull, 1950b]. This suggested that the energetic barrier for nucleation was small. This assumption was supported by the fact that the coordination number for an atom in the liquid is $\sim$ 12 (see section I.4) and hence led to the idea that the liquid phase, of similar density, presented a short range order very similar to the future crystal structure. In other words : the liquid was supposed to be "ready to crystallize".

However, Turnbull himself showed that the supposed small barrier actually came from the heterogeneous nucleation : the formation of the solid phase is catalyzed by the presence of walls which serve as seed (*i. e.* as nucleus) [Turnbull, 1950c]. The quantitative influence of these seeds on the nucleation process is explained in the next section. They can be for instance impurities or more generally the inner wall of a crucible. For example, Turnbull showed that the supercooling of mercury droplets can range from 10 to 80 K depending on the material used for the crucible [Turnbull, 1952].

b Heterogeneous nucleation

In the case of heterogeneous nucleation, the nucleus is represented by a spherical cap in contact with a particle (*i. e.* the substrate) and the liquid phase (see Figure I.18).

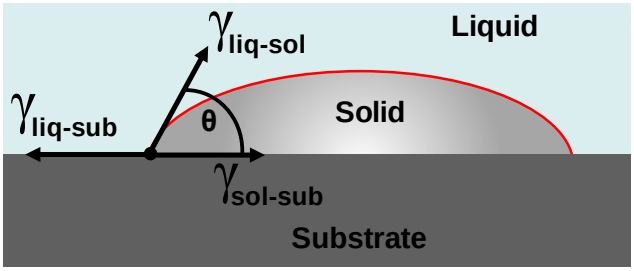

Figure I.18 – Picture of a solid spherical cap in contact with a substrate and its liquid.

The vectors in Figure I.18 represent the surface energies (in the same way as in section I.3.4) arising with the creation of the solid-liquid ($\gamma_{sol-liq}$), the solid-substrate ($\gamma_{sol-sub}$) and the liquid-solid ($\gamma_{liq-sub}$) interfaces. The variation of free enthalpy of the nucleus needs in this case to account for these different surface terms :

$$\Delta G_{nucleus} = \Delta G_{volume} + \Delta G_{surface} \text{ with } \Delta G_{surface} = f(\gamma_{sol-liq}, \gamma_{sol-sub}, \gamma_{liq-sub}) \quad \text{(I.13)}$$

The important feature is to compare how the creation of the nucleus is influenced by the presence of the solid substrate. Equation I.13 describing how the variation of free enthalpy of the nucleus in the heterogeneous case ($\Delta G_{nucleus}(het)$) is related to the one of the homogeneous case ($\Delta G_{nucleus}(hom)$) through the function f that only depends on the wetting angle

Θ :

$$\Delta G_{nucleus}(het) \;=\; \Delta G_{nucleus}(hom) \times f(\theta) \;\; \text{with } f(\theta) = \frac{1}{4}(2 - 3\cos\theta + \cos^3\theta) \qquad \text{(I.14)}$$

For heterogeneous nucleation, the value of the critical radius r^* is still $-2\gamma_{sol-liq}/\Delta T \Delta S_s$ (due to its definition) but the number of atoms in the nucleus, and even more important the nucleation rate, have changed in the same proportion as ΔG. With n and J the number of atoms present in the nucleus and the nucleation rate for the homogeneous case, the number of atoms and the nucleation rate in the heterogeneous case for the same value of r^* are $n_{het} = n\, f(\theta)$ and $J_{het} = J\, f(\theta)$.

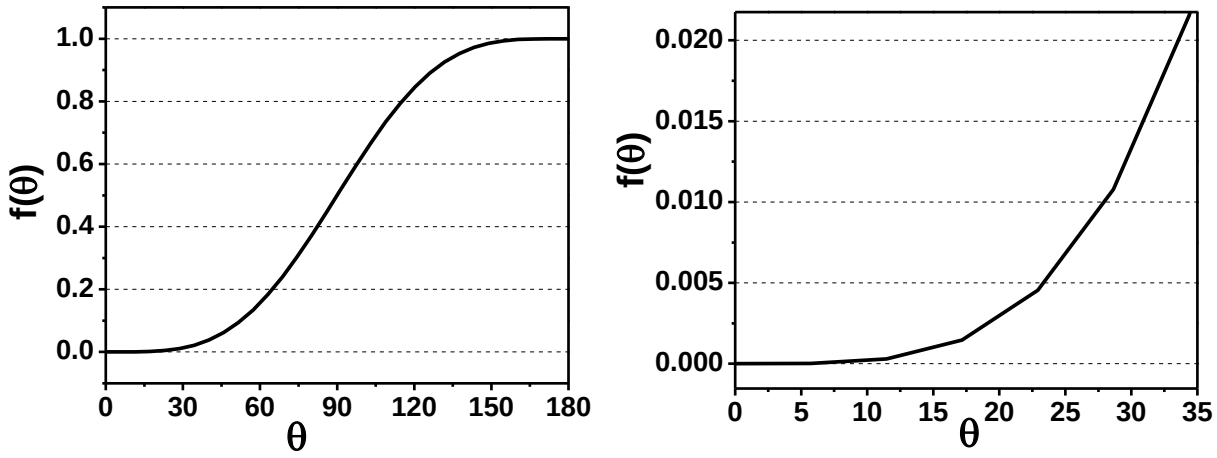

(a) (b)

Figure I.19 – (a) Plot of the function $f(\theta)$, the contact angle θ is taken in the solid phase. (b) Zoom on the low θ values highlighting the large influences undergone by good wetting solids.

The variation of the function $f(\theta)$ is plotted on the graphs in Figure I.19. This factor can extremely decrease the number of atoms of the nucleus as well as the nucleation rate needed to form a stable structure when the solid wets the substrate : $f(\theta) = 1.3\ 10^{-2}$ for $\theta = 30°$). The case $\theta = 180°$, corresponds to a non-wetting solid and thus the homogeneous case ($f(\theta) = 1$) is recovered.

In the light of these considerations on heterogeneous nucleation, experimental set-ups were devised to avoid heterogeneous nucleation. This could be achieved by the emulsification technique in which the liquid metal is separated into multiple droplets surrounded by an inert liquid (organic fluid) or through magnetic levitation (containerless technique) [Perepezko and Paik, 1984]. By use of these processes, it was found that liquid metals could be supercooled down to 20−30% of their melting temperatures before crystallizing.

The thermodynamic models described above (very briefly) are widely used to understand solidification processes or phase transition/equilibrium from a macroscopic point of view.

They can also be extended for example to the case of alloys and predict phase formations by the exploration of the phase diagram.

However, it is the observations of large undercooling of some elements that solidify into close-packed structures as well as the existence of intermetallic eutectics that led F.C. Frank to propose that the liquid structure itself must be responsible for its metastable behaviour.

I.5.2 Beyond the classical model : the icosahedral order

a Frank hypothesis

The Frank postulate, expressed in 1952 [Frank, 1952], pointed out that there exist three possible ways to put 12 spheres in contact with a common 13^{th}. The first two atomic arrangements are the well-known close-packed crystal structures (fcc and hcp). The third one, which he thought was even more trivial as he suggested that it "*comes to the mind of any good schoolboy*", consists in placing the atoms at the center of each face of a dodecahedron, *i. e.* at the vertex of an icosahedron (see Figure I.20). With this assumption, Frank proposed that as metallic liquids cool, local atomic structures containing icosahedral short range order (ISRO) develop in the liquid phase. With a description using this ISRO model, the liquid presents an average coordination number of 12 but is a bit denser[xvii] indicating that the liquid state is, at least locally, more stable.

This energetically favorable environment was confirmed by molecular dynamic simulation at the beginning of the 1980s by Steinhardt *et al.* in a simulated supercooled liquid with a simple Lennard-Jones potential [Steinhardt *et al.*, 1981; 1983]. Subsequently to the work of Frank, Mackay [Mackay, 1962] developed this idea. He showed that an association of distorted fcc tetrahedra can build icosahedron clusters (of more than 13 atoms) presenting 20 external {111} facets. The relation between the number of shells (L) in the cluster and the number of atoms N is given by $N = (10/3)L^3 + 5L^2 + 3L + 1$. For $L = 1$, we obtain the 13 atoms icosahedron (Figure I.20 shows the cases for $L = 2$). These clusters have already been observed experimentally [Ascencio *et al.*, 1998]. However their stability with increasing number of atoms remains unclear and strongly depends on the material.

The model proposed by Frank therefore deviates from the classical theory by the fact that the energy of the liquid is locally minimized by the formation of clusters with fivefold symmetry. Moreover, this pentagonal order[xviii] is incompatible with a translational periodicity so that long range order can not be achieved : it is impossible to tile a 2D space with pentagons nor a 3D space with icosahedron without creating defects (see Figure I.21). As a consequence,

xvii. It is known that the mean distance between neighbouring atoms is slightly smaller in the liquid than in the solid phase

xviii. An icosahedron belongs to the $\overline{m}35$ point group.

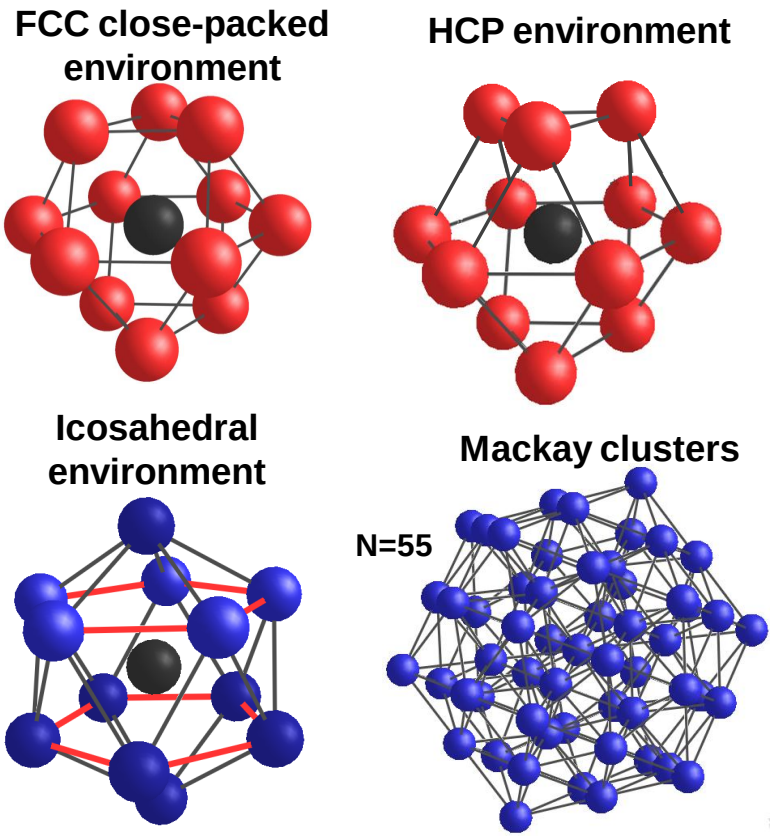

Figure I.20 – Top : Representation of two atoms (black) in different local atomic packings (red). Both are surrounded by 12 other atoms but one is in a FCC close-packed structure (left) and the other in a hexagonal close-packed environment. Both present a three-fold symmetry. Bottom : (left) In this case the black atom is also surrounded by 12 neighbours but is located in an icosahedral environment which presents five-fold symmetry highlighted by the two pentagons plotted in red. (right) Illustration of the Mackay cluster for L=2.

if a large number of atoms in the supercooled liquid are arranged in an icosahedral environment, the liquid-solid transition can take place only through deep configurational changes acting as a natural energetic barrier and the liquid state is favoured. The appearance of this new concept for the description of matter led Nelson and Sachdev to propose a mathematical

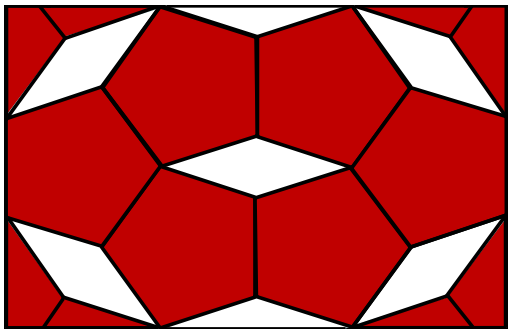

Figure I.21 – The tilling of the sheet plane with pentagonal pieces (in red) cannot be performed without the creation of empty areas (in white).

theory to model pentagonal order and defects in liquids and glasses [Nelson, 1983]. This description led to the conclusion that for a liquid presenting a pronounced ISRO, its classic pair correlation function should be modified by presenting a shoulder on the second peak [Sachdev and Nelson, 1984]. The description of this short range order also soon required a particular framework to distinguish between several local environments. This can be achieved by the use of four integers proposed by Honeycutt and Andersen in 1987 [Honeycutt and Andersen, 1987].

b Description of short range order (SRO) :

The description of the short range order consists in analyzing the distribution of the neighbours surrounding a reference atom. These clusters can have different geometries and the method consists in a nomenclature composed of four indexes. It allows one to distinguish between various local structures such as fcc, hcp, bcc and icosahedral environments by translating into numbers how two atoms are related to each other in a group of atoms. The four indexes are expressed as follows :

- the first indicates whether or not atoms composing the pair studied are near-neighbours,
- the second one corresponds to the number of common nearest neighbours shared by the reference pair,
- the third one is the number of bonds between common nearest neighbours,
- and the last one is used to distinguish structures with the same first three indexes but having different topologies.

Considering this, the fcc structure is described by pairs with 1421 indices whereas 1661 and 1441 pairs are typical of bcc configurations. Five fold symmetries are represented for example by pairs noted 1551 or 1541 and 1431 (for distorted structures) (see Figure I.22).

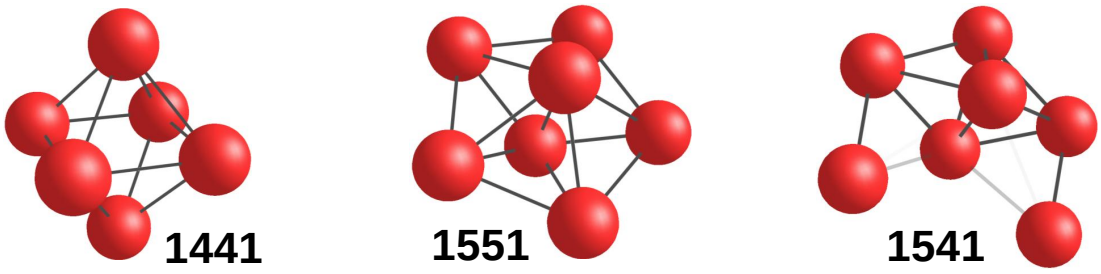

Figure I.22 – Schemes of different local atomic structure using the Honeycutt and Andersen indexes. 1441 (bcc), 1551 (pentagon) and 1541 (distorted pentagon).

The icosahedral order and common-neighbour analysis have been at the heart of many *ab-initio* molecular dynamics simulations studies to understand the structure of undercooled metallic liquids [Jónsson and Andersen, 1988; Jakse and Pasturel, 2003; Wang *et al.*, 2004;

Celino *et al.*, 2007; Kim and Kelton, 2007] and more recently the structure of metallic glasses [Sheng *et al.*, 2006; Jakse and Pasturel, 2008]. Nowadays, these models based on ISRO, already observed in metallic solid alloy AlMn [Shechtman *et al.*, 1984] and being a basic element of quasi-crystal description, are widely accepted as the origin of supercooling in metals.

However, experimental evidences of their existence in a metallic liquid phase only arose after long efforts as they are randomly orientated and are thus hard to reveal with scattering techniques. Formation of pentagonal clusters has first been observed in liquid lead at the interface with a silicon substrate [Reichert *et al.*, 2000]. In 2002, Schenk *et al.* revealed their existence in levitated Ni, Fe and Zr liquids by neutrons scattering [Schenk *et al.*, 2002]. Kelton *et al.* confirmed this by the use of X-rays and made the link between the increasing number of pentagonal clusters and the degree of supercooling, confirming Frank's theory [Kelton *et al.*, 2003; 2006]. Recently, simulations showed that in addition, icosahedral clusters can self-assemble in organized arrangements leading to the formation of defects in the growing crystal [Karayiannis *et al.*, 2011].

The liquid state as well as the solidification processes presented in this section from a general point of view are phenomena that play a significant role in the growth of SC nanowires and have to be controlled to create the desired object. Indeed the VLS growth is based on the use of a metal catalyst that can form a liquid alloy with the SC. Using the particular properties of the metal-SC alloys forming an eutectic, it is possible to grow nanowires at very low temperatures. However, the simple idea that the growth is only governed by the thermodynamic equilibrium composition given by the liquidus line[xix], which is very attractive and true from a macroscopic point of view, seems to be much more challenging to understand when looking a bit closer. The next section presents the difficulties encountered in the studies concerning the formation of eutectics and their use in SC growth.

I.6 Particular liquid behaviour :

Mixing two different materials can lead to many different phases. These different phases depend on the concentration of each element as well as the temperature and can be represented using a phase diagram. A good example of the complexity arising from the study of alloys is given in Figure I.23 which displays the phase diagram of the extensively studied Fe-Fe_3C. This system presents a large variety of different compounds with lots of particular points and equilibrium lines separating the different phases (and only for a Fe_3C concentration ranging

xix. at constant temperature.

from 0 to 7 %) [xx]

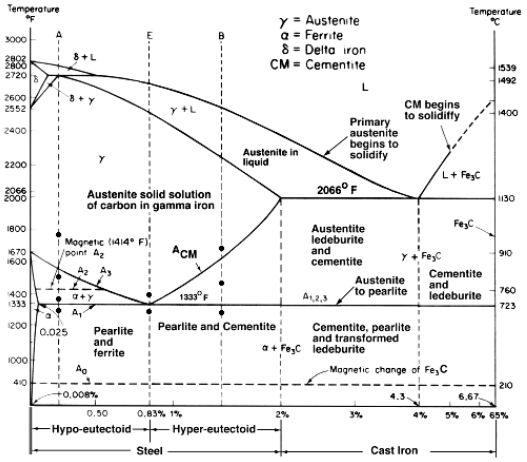

Figure I.23 – Fe-Fe_3C phase diagram [Pollack, 1988].

Here, we are not going to present all the features that can be present in a phase diagram, as it could fill an entire book. However the particular eutectic point already mentioned is of high importance in this study and is presented below in the case of the studied systems.

I.6.1 Thermodynamic and structure

It has already been introduced that the systems studied in this work (mostly AuSi but also AuGe or AlSi) display phase diagrams that are at the same time very simple and very complicated. For instance, the AuSi phase diagram (Figure I.8), is simple because it is only composed of five phases :

- the (AuSi) liquid phase,
- two domains into which the solid <Au> or <Si> and a liquid (AuSi) co-exist,
- and the two distinct fcc <Au> and diamond-like <Si> phases.

Interestingly no AuSi solid alloy exists in the bulk [xxi]. In the Au-Ge and Al-Si system however, a crystalline alloys for small concentration ranges of the SC element can form (often noted α phase).

Deep eutectic in liquid alloys attracted a lot of attention because of their surprisingly low melting temperature compared to the ones of the pure elements. In a sense they can almost be seen as very undercooled liquids. As we have seen, studying the structures of monoatomic liquids is already very complicated. It therefore seems to be even more complicated to deal with such particular eutectic alloys. The central question which still remains unanswered in

xx. Interactive binary phase diagrams can be found on this web page :
http ://www.crct.polymtl.ca/fact/Documentation/SGTE/SGTE_Figs.htm .

xxi. There is no mutual solid solubility of the two materials in bulk structure.

the case of glass-forming metallic alloys is whether or not the liquid/glass structure differs significantly from crystalline phases [Gaskell, 2011]. Many studies tried to answer this tricky question since the discovery of Klement who obtained the first metallic glass by quenching the AuSi eutectic liquid [Klement *et al.*, 1960].

Hume-Rothery and Anderson [Hume-Rothery and Anderson, 1960] were the first to propose an explanation for the compositions observed in eutectic alloys. The Hume-Rothery phases, assumed to form in the alloys, depend on the number of electron of each component by defining the electron atom ratio between the two species.

In the 1970s, thermodynamical studies started to set the first ideas. Calculations taking pure elements as starting points showed that the observed eutectic diverged a lot from prediction and this was explained using the assumed existence of the Au_3Si Hume-Rothery phase [Castanet *et al.*, 1978]. However the general theory proposed by Hume-Rothery *et al.* has encountered quite many exceptions in the description of eutectics an thus can not be taken as a prevailing criterion even if in certain cases their assumption seems to be verified [Tasci *et al.*, 2010].

Models and experiments were combined to describe the atoms interactions and it was proposed that metal-SC bonds were preferred to metal-metal bonds and SC-SC bonds [Waghorne *et al.*, 1976]. They also pointed out that other models that tried to extrapolate solid structures to predict the liquid one were inadequate as they failed to reproduce the density variation between the two states.

This description is supported by recent *ab-initio* simulations showing the Si-alloying effect in the liquid at the eutectic composition and the increase of the ISRO in the undercooled region. A potential correlation between ISRO and the decrease of diffusivity would also explain the tendency for the Au-Si eutectic to create an amorphous alloy [Pasturel *et al.*, 2010]. In addition, X-ray diffraction experiments yield the pair correlation function which was fitted by reverse monte carlo analysis highlighting the breaking of the Au-Au bonds around the eutectic temperature and the increase of the density of the liquid with decreasing temperature [Takeda *et al.*, 2007]. Using complementary neutron diffraction experiments and numerical simulations, it was also found that the mean distance in Au-Si bond for its respective eutectic concentration is 2.4 Å [Chirawatkul *et al.*, 2011].

More recently, the structures of Ag-Ge, Ag-Si, Au-Ge and Au-Si eutectic liquids have been explained through variations of the electrical resistivity which is believed to arise because of concentration fluctuations. These results were obtained consequently to the study of GaSb and InSn liquid alloys with the same technique [Aoki *et al.*, 2002]. Figure I.24 represents the homogeneous eutectic alloy (3) into which concentration fluctuations of the metal (1) and the SC (2) phases are supposed to form. Here, Φ_i and ρ_i are the resistivity and the volume

fraction of domain i, respectively. Assuming that domains 1 and 2 are very small, the relation between their volume fraction and the measured resistivity can be addressed at a given concentration of the alloy [Itami *et al.*, 2007] :

$$\Phi_1 + \Phi_2 = \frac{\Delta\rho}{\rho_3/\Phi_3} \tag{I.15}$$

with $\Delta\rho$ the difference between the reference resistivity for the homogeneous liquid (measured at high T, when no concentration fluctuations arise, for a given concentration) and the measured resistivity at a lower temperature (for the same concentration).

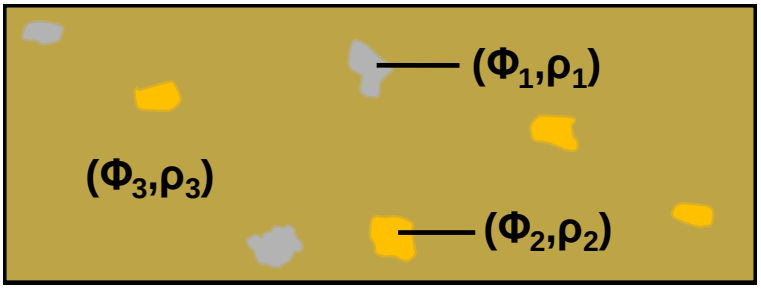

Figure I.24 – Illustration of the concentration fluctuations that are supposed to arise in eutectic liquids from resistivity measurement. The major part of the liquid is composed of an homogeneous metal-SC liquid but some regions present variation of concentration into which pure metal or pure SC phases develop. The concentration fluctuations are larger near the eutectic composition.

Repeating the measurements for several alloy concentrations, it is possible to plot the variation of $\Phi_1 + \Phi_2$ as a function of the alloy concentration for a certain temperature. This is done for the Au-Si alloy at the eutectic temperature in Figure I.25(a) which highlights that the concentration fluctuations are maximum for the eutectic composition. However, although concentration fluctuations are always maximum at the eutectic compositions, they also occur in a wide range of temperature even if they are smaller far from the eutectic temperature. This behavior is not fully understood to date.

It also seems that concentration fluctuations strongly depend on the "shape" of the eutectic. Figure I.25(b) displays the concentration fluctuations values at the eutectic point for several system as a function of the parameter chosen by Ikeda *et al.* [Ikeda *et al.*, 2002] :$\Delta T/\Delta^2 x$. ΔT is the difference between the SC melting temperature and the eutectic temperature T_e, Δx corresponds to the eutectic concentration with the SC phase taken as reference (0.81 for Au-Si and 0.72 for Au-Ge). It shows that a deep eutectic point (such as in the Au-Si system) presents larger concentration fluctuations than other systems (almost twice the amount of the Au-Ge system). This description therefore largely supports that a segregation process (see next section) takes place around the eutectic point and claims for a supposed poor tendency of these alloys to be supercooled below their eutectic point, as reported for the Ni-Nb

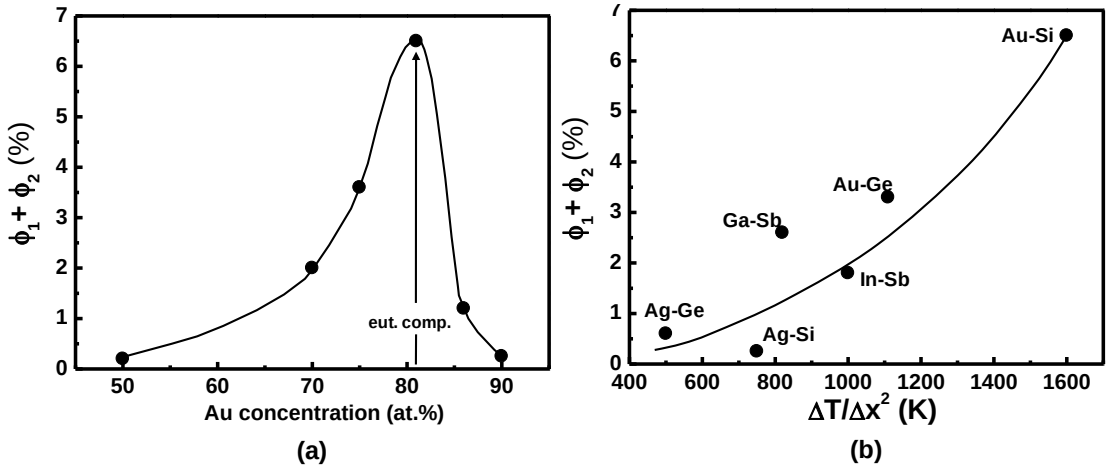

Figure I.25 – (a) Plot of the variation of $\Phi_1 + \Phi_2$ as a function of the gold content at T_e : maximum for the eutectic concentration. (b) Plot of the variation of $\Phi_1 + \Phi_2$ as a function of Ikeda *et al.* parameter [Itami *et al.*, 2007] (see text).

system [Itami *et al.*, 2010].

Through the different aspects described in this section, one can see that the structure of eutectic alloys is very complex and still challenges atomistic descriptions as strong alloying is known to arise in parallel to concentration fluctuations taken as the starting point of the solidification process [xxii].

I.6.2 Solidification of eutectic alloys

The understanding of the solidification process in eutectics and more generally in liquid alloys is very complex and, depending on the parameters [xxiii] as well as on the different components, can lead to many different structures. Detailed studies can be found in [Kurz and Fisher, 1998] and the references therein. Here we will very briefly present the basis of the theory to introduce the parameters that influence the solidification.

The solidification of eutectics and their subsequent morphologies are particular because of the simultaneous solidification of the different components present in the liquid. Let a binary eutectic alloy be solidified from its liquid phase into two lamellar non-miscible solid phases α and β via a thermal gradient (see Figure I.26(a)). The resulting solidification is equivalent to moving the solid-liquid interface at a rate v through the liquid.

This situation, compared to the growth of a single phase that would lead to solute diffusion and supercooling [Kurz and Fisher, 1998], is favourable since the unneeded atoms rejected by one phase serve for the growth of the other phase by the establishment of diffusion fields

xxii. In addition, recent simulations led to the discovery of a potentially stable AuSi solid phase [Tasci *et al.*, 2010].
xxiii. such as the composition or the cooling rate.

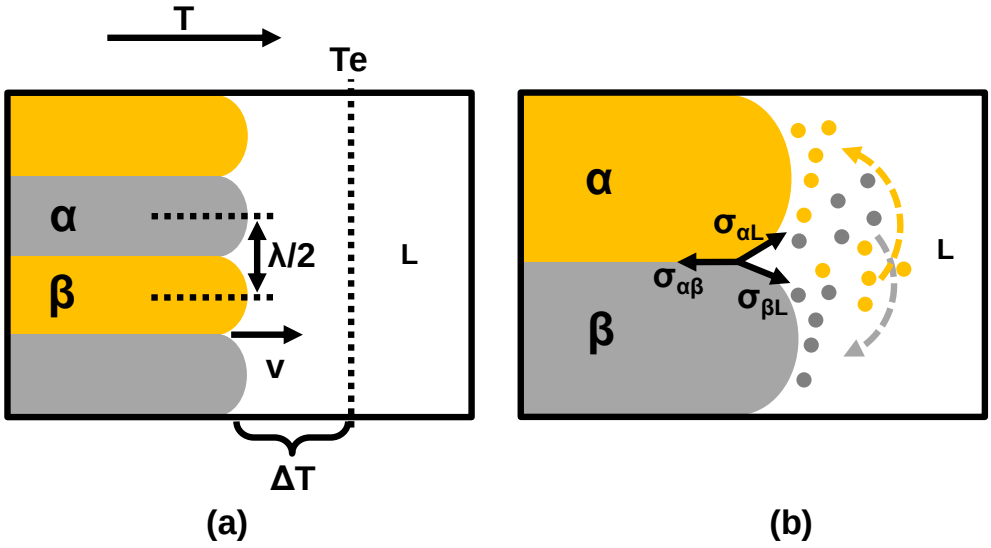

Figure I.26 – (a) Picture of a solidification process from an homogeneous eutectic liquid into two distinct solids separated by $\lambda/2$. The solid-liquid interface, moving at a speed v presents a temperature of solidification T_s differing from T_e. (b) The supercooling values arises from diffusion effects in the liquid in front of the interface and capillary effects at the α/β solid interface.

(see Figure I.26(b)). This clearly highlights the fact that eutectic growth is governed by mass transport in large solidification processes. Without going too much into details here, it is worth to say that the growth rate v, the lamellar spacing λ and the diffusion coefficients of the different components lead to different configurations of the liquid-solid interface as well as concentration variations along the interface. The diffusion and the capillary effects (represented by different vectors in Figure I.26(b)) are at the origin of undercooling ($\Delta T = \Delta T_{diff} + \Delta T_{cap}$). However, their effects vary in opposite directions so that the resulting ΔT value can be considered as constant for a given alloy. This kind of models as well as more refined ones have been used in many studies to understand the casting of alloys, especially in the Fe-C and Al-based system that present great practical uses.

However, despite the possibility of taking advantages of the composite properties of eutectic metal-SC alloys and the understanding we have so far on their casting behaviour, many fundamental questions remain unanswered, especially in their use in new fields such as in nanoscience among which unexpected effects arise.

The case of Al-based alloys upon undercooling and glass forming ability has been studied [Das *et al.*, 2001]. Liu *et al.* reported the microstructural changes of the Al-Ge eutectic for different solidification path [Liu *et al.*, 2003] as well as solidification process in the Al-Si system undercooled by levitation technique [Liu *et al.*, 2004]. Eswaramoorthy *et al.* described the symmetrical concentration changes arising between the solid and the liquid phase in an AlSi-based commercial alloy melted in an ethanol solution [Eswaramoorthy *et al.*, 2007].

In the case of Au-Si and Au-Ge alloys, strong interests arise in the field of metallic glasses since their discovery by Klement [Klement *et al.*, 1960], but also because of their use in nanomaterials production [Wagner and Ellis, 1964]. Gravity segregation experiments illustrated the separation of the elements and the subsequent crystallization at the eutectic temperature [Andersen *et al.*, 1971].

However, Chen and Turnbull studied the heat capacity and the enthalpy of the AuSi eutectic system cooled in fused silica to reproduce homogeneous conditions and reported an undercooling value (between T_e and observed T_s) of 70 K. They also observed the tendency of the liquid to be denser than the solid phase : when the liquid was quenched to create an amorphous alloy, the crucible remained intact whereas it was found broken when slowly cooled down due to the extension of the as-created crystal. At this time Chen and Turnbull already attributed the deep-lying eutectic of this system to the tendency for unlike atoms to associate when in the melts [Chen and Turnbull, 1967], in contrast with their separation to form the solid owing to the high stability of silicon in its covalent crystalline state.

This general approach however seems to be fine to described "bulk processes", whereas unexpected phenomena discovered recently and described in the next section seem to need further studies to be fully understood.

I.7 Specific features concerning nanowires growth

Although this work does not directly deal with nanowires growth, the study of their growth enables the observation of the liquid state in very small liquid droplets as these latter are required to grow small-diameter nanowires. In addition, several peculiar features are typical of nanowire growth and have to be presented here as their existence and their potential influence can be discussed throughout this manuscript.

I.7.1 Liquids in small dimensions

a Surface effects in small dimension

Designing objects at the nanometer scale leads to an increase of the surface-to-volume ratio. Consequently, surface effects can occur and modify the properties of the material. In our case, the important parameter is the equilibrium between the liquid and the solid phase for a given alloy. This is revealed, in the case of bulk alloys, by the phase diagrams presented in section I.3. However, it is possible to calculate how the size of the droplet modifies the eutectic temperature of the considered alloy. This size influence is presented in the work of Schmidt *et al.* who included surface Gibbs free energy in thermodynamical calculations [Schmidt *et al.*,

2010]. Their results, in the case of the Au-Si system, shows that a shift towards the low temperatures of more than 15 K can be expected for droplets smaller than 20 nm in diameter (for example : $\Delta T_e = 30$ K for a 10 nm droplet). The uncertainty of their expectations is however quite large as the experimental parameter values, used in the calculation, are difficult to measure. It is nevertheless commonly assumed that size effects have to be considered for systems presenting typical sizes of 10 nm or less [Schwalbach and Voorhees, 2008].

b Experimental observations

In a recent paper, Adhikari *et al.* presented both a theoretical and experimental work concerning the influence of size in the Au-Ge system [Adhikari *et al.*, 2007]. Their calculations predicted a lowering of the eutectic temperature of 40 K for a 10 nm diameter AuGe droplet at the tip of a Ge nanowire. However, their experimental observations revealed that the droplets could be supercooled about 100 K below the eutectic point. Their experimental results are comparable to those obtain by Kodambaka *et al.* who reported the growth of Ge nanowires through Au catalyst well below the eutectic point [Kodambaka *et al.*, 2007], as well as those presented by Sutter *et al.* describing the modification of the Au-Ge phase diagram for growth at nanoscale [Sutter and Sutter, 2008]. The explanations are however different from a study to another. Kodambaka *et al.* claim for a thermal-history and/or gas pressure dependence as well as a possible growth with a solid gold catalyst (see next section) whereas Adhikari *et al.* assumed that the Ge supersaturation needed to drive the Ge solidification at the interface, combined with an Au energetic homogeneous nucleation barrier due to size can be responsible for large undercooling.

In the case of the Au-Si system, Kim *et al.* studied the growth kinetics of solid Si by oversaturating an (AuSi) liquid droplet at a constant temperature on an amorphous membrane [Kim *et al.*, 2008]. In this study, they concluded that Si nucleation is a heterogeneous process, occurring at the edge of the droplet with no observable size effect down to 12 nm. In a similar subsequent study, 35 nm gold particles were exposed to disilane gas and the transformation of pure <Au> system into the two-phases <Au>+(AuSi) system was followed [Kim *et al.*, 2009]. In this case size effects were pointed out by the observation of a quite instant shrink of the <Au> phase as soon as this latter reached a size of about 8 nm.

Through these few examples, one can see that size effects have to be considered when examining phase transitions at the nanoscale. However, it is important to note here that they are studied most of the time in the particular case of nanowires growth and represent only the tip of the iceberg. Basically, these effects have to be studied in parallel with other modified parameters such as for example capillary effects or modification of the energy of the liquid/solid interface. The following brief presentation of special features about nanowire

growth serves as an illustration to show the difficulties encountered in this field as well as a basis for further discussion.

I.7.2 *In-situ* SC-nanowires growth

a Case of the Vapour-Solid-Solid process

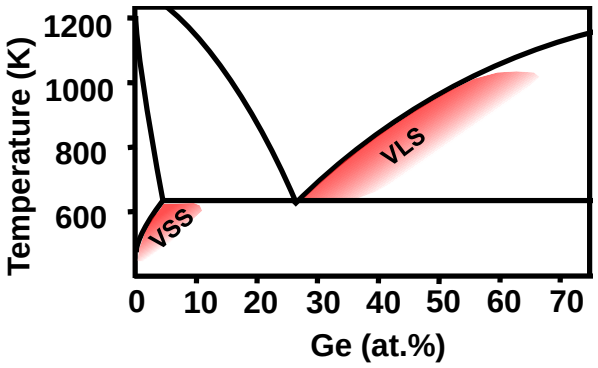

Figure I.27 – Illustration of the domain where VLS ans VSS process can occur in the case of the Au-Ge system phase diagram.

As already mentioned, it has been observed that Ge nanowires can grow below the eutectic temperature in the presence of a solid catalyst [Kodambaka *et al.*, 2007]. This suggests the existence of a Vapour-Solid-Solid process (VSS). This particular process was also supposed to arise during Si nanowires growth using an Al catalyst [Wang *et al.*, 2006] as well as for the tricky formation of sharp Si-Ge interfaces in nanowires heterostructures via a binary AlAu catalyst [Wen *et al.*, 2009]. The VLS process, simply uses the peculiar shape of the phase diagram that is the phase boundary between the (metal-SC) liquid phase and the (metal-SC)+<SC>. In the same way, the VSS process is related to the possible SC solubility in the solid metal, *i. e.* the existence of a <metal-SC> solid phase : increasing the SC content in the solid solution modifies the equilibrium and leads to the precipitation of the SC in excess (see Figure I.27).

As no solubility of Si exists in solid <Au>, these processes can not take place in this peculiar system. The advantages of the VSS process is the lowering of the growth temperature as well as the lowering of the solubility of the SC in the catalyst particle leading to the slowing down of the growth process.

b Equilibrium changes during growth

Figure I.28 displays a very common observation that is the expansion of the nanowire's diameter at its base. This behaviour which seems to be rather insignificant at first glance,

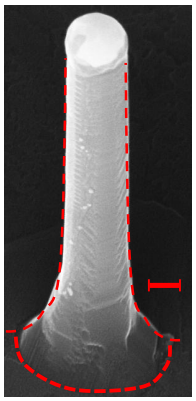

Figure I.28 – SEM picture of a Si nanowire grown on a Si(111) substrate through an AuSi liquid droplet and exposed to disilane. The scale bar is 100 nm [Zhou, 2011]

highlights an important characteristic : the interface energy equilibrium is not the same for a liquid catalyst droplet in contact with the substrate and with the nanowire.

This phenomenon is easy to observe by comparing the wetting angle presented by the catalyst droplet before growth and after. The catalyst droplet in contact with the flat substrate, in the case of the Au-Si system, displays a wetting angle (measured in the liquid phase) of about 43° [Ressel *et al.*, 2003] whereas it presents a much more spherical shape at the top of nanowire. This is due to successive equilibrium variations undergone by the interface as soon as the nanowire starts to grow. This is illustrated in Figure I.29 which shows the evolution of the contact between the droplet and the growing nanowire. This effect is a clear example of the difference that has to be accounted when comparing physical properties of a catalyst droplet at the tip of a nanowire and on a flat substrate.

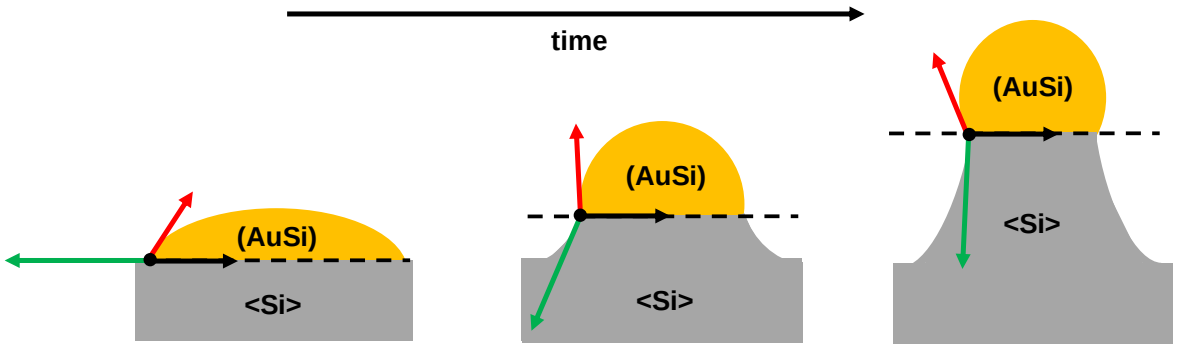

Figure I.29 – Scheme illustrating the change in surface energies during the growth of a nanowire, which can influence the physical behavior of the liquid catalyst.

c Coarsening, tapering and faceting effects during growth

As the topic of this work only concerns the very first events of the interactions between the metal catalyst and its underlying SC substrate, we will only mention here some remarkable features arising during growth. Using electron microscopy, Hannon *et al.* observed a coarsening process, based on the mechanism of Ostwald's ripenning. The surface diffusion of the gold atoms from small to large droplets present at the top of Si nanowires leads to different sizes and shapes of the nanowires (see Figure I.30) [Hannon *et al.*, 2006].

Another common observation is the tapering of nanowires during growth, as represented in the middle of Figure I.30 [Kodambaka *et al.*, 2006]. A tapered nanowire is the consequence of atomic diffusion of the metal catalyst at the surface of the nanowire. Therefore, the diameter of the droplet decreases as well as the one of the nanowire.

Finally, Figure I.30 (bottom) illustrates the faceting behaviour occurring on the nanowires sides [Ross *et al.*, 2005; David *et al.*, 2008]. This effect, mostly studied in the Au-Si system, consists in saw-tooth faceting of the nanowires sides : the nanowires sides perpendicular to the $< \bar{1}\bar{1}2 >$ substrate direction present alternative $(\bar{1}\bar{1}1)$ and $(\bar{1}\bar{1}3)$ orientated facets. These preferred orientations are supposed to depend on geometry and surface energies as well as on the droplet diameter and gold coverage.

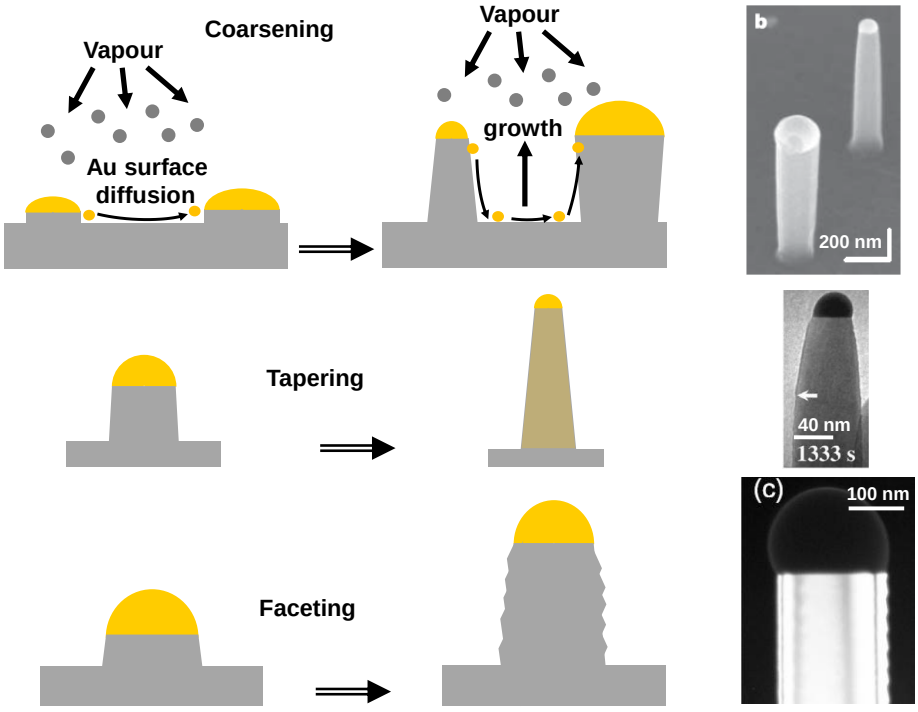

Figure I.30 – Schemes representing different processes influencing the shape of the nanowires. Top : the coarsening, middle : the tapering and bottom : the faceting. The associated pictures illustrating each process are taken from [Hannon *et al.*, 2006],[Kodambaka *et al.*, 2006] and [Ross *et al.*, 2005], respectively.

I.8 Liquid behaviour close to interfaces

I.8.1 Liquid-Vapour interfaces : layering effect

The layering phenomenon in liquids consists in the organization in the form of layers of the atoms just below the surface of a liquid. It has been first observed in complex liquids containing highly anisotropic molecules or liquid crystals and is supposed to arise because of the high length of the structures composing the liquid. In metals, surface melting (liquid formation at the surface of a bulk solid below T_m [xxiv]) is a quite common phenomenon [Frenken and van der Veen, 1985], whereas formation of a solid at the liquid/vapour interface, theoretically predicted in 1981 [D'Evelyn and Rice, 1981], is a more recently discovered feature.

The layering of liquid metals and alloys can be detected by X-ray reflectivity which displays a peak characteristic of the formation of organized layers perpendicular to the interface. In the case of Ga [Regan *et al.*, 1995], In [Tostmann *et al.*, 1999], Hg [Magnussen *et al.*, 1995], Sn and Bi liquids [Pershan *et al.*, 2009b] as well as in eutectic liquid alloys BiSn [Shpyrko *et al.*, 2005] and AuGe [Pershan *et al.*, 2009a], reflectivity experiments revealed that the two to three first liquid layers are well defined such as those at the surface of their respective crystals. For all these cases however, no long range order parallel to the surface has been reported.

In the case of the particular AuSi system, it has been recently reported that the layering effect is much more pronounced and occurs in the first seven to eight layers, as represented in Figure I.31 [Shpyrko *et al.*, 2006].

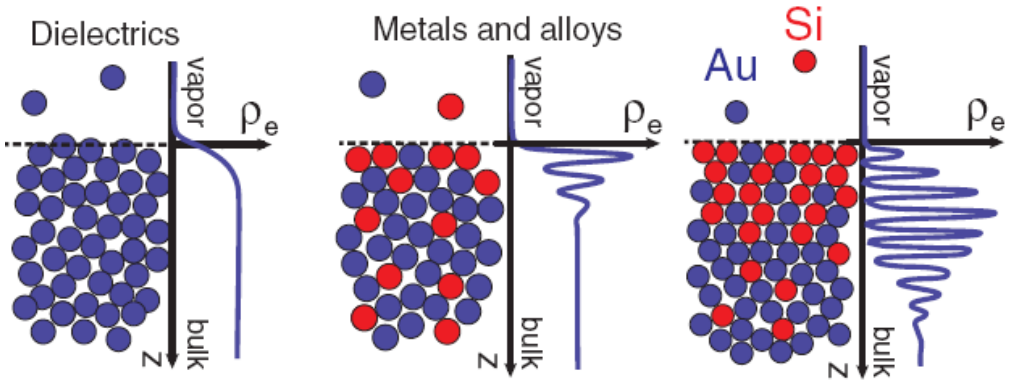

Figure I.31 – Representation of the electronic density variations reflecting the layering effect arising at a vapour-liquid interface and decaying with depth. It is enhanced in the case of metals and alloys (comparing the two first images) and even more pronounced in the case of the Au-Si liquid alloy [Shpyrko *et al.*, 2006].

In addition, contrary to other metals and alloys studied to date, the topmost layer exhibits a lateral long-range crystalline order (2D crystal) (see Figure I.32) whereas the underneath

xxiv. This phenomenon arises for example at the surface of ice makes it (more) slippery.

layers lateral order is liquidlike. This 2D crystal, floating on the layered liquid, is found to be stable up to 700 K and undergoes a solid-solid transition at 640 K between a low temperature (630 K-640 K) and a high temperature (640 K-700 K) phase [Shpyrko *et al.*, 2007]. Further experiments using synchrotron radiation and a more precise model that takes into account surface stiffness revealed that the low-T phase is a bilayer which transforms into the monolayer high-T phase [Mechler *et al.*, 2010].

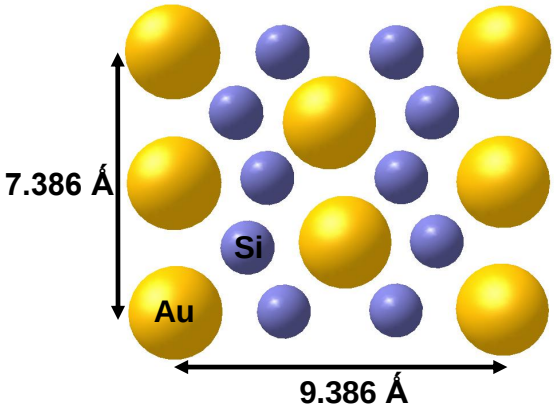

Figure I.32 – Unit cell of the low temperature 2D Au-Si crystal phase existing at the surface of the eutectic AuSi liquid [Shpyrko *et al.*, 2007].

It is worth mentioning here that other Au-SC alloys studied, such as Au-Sn and Au-Ge, do not present 2D surface crystal structure nor enhanced layering. This confirmed the idea that although Ge is very similar to Si, Au-Ge and Au-Si are very different alloys. This is already highlighted by the fact that in spite of similar eutectic temperature, the eutectic composition differs a lot and that a small fraction of Ge is soluble in solid Au.

A comparable situation has to be studied in the case of the liquid structure and concerns the solid-liquid interface. This is the topic of the next section.

I.8.2 Liquid-Solid interfaces

In this section, processes that are known to arise at the interface between a liquid and solid are presented from an atomistic point of view. Theses concepts will be very useful to understand the influence of the substrate's structure on the liquid droplet structure discussed in the last chapter of this manuscript.

In 1975, Spaepen was the first who tried to establish a theory for the influence of the solid's structure on the liquid. His work was based on modeling of hard spheres. Assuming that a certain topological continuity must exist between the solid and the liquid and that the liquid must present a maximum of density via close-packing, he predicted the conditions for placing atoms at the interface in the first two adjacent liquid layers. His results predicted

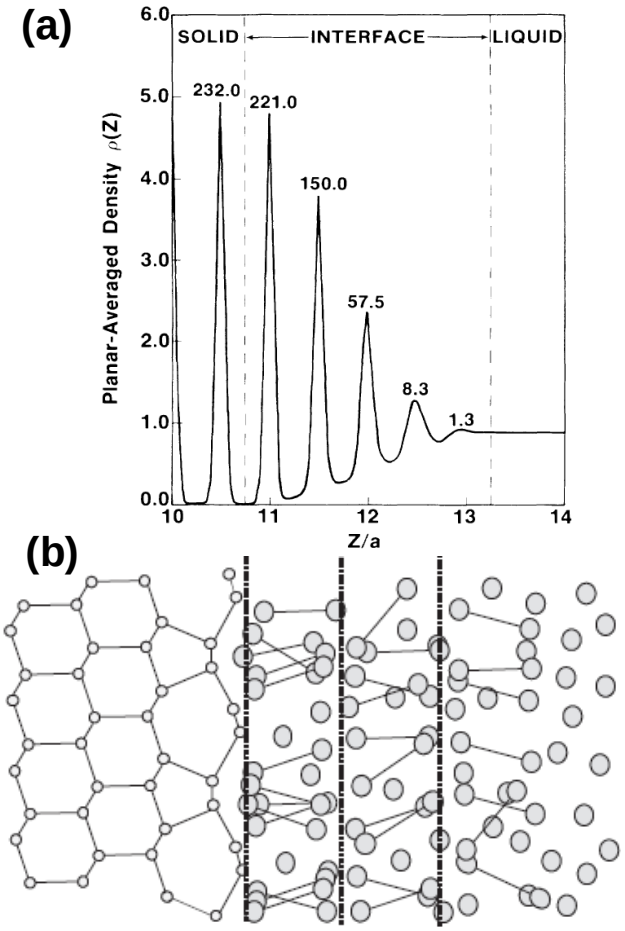

Figure I.33 – (a) Simulation results showing the variation of the planar-averaged density as a function of the distance from the solid phase revealing a kind of transition slice of liquid into which the atoms are ordered. The ordering being lost with the distance from the solid [Curtin, 1987]. (b) Corresponding phenomenon in liquid Ga in contact with a diamond substrate [Huisman *et al.*, 1997].

that the maximum of density found in the liquid and consistent with a long range order can be achieved by filling the first two liquid layers with equal quantity of triangular, rectangular and pentagonal structural units [Spaepen, 1975].

Without regarding the ordering parallel to the solid surface, simulations have predicted that a transition area should exist between the perfectly ordered crystal and the disordered liquid [Curtin, 1987]. As shown in Figure I.33(a), this transition can extend over several atomic layers. However, it has only been demonstrated experimentally in 1997 by Huisman *et al.* [Huisman *et al.*, 1997]. By choosing a low temperature liquid metal (Ga) on a (111) diamond substrate which is transparent to X-ray, reflectivity measurements revealed the organization of the atoms close to the surface into bi-layers (see Figure I.33(b)).

A very nice work, performed by Oh *et al.* with electron microscopy techniques, made possible direct observations of the ordering of liquid Al atoms in contact with a Al_2O_3 solid as shown in Figure I.34 [Oh *et al.*, 2005]. This density fluctuation phenomenon is now widely

accepted to occur and even if further studies are required, it seems reasonable to think that this ordering triggers nucleation processes, the liquid phase starting to adapt the structure of its respective crystal [Greer, 2006].

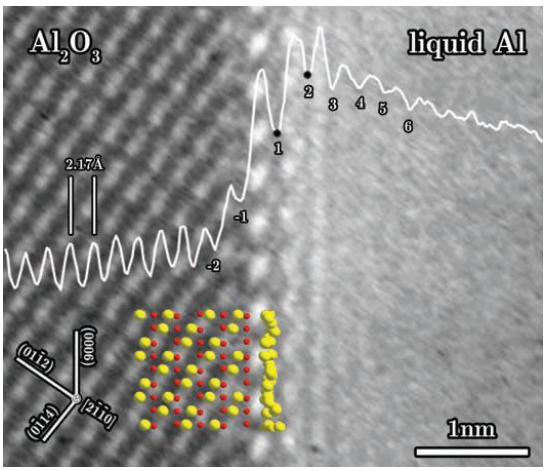

Figure I.34 – Transmission Electronic Microscopy image revealing the layering of the first layers in liquid Al in contact with the Al_2O_3 substrate [Oh *et al.*, 2005]

However, despite continuous improvements of characterization techniques it is still hard to depict clearly the atomic order, if it exists, within a liquid layer or what happens if the liquid material is different from the underlying substrate. Reichert *et al.* reported the first measurement of pentagonal lateral ordering at the interface of liquid lead and a Si(001) substrate [Reichert *et al.*, 2000]. Using extensive Monte Carlo simulations, Heni *et al.* studied the influence of the substrate interface on the pentagonal short range order that can exist in a liquid phase as presented in section I.5.2 [Heni and Lowen, 2002]. They report that an attractive surface, leading to strong attraction between the atoms of the two phases, can locally increase the density and therefore promote five-fold symmetry. These results therefore suppose that if the ordering close to the interface is incompatible with crystal structure, the liquid phase could still be stabilized whereas a solid in contact with the liquid is commonly assumed to trigger heterogeneous solidification.

In this chapter, we have presented the different elements constituting the scientific framework of this study. Before investigating the specific behaviour of Au on Si substrates towards growth and dewetting (Chapter III), formation of reconstruction (Chapter IV) and solidification (Chapter V and VI), we described in the next chapter (Chapter II) the technical aspects constituting the experimental framework.

Chapter II

Methods and experimental set-up

Contents

The aim of this chapter is to explain the basic concepts that are essential to understand the techniques presented and used later in this work. Beyond the results described in the following chapters, it is important to know how they are obtained as well as under what kind of experimental conditions. In a first section, we present some general characteristics on the use of X-ray and give some precisions concerning the investigation of reciprocal space in this particular framework (see section II.1). In a second one, the different techniques using X-ray scattering to probe the matter are described (see section II.2). The experimental set-up is presented in the last section (see section II.3).

II.1 X-ray scattering by a surface

Reflection and refraction phenomena of an electromagnetic wave at an interface are common for all wavelengths and are describe by Snell's law and Fresnel equation. These phenomena, arising at the interface between two media, result from their difference of refractive indexes, which themselves depend on the wavelength. Total reflection happens when the incoming wave travels from a medium with a higher index to a medium with a lower index of refraction. In the case of visible light, most of materials have a refractive index larger than the one of air, therefore, total reflection happens at the material/air interface inside the material. This is called total *internal* reflection and is widely used, for example, to transmit information through optical fibers.

In the case of X-rays (shorter wavelength), the refractive index of most materials becomes slightly smaller than that of air so that total reflection can occur. We will see here how probing surfaces and/or interfaces with X-rays justifies the use of grazing incidence.

II.1.1 X-rays refraction at an interface

As we have seen, the important parameter is the index of refraction n. For X-rays in condensed matter, n is written :

$$n = 1 - \delta + i\beta \tag{II.1}$$

with :

$$\delta = \frac{1}{2\pi}\frac{e^2}{mc^2}N_a\frac{\sum_i(Z_i - f_i')}{\sum_i A_i}\rho\lambda^2 \qquad \text{and} \qquad \beta = \frac{1}{2\pi}\frac{e^2}{mc^2}N_a\frac{\sum_i f_i''}{\sum_i A_i}\rho\lambda^2 \tag{II.2}$$

where N_a is the Avogadro's number, ρ the density (g.cm^{-3}) and λ the wavelength (Å). For each atomic species i, A_i (g.mol^{-1}), Z_i, f_i' and f_i'' are the atomic mass, the scattering factor (equivalent to f_j in section II.1.2), the dispersion factor and the absorption factor, respectively.

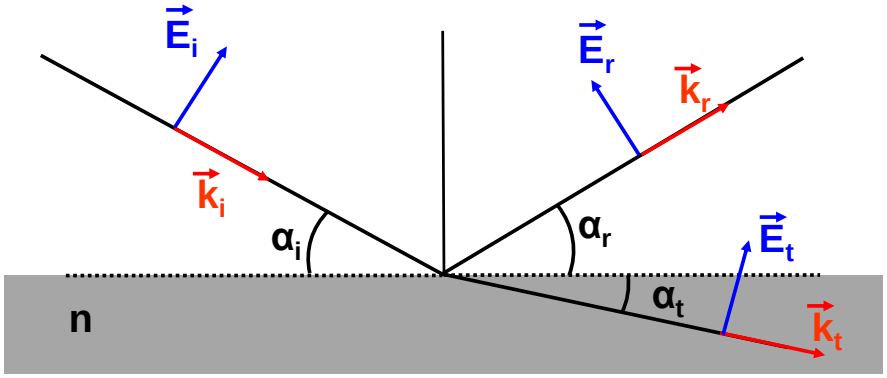

Figure II.1 – Scheme of the refraction of X-rays at an interface (with the polarization in the incident plane)

Typical orders of magnitude are $\sim 10^{-5}$ for δ and $\sim 10^{-6}$ for β which implies that the real part of n is slightly smaller than 1 for X-rays. If we apply the classical Snell-Descartes law to the configuration presented in Figure II.1, it comes :

$$n\cos\alpha_t = \cos\alpha_i \quad \text{which becomes, for small } \alpha_i \text{ and } \alpha_t : \ \alpha_t^2 = \alpha_i^2 - 2\delta + 2i\beta \tag{II.3}$$

The critical angle α_c is a peculiar value of α_i below which total external reflection occurs (*i. e.* α_t=0). From equation (II.3), we can deduce :

$$\alpha_c = \sqrt{2\delta} \tag{II.4}$$

Therefore, α_c as well as δ, depend on the material and on the photon energy (*i. e.* on the wavelength as $1/E \sim \lambda$), its value being of the order of a few tenth of degree. Let us now have a look at the behaviour of the transmitted beam which serves to probe the sample. Its wave vector takes the form :

$$\mathbf{k}_t = k_0 \begin{pmatrix} \cos\alpha_i \\ 0 \\ A - iB \end{pmatrix} \quad \text{with} \quad k_0 = \frac{2\pi}{\lambda} \tag{II.5}$$

with, in the small angle approximation :

$$A = \frac{1}{\sqrt{2}}\left(\sqrt{(\alpha_i^2-\alpha_c^2)^2+4\beta^2}+\alpha_i^2-\alpha_c^2\right)^{1/2} ; B = \frac{1}{\sqrt{2}}\left(\sqrt{(\alpha_i^2-\alpha_c^2)^2+4\beta^2}+\alpha_c^2-\alpha_i^2\right)^{1/2} \tag{II.6}$$

The amplitude of the transmitted wave (A_t) at a point $\mathbf{r}$ is proportional to $e^{-i\mathbf{k}_t\cdot\mathbf{r}}$:

$$A_t \propto e^{-ik_0(x\cos\alpha_i + Az - iBz)} \propto e^{-ik_0(x\cos\alpha_i + Az)} e^{-k_0 Bz} \propto e^{-i\mathrm{Re}(\mathbf{k}_t)\cdot\mathbf{r}} e^{-k_0 Bz} \tag{II.7}$$

We can thus write the expression of the transmitted intensity I_t :

$$I_t = A_t A_t^* \propto e^{-i2\mathrm{Re}(\boldsymbol{k}_t)\cdot\boldsymbol{r}} e^{-2k_0 Bz} \propto e^{-i2\mathrm{Re}(\mathbf{k}_t)\cdot\mathbf{r}} e^{-z/l} \quad \text{with } l = \frac{1}{2k_0 B} = \frac{\lambda}{4\pi B} \tag{II.8}$$

The transmitted intensity decreases exponentially, with l its penetration depth. Figure II.2(a) shows the variation of the penetration depth for different energies. For $\alpha_i < \alpha_c$, l is no longer energy dependent, but only material dependent.

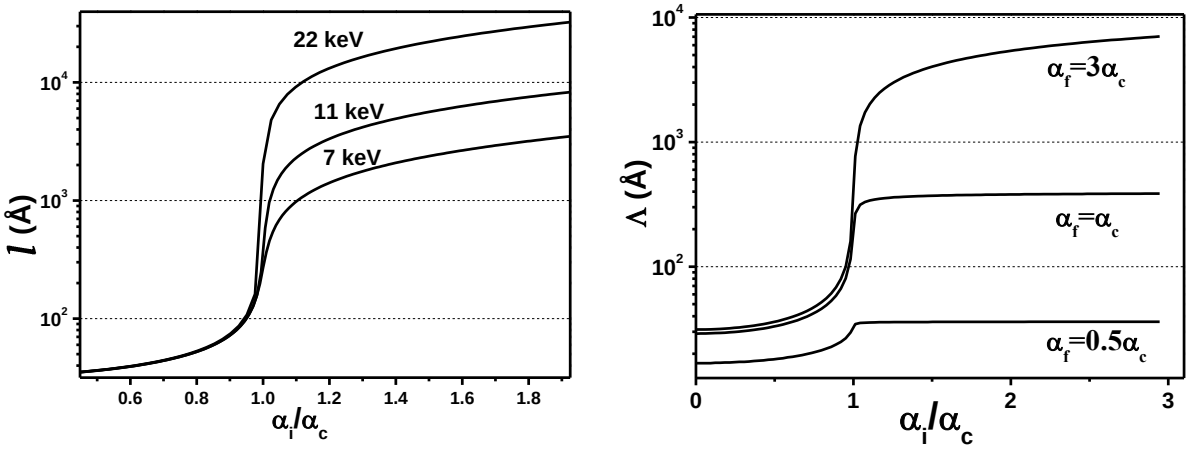

(a) (b)

Figure II.2 – Variations of the scattering depth (a) as a function of the incident angle for three different energies, (b) as a function of the incident angle for exit angles equal to half, one and three time the critical angle for a Si surface and an incident wavelength of 1.1 Å (*i. e.* 11 keV, δ=4.03 10^{-6} and β=5.04 10^{-8}).

However, as the scattered intensity is measured outside the material, the same procedure must be applied to the wave which goes through the material to the air. The Helmotz's reciprocity principle ensure a symmetrical solution so that α_i can be replace by α_f for identical formulations. The scattering depth therefore becomes :

$$\Lambda = \frac{\lambda}{4\pi(B_i + B_f)} \tag{II.9}$$

where i and f indicate the use of α_i and/or α_f in all the previous formula. The variation of the scattering depth as a function of the incident angle for several values of the exit angle is plotted in Figure II.2(b).

A convenient way to illustrate the propagation of X-ray in the material also consists in neglecting the absorption, which means that β=0 in the equations. With this assumption, for $\alpha_i < \alpha_c$, the real part of k_z equals zero (*i. e.* α_i becomes imaginary in equation (II.6) for A), therefore $\mathbf{k}$ has a real component only along $\mathbf{x}$. This means that the wave propagates only along the interface with an amplitude decreasing quickly perpendicular to the interface. For

incident and exit angles with values close to the critical angle, the propagation takes place from 10 to 100 Å below the interface (Figure II.2(b)).

Still in the small angle approximation, we recall here the equations for the amplitude reflection r ($|\mathbf{E}_r| = r\,|\mathbf{E}_i|$) and transmission t ($|\mathbf{E}_t| = t\,|\mathbf{E}_i|$) coefficients :

$$r = \left(\frac{\alpha_i^2 - 2\alpha_i A + A^2 + B^2}{\alpha_i^2 + 2\alpha_i A + A^2 + B^2}\right)^{1/2} \qquad t = \frac{2\alpha_i}{(\alpha_i^2 - 2\alpha_i A + A^2 + B^2)^{1/2}} \tag{II.10}$$

The square of these coefficients (R=r^2, T=t^2) illustrate the intensity variation during the process. Their variations as a function of the incident angle are plotted in Figure II.3.

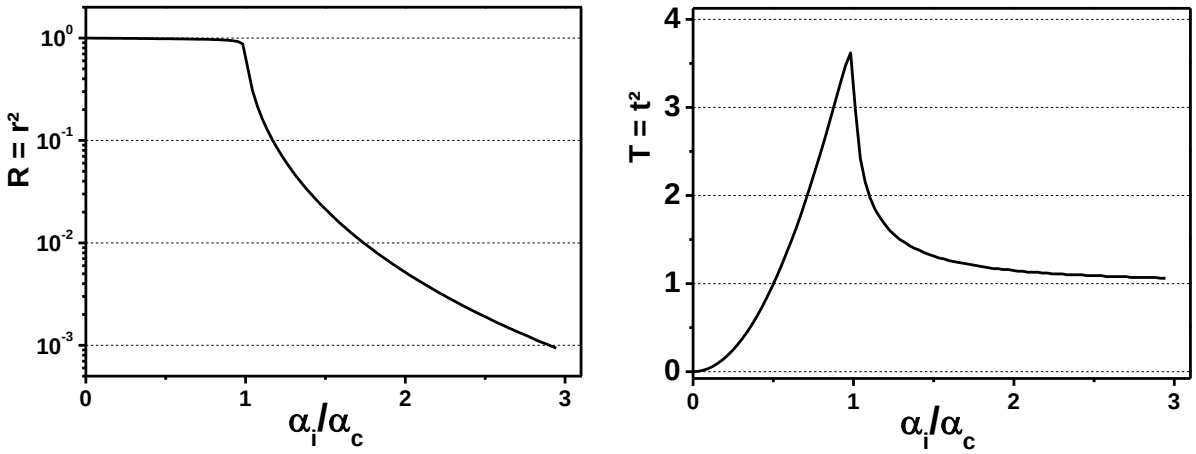

(a) (b)

Figure II.3 – (a) Reflection and (b) transmission coefficients for the intensity as a function of the incident angle for a Si surface and 1.1 Å wavelength (11 keV).

For $\alpha_i \leq \alpha_f$, R=1 which corresponds to total external reflection. At the same time, the transmission coefficient reaches a maximum : t=2 (when neglecting absorption) for $\alpha_i = \alpha_f$ which means that the amplitude of the transmitted wave is twice its amplitude in vacuum.

All these considerations claim for the use of grazing incidence. When working with α_i and/or α_f very close to the critical angle, the scattering by the surface atoms is enhanced while the bulk signal is reduced to its minimum. With this technique, the atoms that are probed are those contained between the surface and a depth of the order of Λ.

II.1.2 Basic X-rays diffraction

In this section, we simply recall the basic equations governing the intensity scattered by a three-dimensional crystal. We also present some specific features encountered in the specific case of surface diffraction. A detailed description of X-ray diffraction is available in standard textbooks [Warren, 1969; James, 1982].

a Diffraction by a 3D crystal

The intensity scattered by solid structure into which the atoms are distributed in N_1, N_2 and N_3 unit cells along the three crystal directions defined by the vector $\mathbf{a}_1$, $\mathbf{a}_2$ and $\mathbf{a}_3$ is given by :

$$I(\mathbf{Q}) = CF^2(\mathbf{Q})S^2_{N_1}(\mathbf{Q}\cdot\mathbf{a}_1)S^2_{N_2}(\mathbf{Q}\cdot\mathbf{a}_2)S^2_{N_3}(\mathbf{Q}\cdot\mathbf{a}_3) \tag{II.11}$$

where C is a constant and :

$$S_N(\mathbf{Q}\cdot\mathbf{a}_j) = \sum_{n=0}^{N-1} e^{i\mathbf{Q}\cdot\mathbf{a}_j\cdot n}, \quad j = 1,2,3 \tag{II.12}$$

The structure factor $F(\mathbf{Q})$ is expressed as :

$$F(\mathbf{Q}) = \sum_{j \text{ unit cell}} f_j e^{i\mathbf{Q}\cdot\mathbf{r}_j} \tag{II.13}$$

where $\mathbf{r}_j$ indicates the atomic position within the unit cell and f_j is the scattering factor of atom j. Moreover the interference function of N_j diffracting units is given by :

$$S^2_{N_j}(\mathbf{Q}\cdot\mathbf{a}_j) = \frac{\sin^2(N_j\mathbf{Q}\cdot\mathbf{a}_j/2)}{\sin^2(\mathbf{Q}\cdot\mathbf{a}_j/2)}, \quad j = 1,2,3 \tag{II.14}$$

The intensity is therefore the combination of the structure factor which only depends on the positions of the atoms within the unit cell, and the form factor representing the shape of the crystal. With this description, it becomes clear that the intensity function $I(\mathbf{Q})$ presents maxima (*i. e.* existence of Bragg peaks) for particular values, which are called the Laue conditions :

$$\begin{cases} \mathbf{Q}\cdot\mathbf{a}_1 = 2\pi h \\ \mathbf{Q}\cdot\mathbf{a}_2 = 2\pi k \qquad \text{where } h, k \text{ and } l \in \mathbb{Z} \\ \mathbf{Q}\cdot\mathbf{a}_3 = 2\pi l \end{cases} \tag{II.15}$$

The intensity is therefore equal to zero unless $\mathbf{Q}$ is a vector of a lattice defined by basic vectors ($\mathbf{b}_1$,$\mathbf{b}_2$,$\mathbf{b}_3$) into which $\mathbf{Q} = h\mathbf{b}_1 + k\mathbf{b}_2 + l\mathbf{b}_3$. The diffraction process are thus measured in the reciprocal space described by this new lattice called the reciprocal lattice, related to the real lattice ($\mathbf{a}_1$,$\mathbf{a}_2$,$\mathbf{a}_3$) by :

$$\mathbf{b}_1 = \frac{\mathbf{a}_2 \wedge \mathbf{a}_3}{\mathbf{a}_1\cdot\mathbf{a}_2\wedge\mathbf{a}_3}; \qquad \mathbf{b}_2 = \frac{\mathbf{a}_3 \wedge \mathbf{a}_1}{\mathbf{a}_2\cdot\mathbf{a}_3\wedge\mathbf{a}_1}; \qquad \mathbf{b}_3 = \frac{\mathbf{a}_1 \wedge \mathbf{a}_2}{\mathbf{a}_3\cdot\mathbf{a}_1\wedge\mathbf{a}_2} \tag{II.16}$$

With this definition : $\mathbf{Q} = h\mathbf{b}_1 + k\mathbf{b}_2 + l\mathbf{b}_3 = \mathbf{Q}_{hkl}$. For a 3D infinite crystal without defect, the reciprocal space is thus composed of (h, k, l) points of intensity (called Bragg

reflections) forming a periodic network. Each (h, k, l) reciprocal reflection corresponds to a family of periodic atomic planes composing the crystal which interfere with the incoming wave in a constructive way[i]. The distance d_{hkl} between two (h, k, l) planes of this family is given by $d_{hkl} = 2\pi/|\mathbf{Q}_{hkl}|$. Moreover, $\mathbf{Q}_{hkl}$ is perpendicular to the (h, k, l) plane and its length is $|\mathbf{Q}_{hkl}| = 4\pi\sin(\theta)/\lambda$[i]. From this we can extract the well known Bragg's law :

$$2d_{hkl}\sin(\theta) = \lambda \tag{II.17}$$

When the Laue conditions are fulfilled (*i. e.* at the position of a reflection), the intensity is thus given by :

$$I_{hkl} = CF_{hkl}^2 N_1^2 N_2^2 N_3^2 \tag{II.18}$$

and the structure factor takes the form :

$$F_{hkl} = \sum_{j \text{ unit cell}} f_j e^{2\pi i(hx_j+ky_j+lz_j)} e^{-M_j} \tag{II.19}$$

where x_j, y_j and z_j are the fractional coordinates of the considered atom j in the unit cell and M_j its Debye-Waller factor.

b Diffraction by a reconstructed surface : rods of scattering

In the case of surface reconstruction (see section I.3.2), the crystal is a quasi 2D structure with a finite thickness. Taking the vector $\mathbf{a}_3$ equal to this thickness corresponds to set N_3 equal to 1 in equation II.18. Therefore, in the Laue condition $\mathbf{Q}\cdot\mathbf{a}_3 = 2\pi l$, l is now a continuous variable as the intensity is no longer equal to zero for non-integer value of l. The intensity becomes :

$$I_{hkl} = CF_{hkl}^2 N_1^2 N_2^2 \tag{II.20}$$

The variation of the intensity along the rod gives information on the structure in the z direction. The modulation period is related to the thickness whereas the modulation amplitude indicates the normal atomic displacements. The diffracted signal recorded in the presence of a surface reconstruction is therefore a mesh of rods perpendicular to the surface and located at fractional order in between the bulk Bragg peaks (see Figure II.4). The distribution of the rods depends on the periodicity of the reconstruction compared to the unreconstructed surface. For example, the Si(111)-(7×7) reconstruction displays 6 rods (7 intervals) between

i. We note here that the existence and the construction of the reciprocal lattice is not a mathematical creation as often presented in many school courses but arises from physical process and describes the scattered intensity distribution in space.

i. With θ the scattering angle.

two Bragg peaks (or crystal truncation rod).

c Diffraction by an ideal surface : Crystal Truncation Rods (CTR)

A semi-infinite crystal, *i. e.* a infinite crystal truncated by a sharp interface, can be seen as a infinite crystal with one half of its volume presenting an electron density equals to zero. The diffraction pattern therefore consists in the convolution of the 3D reciprocal lattice with the Fourier transform of the step function. This convolution leads to a non-zero intensity distribution between the Bragg peaks along the l direction (see Figure II.4). These crystal truncation rods extend perpendicularly to the surface and connect bulk Bragg peaks.

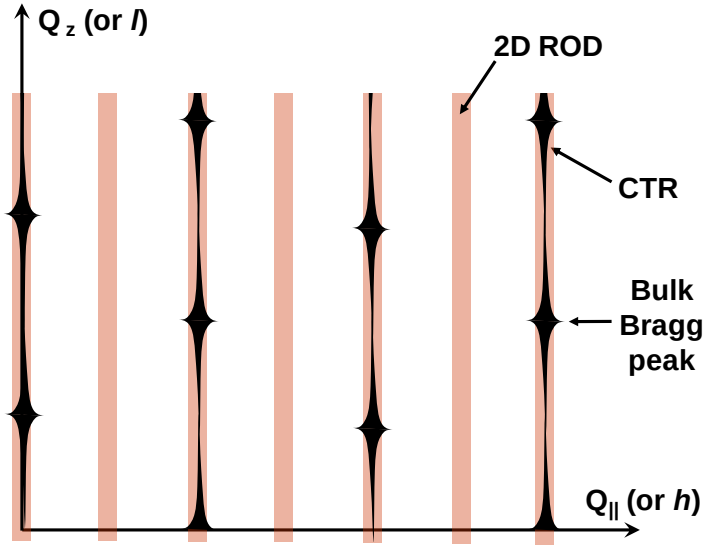

Figure II.4 – Schematic representation of the continuous rods (shaded red) arising from a reconstructed surface and the crystal truncation rods arising from a crystal truncated by a surface (black), the maximum intensity is at the bulk Bragg positions and quickly decreases in between. From [Renaud, 1998].

The intensity is given by replacing $S_{N_3}(Q_3 a_3)$ by $\sum_{n_3=-\infty}^{n_3=0} e^{iQ_3 a_3 n_3}$ Equation (II.11) which gives :

$$I_{hkl}(CTR) = C \ |F(\mathbf{Q})|^2 \ \frac{\sin^2(\frac{1}{2}N_1\mathbf{Q}\cdot\mathbf{a}_1)}{\sin^2(\frac{1}{2}\mathbf{Q}\cdot\mathbf{a}_1)} \frac{\sin^2(\frac{1}{2}N_2\mathbf{Q}\cdot\mathbf{a}_2)}{\sin^2(\frac{1}{2}\mathbf{Q}\cdot\mathbf{a}_2)} \frac{1}{2\sin(\frac{1}{2}\mathbf{Q}\cdot\mathbf{a}_3)} \tag{II.21}$$

As the CTR therefore reflects the atomic organization at the surface of the crystal, an accurate study of their intensity distribution gives important information on the surface structure such as surface roughness, surface relaxation or the formation of a layer during growth.

II.2 Characterization methods

In the previous sections we have seen how X-rays interact with matter and the basis of the diffraction phenomena. In this section we will now focus on a particular use of this concept in order to extract structural information on surfaces and interfaces.

II.2.1 Grazing incidence X-ray Scattering (GIXS)

Figure II.5 is a scheme showing the Grazing Incidence X-ray Scattering geometry where α_i and α_f are the incident and exit angles, respectively. In this configuration δ is the projection of the scattering angle 2θ (between $\mathbf{k}_i$ and $\mathbf{k}_f$) and ω corresponds to the rotation of the sample around its surface normal. The total momentum transfer Q is composed of an in-plane $Q_{\parallel}$ [i] and out-of-plane $Q_{\perp}$ [ii] component. Therefore, in the grazing incidence geometry, Q is almost to $Q_{\parallel}$ ($(Q_{\perp})$ is very small) and $\delta \sim 2\theta$.

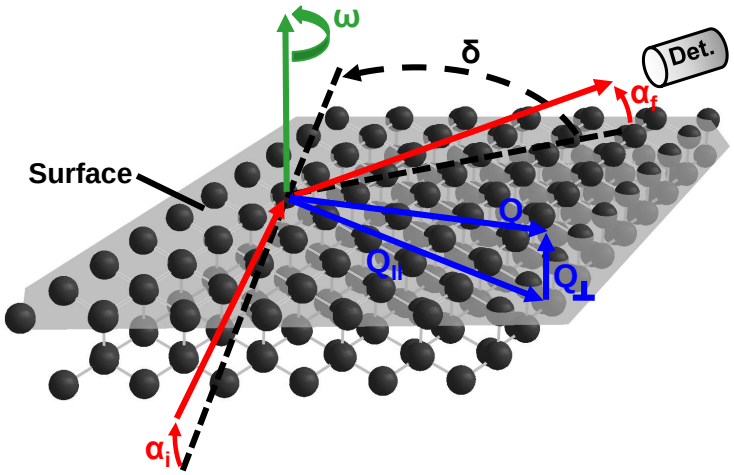

Figure II.5 – Scheme of the GIXS geometry. The grey surface intersects the first atomic layer.

a Definitions of the different scans

Figure II.6(a) represents what is usually called the sphere of reflection (the Ewald's sphere). Its construction allows an easy visualization of the conditions of diffraction. The little grey sphere corresponds to an (hkl) nodes of the reciprocal lattice. This node has a certain size due to the finite size of the diffracting object. The direction of the incident beam is given by the vector $\mathbf{k}_i$ which terminates at the origin of the reciprocal space. Its length $2\pi/\lambda$ defines the radius of the sphere which passes through the origin. The diffracted beam (represented by $\mathbf{k}_f$) is also represented so that $\mathbf{Q}$=$\mathbf{k}_f$-$\mathbf{k}_i$ can be defined : it is thus a chord

i. $Q_{\parallel} = (4\pi/\lambda)\sin(\delta/2)$.
ii. $Q_{\perp} = k_0(\sin\alpha_i + \sin\alpha_f)$

of the sphere. This construction immediately implies that the (hkl) nodes intersected by the sphere satisfy the Bragg's law (see II.1.2).

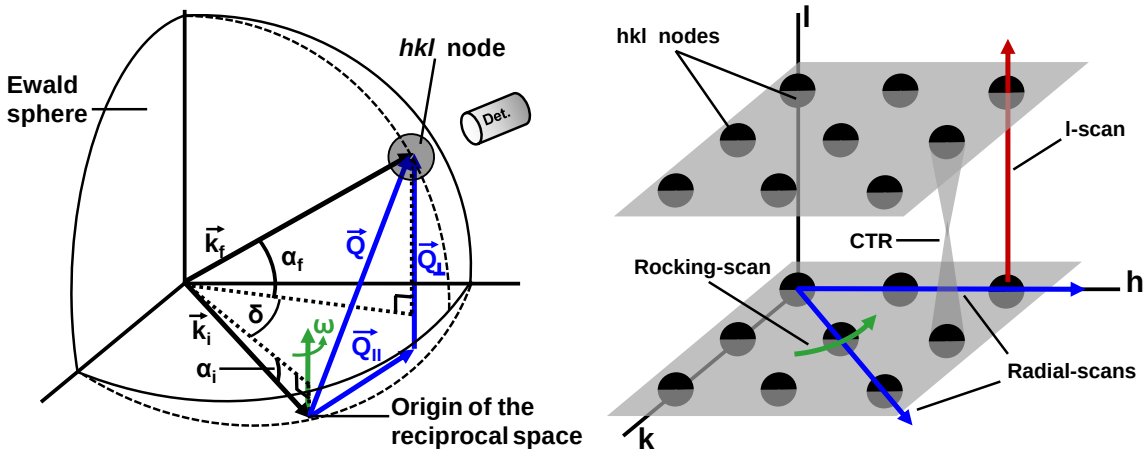

(a) (b)

Figure II.6 – (a) Construction of the Ewald's sphere.(b) Sketch representing several Bragg reflections (and one CTR) composing the reciprocal space. The arrows illustrate typical scans performed in this work and are commented in the text.

The measurement of a reflection during an experiment is possible under two conditions :

- the Ewald's sphere has to intersect the reflection. For a given α_i, this is done by turning the crystal around its surface normal (rotation of ω). It can also be done by changing the energy (the radius of sphere is changed) but it is rarely done due to technical considerations on our beamline.
- the detector has to be placed at the right position. This is done by changing the angles δ and α_f.

The peak intensity in the reciprocal space can therefore be measured along different directions. This is illustrated in Figure II.6(b) which presents typical scans performed in this work, which are :

- *radial-scans* : which consists in scanning reciprocal space in a radial direction by varying the length of $\mathbf{Q}$, as a conventional θ-2θ scan in which here $2\theta = \delta$ and $\theta = (\omega - \omega_0)$. In this study, all the *radial-scans* are performed in the plane (along $\mathbf{Q}_{\parallel}$) along an azimuth specified for each scan ;
- *l-scans* : corresponding to out-of-plane scans along $\mathbf{Q}_\perp$;
- and *rocking-scans* performed at constant $|\mathbf{Q}|$ by rotating the sample around its surface normal.

b Shape of a diffraction peak

The finite size of the crystal in the surface plane leads to the fact that the Bragg peaks are not perfect Dirac functions but present a finite width. The Full Width at Half Maximum (FWHM) of a Bragg peak (see Figure II.7), is directly related to the average size D of the scattering domains. In terms of variation of the momentum transfer, the FWHM for *radial-scans*, *l-scans* and *rocking-scans* are $\Delta Q_{\parallel}$, $\Delta Q_{\perp}$ and $\Delta\omega$, respectively. A good approximation of the domain size[i] in the direction of the measurement is given by :

$$D_{radial} = \frac{2\pi}{\Delta Q_{\parallel}} \; ; \qquad D_{l} = \frac{2\pi}{\Delta Q_{\perp}} \; ; \qquad D_{rocking} = \frac{2\pi}{Q_{\parallel}\Delta\omega} \tag{II.22}$$

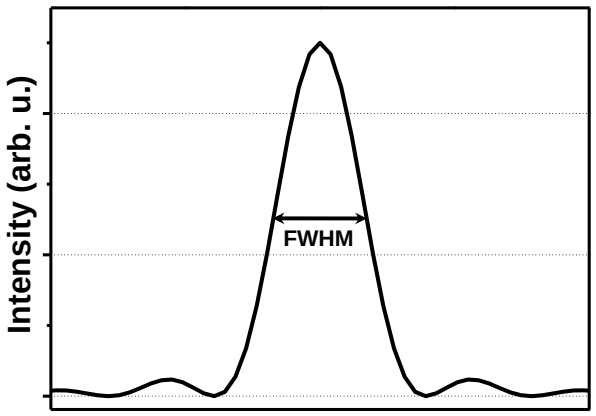

Figure II.7 – Illustration of the FWHM measurement of a Bragg peak.

The approximation on the value of the size comes from the fact that D corresponds to the domains which scatter coherently. The measurement is therefore limited by the coherent length of the incident beam in the direction parallel to the surface. The description of the peak shape can be refined using a correlation function C($\mathbf{r}$) which takes into account the probability of coherent scattering between two atoms separated by $\mathbf{r}$: $C_{r\to 0}$=1, $C_{r\to\infty}$=0. The intensity distribution of the peak can therefore be seen as the convolution of the theoretical perfect Dirac function array and the Fourier Transform (FT) of the correlation function.

c In-plane reciprocal space map

As presented in section I.2.1, silicon has the diamond-crystal structure so that the Si(111) surface presents an hexagonal geometry (Figure II.8(a)).

i. The potential mosaic spread (Ω) has to be included in the estimation of domain sizes in *rocking-scans* by : $\Delta\omega = \sqrt{(\Delta Q/Q)^2 + \Omega^2}$. Ω can be estimated by measuring several orders of a reflection.

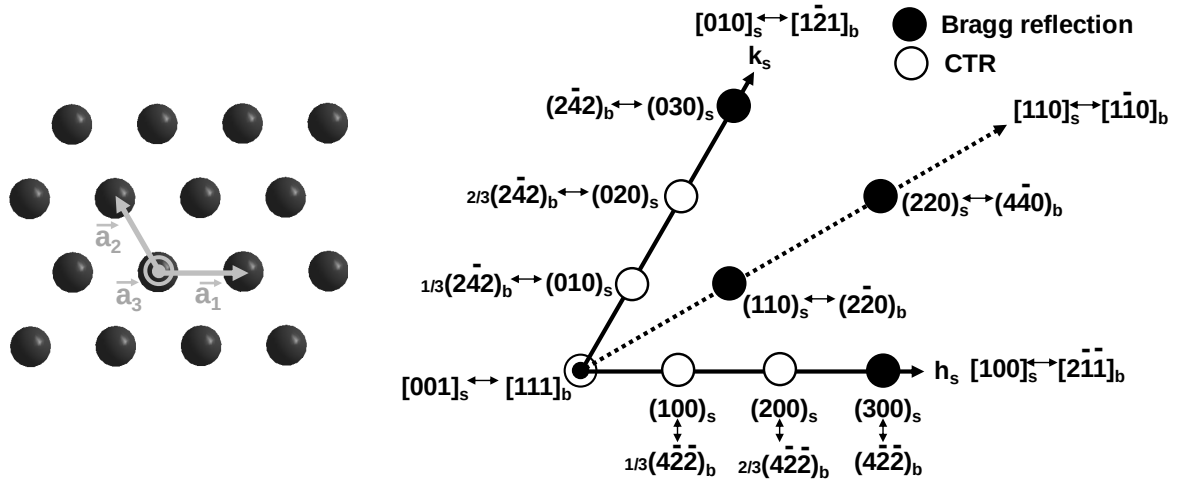

(a) (b)

Figure II.8 – (a) Image of the first layer of the Si(111) surface illustrating the hexagonal geometry. (b) Representation of 60° of the in-plane reciprocal lattice for the Si(111) surface, the relationship between experimental surface indexes and conventional bulk indexes are indicated.

In surface science, it is the convention to define two of the primitive lattice vectors parallel to the surface and the last vector perpendicular. In the case of a (111) orientated surface of a diamond-like crystal (such as Si(111)) the primitive lattice vector (with the bulk Miller index) are (see Figure II.8(a)) :

$$\mathbf{a}_1 = \frac{1}{2}\left[1\ 0\ \bar{1}\right]_b ; \qquad \mathbf{a}_2 = \frac{1}{2}\left[0\ \bar{1}\ 1\right]_b ; \qquad \mathbf{a}_3 = \frac{1}{3}\left[1\ 1\ 1\right]_b \tag{II.23}$$

The corresponding reciprocal lattice ($\mathbf{b}_1$,$\mathbf{b}_2$,$\mathbf{b}_3$) can thus be calculated using equation (II.16). It comes :

$$\mathbf{b}_1 = \frac{2}{3}\left[2\ \bar{1}\ \bar{1}\right]_b ; \qquad \mathbf{b}_2 = \frac{2}{3}\left[1\ \bar{2}\ 1\right]_b ; \qquad \mathbf{b}_3 = \left[1\ 1\ 1\right]_b \tag{II.24}$$

During the experiments it is even more convenient to define a reciprocal surface lattice : ($[h\ 0\ 0]_s$, $[0\ k\ 0]_s$, $[0\ 0\ l]_s$). The correspondence between the bulk and the surface indexes is given in Figure II.8(b) which depicts 60° of the reciprocal space for the Si(111) surface at l=0. In this study, most of the *radial-scans* (or *l-scans*) are presented as a function of the momentum transfer so that only the reciprocal direction expressed in bulk coordinate is given. However in Chapter IV we present the scans as a function of the surface reciprocal lattice unit as it allows to quickly remark the periodicity of special features such as CTRs or reconstruction peaks.

The synchrotron powerful beam (see section II.3.1) allows the acquisition of many scans in a short period of time [ii]. We can therefore perform what we call extended reciprocal space

ii. compared to laboratory sources such as rotating anode.

maps which consist in mapping a part of reciprocal space. This is achieved by performing many *rocking-scans* at different values of the momentum transfer. Plotting them together provides a qualitative observation of the scattering distribution in reciprocal space. The green area in Figure II.9 illustrates a reciprocal space map for a variation of ω of 60°, three different *rocking-scans* are represented. The duration of acquisition and the accuracy of these kinds of maps depend on the counting rate and the step between two Q values. In general a map covering 30° degrees for Q ranging from 0.5 Å^{-1} to 8 Å^{-1} is recorded in about 8 hours.

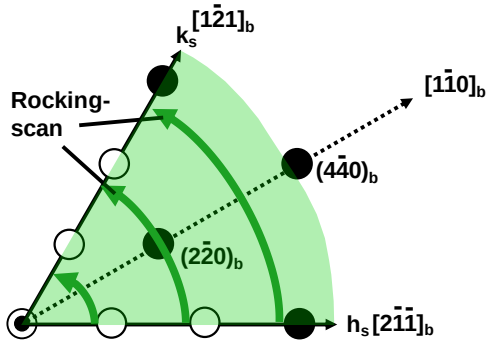

Figure II.9 – Illustration of the acquisition of an extended reciprocal space map. The green area corresponds to the recorded surface by the acquisition of many *rocking-scans*.

II.2.2 Surface X-ray diffraction (SXRD)

Surface X-ray Diffraction consists in a quantitative approach of GIXS. The aim is to determine the positions of the atoms of the studied structure, as presented in Chapter IV concerning the determination of the Si(111)-(6×6)Au reconstruction. The structural information is contained in the structure factors which are obtained by measuring the integrated intensity of each reflection.

a Integrated intensity

Highly resolved *rocking-scans* are performed on each reflection. The M points composing the scan are separated in M_n points containing the noise (N_j) and M_s points containing the signal (S_i). Considering a constant noise, the integrated intensity is given by :

$$I = \sum_{i=1}^{M_s} S_i - \frac{M_s}{M_n} \sum_{j=1}^{M_n} N_j \tag{II.25}$$

In addition, several corrections have to be applied to take into account the errors generated by the apparatus and the measurement itself. They are presented in section II.3.3 after the presentation of the experimental set-up. For a detailed description of these corrections, the

reader can refer to [Vlieg, 1997; Robach *et al.*, 2000]. A complete set of measurements consist in integrating all the accessible reflections. The systematic error being deduced by recording several equivalent reflections related by symmetry (see section IV.3.1).

b Structure factor analysis

From the measured structure factors, standard methods[i] can be applied to obtain a simple structure which can serve as a starting point. The theoretical structure factor of the proposed model can be calculated and compared to the experimental ones. The classical way to refine the model consists in a minimization of functions comparing the experimental and the calculated structure factors. The functions that have to be minimized are :

$$\chi^2 = \frac{1}{N-p}\sum_{hkl}\frac{\left(|F_{hkl}^{exp}| - \left|F_{hkl}^{calc}\right|\right)^2}{\sigma_{exp}^2} \text{ and } R = \frac{\sum_{hkl}\left||F_{hkl}^{exp}| - \left|F_{hkl}^{calc}\right|\right|}{\sum_{hkl}|F_{hkl}^{exp}|} \tag{II.26}$$

where N is the number of measured reflections, p the number of parameter and σ_{exp}^2 the experimental uncertainties. R is called the reliability factor. In this study, minimizations have been performed (see section IV.3.2) using the ROD software for surface structure analysis [Vlieg, 2000]. It consists in finding the smallest value of χ^2 by fitting several parameters[i]. More details on surface structure determination methods and examples can be found in [Feidenhans'l, 1989].

II.2.3 Grazing incidence small angle X-ray scattering (GISAXS)

GISAXS is GIXS except that all the considered angles are taken less than a few degrees. The reciprocal space and the angular coordinates, represented in Figure II.10 are linked by :

$$\begin{cases} q_x \simeq 0 \quad \text{because of small angles, the Ewald's sphere curvature can be neglected} \\ q_y \simeq k_0 \sin(2\theta) \simeq k_0 2\theta \\ q_z \simeq k_0 \alpha_f \end{cases} \tag{II.27}$$

with k_0=$2\pi/\lambda$. In this configuration the scattered intensity is measured very close to the origin of the reciprocal space.

At this position, the scattering comes from in-homogeneities of electron density : roughness or presence of islands for instance. The scattering intensity and shape depend on the morphology and the topography of the scattering object. It is therefore a way to study them. GISAXS characterization has become a very powerful technique these past few years and

i. Such as Patterson or electron-density difference maps.
i. Typically : symmetry, domains, atomic positions, Debye-Waller factors and occupancy.

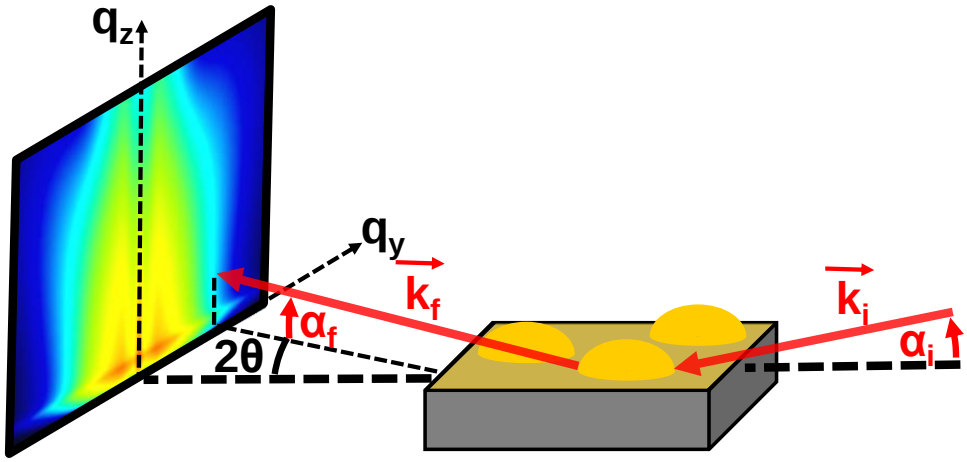

Figure II.10 – Illustration of the GISAXS technique.

allows accurate studies in surface science. In this work, GISAXS experiments were used to characterize the average morphological parameters (inter-islands distance, in-plane size and height) of gold nano-islands spread on the silicon substrate. Here will be presented the essential basis to access these parameters from the study of the diffraction pattern. The complete theoretical and experimental details of the GISAXS technique are described in [Renaud *et al.*, 2009].

Two dimensional GISAXS patterns are recorded with a 2D detector placed perpendicular to the incident beam (see Figure II.10). The intensity for an homogeneous group of nano-objects on a surface can be written, in first approximation :

$$I(\mathbf{Q}) \;=\; F(\mathbf{Q}) \cdot S(\mathbf{Q}) \tag{II.28}$$

with S the Fourier transform of the island-island pair correlation function (also called the interference function) and F the Fourier transform of the island shape (the form factor). The intensity is therefore a combination of a signal containing information on the average shape of the objects (F) and a second one (S) describing how these objects are distributed on the surface. S($\mathbf{Q}$) contains the information on the lateral positions of the islands :

$$S(\mathbf{Q}_{xy}) \;=\; 1 + \rho_s \int \left[g(\mathbf{r}) - 1\right] e^{-i\mathbf{Q}_{xy}\cdot\mathbf{r}} \mathrm{d}\mathbf{r} \tag{II.29}$$

with ρ_s the particle mean density and $g(\mathbf{r})$ the island-island pair correlation function. The form factor of an island can be written as the Fourier transform of the electron density $\rho(\mathbf{r})$ over the island's volume :

$$F(\mathbf{Q}) = \int_V \rho(\mathbf{r}) e^{i\mathbf{Q}_{xy}\cdot\mathbf{r}} \mathrm{d}V \tag{II.30}$$

However a better description is given using the Distorted Wave Born Approximation (DWBA) into which the form factor is the coherent sum of four terms taking into account the different scattering paths represented in Figure II.11 [Rauscher *et al.*, 1999].

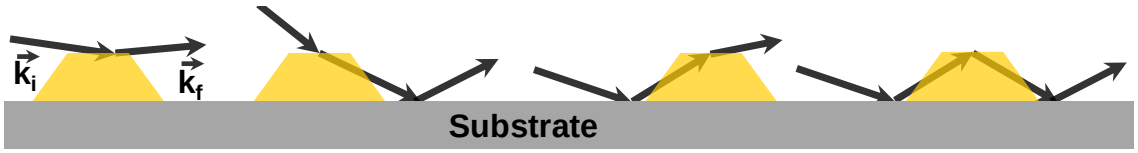

Figure II.11 – Illustration of the four scattering paths involved in the DWBA for X-rays interacting with islands on a surface.

A quick analysis of the 2D GISAXS pattern allows one to obtain the lateral sizes d and the height h of the islands : these parameters are inversely proportional to the spread of the intensity along $\mathbf{Q}_y$ and $\mathbf{Q}_z$, respectively (see Figure II.12). The mean distance D between two islands is given by the inverse of the distance separating the main correlation peaks along the parallel direction. In practice, to perform a quantitative analysis, we will see in section III.1 that we can use the IsGISAXS program [Lazzari, 2002].

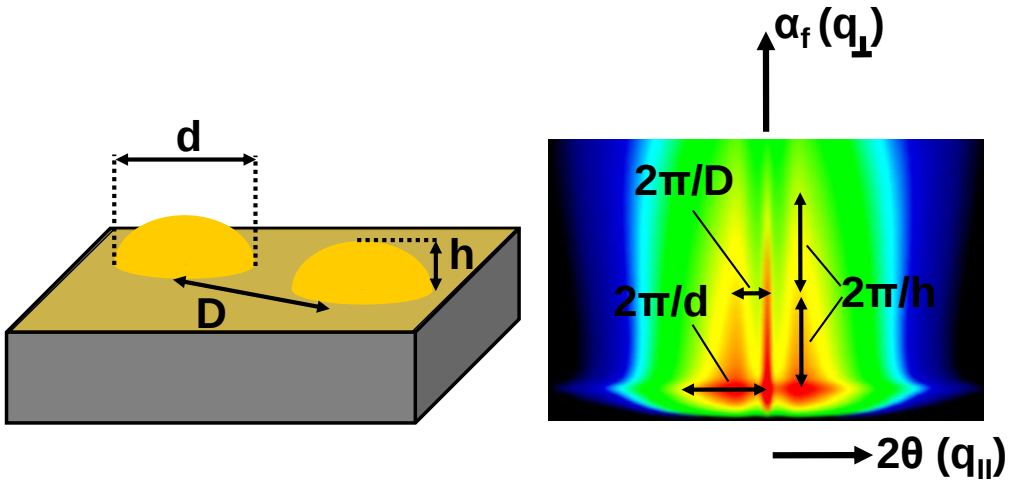

Figure II.12 – Example of a 2D GISAXS pattern (right) onto which several information on the droplets morphology (left) can be measured.

It includes a fitting procedure of parallel and perpendicular cross sections of the 2D pattern to deduce the morphological parameters. The software provides many nanoparticle shapes as well as several theoretical interference functions that are used to calculate the theoretical GISAXS pattern/cross-section and compare it to the experimental one.

II.3 Experimental set-up

The experiments realized for this present work were carried out at the European Synchrotron Radiation Facility in Grenoble, France. Most of the experiments were performed on the BM32 beamline and some others on the ID03 beamline. Both allow *in-situ* characterization of surfaces and growth of nanoobject in ultra-high-vacuum. In this section, brief description of the synchrotron is given, the BM32 beamline will be presented as well as the experimental set-up.

II.3.1 The synchrotron and the BM32 beamline

a The European Synchrotron Research Facilities

We present here only a very short description of the main qualitative features of the synchrotron radiation. For additional information, the reader can refer to the ESRF website [ii] or to textbooks such as [Als-Nielsen *et al.*,].

Synchrotron radiation is the electromagnetic field that is emitted by relativistic accelerated charged particles. The acceleration is achieved by the use of the well known Lorentz force and consists in applying a static magnetic field to the charged particle [iii]. For non relativistic accelerated charges, the radiated flux is isotropically spread around the acceleration (see left hand side of Figure II.13). For relativistic particles, their energy is given by : $E = \gamma mc^2$ with $\gamma >> 1$, with c the speed of light and m the rest mass. Their velocity is $v = c\beta$ with $\beta = (1 - 1/\gamma^2)^{1/2}$ which gives $v \sim c$ for $\gamma >> 1$. In this case the radiation is emitted in the direction of the motion due to the relativistic space-time Lorentz transformations (see right hand side of Figure II.13).

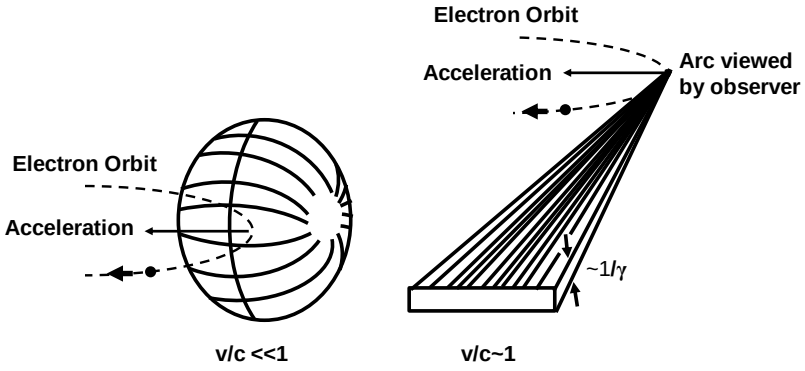

Figure II.13 – Illustration of the radiation emission of electrons in circular motion. Left : non-relativistic case, right : relativistic case. From [Als-Nielsen *et al.*,].

ii. http ://www.esrf.fr
iii. $\mathbf{F}=e\mathbf{v}\wedge\mathbf{B}$, with $\mathbf{F}$ the Lorentz force, $\mathbf{B}$ the magnetic field, e the charge and $\mathbf{v}$ the speed of the particle.

The light radiated at an angle θ' with respect to the trajectory of the charge in its associated frame is seen by the observer in the laboratory frame at an angle θ given by the relation :

$$\tan\theta \approx \frac{1}{\gamma}\tan\left(\frac{\theta'}{2}\right) \tag{II.31}$$

For $\theta' = 90$, $\theta \approx \tan\theta \approx 1/\gamma$. The opening angle of the radiation is thus of the order of $1/\gamma$.

At the ESRF, the electrons are accelerated to 6 GeV, as $\gamma = 1957$ E GeV, the typical aperture of the source is 80 μrad. Figure II.13 (right) shows the interaction between the charged electron and a steady acceleration (perpendicular to the motion) provided by a bending magnet (BM). In this case, the collimation is conserved only in the vertical direction. There are beamlines using a bending magnet at the ESRF. To improve the collection of the synchrotron radiation, the other beamlines use what is called multipole insertion devices (ID). In this case, the electrons are submitted to successive opposite magnetic fields orientated perpendicularly to the direction of motion. Therefore, the electrons oscillate, the collimation is conserved in both directions which increases the photon flux[i] (see Figure II.14).

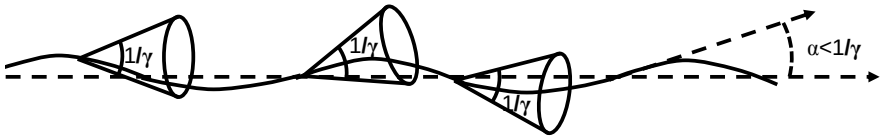

Figure II.14 – Schematic illustration of the undulator regime. From [Als-Nielsen *et al.*,].

More than the photon flux, the relevant parameter when using the synchrotron light is the photon density in the image spot, in unit of solid angle and in a narrow energy bandwidth. This is call the brilliance, its evolution over the years and the technological advancements is shown in Figure II.15. A high brilliance offers great signal-to-background ratio and is thus a perfect tools to probe object at the nanoscale.

b The BM32 beamline

The white beam created in the synchrotron by the interaction between the electrons and the bending magnet is first collimated by a mirror coated with iridium. Then the beam propagates through a double Si(111) crystal : the first crystal enables to choose the beam energy (*i. e.* wavelength) from 7 to 30 keV, the second one focuses the beam in the horizontal direction. A second mirror is then used to focus the beam vertically. With this configuration, the resulting beam size would be 0.25 mm horizontally and 0.15 mm vertically at the sample location with a flux of $5 \cdot 10^{11}$ ph.s^{-1} (at 20 keV). It is then better defined by the use of a set of vertical and horizontal slits. The vertical slits allows to obtain a beam size of typically

i. If the angular deviation α is less than $1/\gamma$, the different pulses interfere.

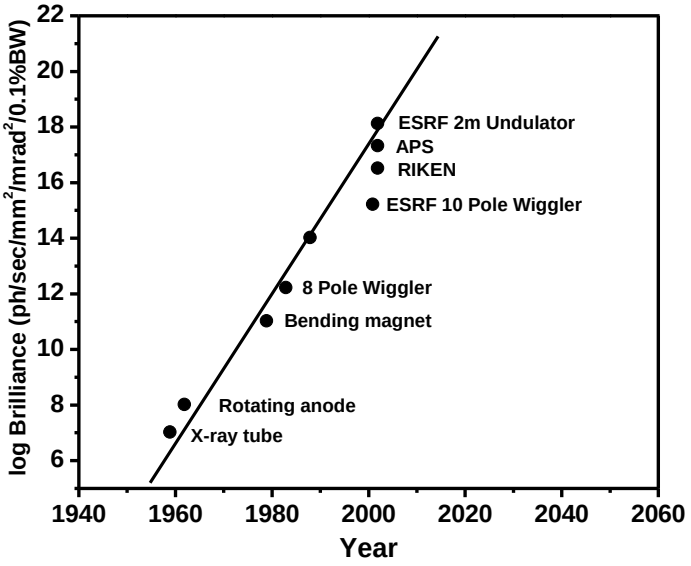

Figure II.15 – Historical evolution of the brilliance with X-ray photon sources. From [Als-Nielsen *et al.*,].

0.3 mm and the horizontal ones eliminate the scattering signal coming from the first slits. The beam then goes through a set of filters and a Kapton foil which serves as a monitor as it is connected to two diodes measuring its scattering. The as-defined incident beam can then be used for the experiment which takes place in the UHV chamber.

II.3.2 *In-situ growth of Nanostructure on Surface* (INS) : the experimental hutch

The UHV chamber, coupled to a diffractometer, is dedicated to *in-situ* characterization of surfaces/interfaces. It consists in a complete equipment to prepare, control and study surfaces and is fully described in [Renaud *et al.*, 2004]. However, technical components are in constant evolution so that some details can differ from the description and the existing set-up. Here are presented the general components illustrating the principal characteristics of the set-up used in the present work.

a The chamber

The ultra high vacuum is maintained in the chamber by a 200 $l.s^{-1}$ turbomolecular pump combined with a 400 $l.s^{-1}$ ion pump and a LN_2 (liquid nitrogen)-cooled titanium sublimation pump. The bake-out of the whole apparatus at 160°C enables a base pressure of 10^{-11} mbar. The main chamber is coupled to a load-lock system composed of two parts : one part allowing the introduction of the sample, a second in UHV equipped with a furnace used for long degazing treatment without polluting the main chamber. The sample is transfered in the

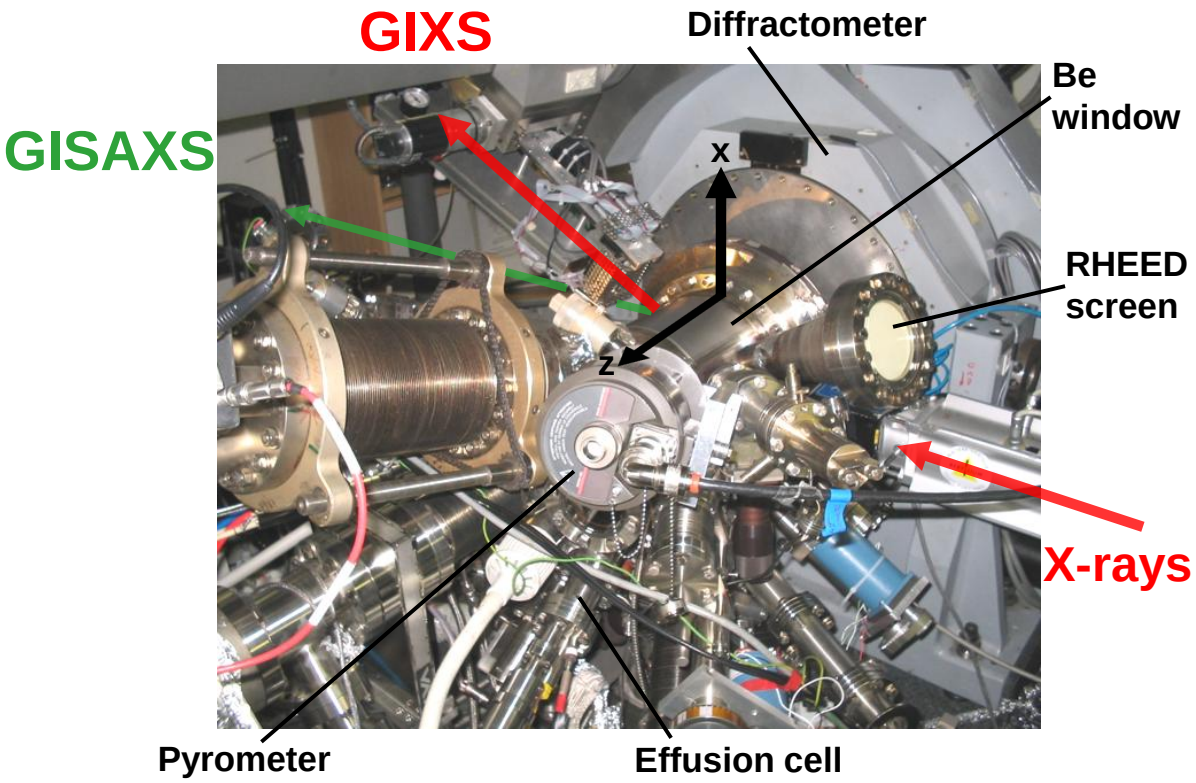

Figure II.16 – Experimental set-up on BM32

X-ray chamber via a transfer rod. The molybdenum sample holder, onto which the sample is stuck, is held on the furnace vertically. It can be heated by radiation (up to 1000 K) and by electron bombardment (up to 1700 K). A narrow input Be window (for X-ray transparency) allows the entrance of the incident beam which interacts with the sample, a wide part of the scattered intensity can be collected thanks to the large output window.

For MBE deposit, the chamber is equipped with several evaporation Knudsen cell which are calibrated using a quartz microbalance. The cleaning of surfaces can be carried out with ion bombardment. In the present set-up, Reflection High-Energy Electron Diffraction (RHEED) is used for a fast and qualitative characterization of the surfaces (roughness and reconstruction) : the resulting diffraction patterns can be visualized on the fluorescent screen. A quadrupole mass analyzer allows the detection of residual gases or even potential leaks. The temperature of the sample is measured thanks to IRCON infra-red pyrometers placed outside, behind a sapphire viewport. Their calibrations for accurate temperature control are detailed in the next section. As already mentioned in Chapter I, the INS scientific interests are moving toward the characterization of nano-objects grown through the CVD technique. The chamber has thus been recently equipped with gaze sources of disilane and digermane.

As the Be windows and beamline components (slits and windows) induce background scattering, several tools have to be placed to suppress this effect. To do so, anti-scattering

slits (of 0.25, 0.3 and 0.35 mm) are added in UHV just behind the entrance Be window. A set of horizontal and vertical slits are also placed outside the chamber between the exit Be windows and the detector (0D or 1D) for the GIXS characterization for the same purpose. In addition, as the sample is placed vertically and the incident angle is very low, the horizontal beam size is larger than the projected sample size, a major part of the intensity must be removed in this direction. The part on the back side is suppressed by the molybdenum sample holder and the part on the front side is stopped by a tungsten knife-edge.

The 2D charge-couple device (CCD) camera is placed in the direction of the low angles, at a variable distance from the sample (between 0.5 m and 4 m). To protect it from the incident and specularly reflected beam, a tungsten beam stop is placed just before the exit windows. To avoid scattering from the air a He-filled tube is also present between the exit window and the CCD camera.

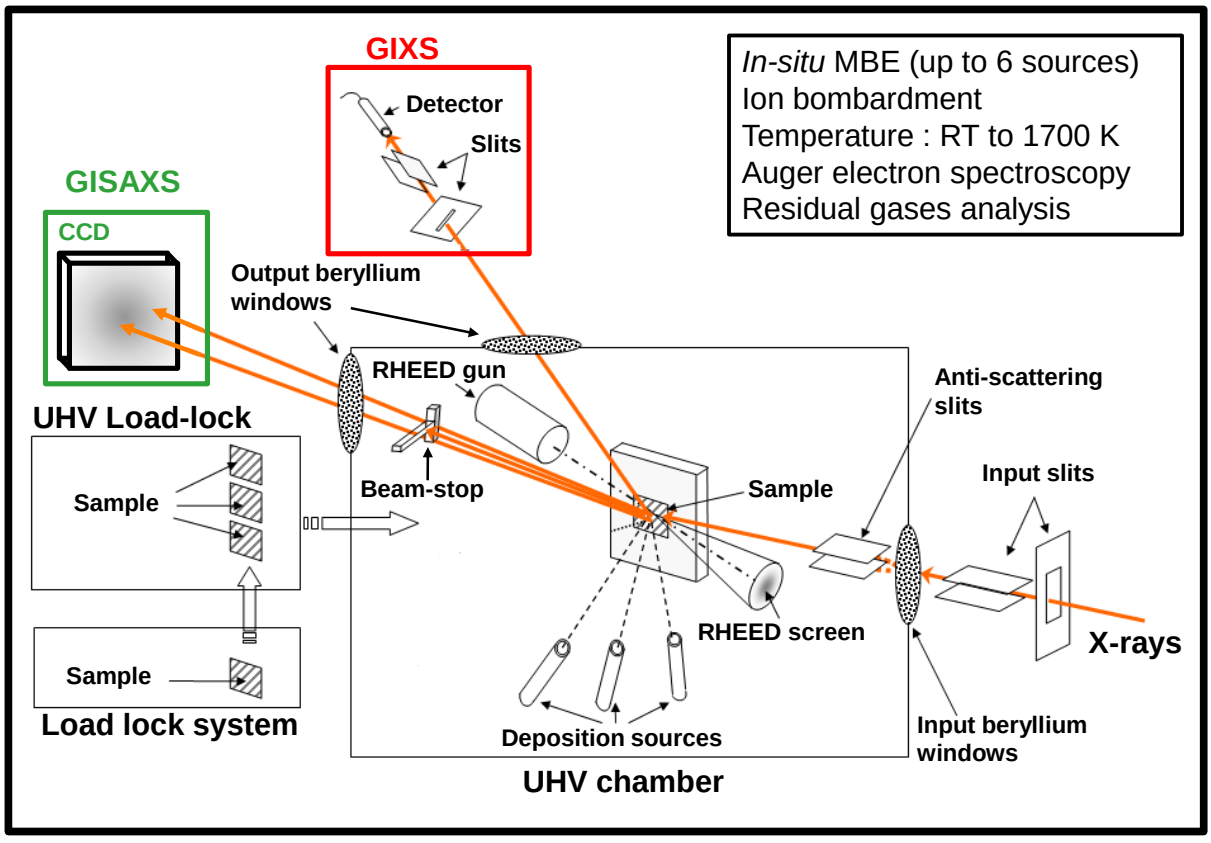

Figure II.17 – Scheme of the experimental set-up on BM32

b Temperature control

Based on the Planck relation describing the radiation of a black body[i] and the Wien equation[i], a fundamental relation in pyrometry can be addressed :

$$\frac{1}{T_\lambda} - \frac{1}{T} = \frac{k\lambda}{hc} \ln(\epsilon_\lambda) \tag{II.32}$$

where k, h, λ and c are the Boltzmann constant, the Planck constant, the speed of light and the wavelength of the radiation emitted by the object, respectively. ϵ_λ is the spectral emissivity and T_λ the brightness temperature which is measured by the pyrometer. On Figure II.18(a) we can see that when the sample is heated at high temperature, its emission is in the orange∼red range. To calibrate the pyrometer for the silicon substrate we need to known its emissivity in the experimental conditions.

To do so a wire of ultra pure lead has been fixed on the Molyblock, next to the Si sample, in a way that the shadow of the wire can be seen on the RHEED screen. The sample was heated very slowly while the temperature was measured. The emissivity was then fixed at a value for which the pyrometers displayed the melting temperature of ultra pure lead (600 K) as soon as the lead wire was observed to melt. This typical temperature was chosen to insure an accurate measure in this range of temperature (around the AuSi eutectic temperature). The accuracy of the temperature measurement is evaluated to ± 5 K. However the important parameter in this study is more the relative temperature (for measuring supercooling for instance) than the absolute one.

c Substrates preparation

The substrate preparation is an important step as we need to work with very clean surfaces. The 10×10 mm^2 Si(111) sample is stuck on the sample holder by the use of a very thin layer of liquid indium. The sample holder (Molyblock) is made in molybdenum which has been previously chemically cleaned[i] and outgassed on the furnace in the load-lock system. The ensemble is then placed in the preparation chamber and outgassed at 500 K during 24 hours to remove organics impurities before being transferred into the growth chamber under

i. A black body is an ideal object that would absorb all the electromagnetic radiations without transmitting nor reflecting them. The Planck's law states that the spectral brightness l_0^λ of the black body only depends on the wavelength λ and the temperature as : $l_0^\lambda(\lambda, T) = (C_1\lambda^{-5})/(e^{C_2/\lambda T} - 1)$, with $C_1 = 2hc^2$ and $C_2 = hc/k$.

i. The Wien's law derives from the Planck's law and stipulates that the wavelength for which the highest energy radiation is emitted by the black body is inversely proportional to the temperature : $\lambda_{Emax} = hc/4.965kT$, with λ in meters and T in K.

i. The Molyblock is placed in a bath of trichloroethane with ultrasonic sound and then washed with acetone, then in ethanol. A chemical etch (in *aqua Regia*) may also be used to remove possible metallic contaminants.

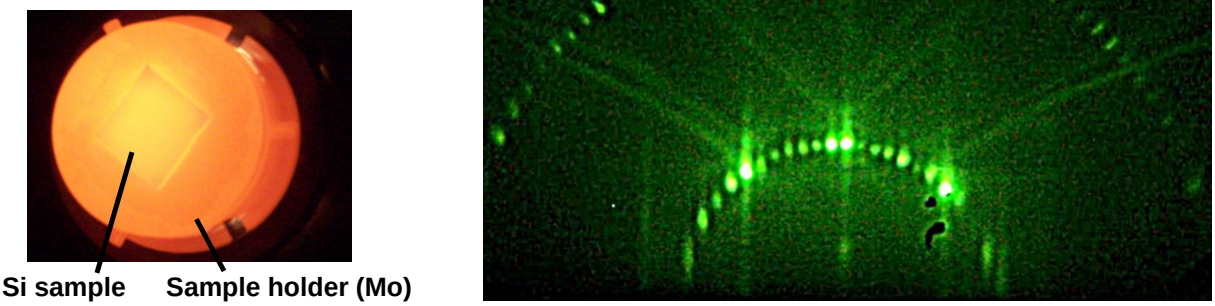

(a) (b)

Figure II.18 – (a) Picture of the sample stuck on the sample holder and heated for de-oxidation. (b) Picture of the RHEED screen for a Si(111) surface reconstructed (7×7) : between two Bragg reflection, six fractional order reflections can be counted.

UHV. The sample is then slowly heated to 1200 K (Figure II.18(a)) to be deoxidized for about 10 minutes. Upon cooling RHEED characterizations are performed : the diffraction pattern reveals the formation a well-defined Si(111)-(7×7) surface reconstruction (Figure II.18(b)), a typical sign for a clean Si(111) surface [Mark *et al.*, 1977].

The procedure to prepare Si(001) and Ge(111) are quite similar, the purity being controlled by the presence of a (2×1) surface reconstruction RHEED pattern.

d The diffractometer

The UHV chamber described in the previous section is mounted on a 6-circle diffractometer presenting a "z-axis" geometry with the sample positioned vertically (see Figure II.19). This configuration has been chosen to avoid signal extinction due to polarization factors equal to zero for scattering angles of the order of 90° in the horizontal plane (see section (II.3.3))

The incident angle α_i can be set by a rotation of the whole ensemble around the vertical axis X. The two cradles χ_1 and χ_2 allow rotation of the sample around X and Y ($\pm 3°$ with 0.001° resolution) to set its surface perpendicularly to the Z axis. The positioning of the sample in the beam is done via a translation along Z with an accuracy of 10 μm. The detector position in the (X,Y,0) and (0,Y,Z) planes are enable by rotations of δ and α_f, respectively. The δ angle corresponds to the Bragg angle projection parallel to the surface and the α_f angle to its perpendicular projection. A rotation of 360° of the sample around its surface normal (rotation of ω) is allowed by the rotation the whole goniometric head thanks

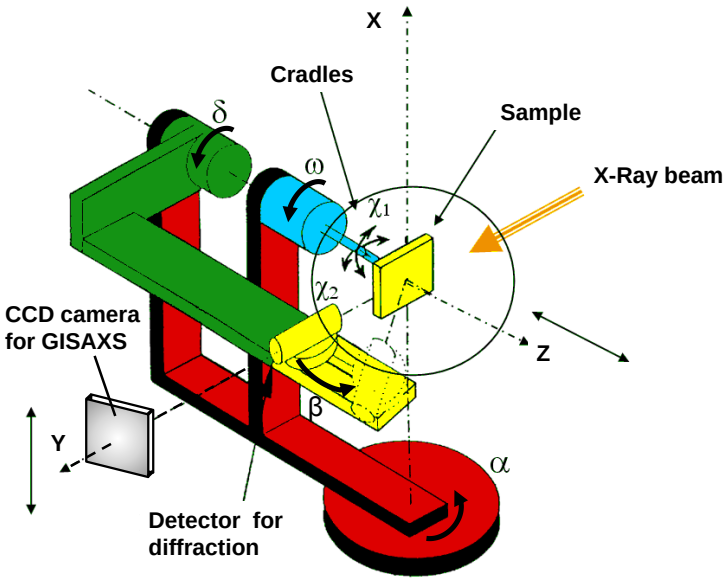

Figure II.19 – Schematic representation of the main motions of the INS-Diffractometer. The different colors refer to different part that can move independently from each other. All the angles and axes are defined in the text.

to a differentially pumped rotary feedthrough.

II.3.3 Corrections factors

In sections II.1 and II.3, we focused on theoretical aspects of surface diffraction. We discuss now the factors that are generated by the experimental measurements (coming from the detector, sample, etc...) and has to be corrected for a quantitative study and/or to compare different experiments. These corrections depend on the characteristics of the incident radiation, on the diffractometer geometry and even also on the sample used. They are presented here in the case of a synchrotron radiation provided by a bending magnet and the z-axis diffractometer geometry presented in the previous section.

a The resolution function

When performing a scan, it is useful to know what is the accuracy of our measurement. This is done by determining the resolution function which depends on the angular divergence of the incident beam, the energy resolution ($\Delta E/E = \Delta k/k$) and the angular acceptance of the detector. The in-plane divergence of the beam on BM32 is ∼0.13 mrad whereas the angular acceptance depends on the aperture of the slits used during the experiment. However the angular acceptance is larger than the in-plane divergence of the beam and results in a highly asymmetric resolution function presenting a parallelepiped shape tangent to the Ewal-

d's sphere (see Figure II.20). As a consequence, the resolution of a *rocking-scan* is better than the one of a *radial-scan* which is proportionally linked to the aperture of the detection slits. This is the reason why the collection of the data for a quantitative analysis (see section IV.3.1) is done by measuring the reconstruction rods through highly resolved *rocking-scans*.

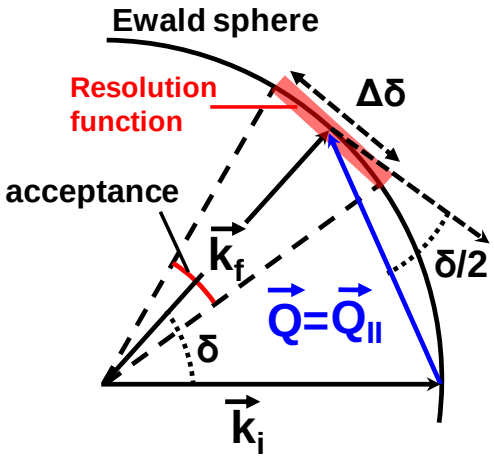

Figure II.20 – Sketch of the in-plane projection of the Ewald's sphere construction and the resolution function

b Sample correction

The integrated intensity must also be corrected from a geometrical factor corresponding to the surface. The illuminated part is called the active surface and can be defined with the opening of the slits placed before the sample and between the sample and the detector position (see Figure II.21). The in-plane illuminated surface area A [i] is given by $A = d_i d_o / \sin(\delta)$.

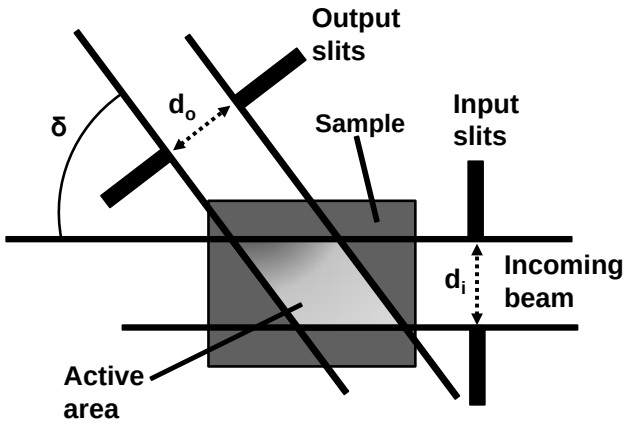

Figure II.21 – Illuminated area defined by the two sets of slits

i. This is not valid for small values of δ for which better corrections must be applied.

c Polarization factor

The polarization factor P is defined by the square cosine of the angle between the direction of observation and the polarization direction. For synchrotron radiations, the polarization is almost completely horizontal (95% for bending magnet) and we use a z-axis diffractometer so that the vertical polarization can be neglected. The horizontal polarization is given by :

$$\begin{aligned} P_h &= 1 - (\sin\,\alpha_i\,\cos\,\delta\,\cos\,\alpha_f + \cos\,\alpha_i\,\sin\alpha_f)^2 \\ &\approx 1 - \sin^2\,\alpha_f = \cos^2\,\alpha_f \qquad (\sin\alpha_i \approx 0 \text{ and } \cos\alpha_i \approx 1 \text{ for grazing incidence}) \end{aligned} \tag{II.33}$$

For in-plane reflections ($\alpha_f \sim 0$), P is almost equals to one so that no polarization corrections are needed.

d Lorentz factor

The Lorentz factor accounts for the scanning differences that arise in probing reflections at different positions in the reciprocal space. Scanning a reflection means moving the sample and the detector so that the reflection crosses the Ewald's sphere. However, depending on the reflection, the time for this latter to crosses the Ewald's sphere changes. To compare the integrated intensity measured at different locations in the reciprocal space, the measured intensity must be multiplied by a factor L which represents the integrated volume (as a function of the diffractometer angles) in the direction of the scan. For a *rocking-scan* :

$$L_{rocking-scan} = \frac{1}{\sin\,\delta\,\cos\,\alpha_i\,\cos\,\alpha_f} \tag{II.34}$$

For more details concerning the Lorentz factor, the reader can refer to [Vlieg, 1997; Robach *et al.*, 2000]

II.4 Numerical simulations

In parallel to the experimental results obtained thanks to the combination of the UHV chamber and the synchrotron light, *ab-initio* simulations have been performed on the Au-Si system in the frame of a collaboration. This part of the work has been managed by Alain Pasturel, Thomas Nogaret and Noel Jakse from the SIMAP-LPMMC [i] laboratory, co-directed by the Université Joseph-Fourier (UJF) de Grenoble and the Centre National de la Recherche Scientifique (CNRS). For the *ab-initio* molecular dynamics simulations, canonical

i. Science et Ingénieurie des MAtériaux et Procédés - Laboratoire de Physique et Modélisation des Milieux Condensés.

NVT (constant number, volume, temperature) ensembles were used using the Vienna *ab-initio* simulation package [Kresse and Joubert, 1999]. Projected augmented plane waves (PAWs) with the Perdew-Wang exchange-correlation potentials have been adopted [Wang and Perdew, 1991; Kresse and Furthmullers, 1996; Kresse and Furthmuller, 1996]. The valence state of each element has been previously defined in the provided PAW potentials. We do not describe here further technical details concerning the simulation method as the large majority of this work is experimental. The simulation results are simply displayed in addition to the experimental ones to discuss the different key points so that technical details are not mandatory to understand the purpose of this work.

Chapter III

Growth of Au on Si(111)

Contents

A important part of this thesis is the study of the interactions between the AuSi liquid droplets and the substrates to improve our knowledge of the VLS process. However, a key parameter is to understand in details how these droplets had formed on the substrate. To do so, we present in this chapter the results concerning the deposition process and the annealing of the sample to the eutectic temperature. In section III.1, we focus on the morphological parameters of the small deposits (∼2 ML) using the GISAXS technique whereas in section III.2 we present the structural information obtained by GIXS measurements for thicker deposits (∼7 ML). A special attention has been paid on the structure of the Au/Si interface and its evolution with increasing temperature.

III.1 GISAXS study for low coverage experiments

We have performed GISAXS measurements to shed light on the morphologies of gold islands that form on the Si(111) substrates. The growth of gold nano-islands was achieved by two different ways :

1. successive Au deposits (1.4 $\rightarrow$ 2.2 ML) at a constant temperature of 570 K, which is 60 K below T_e.
2. a single deposit of 2 ML at RT progressively annealed up to T_e.

GISAXS probes regions with different electronic density than that of Si substrate. The GISAXS patterns are characterized by two lobes originating from the constructive interferences between the waves scattered by nearby particles. The width W and the height H of the islands are derived from the width and height of the lobes, respectively (see Figure II.12). The inter-island distance D is derived from the distance between the lobes along the direction parallel to the surface q_y. A quantitative GISAXS analysis was performed with the IsGISAXS software [Lazzari, 2002]. The interference function was modeled with the paracrystal theory making the link between a regular lattice and fully disordered structures.

III.1.1 Growth at 570 K

Figure III.1 shows the successive GISAXS patterns recorded at 570 K for increasing gold deposit. At 1.4 ML, the presence of assymetrical lobes can be attributed to experimental issues, however the intensity along q_z is quite low and is assumed to be due to the creation of the wetting layer at this coverage. Indeed the image at 2 ML shows a an increase of intensity along q_z as well as a change in the lobes shape indicating the formation gold islands.

From GISAXS images, parallel and perpendicular cuts were extracted at positions marked by the dotted lines on the last picture of Figure III.1 and fitted with the IsGISAXS soft-

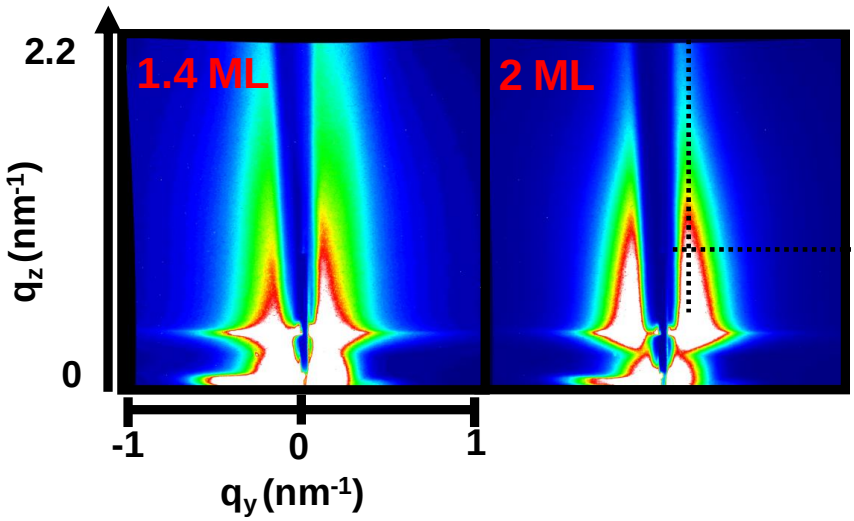

Figure III.1 – Evolution of the GISAXS pattern coming from Au deposit at 570 K with increasing coverage.

ware [Lazzari, 2002]. Figure III.2 displays the two cuts for the deposit thickness of 2 ML. In the STM study of Rota *et al.* , gold islands were elaborated under similar conditions (but on vicinal surface) and were found to be 3D [Rota *et al.*, 2006]. To compare to the experimental measurements, the chosen model is thus an average island shape being a truncated sphere on top of a wetting layer. The agreement between the model and the experimental curve is very good and allows the extraction of the different morphological parameters presented in Table III.1 for 1.4 ML and 2 ML.

	D(nm)	W(nm)	H(nm)	θ(°)	Equ. thick. (nm)	Exp. thick. (nm)
1.4 ML	52±5	12.0±1.2	2.5±0.2	37.4±4	0.30	0.32
2 ML	32±3	12.5±1.2	2.7±0.3	38.7±4	0.45	0.45
2 ML*	32	9	-	-	-	-

Table III.1 – Average morphological dimensions of Au islands on Si(111) at 570 K for 1.4 and 2 ML. The dimensions D, W and H are obtained from a quantitative GISAXS analysis and represent the inter-islands distance, width and height of the structures, respectively. The contact angle θ and the equivalent thickness (Equ. thick.) are calculated from the morphological dimensions and the experimental deposited Au thickness (Exp. thick.) is indicated for comparison. $*$ [Rota *et al.*, 2006].

The inter-island distance decreases from 52 nm to 32 nm from 1.4 to 2 ML while the islands size remains quite the same. This corresponds to the nucleation of new Au particles on the WL, between the islands that have formed first, as previously observed by STM [Rota *et al.*, 2006]. The average shape is a truncated sphere with a contact angle in the island of approximately 38°. Interestingly, the coverage of the surface by the islands can be estimated from the inter-particle distance and the island width. For example, at 2 ML, the coverage of the WL by the islands is 13% of the total surface. In addition, the equivalent thickness

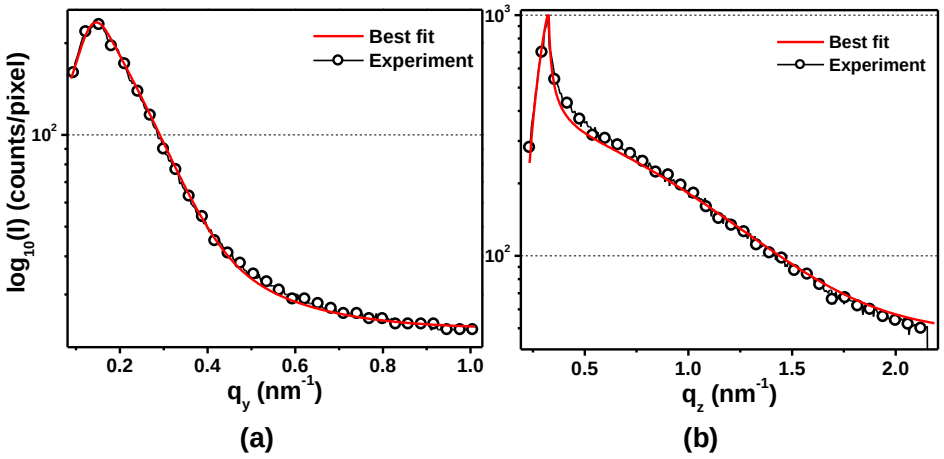

Figure III.2 – GISAXS cut extracted along the dotted lines in Figure III.1 for the 2 ML deposit (a) parallel to the surface at q_z= 0.85 nm^{-1} and (b) perpendicular to the surface at the position of maximum intensity, *i. e.* at q_y= 0.15 nm^{-1} for 2 ML at 570 K. The black (open circles) lines correspond to the experimental data and the red (no symbols) line to the best fit with the IsGISAXS software. The intensity is represented on a logarithmic scale.

of the islands can be deduced from the morphological dimensions obtained by GISAXS. The total thickness of the islands plus the 1 ML WL well agrees with the experimental deposited thickness (Table III.1). Moreover, the morphological dimensions can be compared with those obtained by STM, when available [Rota *et al.*, 2006]. At 2 ML, there is a very good agreement for the inter-island distance and the islands widths obtained by STM and by GISAXS are similar by taking into account the error bars.

Despite the lack of quantitative information for lower coverage (between 0 and 1 ML), the growth of gold on Si(111) thus seems to follow a Stranski-Krastanow mode at relatively high temperature (570 K), consisting in first the growth of a 1 ML-thick Au wetting layer and then in islands nucleation on top of it by agglomeration of the following deposited atoms. For 2 ML the islands are 2.5 nm±0.2 nm high, 12 nm±1 nm wide and separated by 32 nm±2 nm (see Figure III.3).

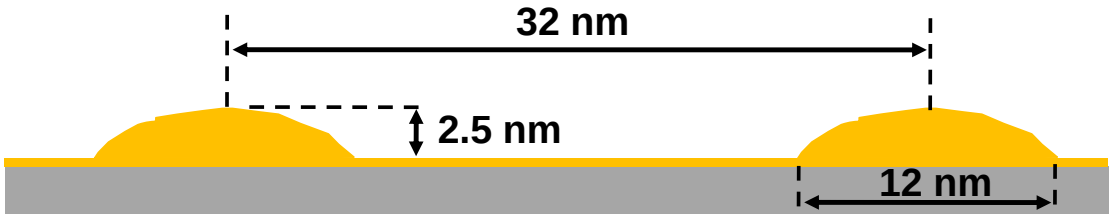

Figure III.3 – Illustration of the gold islands morphology at 570 K for a 2 ML deposit.

We now focus on the annealing of a 2 ML deposit performed at RT to compare with the results obtained in the case described above.

III.1.2 Deposit at RT and annealing

a Morphological evolution with annealing

GISAXS images were recorded during the annealing of the deposit. Figure III.4 displays them at 480 K, 560 K, 600 K and 630 K to qualitatively illustrate the dewetting process. Below 480 K, no measurement of the exact temperature is available [i] and the GISAXS images from RT to 480 K do not present any difference unless a slight decrease of the intensity along q_z which may indicate that the thin deposited film has already started to dewet. Above 480 K, the continuous shrinkage of the intensity along q_z reflects the increasing height of the Au particles. In this experiment, parallel and perpendicular cuts were extracted and fitted from 480 K to 630 K (every 10 K) with the forming islands still modeled by truncated spheres.

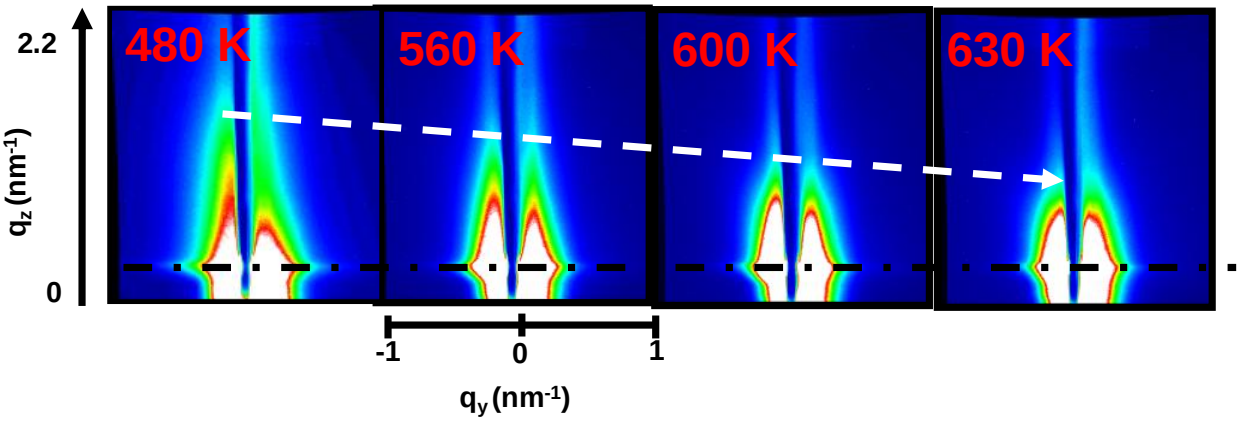

Figure III.4 – Evolution of the GISAXS pattern of a 2 ML-thick Au deposit on Si(111) performed at RT, for increasing temperatures between 480 K and 630 K.

Figure III.5(a) shows that, from 540 K to 630 K, the inter-island distance linearly increases from 25 to 50 nm, indicating either the coalescence of the islands or the agglomeration of atoms from a potential residual thin film leaving wider area in between. The island width first increases, before being approximately constant from 490 K to 630 K while their height increases from 3.7 nm to 6.2 nm (Figure III.5(b)). The contact angle increases from 53° to 73° (Figure III.5(c)) . At T_e, the melting of the system leaves droplets presenting an average separation of ∼48 nm, a width of ∼17 nm, a height of ∼6 nm, a contact angle in the liquid phase of ∼73°.

The dewetting process thus implies that the parameters W, H and θ increase with temperature. Moreover, a closer look to the slope of the curves in Figure III.5(a), (b) (and (c)) reveals that this increase can schematically be seen as a two regimes process. Indeed, below 560∼570 K, the variation of each parameter is very small, almost constant, whereas the

i. The lowest accessible temperature of the pyrometers being about 470 K.

slope becomes steeper above this temperature. In other words the deweeting process is enhanced above 560 K. This assumption is further supported by GIXS measurements during the annealing of 7 ML (see section III.2.1) and will be discussed in section III.2.2.

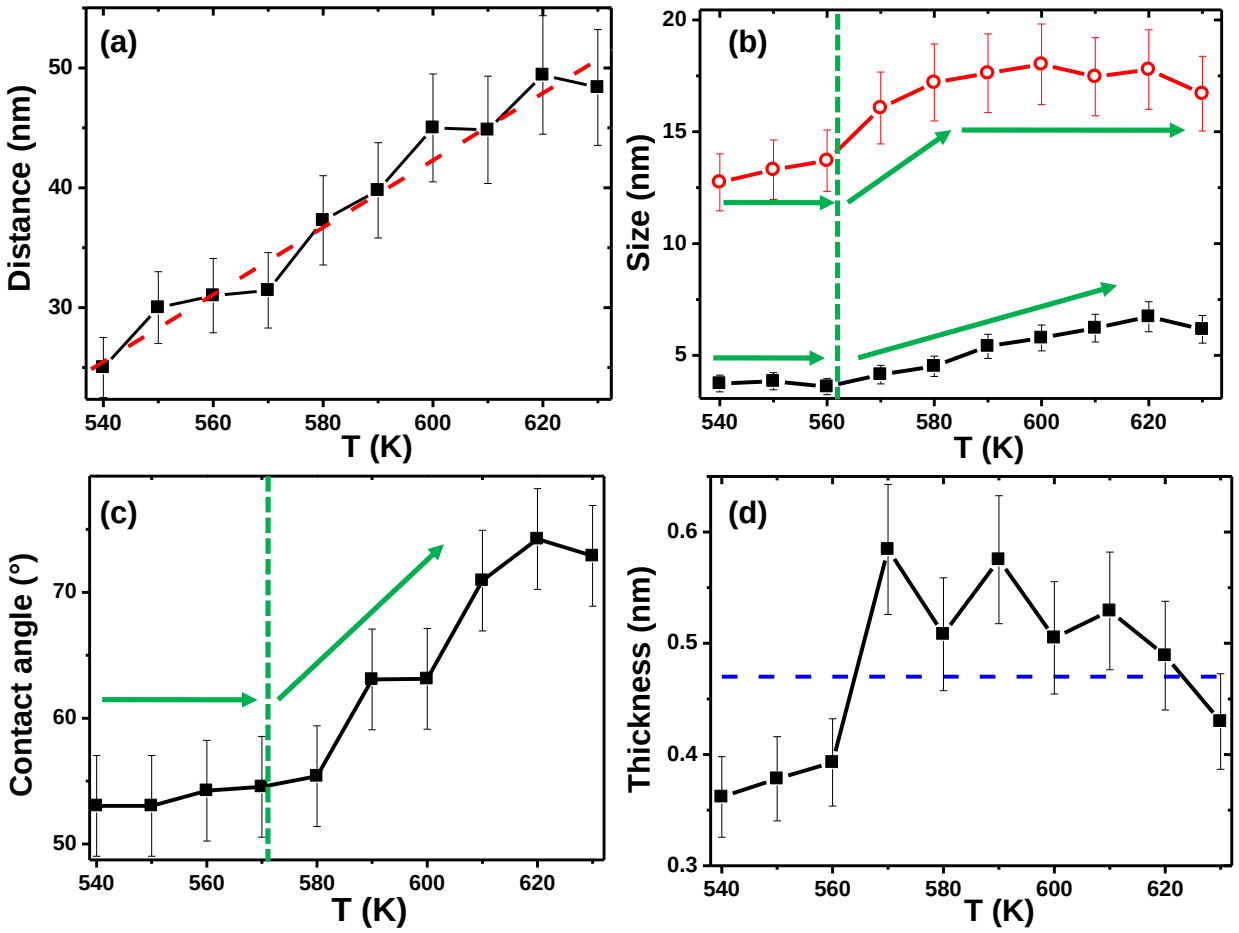

Figure III.5 – Morphological parameters deduced from the fits of GISAXS data for increasing annealing temperatures, from 540 K to 630 K of a 2 ML-thick Au deposit. (a) the inter-island distance, the dashed-red line is a linear fit illustrating the coalescence process (b) the width (red/open circles) and height (black/squares) of the islands and (c) the aspect ratio as a function of the temperature. (d) Calculated equivalent thickness for each fit in comparison with the experimental one (dashed-blue line). The vertical green-dashed line marks the supposed critical temperature separating the two dewetting regimes (see text). The arrows are guides to the eyes showing the abrupt change of the slope.

b Estimation of the interface energy at T_e

In Chapter I, we have seen that the Young's equation describes the relationship between the contact angle and the different surface energies, which are key parameters to model the epitaxial growth of NWs by the VLS process (see section I.3.4). For micrometer-sized droplets, the contact angle is approximately 43° [Ressel *et al.*, 2003], while in the present study, the contact angle is 73° for a droplet width of 17 nm at T_e. It therefore confirms that the contact

angle is inversely proportional to the cluster size [Li, 1996]. Hence, the contact angle of a nanometer-sized droplet measured here can be used for an accurate determination of the interface tension leading to a proper model of epitaxial NW growth.

Using the same surface energy values as in Chapter I, *i. e.* $\gamma_{sol-vap} = 1.25$ J.m^{-2} and $\gamma_{liq-vap} = 0.85$ J.m^{-2}, yields the liquid-solid interface tension of 1.0 J.m^{-2} for a contact angle of 73° at T_e. As expected, this value is larger than that of 0.62 J.m^{-2} obtained for a micrometer-sized droplet [Schmidt *et al.*, 2010].

c Discussion on the calculated equivalent thickness

The equivalent thickness of the particles varies with the annealing temperature. It increases above 560 K and is even larger than the experimental Au thickness between 570 K and 620 K (Figure III.5(d)). We suggest that this variation could be linked to an Au-silicide on the surface of the islands.

Indeed, surface enrichment in Si may be driven by the lower surface energy of Si relative to Au. The Au-silicide formation in similar experiments faced an intense debate in literature [Yeh *et al.*, 1993]. Calliari *et al.* applied spatially resolved Auger line shape analysis to 30 ML Au/Si(111) annealed up to 770 K and concluded to an intermixed Si-Au skin on top of the islands [Calliari *et al.*, 1984]. Ressel *et al.* studied microscopic liquid droplets of the Au/Si(111) system with photoemission spectroscopy and showed that the surface of the liquid Au-Si droplets is enriched with Si [Ressel *et al.*, 2000]. X-ray photoemission spectroscopy (XPS) supports the idea that for small deposit of Au,*i. e.* below 2 ML, an Au-Si alloy film is formed at room temperature (RT). Subsequent deposition leads to the nucleation of gold below the alloy with an abrupt Au/Si(111) interface [Yeh *et al.*, 1993; Hoshino *et al.*, 2008]. This observation is supported by our GIXS experiment presented in the next section (section III.2), which highlights preferred epitaxial orientations of the Au(111) crystal plane with respect to Si(111) and thus claims for the presence of a sharp interface. In addition, above T_e, X-ray diffraction revealed similar 2D crystalline gold silicide as presented in Chapter I, floating below the surface of the liquid eutectic $Au_{81}Si_{19}$ alloy with a Si atomic composition of approximately 70 at.% in the topmost surface layer [Shpyrko *et al.*, 2006; Mechler *et al.*, 2010].

During the GISAXS experiment presented here, some GIXD measurements were also performed. In particular, *radial-scans* at 300 K during the deposition (see Figure III.6). For 0.6 ML, the scan displays no clear diffraction signal from Au but the Si(111)-(7×7) reconstruction peaks are recorded. This may arise because in the sub-monolayer range, the gold atoms occupy some special sites of the Si reconstruction which conserves its structure [Wu *et al.*, 2010]. For 2 ML, the substrate reconstruction peaks vanish and the Au(111) peak

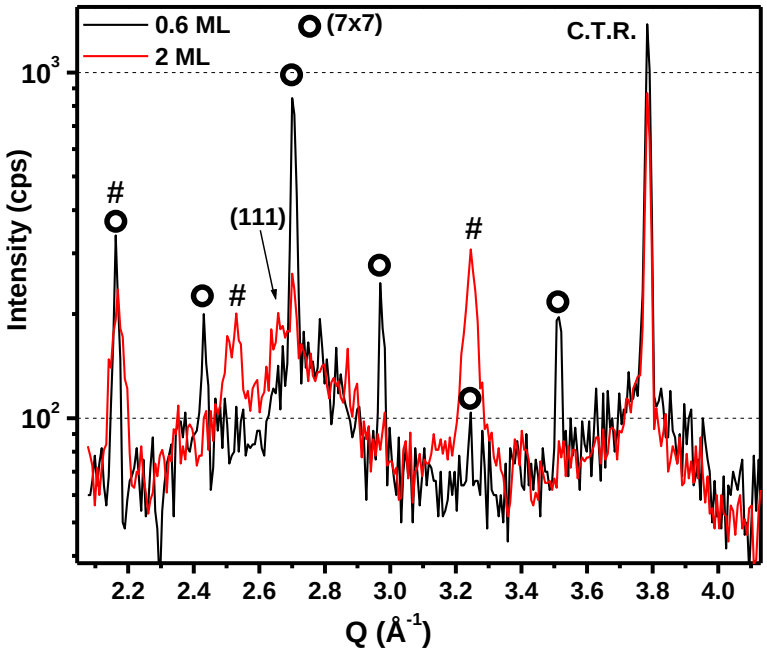

Figure III.6 – *Radial-scans* along the Si[1$\bar{2}$1] azimuth for 0.6 ML and 2 ML Au deposits at 300 K. The peaks marked with a circle are Si-(7×7) reconstruction peaks, the ones marked with # are unassigned peaks.

emerges. Interestingly, we observe the appearance of three unassigned peaks (marked with #) : two peaks sitting at the (7×7) positions (at 2.15 and 3.25 Å^{-1}) but that are not supposed to be reconstruction peaks [i], as well as a less intense one at 2.53 Å^{-1}. These peaks might indicate the formation of a AuSi crystalline compound (see section V.2 and VI.1). Indeed, in his PhD thesis, Agnus G. studied the self-organized growth of Au on Si(111) [Agnus, 2007]. One of his interesting results concerns TEM pictures of some islands displaying atomic plane spacing that do not correspond to any inter-planar distance in fcc gold. The author explains this by the formation of islands composed of gold-silicides. Table III.2 has been taken from [Agnus, 2007] and lists some gold-silicide compounds reported in literature and supposed to be metastable. The diversity of these structures is however not very helpful as many inter-planar distances, from several compounds could be at the origin of the unassigned peaks. For example, the best inter-planar distances corresponding to the # peaks at 2.18, 2.53 and 3.22 Å, are the $Au_{0.77}Si_{0.23}$(311), the Au_7Si(400) and the Au_2Si(800), respectively.

In addition, GIXD in-plane and out-of-plane measurements were carried out at 620 K and yield an average width and height of 15 nm and 4 nm respectively. These values correspond to the largest crystallites in the islands. The corresponding GISAXS measurements yield an average width and height of 17.8±1.8 nm and 6.7±0.7 nm respectively. These values correspond to the whole island whatever its crystalline state. The comparison between the

i. Their shape are different than typical reconstruction peaks.

Compound	Symmetry	Lattice parameters in Å
$Au_{0.77}Si_{0.23}$	Tetragonal	a=9.6
Au_5Si_2	Hexagonal	a=9.38 ; c=15.46
Au_5Si	Tetragonal	a=6.75
Au_2Si	Tetragonal	a=19.50
Au_7Si	Tetragonal	a=7.84
Au_3Si	Orthorhombic	a=7.82 ; b=5.55 ; c=11.16
Au_4Si	Tetragonal	a=5.55

Table III.2 – Crystal structure of some gold-silicide compounds, from [Agnus, 2007] and references therein.

two values claims for the major part of the islands being a single-crystal. The difference might arise from the formation of the AuSi shell at the surface of the islands resulting from the agglomeration of the atoms that compose the Au-silicide thin film that can potentially forms at RT. The difference of sizes obtained by GISAXS and GIXD yields the maximum thickness of the AuSi shell i.e. approximately 2 nm. A combined XPS and medium energy ion scattering study estimated a thickness of 3-4 ML, i.e. approximately 1 nm, at the surface for a nominal 2 ML coverage at RT [Hoshino *et al.*, 2008]. Finally, the upper limit of 2 nm at 620 K is of the same order as the estimation of 1 nm at RT.

III.1.3 Comparison between the two growth modes

	D (nm)	W (nm)	H (nm)	θ (°)
Growth	32±3	12.5±1.2	2.7±0.3	38.7±4
Dewetting	31±3	16.1±1.6	4.1±0.4	54.5±4

Table III.3 – Morphological characteristics of the 2 ML Au/Si(111) at 570 K obtained either by successive deposits at constant temperature (growth) or by a deposit followed by successive thermal annealing (dewetting).

In the first Au/Si(111) series, the growth is made up to 2 ML at 570 K. In the second series, the dewetting of the 2 ML deposit is performed at increasing temperatures with one characterization step at 570 K. In both cases, the islands are truncated spheres. Remarkably, in spite of different elaboration methods, the inter-island distance of both samples is the same (Table III.3). This is thus a stable configuration, which minimizes the energy of the system. However, the island size obtained by dewetting is larger than that obtained by growth. During the dewetting, Si atoms may agglomerate in the islands and get alloyed with Au atoms. The difference in sizes between both processes is likely to be attributed to the minimum thickness of the AuSi shell, approximately 1 nm at 570 K. Moreover, the contact angle is larger in case of dewetting. A higher contact angle in the case of dewetting may arise because this process

tends to reduce the surface-to-volume ratio and therefore leads to more round-shaped islands.

III.2 GIXS study of the interface epitaxial relationships

In the previous section, the GISAXS study aimed at getting some morphological information on the shape of the particles during the growth/annealing of Au on Si(111). In this section, we focus on how thicker gold films and/or islands are related to the substrate from an atomistic point of view. In other words, GIXS experiments here make possible the study of the interface structure between the two solids.

III.2.1 Experimental results

a Deposition at room temperature

A first step consists in characterizing the system after the gold deposit at RT. To do so a *radial-scan* is performed along the Si[1$\bar{1}$0] azimuth just after a deposit of 7 ML of gold (Figure III.7(a)). As expected it displays the two Bragg peaks of the silicon single crystal found in this direction. In addition, all the allowed Bragg peaks of gold are recorded, which indicates that the deposited thin film is a polycrystal. Along this direction, these peaks can be gathered into three families corresponding to three types of interface orientation perpendicular to the surface :

- Au(111)||Si(111) (type A in red),
- Au(1$\bar{1}$0)||Si(111) (type B in green),
- and Au(00$\bar{1}$)||Si(111) (type C in blue).

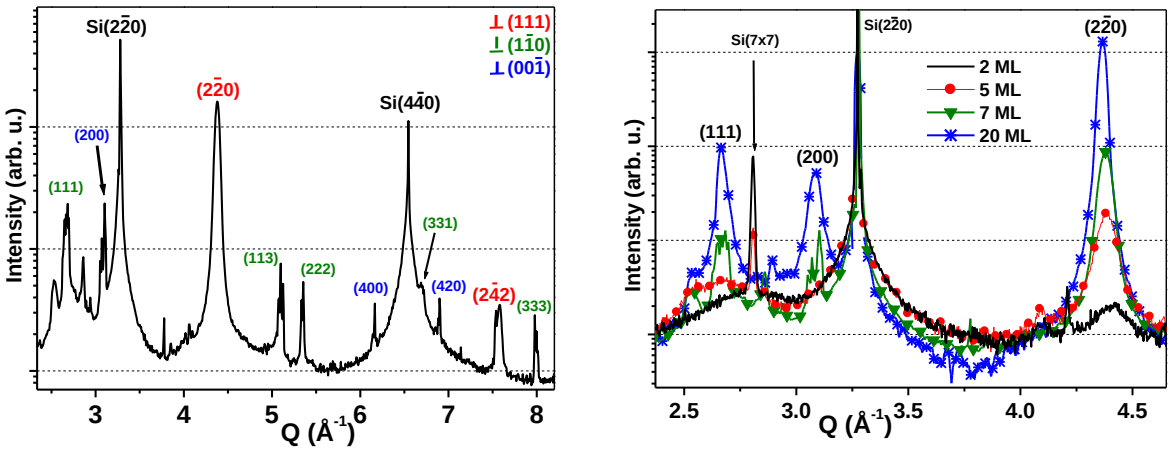

(a) (b)

Figure III.7 – (a) *Radial-scan* along the [1$\bar{1}$0] azimuth performed at RT after a deposit of 7 ML, (b) *Radial-scan* along the [1$\bar{1}$0] azimuth performed at RT after deposits of 2, 5, 7 and 20 ML.

Obviously, some of them can belong to more than one type but it is impossible to distinguish between two types for a single peak. Here, we take the Au($2\bar{2}0$), Au(111) and Au(200) peaks as signature of types A, B and C, respectively. We can also notice that the film is very textured, the Au($2\bar{2}0$) peak being by far the most intense. In Figure III.7(b) is plotted the same *radial-scan* as in the Figure III.7(a) but for different deposited amount : 2, 5, 7 and 20 ML. What is important here is to observe the evolution of the three out-of-plane epitaxial relationships with the deposit. For 2 and 5 ML, only the Au($2\bar{2}0$) peak is present which means that the gold crystallites present the A type epitaxy only. For 7 ML, the Au(111) and the Au(200) peaks show up (i.e B and C types appear) but the Au($2\bar{2}0$) peak is still the most intense (*i. e.* epitaxy A is preponderant). For higher coverage (20 ML) the three modes coexist with still a majority of the gold structures in A-type epitaxy. This shows that the out-of-plane epitaxy type depends on the coverage but with a dominant type A. The critical coverage at which epitaxies B and C appear could not be determined accurately as they were observed sometimes even at 5 ML. It is also important to note here that a Si-(7×7) reconstruction peak is still recorded for samples onto which 2 and 5 ML were deposited. This behavior can have different origins : either the surface is not completely covered by the gold film, or the gold atoms sit on peculiar (7×7) reconstruction sites which preserve the positions of the silicon atoms in the first layer of the substrate [Wu *et al.*, 2010].

b Evolution upon heating

It is now interesting to have a look on how the epitaxial relationships evolves if we heat the sample.

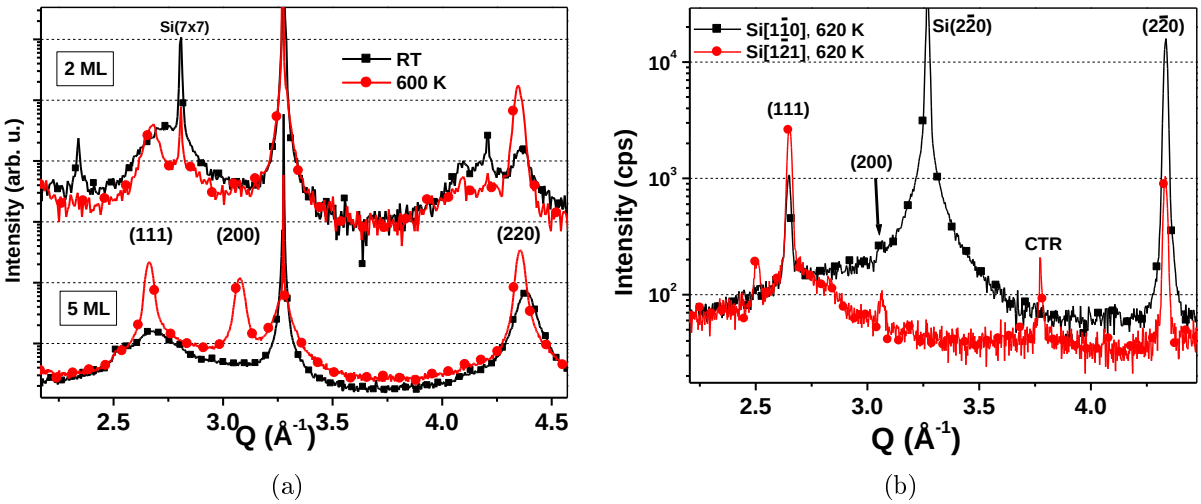

Figure III.8 – (a) *Radial-scans* along the [1$\bar{1}$0] azimuth for a 2 ML and a 5 ML deposit at RT and 600 K,(b) *Radial-scans* along the [1$\bar{1}$0] and [1$\bar{2}$1] azimuths for a 5 ML deposit at 620 K. A *radial-scan* performed at 630 K displaying a liquid structure signal is also plotted.

On the *radial-scans* plotted in Figure III.8(a) for 2 (top) and 5 ML (down) at 300 K, only the A epitaxy is clearly identified. The corresponding *radial-scans* at 600 K (36 K below the Au-Si eutectic point) show that, in both cases, the Au(111) and the Au(2$\bar{2}$0) peaks intensity increase and that for 5 ML, the Au(200) peak appears. Annealing of the samples thus induces a better crystallinity and a modification of the epitaxial relationship. It is also interesting to compare the difference between two scans performed along different Si azimuths. This is done in Figure III.8(b) which compares, for 5 ML, the scans along the Si[1$\bar{1}$0] and the Si[1$\bar{2}$1] directions. The intensities of the peaks vary largely with the azimuth, revealing an in-plane texture of the grains. Indeed untextured polycristalline gold composed of randomly orientated grains would lead to a constant intensity along the Debye-Scherrer rings (i.e with a rotation of the sample around its surface normal).

The suspected specific in-plane orientations for the different out-of-plane epitaxies can be found and highlighted with a reciprocal space map such as that recorded at 620 K and plotted in Figure III.9(a). It has been recorded just before melting, by recording the intensity in a sector located between the Si[1$\bar{1}$0] and Si[1$\bar{2}$1] axes. The Si(2$\bar{2}$0) Bragg peak is clearly visible, together with Debye-Scherrer rings of the polycrystalline gold (Au(111), Au(200) and Au(220)). The intensity of the Au(220) ring presents maxima for different in-plane directions revealing a texture with additional favorable in-plane orientations with respect to the ones observed by comparing the two Si azimuths in Figure III.8(b). This indicates that for the dominant A type epitaxy (Au(111)‖Si(111)), different in-plane orientation relationships (ORs) can be found. As far as the two other rings are concerned, corresponding to the other out-of-plane epitaxies (B and C), the map also reveals intensity variations with ω. However,

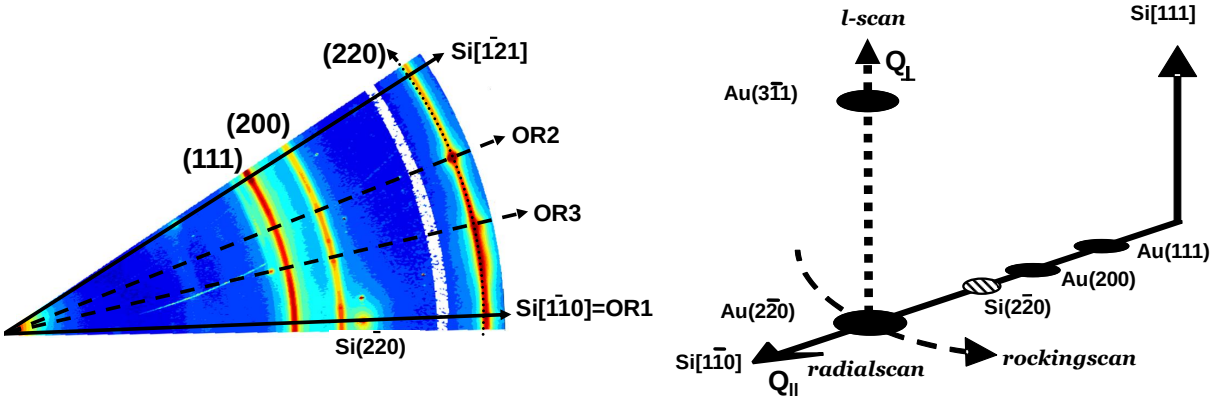

(a) (b)

Figure III.9 – (a) In-plane Reciprocal Space Map covering 30° of the reciprocal space (red : high intensity, blue : low intensity, yellow : intermediate) at 620 K. The white ring corresponds to a loss of the synchrotron beam during the acquisition time. (b) Scheme of the measurements performed in reciprocal space around the Au(2$\bar{2}$0) peak.

the in-plane orientation relationships for type B and C were observed only few times, with no clear reproducible trend from one experiment to another. As it appears that the strongly dominant out-of-plane epitaxy is by far of type A, we thus focus on the A epitaxy as the measurements revealed a systematic behavior of the evolution of its in-plane OR with temperature. By measuring the Au(220) ring in several ways (see Figure III.9(b)) for different temperatures upon annealing, it has been possible to follow several parameters such as the solid dewetting or the in-plane orientation changes.

Gold thermal expansion

Figure III.10(a) shows the radial evolution of the Au($2\bar{2}0$) peak with temperature. At 300 K, the peak is at $Q_{\parallel} = 4.36$ Å^{-1} in reciprocal space, which is equivalent to a (220) d-spacing of its theoretical position calculated by $Q = (2\pi\sqrt{h^2+k^2+l^2})/a_{Au}^2$ with a_{Au} the lattice parameter of gold at 300 K (4.079 Å) and (h,k,l) the Miller's indexes ((2,$\bar{2}$,0) in this case). The corresponding Au crystals are thus not strained. Upon heating, the peak shifts from 4.36 Å^{-1} to 4.33 Å^{-1} at 620 K illustrating the expansion of gold with increasing temperature. A value of $\alpha_{Au} = 15.10^{-6}$ K^{-1} is deduced for the linear thermal expansion coefficient of gold, in very good agreement with literature [Nix and MacNair, 1941]. The Au peak also narrows and increases in intensity with increasing temperatures, reflecting the growth of the crystallites thanks to higher atomic mobility.

Following the dewetting

l-scans (along $Q_{\perp}$) at the $Q_{\parallel}$ value of the Au($2\bar{2}0$) peak are reported in Figure III.10(b). A peak around $Q_{\perp} = 2.5$ Å^{-1} is found, corresponding to the Au($3\bar{1}1$) Bragg position, which

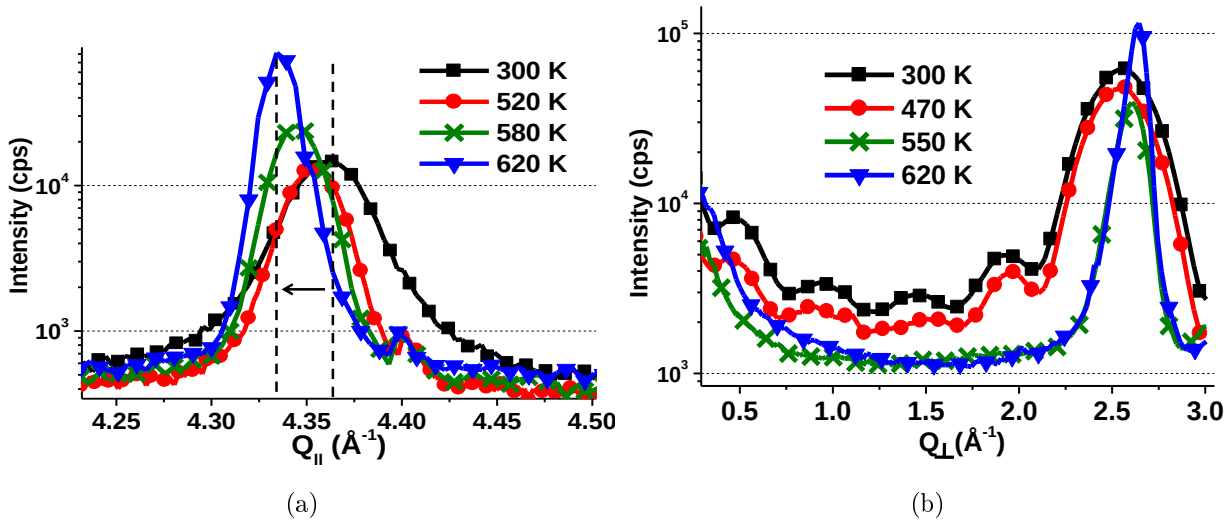

Figure III.10 – (a) *Radial-scans* on the Au($2\bar{2}0$) peak along the Si[$1\bar{1}0$] direction at 300 K, 520 K, 580 K and 620 K, the shift of the peak shows the expansion of gold with annealing. (b) *l-scans* (along $\boldsymbol{Q}_{\perp}$) crossing the Au($3\bar{1}1$) Bragg peak at 300 K, 470 K, 550 K and 620 K

confirms that the Au(111) planes are parallel to the Si(111) planes. At 300 K, the peak width (FWHM=0.37 $Å^{-1}$) and the oscillation period correspond to a film thickness of 16.8 Å (∼7 ML) with a low roughness. At increasing temperatures, the oscillations disappear and the Au(3$\bar{1}$1) peak becomes narrower, reflecting that the film first roughens before the dewetting process takes place : the film turns into islands. At 620 K the FWHM of the peak is 0.09 $Å^{-1}$, which corresponds to an average island's height of about 70 Å.

Evolution of the in-plane epitaxial relationships

The *rocking-scans* on the Au(220) Debye-Scherrer ring provide information on the in-plane crystallographic orientation of the grains composing the gold film and/or the gold islands. As shown in Figure III.11, at 300 K the scan displays a large and broad peak centered on the Si[1$\bar{1}$0] direction and two narrow satellites peaks (which are equivalent because of six-fold symmetry) at ±19.1° corresponding to the Si[2$\bar{3}$1] in-plane direction. This reveals two preferred in-plane orientations of the gold structures with respect to the substrate at 300 K.

The first orientation relationship (OR1) related to the central peak is [1$\bar{1}$0]Au(111)‖[1$\bar{1}$0]Si(111) and corresponds to identical orientation of the Au crystals and the Si substrate. The second orientation relationship (OR2), rotated in the plane by 19.1°, is [2$\bar{3}$1]Au(111)‖[1$\bar{1}$0]Si(111), for which the [2$\bar{3}$1] rows of Au are parallel to the Si[1$\bar{1}$0] axis. At 300 K, a majority of the grains (∼92%) are in OR1 configuration as deduced from the integrated intensity. OR1 is thus the preferred orientation.

After annealing the sample at 620 K and dewetting of the film into islands (still solid), a new peak shows up at ±11.9° (Figure III.11) attesting the emergence of a third epitaxial

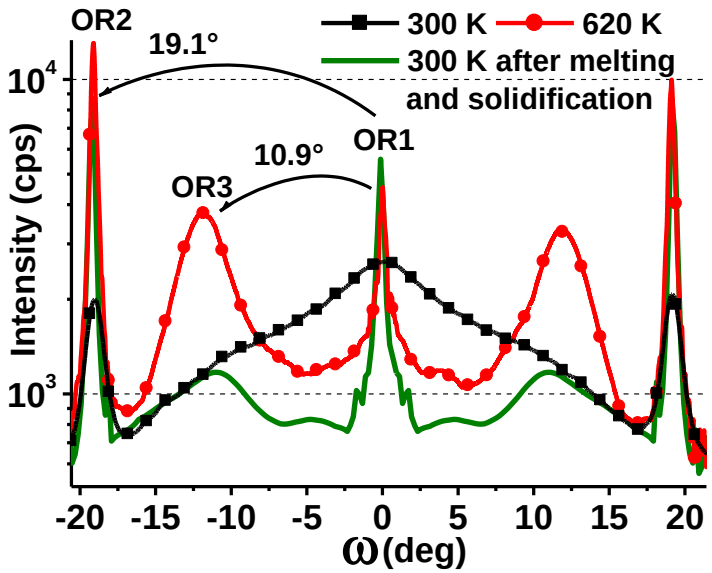

Figure III.11 – *Rocking-scans* on the Au(220) ring at 300 K, 620 K and again at 300 K after melting and subsequent cooling. The peaks correspond to the directional relationships in the plane between the gold and the silicon substrate

orientation (called OR3) of gold islands with the silicon substrate. This epitaxial orientation could be either the $[7\bar{9}2]Au(111)\|[1\bar{1}0]Si(111)$ relationship already reported by Chen *et al.* [Chen and Chen, 1996] which would yield a peak at 12.21° or the $[4\bar{5}1]Au(111)\|[1\bar{1}0]Si(111)$ which would yield a peak at 10.89°. We will see later that the latter is the correct one, and that it should be re-written $[1\bar{2}1]Au(111)\|[2\bar{3}1]Si(111)$. We can also notice that at 620 K, the central peak is narrower and less intense than the 19.1° one. From the integrated peak intensity, we deduce that half of the islands now adopt the OR2 configuration. Hence, the dewetting process taking place from RT to 620 K is accompanied by a change in the epitaxial relationships from OR1 to OR2, as represented in Figure III.12.

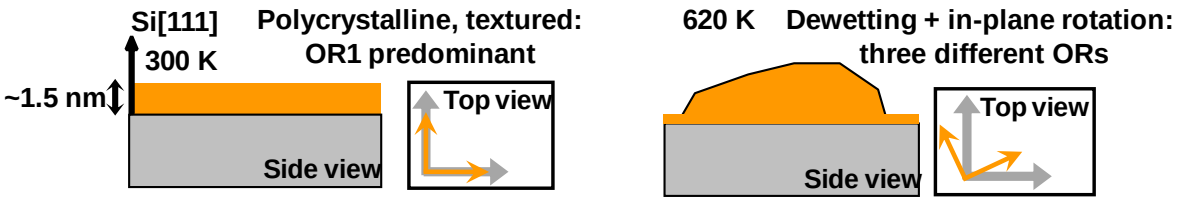

Figure III.12 – Illustration summarizing the evolution of the system : the deposit of 7 ML at 300 K forms a thin film with a "cube on cube" epitaxy. Heating induces a dewetting and the islands appears with a change in epitaxial relationship.

It is interesting to note here, that in the case of a 2 ML deposit, the OR1 was found to be the dominant in-plane orientation, even after annealing at 620 K. This is shown in Figure III.13 which displays a more intense peak for the OR1 for the two temperatures. As a smaller amount of deposited material logically leads to smaller islands with the dewetting (see section III.1.2), a possible link between the size of the islands and the in-plane orientations can not be excluded. The potential connection between the two as well as with the crystalline structure is discussed at the end of this chapter (see section III.2.2.d)

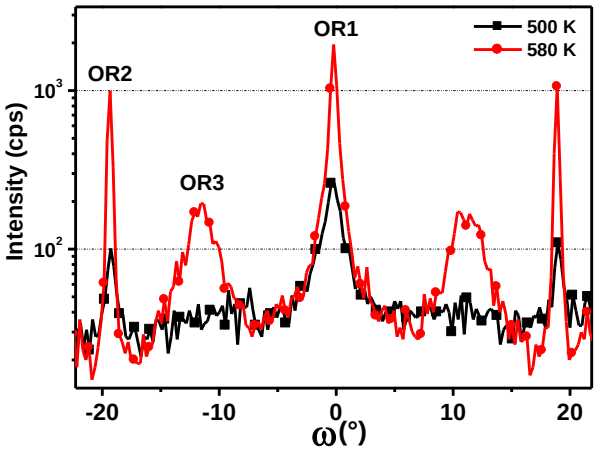

Figure III.13 – *Rocking-scans* on the Au(220) ring at 500 K, 580 K, for a 2 ML deposit.

III.2.2 Discussion on growth and dewetting of Au on Si(111)

The *l-scan* plotted in Figure III.10(b) shows that the 7 ML deposit of gold at RT consists in a flat film which turns into islands with increasing temperature. The dewetting process is driven by the minimization of the surface-to-volume ratio and is a diffusion limited process (see Chapter I, section I.3.3). As a consequence, the atomic mobility offered by the annealing allows the system to reduce its surface area through agglomeration of the atoms [Jiran and Thompson, 1992].

In the case of Au growth on Si(111), as the surface energy of gold (γ_{Au}=1.5 J.m^{-2}) [Tyson and Miller, 1977] is higher than the Si(111) plane energy (γ_{Si}=1.2 J.m^{-2}) [Tanaka *et al.*, 2006], a VW growth mode is expected [Bauer and Poppa, 1972]. However, the growth of Au on Si(111) substrates is known to follow a SK mode (1ML-high wetting layer + 3D growth) at relatively high temperature (above 500 K) [Bauer and Poppa, 1972; Swiech *et al.*, 1991; Hibino and Watanabe, 2005; Fuchigami and Ichimiya, 1996] but also sometimes at RT [Kirakosian *et al.*, 2001]. A quasi-Frank-van der Merwe (FM) growth mode (layer by layer growth on several disordered layers) has also been reported for deposits performed at low temperature (100 K) [Jalochowski and Bauer, 1988] and 3D or 2D growth has been observed at RT depending on the substrate quality [Katzel and Meinel, 1989]. It is also known that Au grows in a layer by layer mode at RT on the low density plane Si(001) [Kim *et al.*, 1996]. The different observed growth modes in this peculiar system may arise because of the relatively close values of the surface energies as well as the uncertainty that seems to exist on the γ_{Au} value (see Chapter I, section I.3.4).

The interface energy between the substrate and the growing film depends on the interaction energy between the two crystals. Following Lojkowski *et al.* [Lojkowski and Fecht, 2000], the interface energy (γ_I) between gold and silicon is given by :

$$\gamma_I = \gamma_{Si} + \gamma_{Au} - \gamma_{adh}, \tag{III.1}$$

where γ_{adh} is the adhesion energy. Therefore, the most stable interface (small γ_I) corresponds to small γ_{Si} and γ_{Au} values and large γ_{adh} ones. For Si, the (111) plane has the lowest surface energy as it is the densest, which explains, for example, that Si nanowires naturally grow along this direction. For fcc metals such as gold, the low energy surfaces are closely packed planes, with $\gamma_{Au(111)} < \gamma_{Au(001)} < \gamma_{Au(011)}$ [Vitos *et al.*, 1998]. It therefore explains why the Au(111)‖Si(111) epitaxy (type A), which is energetically favoured, is the prominent epitaxy.

In addition to surface energies of Au and Si, two other parameters can influence the growth mode : the lattice misfit as well as the interfacial bonding. In some ways, they are related to γ_{adh} : γ_{adh} increases (*i.e.* γ_I decreases) when the interfacial bonding is stronger

than the bonding in the deposit itself and when the misfit between the two materials is low (see next section).

For a 2 ML deposit at RT, Figure III.8(a)(A) and III.7(b) display gold peaks of very low and broad intensity reminding more an amorphous signature. However they can also be due to very small crystal grains. These measurements claim for a gold film with poor crystallite quality into which Au-Si bonds may be preferred to Au-Au bonds, thus lowering γ_I. This observation agrees well with the process proposed by Yeh *et al.* as well as Hoshino *et al.* who measured that for small deposits of Au (below 2∼3 ML), an Au-Si alloy film can form at RT [Yeh *et al.*, 1993; Hoshino *et al.*, 2008]. For subsequent deposition, their studies pointed out that the nucleation of the gold film occurs below the alloy with an abrupt Au/Si(111) interface. The appearance of the Au($2\bar{2}0$) peaks for 5 ML (Figure III.7(b)) and the presence of potential crystalline Au-Si phases in the experiments performed with 2 ML (section III.1.2) support this idea.

When annealing at increasing temperatures, atomic diffusion increases and the dewetting process, which is assumed to start at the grain boundaries of the film [Jiran and Thompson, 1992], takes place (Figures III.10(b)). The increase withe temperature of the gold Bragg peaks intensity in Figure III.8(a) reveals the changes that take place in chemical bondings to form Au-Au instead of Au-Si bonds. The dewetting, which occurs in the solid state, leads to crystalline islands distributed on a wetting layer [Hannon *et al.*, 2006]. Remarkably, the disappearance of the oscillations at 580 K in the *l-scan* clearly underlines the destruction of the film at this temperature. This agrees very well with the assumption that 570 K is a critical temperature above which the dewetting process is enhanced.

In addition to the morphological aspects described previously (section III.1.2), we have shown that the dewetting process is accompanied by changes in the in-plane epitaxial relationships between the emerging islands and the Si substrate. To explain this behaviour, the next section (section III.2.3) focuses on the atomic description of the process that arises at the interface.

III.2.3 Atomic configurations of the interface

a Coincidence Site Lattice theory

Let us simply assume that the adhesion energy is linearly linked with the bonding energy E_{AuSi} between Si and Au atoms "in position of good matching" as follows [Lojkowski and Fecht, 2000] :

$$\gamma_{adh} = \eta \frac{E_{AuSi}}{\Omega^{2/3}}, \tag{III.2}$$

Where Ω is the average atomic volume and η represents the fraction of perfect bonds and can thus be seen as the degree of good matching between the two planes. Equation III.2 means that the better the matching, the higher γ_{adh}, the lower the interface energy (equation (III.1)).

This statement has to be linked to a common geometrical criterion proposed by Bollman *et al.* [Bollmann and Nissen, 1968]. The criterion, called "coincidence site lattice" (CSL), consists in bringing the two different lattices into partial self coincidence. The common lattice sites form the nodes (the "0-points") of a super-lattice. The preferred orientation relationship (OR) corresponds to the maximum density of approximate CSL nodes ("0" lattice nodes), i.e to a large η in equation (III.2) and therefore to a low interface energy. However, despite many experimental studies on surface/interface and other theoretical models[Dahmen, 1982; Kato, 1989; Ikuhara and Pirouz, 1996], to date, no simple criterion exists to predict epitaxial configuration. However, Kato *et al.*[Kato, 1989] concluded that the OR chosen by a system is more dictated by the lowering of the elastic strain. Ikuhara *et al.*[Ikuhara and Pirouz, 1996] proposed a clever geometrical method, similar to Bollmann, to describe epitaxial relationship : by calculating the overlap of the reciprocal lattice points (represented by spheres) of both crystals : the configuration that maximizes the overlapped volume gives the most expected orientation relationship.

b Evolution of the mismatch with T

As the interface between Au and Si(111) is known to be sharp (i.e without intermixing)[Yeh *et al.*, 1993; Hoshino *et al.*, 2008; Chen and Chen, 1996] at least well below the eutectic temperature, let us focus on the way the Au(111) plane is related to the substrate for the three epitaxial OR in terms of atomic matching in real space and apply Bollmann's criterion. The lattice parameters of the two crystals (a_{Si} = 5.431 Å and a_{Au} = 4.079 Å, at 300 K) differ largely resulting in a large misfit given by : $\psi = |a_{Au} - a_{Si}| / a_{Si} = 0.25$ and hence in a poor atomic matching. The three epitaxial configurations revealed by X-ray are represented in real space in Figure III.14 by superposing the Au(111) plane (yellow atoms) with the Si(111) plane (black atoms) at 300 K. Figure III.14(a) corresponds to the OR1 configuration in which the $[1\bar{1}0]$ rows of the two crystals are parallel. In this configuration, each fourth atom of the Au$[1\bar{1}0]$ row coincides with the third atom of the Si$[1\bar{1}0]$ one. It reveals an hexagonal CSL (highlighted in red/dashed) of periodicity L_1(11.52 Å). The rotations by 19.1° and 10.9° of the Au(111) planes around the [111] axis bringing the system into OR2 and OR3 configurations are represented in Figure III.14(b) and III.14(c), respectively. The OR2 configuration leads to a CSL of periodicity L_2(7.68Å) : the first atom of the Au$[2\bar{3}1]$ row falling in good coincidence on the second of the Si$[1\bar{1}0]$ row. The CSL periodicity of the OR3 is L_3(10Å), the

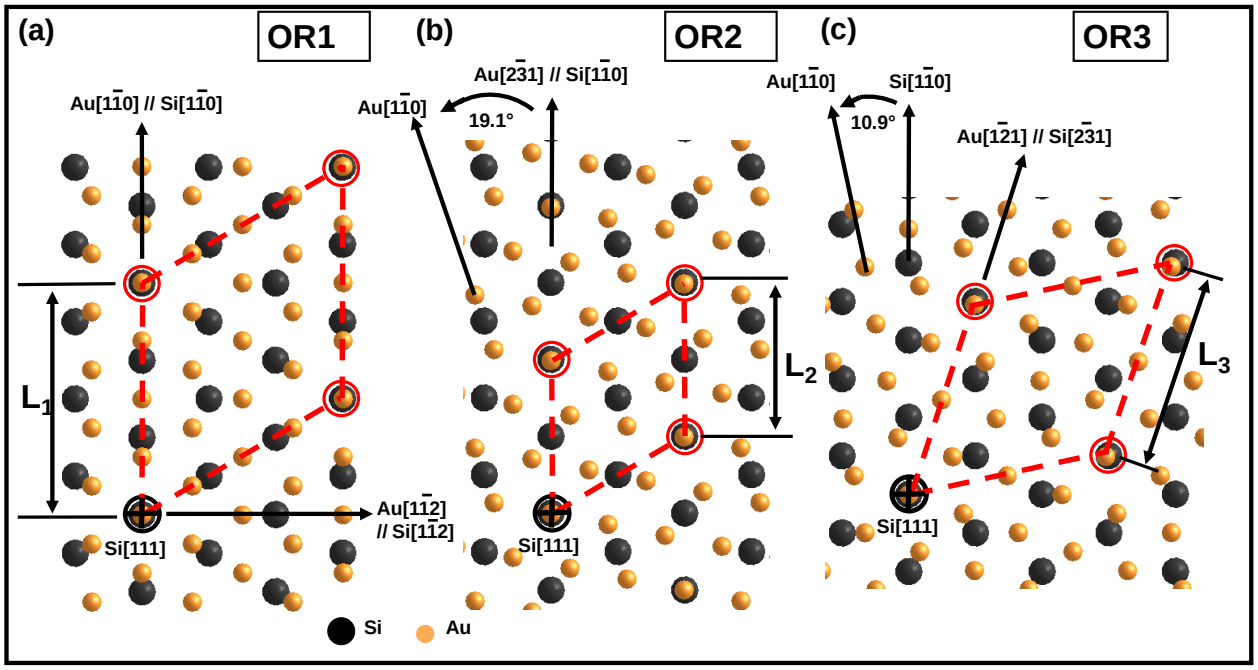

Figure III.14 – Plane view of the interface represented by the superposition of the Au(111) plane above the Si(111) plane, the lattice parameters values are taken at 300 K. The Au(111) plane is rotated around the Si[111] axis by (a) 0°(OR1), (b) 19.1°(OR2) (c) and 10.9°(OR3). The atoms marked with a black cross are in perfect coincidence. For each case, the Coincidence Site Lattice is plotted in red (dashed) and the periodicity (L_x) is indicated. It reveals that : $L_2 < L_3 < L_1$.

coincidence being almost achieved for the second atom of the Au[1$\bar{2}$1] row with the first of the Si[2$\bar{3}$1] row. Note that the third epitaxy is identical to that already reported by Chen *et al.* written [7$\bar{9}$2]Au(111)‖[1$\bar{1}$0]Si(111). Our notation [1$\bar{2}$1]Au(111)‖[2$\bar{3}$1]Si(111) emphasizes the parallel rows of the two crystal along which the coincidence sites are found.

Therefore, according to the "0" lattice criterion of Bollmann and the related interface energy, the OR2 should be favoured with respect to the OR3, itself more favorable than the OR1 ($L_2 < L_3 < L_1$). Experimentally, if OR2 is indeed the preferred orientation relationship at 620 K, this is not the case at RT, where the OR1 is more favourable. Hence, the "0" lattice theory has to be refined by taking the OR mismatch into account. Indeed, to understand this effect, one must take a closer look to what extent the "good matching" really is and how it evolves with temperature. The mismatch of the OR $[hkl]$Au(111)‖$[h'k'l']$Si(111) represents the relative error between the theoretical perfect coincidence point and the real places where the gold atoms are located. It can be expressed as :

$$\chi_{ORx} = \frac{\left| i \times d_{Au[hkl]} - j \times d_{Si[h'k'l']} \right|}{(j \times d_{Si[h'k'l']})}, x \in (1,2,3) \qquad \text{(III.3)}$$

where $d_{Au[hkl]}$ and $d_{Si[h'k'l']}$ are the distances between two atoms in the gold $[hkl]$ and silicon $[h'k'l']$ rows, respectively (for example $d_{Si[1\bar{1}0]}$ =3.84 Å at 300 K). i is the i^{th} atom of

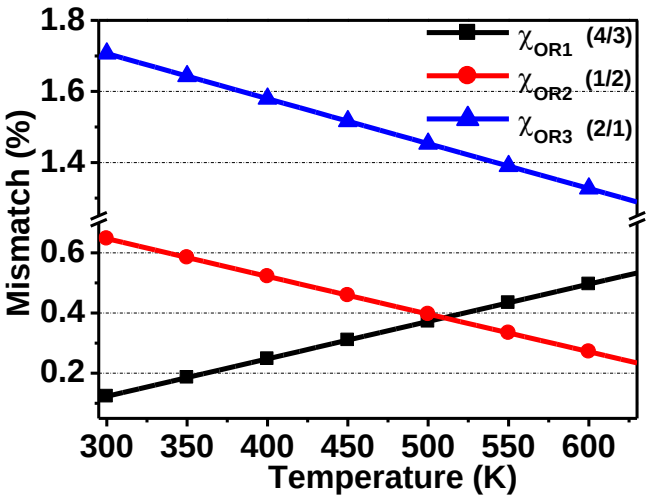

Figure III.15 – Temperature dependence of the mismatch value χ for the three orientation relationships. The ratio m/n is given in the caption next to the concerned epitaxy.

the considered gold row that almost matches the j^{th} atom of the Si row.

In this range of temperature, the thermal expansion coefficients of the two materials can be considered as constant but have very different values : α_{Au}=14.5×10^{-6} K^{-1} and α_{Si}=2.6×10^{-6} K^{-1}. As a consequence, gold expands much more than silicon and the mismatch values are modified upon heating (see Figure III.15). At 300 K, $\chi_{OR1} = 0.13\%$ and $\chi_{OR2} = 0.63\%$, the shortest periodicity is thus offered by the OR2 relationship but the best matching is achieved by the OR1 one. As far as the OR3 is concerned, its mismatch value is so high ($\chi_{OR3} = 1.7\%$) that no grain presents this epitaxial orientation. With increasing temperature χ_{OR2} decreases (as well as χ_{OR3}) and χ_{OR1} increases, a crossover is found around 500 K. At 620 K : $\chi_{OR1} = 0.53\%$ and $\chi_{OR2} = 0.23\%$, the OR2 configuration is therefore pre-

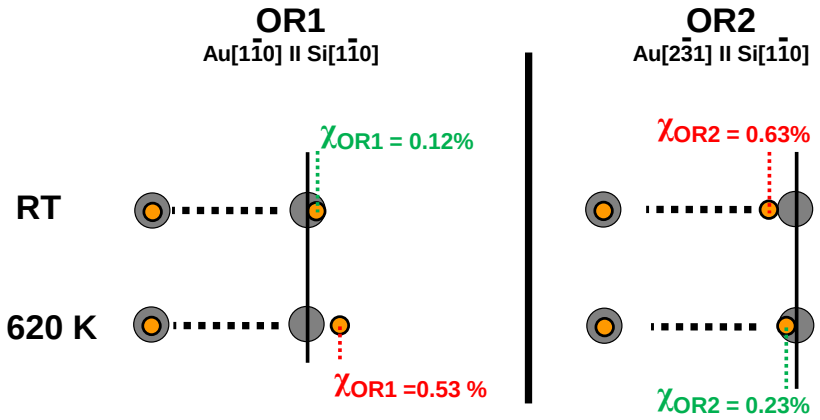

Figure III.16 – Scheme summarizing the mismatch difference between RT and 620 K for the OR1 and the OR2. The origin and the first coincidence site are represented along the parallel Au and Si rows recalled above. At RT the smallest mismatch is provided by OR1 whereas OR2 is more favourable at higher temperatures.

ferred to the OR1 and the OR3 emerges because its mismatch value is reduced.

Here, the experimental measurements clearly underline that the prevailing criterion for the Au/Si(111) interface in this experiment is the "matching quality",*i. e.* the minimization of the mismatch, as recapitulated in Figure III.16.

c Energetic information provided by simulations

The three ORs were also studied by *ab-initio* calculations. The simulation cells are constituted of a 10 Å vacuum layer and a 4 layers Au slab on top of 6 Si(111) bilayers whose bottom layer dangling bonds are hydrogenated by H atoms. The calculated Au and Si equilibrium lattice parameters provided by the simulations are 4.137 and 5.463 Å. As a consequence, OR1, OR2 and OR3 have lattice mismatch of +1.0%, +0.2% and -0.8% compared to the Si substrate, and the Au layers are strained because of the simulation cell periodicity.

The calculation of the formation energies E_f is obtained by :

$$E_f = \left[E_{tot} - (n_{Si}\mu_{Si} - n_{Au}\mu_{Au} - n_H\mu_H)\right]/A_{surf} - E_{Si-H}$$

where E_{tot} is the total energy of the system, n and μ represent the numbers of atoms and the atomic cohesion energies of Si, Au and H. A_{surf} is the unit cell surface and E_{Si-H} is the hydrogenated Si surface energy.

The three ORs have formation energies around 0.9 J.m^{-2}. As the relaxed Si(1×1) and Si(111)-(7×7) DAS surface energies are 1.573 and 1.219 J.m^{-2}, the Au deposition decreases the surface energy of the system, which is in agreement with the experimentally observed good Au wettability. In Table III.4 are gathered the formation energies of the three ORs with OR2 presenting the lowest one. It thus confirms the arguments of lower coincidence site lattice and mismatch we proposed. However these rules do not work for the relative formation energies between OR1 and OR3. This vision is thus a good starting guide to search for good OR, but it is at the moment too simple for accurate quantifications. The reason might be that all the AuSi bonds, not only the AuSi with perfect site coincidence, need to be taken into account to study in detail the relative stability of the various ORs.

OR	Formation energy (J.m^{-2})
OR1	0.886
OR2	**0.857**
OR3	0.908

Table III.4 – Formation energies obtained by *ab-initio* calculations for the different ORs.

d Discussion on size-dependent atomic structure.

At the end of section III.2.1, it was pointed out that for a 2 ML deposit, the OR1 peak in the *rocking-scan* at 620 K (Figure III.13) was more intense than the two others (corresponding to OR2 and OR3). It thus suggests that in the case of a smaller deposit, which leads to smaller islands upon dewetting, the OR1 is favoured. In other words, it seems that small islands do not need to change their in-plane OR to compensate the thermal expansion. This behaviour can be explained when one looks at the variation of the mismatch value along a single crystallographic row. In Figure III.15 and III.16 , the values of the mismatch are given for the closest coincidence site from the atom taken as origin. However, for the other coincidence sites (along the same row), the mismatch values are larger and increase proportionally with the distance from the origin. Therefore, at 620 K, for which χ_{OR1} is larger than χ_{OR2}, larger islands are likely to favour the OR2 whereas smaller islands can remain with OR1. This assumption is further supported by the fact that the OR3 presents the largest mismatch value in any case, with a corresponding peak displaying the largest FWHM (*i. e.* the smallest structures).

However, the above description is valid only if we assume that islands have single-crystal structures. Indeed, the measurement of the FWHM in a peak only gives information on the grain sizes. The question raised here is therefore to know whether the islands have a single or poly-crystalline structure.

For 2 ML, the lateral sizes of the grains extracted from the FWHM in the *rocking-scans* in Figure III.13 at 580 K are $\sim$14 nm and $\sim$18 nm for the OR1 and OR2 peaks, respectively. In addition, the FWHM of a *radial-scan* on the Au(220) peak gives $\sim$15 nm. These lateral size values are remarkably close to the ones obtained in section III.1.2 by GISAXS measurements ($\sim$16 nm). As GISAXS measurements are related to the shape of the islands, these results claim for islands with single-crystal structures[i], the largest displaying the OR2 and the smallest the OR1.

However, for thicker deposits, it seems a bit more tricky. In the case of a 7 ML deposit, the mean lateral size of the grains at 620 K, extracted from a *radial-scan* on the Au(220) peak, is $\sim$30 nm. From the *rocking-scans* in Figure III.11, it comes 22.5, 17.5 and 3 nm for OR2, OR1 and OR3, respectively. A relative comparison between these values supports the assumption that the size of the grain is related to the OR. However, their absolute value seem to be very underestimated. The errors on the lateral size of the grains can be attributed to a low point density in the scans, the miss of the maximum ring intensity or the presence of a mosaic term. Additional information can be obtained by measuring the grain size thank to the investigation of out-of-plane scans in the different orientations. To do so, *l-scans* similar

i. with a possible formation of a AuSi shell (see section III.1.2(c)).

as in Figure III.10(b) were performed, at the Au(220) $Q_{\parallel}$ position and for three different ω values corresponding to the three ORs, at 520 K, 580 K and 620 K. For each OR, the height of the structures can be extracted at each temperature, their evolution are plotted in Figure III.17.

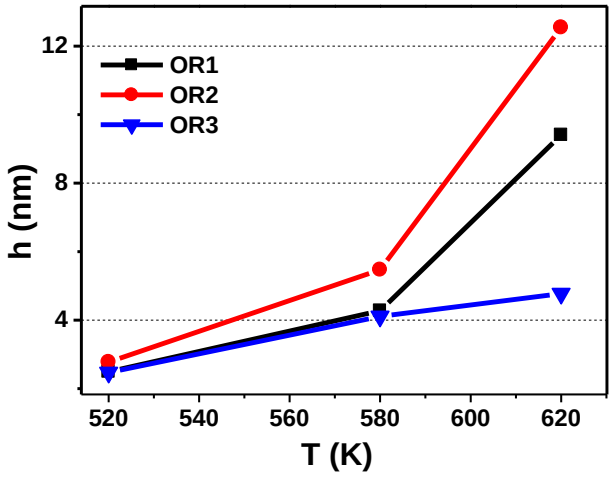

Figure III.17 – Evolution of the height (h) of the structures as a function of the temperature, for the three different ORs.

At 520 K, the height sizes are equivalent for each OR and equal $\sim$2.5 nm. The deposit is still under the form of a rough film, confirming the results obtained in section III.1.2(a) that claimed for a critical dewetting temperature of 560 K. However, the three ORs are already present, which means that grains are likely to start to turn to adjust their in-plane orientation. With further annealing, different heights are attributed to each OR with 12.5, 9.4 and 4.8 nm at 620 K for OR1, OR2 and OR3 respectively. Assuming that the height is proportionally linked to the lateral size, these results support the size-dependence of the adopted OR by the crystallites.

Furthermore, the size of the islands can be studied *ex-situ*. Figure III.18(a) shows a SEM image corresponding to a sample onto which a deposit of about 7 ML of gold was performed at RT, followed by annealing at 620 K, below the eutectic temperature, to avoid the melting of the islands Figure III.18(a). The extraction of the size distribution from the picture is shown in Figure III.18(b) and ranges from 20 nm to 150 nm. Moreover, a quick analyzis reveals a slight bi-modal distribution with small and large islands displaying mean sizes of $\sim$55 nm and $\sim$122 nm, respectively. However the standard deviation is large for both characteristic sizes. This observation also supports the idea of size-dependent OR. However, the sizes extracted from the SEM image do not match the sizes determined by GIXS measurements which provide significant smaller values. Compared to the 2 ML sample case, one would rather conclude here to polycrystalline islands. In addition, Figure III.19 present the AFM study carried out on the sample of the SEM image. The extracted profiles on a large islands (1) gives : $H \approx 20$ nm

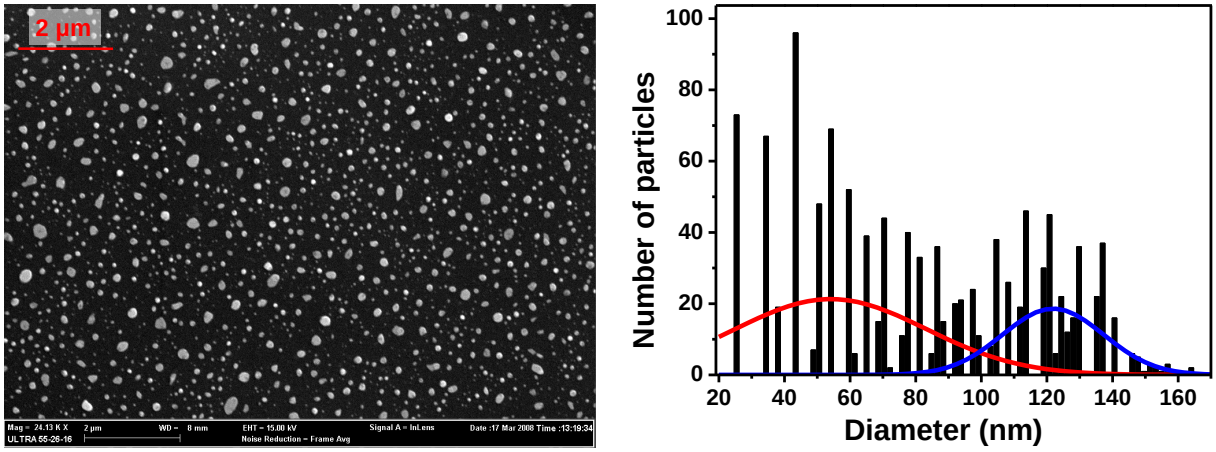

(a) (b)

Figure III.18 – (a) SEM image of ∼7 ML sample annealed at 620 K.(b) Lateral size distribution extracted from the SEM image displaying two characteristic sizes.

and $W \approx 150$ nm. By modeling the shape of the island by a truncated sphere, a rough[i] estimation of the contact angle θ is given by $\theta = acos(1 - (H/0.5W))$ and gives $\sim 45°$, in good agreement with Ressel *et al.* [Ressel *et al.*, 2003]. For the smaller island (2) we obtain : $H = 8$ nm, $W = 90$ nm and thus a θ value of 37°. This result varies in opposite way with the statement that a smaller island should display a larger contact angle (see section III.1.2). However this result only acquaints for one island and is supposed to be within the error bar. It is therefore more a relevant example of the large distribution of the morphological parameters in the self-organization of Au islands on Si(111) [Agnus, 2007].

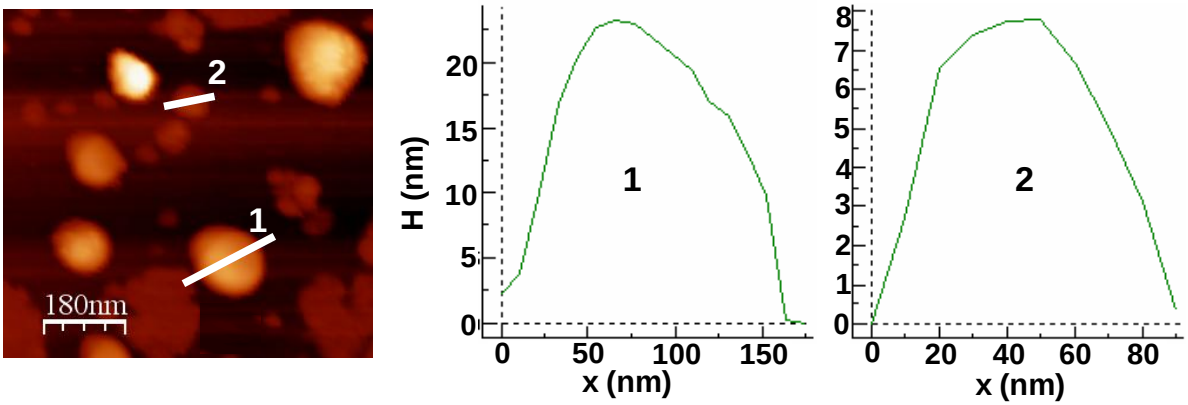

Figure III.19 – AFM image of a reduced area of the same sample presented in Figure III.18(a) and the two correponding two profiles.

In the light of these experimental results, it is likely that small islands obtained with a 2 ML deposit are single-crystal islands. In the case of larger islands obtained with a 7 ML

i. We neglect here the convolution with the AFM tip.

deposit, a polycrystalline structure is maybe more conclusive. In addition, the relationship between the size of the grains and their preferential OR seem to be a reasonable assumption. However, further experiments are clearly needed to get more precise information on the islands' structure.

In this chapter we have described in a first part the morphological parameters of the golds islands in the case of Au growth for small deposits. In a second part, we have presented the dewetting process undergone by a thicker gold film when the temperature is increased as well as the modifications of the interface relationship between the two crystal lattices. In addition, we have mentioned the presence of a wetting layer together with the islands. The next chapter present the results obtained on the study concerning the formation and the atomic structure of this wetting layer which has been found to undergone surface reconstructions.

Summary of Chapter III

Study of small deposits (∼2 ML) :

- The growth of Au on Si(111) at 570 K follows a Stranski-Krastanow mode and results in islands of 2.7 nm in height and of 12.5 nm in width, separated by about 32 nm.
- The islands obtained by dewetting from RT to 570 K present the same inter-islands distance (31 nm) but are a bit larger with a mean height of 4.1 nm and a mean width of 16 nm.
- The comparison between the morphological parameters obtained by GISAXS and the sizes of the grains obtained by GIXS claims for islands with a single-crystal structure.
- In the case of dewetting, the comparison between the GISAXS model and the experimental deposit makes believe that a AuSi shell can form at the surface of the islands. The GIXS measurements support this idea with the presence of unassigned peaks in the scans that could be attributed to AuSi metastable phases. At least they show an alloying effect at RT for small deposits.
- At T_e, the nanosized droplets obtained by dewetting present a contact angle of 73° which is much larger than the one of microscopic droplets (43°).

Study of larger deposits (∼7 ML) :

- The deposit of about 7 ML of Au on Si(111) at RT results in a flat polycrystalline film.
- At RT, the majority of the grains present the orientation relationship : $[1\bar{1}0]$Au(111)$\|\|[1\bar{1}0]$Si(111) (OR1).
- With the increase of the temperature, the film roughens. The formation of the voids is supposed to take place around 560 K, the critical temperature at which the film turns into islands.
- During the dewetting process, the in-plane epitaxial relationships are found to change because of differing thermal expansion of the two materials. This effect modifies the mismatch value at the interface and the most stable in-plane orientation relationship at 620 K becomes : $[2\bar{3}1]$Au(111)$\|\|[1\bar{1}0]$Si(111) (OR2).
- The three different observed orientation relationships are explained using the CSL theory and the quality of the matching. The simulation results support that the three ORs are energetically favourable in terms of surface energies presenting the same ranking. However, the calculated adhesion energies varies in the other way with the OR3 that would present the most favourable interface energy revealing the limits of the CSL theory.
- The size of the grains is likely to be related to its epitaxial relationship with the substrate. The islands are supposed to be polycrystalline for such islands.

Chapter IV

Au-induced reconstructions of Si(111) : (6×6)Au , $(\sqrt{3}\times\sqrt{3})$R30°Au

Contents

In section I.3.2 the surface reconstructions that can form in the Au-Si(111) system have been briefly presented. A major part of this work deals with the understanding of the formation of the Si(111)-(6×6)Au reconstruction, its stability and its structure. In the past, this reconstruction has been mostly studied in the sub-monolayer regime whereas it is studied here in the presence of islands (or droplets) that form for deposits larger than 2 ML as explained in the previous chapter. In this chapter we first present a literature review (section IV.1) to get an overview of the knowledge on the surface reconstructions in the Au-Si(111) system, then we describe our experimental results concerning its formation and its stability (section IV.2). Finally, we present the particular atomic structure of the (6×6) reconstruction and how this latter has been refined (section IV.3).

IV.1 Literature review

As already mentioned in Chapter I gold is a metal known to induce many surface reconstructions when it is deposited on a Si(111) substrate. For coverage ranging from 0 to 2 ML, the (5x2), $(\sqrt{3}\times\sqrt{3})$R30° and the (6×6) reconstructions are the most common and have been intensively studied over the last two decades. Many attempts have been made to draw a correct picture of the phase diagram presenting the different reconstructions as a function of coverage and temperature. Plass *et al.* [Plass and Marks, 1997] proposed a submonolayer phase diagram of the system and their work was then further developed by Grozea *et al.* [Grozea *et al.*, 2000] to extend the diagram up to 2 ML coverage (see Figure IV.1).

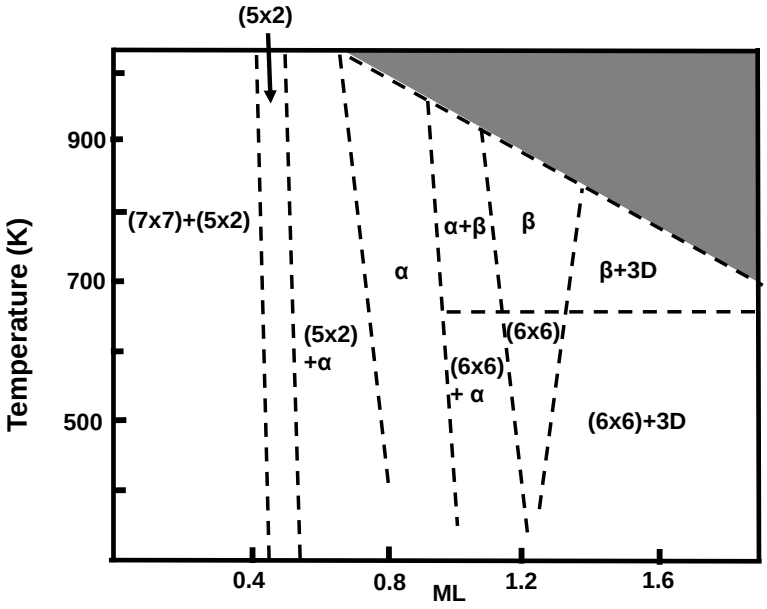

Figure IV.1 – Simplified surface reconstruction phase diagram of Au on Si(111), taken from [Grozea *et al.*, 2000]. α and β are two different $(\sqrt{3}\times\sqrt{3})$R30° reconstruction.

Their work illustrates the complexity of this system in which the domains of existence of the reconstruction are difficult to define precisely as they depend over wide ranges on the amount deposited and on the temperature. In addition, the phase transitions are still unclear due to the difficulties to get the detailed atomic structures of each phase, which are still under debate. This is even more complicated considering that small Au particles can nucleate and grow at various temperatures in parallel to the different reconstructions [Swiech *et al.*, 1991; Nakajima *et al.*, 1997]. The (5×2) reconstruction is known to form in the submonolayer regime in a quite wide coverage range at low temperature (400 K) from 0.1 ML up to 0.7 ML, which narrows with increasing temperature (only up to 0.5 ML at 1000 K). The ($\sqrt{3}\times\sqrt{3}$)R30° surface reconstruction can be found in a wide range of coverage and temperature. Moreover, it is necessary to distinguish between the two phases α-($\sqrt{3}\times\sqrt{3}$)R30° (0.5-1 ML, 400-900 K) and β-($\sqrt{3}\times\sqrt{3}$)R30° (1-2 ML, 650-800 K). These two structures, which have the same periodicity, seem to differ in their chemical environment and in the density of their domain walls [Okuda *et al.*, 1996]. The (6×6) is known to form generally above 1 ML and is stable up to about 700 K. All these reconstructions were found to be stable above the eutectic temperature (T_e=636 K), suggesting potential stabilization of Au-Si bonds by surface processes. Other reconstructions were also reported such as (2×2) [Seifert *et al.*, 2001], (2$\sqrt{3}$×2$\sqrt{3}$) and (2$\sqrt{21}$×2$\sqrt{21}$)R±10.9° [Sakai *et al.*, 1998]. Note, that the latter is related to the in-plane orientation relationship reported in this work in Chapter III.

The first observation of the (6×6) reconstruction was reported by Lander [Lander, 1964]. It has been studied using scanning tunneling microscopy (STM) [Shibata *et al.*, 1992; Takami *et al.*, 1994; Higashiyama *et al.*, 1986b; 2001; Nagao *et al.*, 1998], transmission electron diffraction (TED) [Takahashi *et al.*, 1991; Plass and Marks, 1995], Auger electron spectroscopy [Salvan *et al.*, 1985], X-ray diffraction (XRD) [Dornisch *et al.*, 1991; Grozea *et al.*, 1998], low energy electron diffraction (LEED) [Nakajima *et al.*, 1997; Lander, 1964; Takami *et al.*, 1994; Higashiyama *et al.*, 1986a; 2001; Salvan *et al.*, 1985; Nogami *et al.*, 1990] , impact-collision ion-scattering spectroscopy (ICISS) [Huang and Williams, 1988] and reflection high energy electron diffraction (RHEED) [Sakai *et al.*, 1998; Khramtsova and Ichimiya, 1998; Khramtsova *et al.*, 1999]. Dealing with the (6×6) reconstruction can not be done without mentioning the ($\sqrt{3}\times\sqrt{3}$)R30° as many studies reveal a clear link between the two structures. The LEED study of Higashiyama *et al.* [Higashiyama *et al.*, 1986a] reports a transition from a (6×6) pattern into a ($\sqrt{3}\times\sqrt{3}$)R30° + ring like pattern by annealing at high temperature, the transition being reversible. This agrees well with TED measurement [Takahashi *et al.*, 1991] which revealed that the (6×6) pattern can arise from the low temperature ($\sqrt{3}\times\sqrt{3}$)R30° +star pattern by increasing coverage or by decreasing the temperature at high coverage from the ($\sqrt{3}\times\sqrt{3}$)R30° + ring/hexagon pattern. The creation of the (6×6) reconstruction by cooling

the sample from higher temperatures whose the reconstruction is $(\sqrt{3}\times\sqrt{3})$R30° indicates a need of activation energy but at the same time, the (6×6) was also found to be instable above 600 K claiming for weak binding energy in this study. The cooling rate was also reported to influence the resulting surface structure [Nagao *et al.*, 1998]. STM observations performed at room temperature and reported by Nogami *et al.* [Nogami *et al.*, 1990] also revealed a continuous transition from $(\sqrt{3}\times\sqrt{3})$R30° to (6×6) : the $(\sqrt{3}\times\sqrt{3})$R30° domains (with domain wall running along the <121> substrate directions) decrease in size with increasing coverage to form a well ordered (6×6) structure. In this study the transition was not found to be reversible.

A complementary STM/LEED study [Takami *et al.*, 1994] claims for the co-existence of two $(\sqrt{3}\times\sqrt{3})$R30° domains (one ordered and one disordered) at 0.7 ML. With increasing coverage, the ordered domains disappear and LEED measurements show that disordered domains turn into (6×6) structures. At the same time, the (6×6) unit cell is not visible by STM whereas rectangular arrays of "protrusion" with smaller periodicity than the (6×6) are seen. The authors concluded that the (6×6) structure consists in a network which composes the domain walls that separate the $(\sqrt{3}\times\sqrt{3})$R30° domains. Another combined LEED/STM study from Salvan *et al.* [Salvan *et al.*, 1985] reports the observation, at 1 ML Au coverage, of a $(\sqrt{3}\times\sqrt{3})$R30° LEED pattern but with STM images displaying local (6×6) structures : the proposed model consists in a (6×6) structure composed of structural units of $\sqrt{3}$ periodicity. Thanks to the ICISS technique, a study [Huang and Williams, 1988] proposed a model of the (6×6) consisting of a combination of simple honeycomb and centered hexagons with no position variations of the underlying Si atoms as well as no mixing between the species. The $(\sqrt{3}\times\sqrt{3})$R30° structure, with empty hexagons presenting no long range order, is seen as a precursor of the (6×6) which forms by filling the hexagons with additional Au atoms. Dornisch *et al.* [Dornisch *et al.*, 1991] used in-plane surface X-ray diffraction which is a very suitable technique to solve the atomic structure. Their study confirmed the trimer model for the $(\sqrt{3}\times\sqrt{3})$R30° previously proposed by Oura *et al.* [Oura *et al.*, 1985]. They claim that the (6×6) is not a superstructure of the $(\sqrt{3}\times\sqrt{3})$R30° but that the atoms deeply rearrange themselves in a structure composed of two sixfold twinned domains. The gold atoms arrange themselves in turned trimer triplets with additional Au sites in between. From Patterson function, the Au-Au distance was found to be 2.8 Å. This trimer organization is also supported by TED and HRTEM measurements from Plass *et al.* [Plass and Marks, 1995] and a recent STM+LEED study in which partial disorder in the (6×6) structure was observed [Higashiyama *et al.*, 2001].

A more complex model has been suggested by Grozea *et al.* [Grozea *et al.*, 1998] by re-analyzing the surface X-ray diffraction data of Dornisch *et al.* using a "direct method" [Gil-

more *et al.*, 1997; Marks *et al.*, 1998] to determine the surface structure. They proposed that the (6×6) atomic structure can be described as a combination of pentagonal units and trimers with a fixed Au-Au distance.

In the next section (IV.2) of this Chapter, we first focus on the conditions of formation of the Si(111)-(6×6)Au reconstruction (as well as on the Si(111)-($\sqrt{3}\times\sqrt{3}$)R30°Au) in the experimental conditions of the present study. In this work, we investigate the reconstructions that appear for thick deposited gold films that dewet with annealing and form islands/droplets in coexistence with a wetting layer of the order of one monolayer thickness.

IV.2 Experimental results

IV.2.1 Conditions of formation of the gold reconstruction

A standard experiment consists in depositing a gold film of several ML (typically 7 ML) at RT followed by annealing of the sample (as detailed in Chapter III). At the Au-Si eutectic temperature, the Si atoms diffuse into the islands which have formed during the dewetting of the film, and the system melts.

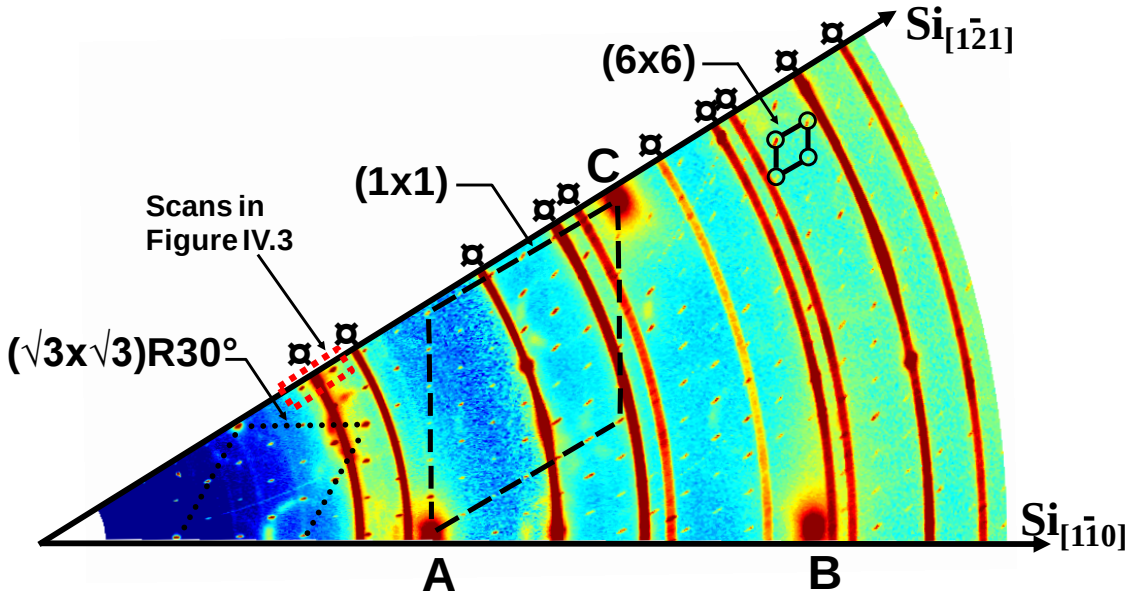

Figure IV.2 – Reciprocal space map covering 30° of the reciprocal space (between the silicon [1$\bar{1}$0] and [1$\bar{2}$1] azimuths) recorded in the solid state at RT after a 7 ML deposit performed at RT, annealed at 700 K (liquid) and subsequent cooling. The red colors correspond to high intensities whereas blue ones correspond to low intensities and yellow to intermediate. This map clearly shows the Si monocrystal Bragg peaks (A :(2$\bar{2}$0), B :(4$\bar{4}$0), C :(2$\bar{4}$2)) together with the Au polycrystalline Debye-Scherrer rings (symbol) as well as the mesh of thin peaks corresponding to the (6×6) reconstruction.

The system was annealed at about 700 K. After the return at RT, a reciprocal space map, plotted in Figure IV.2, was recorded. It was obtained by plotting together 480 *rocking-scans*,

each performed at a different Q value. This map displays three bulk Bragg peaks together with powder diffraction rings from polycrystalline gold. In addition, a mesh of smaller peaks can clearly be seen, corresponding to a (6×6) surface periodic superstructure as the smallest unit of the mesh is six times smaller than the one composed by the Si surface Bragg peaks in reciprocal space. The corresponding structure in real space is therefore 6 times larger. On the map is also plotted the reciprocal space unit cell of the $(\sqrt{3}\times\sqrt{3})$R30° reconstruction ($\sqrt{3}$ times smaller). The peaks form a mesh turned by 30° and are common with some of the (6×6) reconstruction peaks.

In our experiments, annealing the sample above T_e was found to be a necessary step to obtain the (6×6) reconstruction which forms upon subsequent cooling around 670 K. If the sample is not annealed high enough, only a $(\sqrt{3}\times\sqrt{3})$R30° reconstruction remains upon cooling [Schülli *et al.*, 2010].

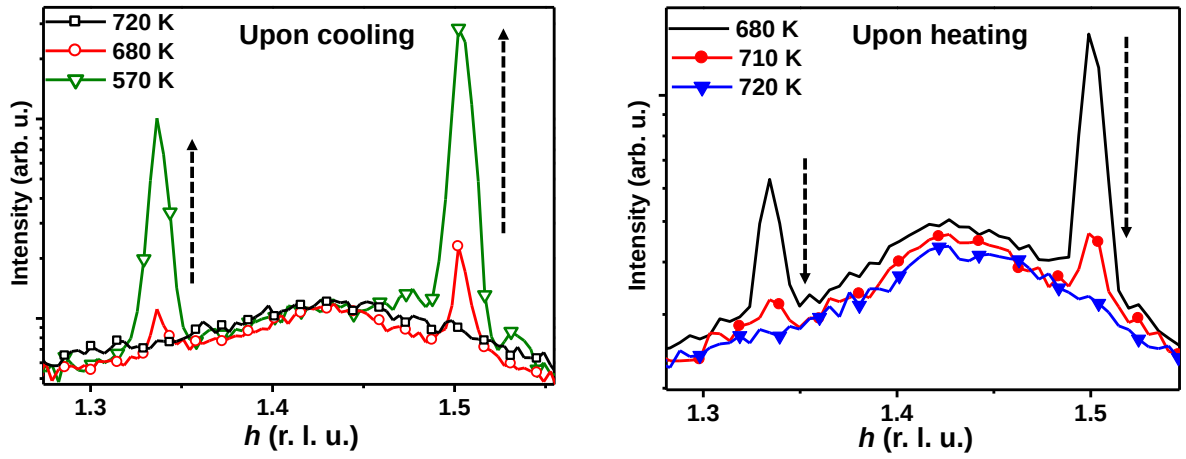

(a) (b)

Figure IV.3 – *Radial-scans* performed along the Si[1$\bar{2}$1] azimuth at the location highlighted in Figure IV.2 on the first maximum of the liquid signal crossing two (6×6) peaks. (a) For a 5 ML deposit, annealed at 720 K, 680 K and 570 K. (b) upon heating at 680 K, 710 K and 720 K. h is given in terms of reciprocal lattice unit (r.l.u) defined in the basis of the unreconstructed surface unit cell (see Figure II.8). The two recorded (6×6) reconstruction peaks are thus located at 1.33 (8/6) and 1.5 (9/6).

Figure IV.3(a) illustrates this statement : the *radial-scans* recorded on the first maximum of the liquid signal, along the Si[1$\bar{2}$1] azimuth, reveal no (6×6) peaks at 720 K. They only appear at 680 K. Upon further cooling, their intensity increases to reach a maximum at 570 K in the supercooled regime. If the sample is heated again, the (6×6) reconstruction vanishes around 680 K as it is illustrated in Figure IV.3(b). The $(\sqrt{3}\times\sqrt{3})$R30° to (6×6) transition is thus found to be reversible and takes place at 680 K. It is however important to keep in mind here that the appearance of the (6×6) peaks overlap the ones of the $(\sqrt{3}\times\sqrt{3})$R30° reconstruction. We therefore observe the formation of the (6×6) reconstruction but it is

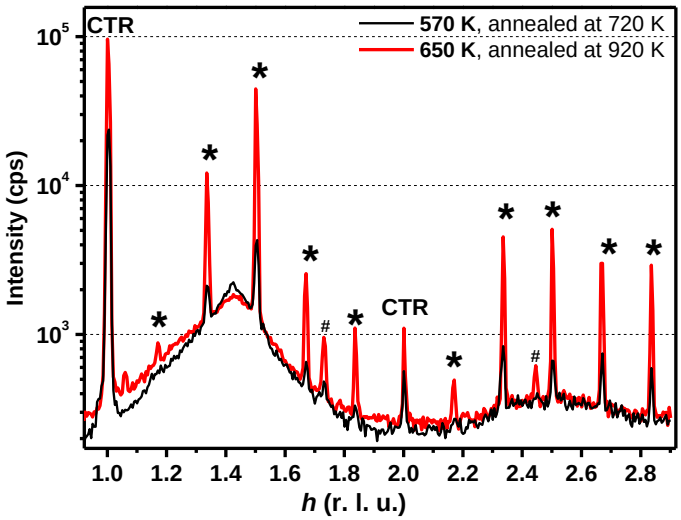

Figure IV.4 – *Radial-scans* along the Si[1$\bar{2}$1] azimuth highlighting the liquid structure factor and the (6×6) signature (stars) for a 30 ML deposit of gold annealed at different temperature (720 K and 920 K).

impossible to know whether or not the ($\sqrt{3}\times\sqrt{3}$)R30° is still present. It is possible that both are present at the same time below 680 K.

The same experimental procedure was applied to a sample onto which 30 ML of gold were deposited. After annealing at 720 K and cooling down to 570 K, the sample presents a nice liquid signal together with "classical" (6×6) peaks as plotted in Figure IV.4. When the sample is annealed at higher temperature (i.e 920 K, below the gold evaporation temperature of 1200 K [Ressel *et al.*, 2003]), a highly enhanced (6×6) signal is measured upon cooling, even at a relatively high temperature (650 K). Unassigned peaks (#) are also recorded and are assumed to arise because of the presence of the 2D AuSi crystal discovered by Shpyrko *et al.* [Shpyrko *et al.*, 2006]. The presence of these structures is discussed in more details in the next chapter. Furthermore, the domains are wider as the FWHM of the reconstruction peaks decreases. In addition, the intensities of the crystal truncation rods (which reflect the Si surface quality) increase when the sample is annealed at a higher temperature suggesting that gold can have a potential influence on the atomic organization of the substrate. This question will be discussed in more details in the light of additional experiments presented hereafter.

IV.2.2 Stability

During the same experiment, ion bombardment (IB) was performed on the sample in the supercooled regime (at 600 K). The (6×6) reconstruction peaks disappeared in only 10 s of bombardment (see Figure IV.5), which implies that the long-range ordering of the reconstruction was destroyed in between the droplets. The sample was then kept at a constant tempe-

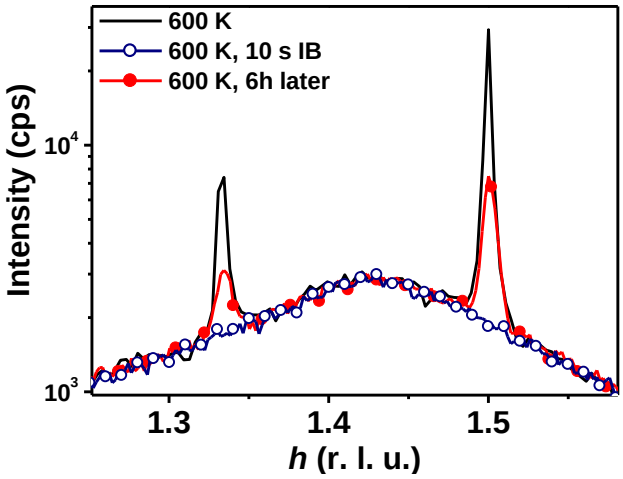

Figure IV.5 – *Radial-scans* performed on the first maximum of the liquid signal and crossing two (6×6) reconstruction peaks (same azimuth as in Figure IV.3) at 600 K : before proceeding to IB, after 10 seconds of Ar+ bombardment and six hours later. Between the three scans, the temperature was kept constant.

rature (600 K) for around six hours. After this period the *radial-scan* shows the reappearance of the reconstruction. The peaks are smaller and wider, indicating that the reconstruction is less structured and presents smaller domains. These observations highlight different facts :

1. the system has to be annealed at least at 690 K,*i. e.* 60 K above T_e to form the (6×6) upon cooling. The (6×6) reconstruction is found to appear around 680 K ;
2. the higher the sample is annealed, the better the reconstruction is defined (*i. e.* larger domain sizes) ;
3. the reconstruction can re-form even at low temperature (600 K) in the presence of gold liquid droplet which seem to serve as a reservoir, as suggested in Figure IV.6.

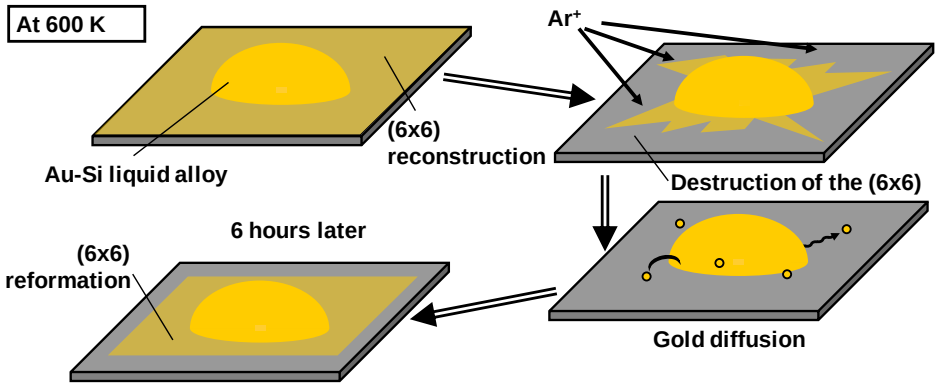

Figure IV.6 – Scheme illustrating the reformation of the (6×6) reconstruction at 600 K. Before bombardment the droplets of AuSi alloy are surrounded by the wetting layer reconstructed (6×6) , the reconstruction is then destroyed by ion bombardment, the (6×6) wetting layer re-forms by diffusion of gold atoms.

A similar experiment has been performed but in this case the system was in the solid state. The ion bombardment was performed at RT after annealing at 720 K. Figure IV.7(a) displays the *radial-scans* performed along the Si[1$\bar{2}$1] direction before and after the bombardment. The comparison of the two scans reveals that the gold peaks remain the same showing that the gold islands are unaffected by the IB whereas, as for IB performed in the supercooled regime, the (6×6) peaks disappear due to the destruction of the surface structure. The interesting feature in this case concerns the observation of the CTR evolution as their intensity (and shape) yields information on the surface roughness (see Chapter II).

Figure IV.7(b) shows an almost complete disappearance of the CTR with the bombardment. This means that, in addition to the destruction of the (6×6) , the bombardment also roughens the substrate surface. If the sample is annealed again at 600 K, which is still below T_e, the CTR intensity is recovered (see Figure IV.7(b)) : the substrate's smoothness improves with annealing. However, the temperature is too low to offer to the Si atoms the necessary mobility to refine the surface. As we have seen that at 600 K the Au atoms diffuse from the droplets to the substrate surface and can reform the (6×6) reconstruction, it is likely that the smoothing of the substrate surface is due to the surface diffusion of the gold atoms which interact with the Si surface atoms and make their displacements possible. Indeed, it has already been reported that gold is an effective surfactant for the homoepitaxial growth of Si on Si(111) substrates. A temperature of at least 920 K is required to form Si thin films of high quality on a bare surfacess [Allen and Kasper, 1988]. However, using LEED and Rutherford backscattering spectrometry (RBS), Wilk *et al.* reported the formation of homoepitaxial Si films through an overlayer of Au at lower temperatures (720-770 K) [Wilk

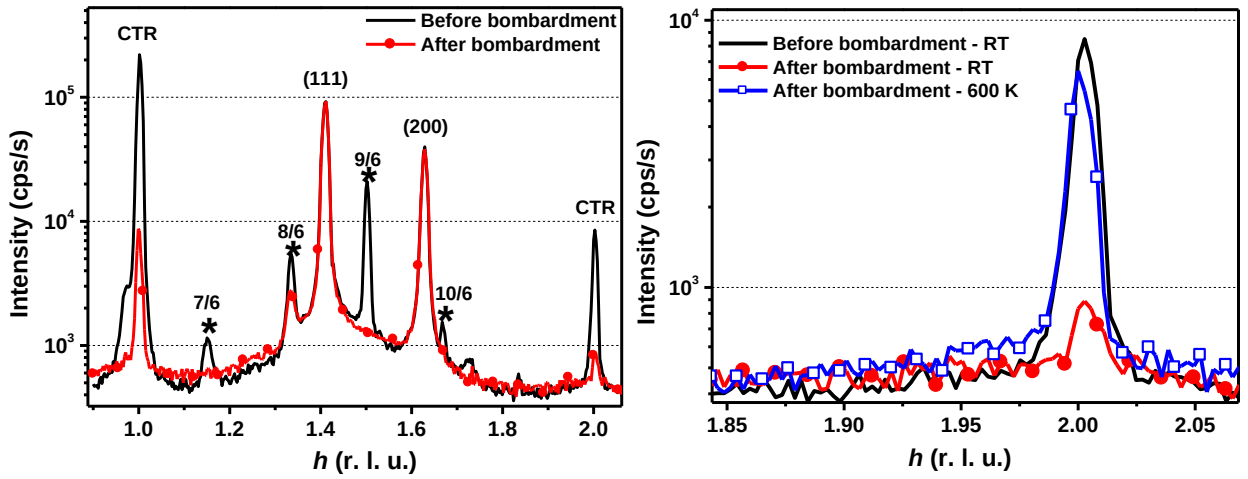

(a) (b)

Figure IV.7 – (a) *Radial-scans* performed along the Si[1$\bar{2}$1] azimuth, at RT, before and after IB. (b) *Radial-scans* on the Si substrate CTR at RT before IB, at RT after IB and annealed at 600 K.

et al., 1994]. Similar results were obtained by Minoda *et al.* by depositing the Si atoms on a Si(111)-(5×2)Au reconstructed surface [Minoda *et al.*, 1992]. The gold-covered surface was found to replace the two-dimensional growth of Si (which only occurs at the domain walls of the reconstruction) by the formation of a thin Si film between the gold reconstruction and the Si surface. A similar experiment has been performed in this work, and is described in the section VII. It shows the layer by layer growth of Si in the presence of a Si(111)-(6×6)Au reconstruction at 620 K.

A few papers have studied the AuSi droplets in parallel with the surface reconstruction. Swiech *et al.* [Swiech *et al.*, 1991] pointed out that the AuSi droplets are very mobile even at low temperature (but above 550 K). Their displacements were found to leave tracks on the substrate which prevent the formation of the (6×6) . Conversely, the (6×6) formation was observed to start at the edges of big particles. The tracks formation has been explained later on, thanks to the SEM technique [Ressel *et al.*, 2003]. Upon cooling, the Si present in excess in the droplet is deposited on the substrate, the particle migrates leaving a track of Si behind it with horizontal facets orientated (111). The liquid/solid interface is therefore assumed to be very flat.

Reversely, upon heating, the particles move by dissolution of the Si into the droplets. Now that the (6×6) reconstruction formation and stability conditions have been described, we focus, in the next section, on its atomic structure.

IV.3 Si(111)-(6×6)Au structure

IV.3.1 Data collection and symmetry averaging

a Data collection

A thin film of gold (about 7 ML) was deposited at RT, annealed at 720 K and subsequently cooled down back to RT. The remaining system consists in polycrystalline gold islands together with a Au-(6×6) reconstruction as presented in section IV.2.1 in Figure IV.2. The collection of the set of data consisted in performing highly resolved *rocking-scans* on each (6×6) reflection, over a 120° segment of reciprocal space. All reflections were integrated and monitor, area, Lorentz and polarization corrections were applied (see Chapter II). The substrates' Bragg reflections and CTRs were removed to avoid bulk contributions, the remaining set of data thus consists in 976 in-plane reconstruction structure factors represented in Figure IV.8(a). This figure clearly reveals rotational and mirror symmetries which means that equivalent reflections were recorded.

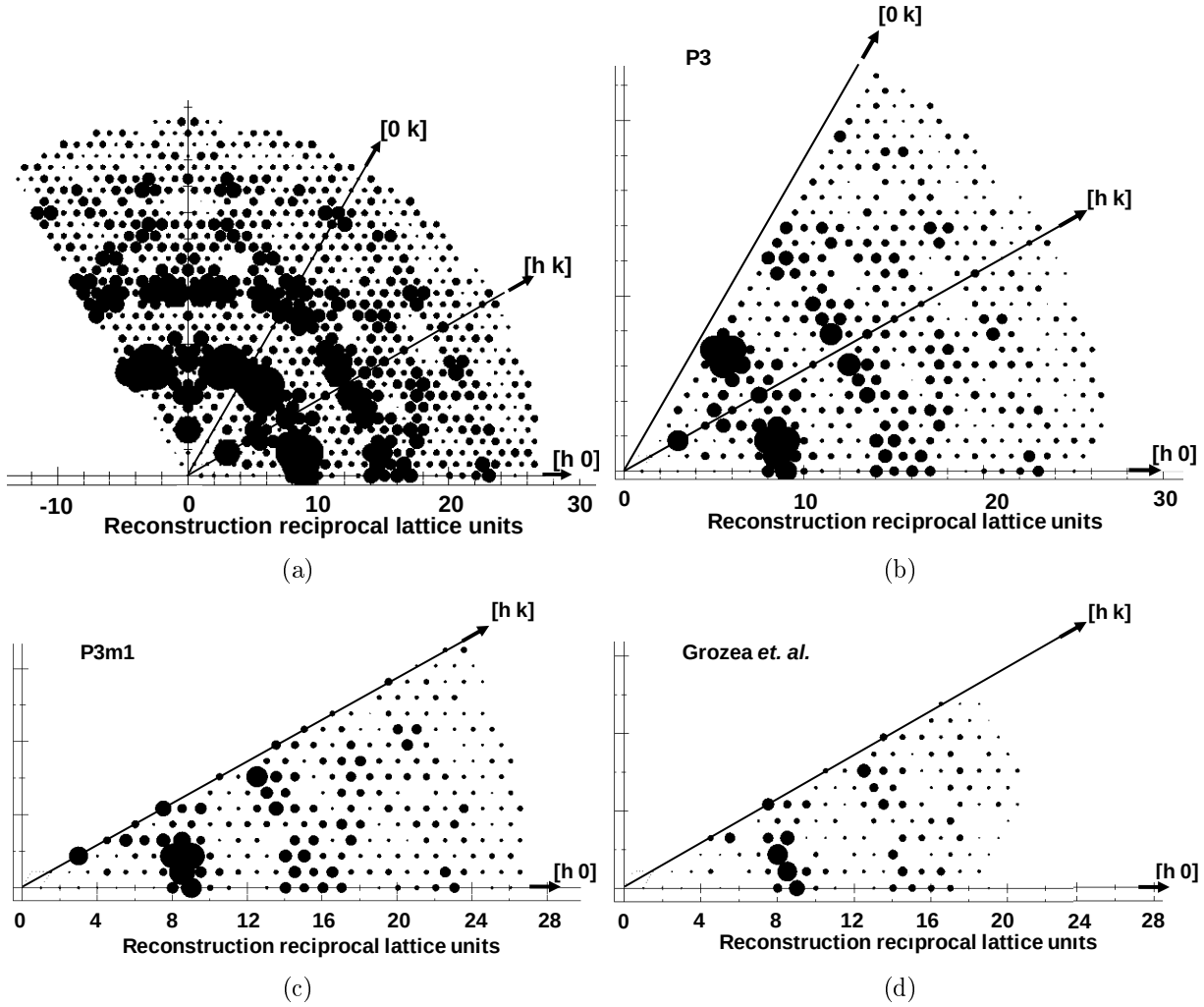

Figure IV.8 – (a) Experimental structure factors. (b) Averaged experimental structure factors using *p3* symmetry.(c) Averaged experimental structure factors using *p3m1* symmetry. (d) Averaged structure factor used in Grozea *et al.* [Grozea *et al.*, 1998] in *p6mm* symmetry. The surface of the circle is proportional to the reflection's intensity. h and k are expressed in the reciprocal units of the (6×6) reconstruction.

b Symmetry and averaging

The measurement of equivalent reflections is not a waste of time but an improvement of the dataset quality as it allows a reduction of the systematic error by averaging of the equivalent intensities [Feidenhans'l, 1989]. The use of a program called AVE [Vlieg, 2000] makes possible the averaging in different symmetry groups. Figure IV.8(b) shows our data averaged in *p3* symmetry. It clearly displays a mirror plane suggesting that the data can be averaged using a more symmetrical group. The AVE program provides an "average agreement factor" corresponding to a measure of the systematic error in the dataset. This factor represents, for a given symmetry group, the difference between theoretically perfectly equivalent reflections for the recorded data. For our dataset, the lowest average agreement factor is obtained for

the *p3m1* symmetry. The compilation of our data set in this symmetry group reduces the number of independent reflections to 441 with a mean systematic error ϵ of 3.9 %. The result is plotted in Figure IV.8(c) for the *p3m1* symmetry. All independent experimental structure factors are listed in Table VII in Annexe. The errors σ [i] are also given together with the theoretical structure factors deduced from the refined model presented in section IV.3.2. The comparison with the experimental ones is provided by the partial χ^2 .

IV.3.2 Model Evaluation

a Thickness and domain size

A quick analysis of several (6×6) peaks yields information on the average domain size. In Figure IV.9(a) is plotted a *rocking-scan* performed on one of the most intense fractional-order (6×6) peak for which a Lorentzian fit provides a FWHM of 0.102° (*i. e.* 0.0018 rad. at Q=2.89 Å^{-1}). The average size of the domain of this reconstruction is thus of 112 nm (exponentially decaying correlation length of 56 nm), which shows that the (6×6) reconstruction is of high quality.

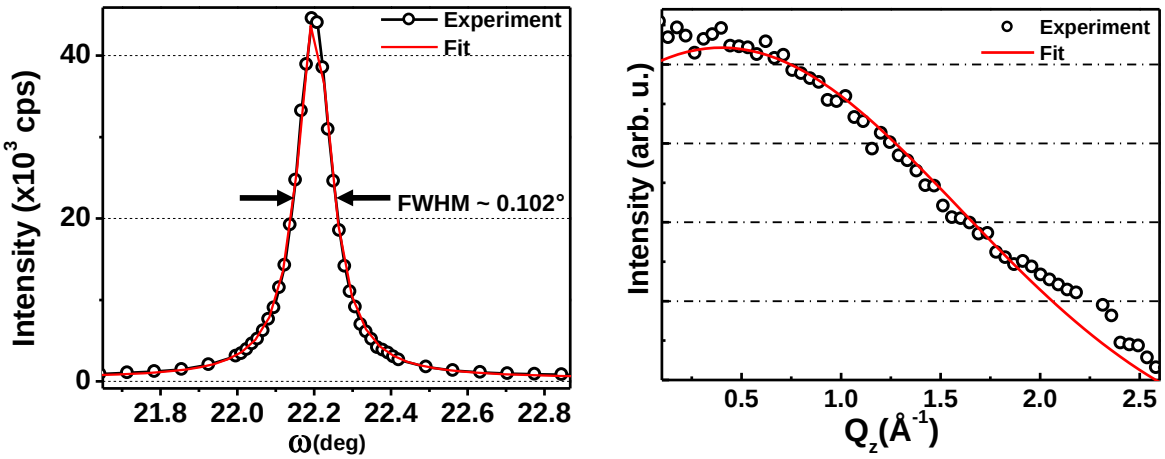

Figure IV.9 – (a) *Rocking-scan* performed on the (8/6 ,2/6, 0.096) reconstruction peak.(b) Representative out-of-plane scans performed along the (2/6 ,1/6, l) reconstruction rod.

Figure (b) displays a *l-scan* performed on a (6×6) peak (the (2/6 ,1/6, l)) and reveals a slow decrease in intensity perpendicular to the surface. This is typical for a rod-like shape of signals arising from surface structures, the FWHM (measured on several (6×6) rods) indicates that the thickness of this reconstruction is of the order of one monolayer.

i. $\sigma = \sqrt{\epsilon^2 F_{hkl}^2 + \sigma_{stat.}^2}$, with $\sigma_{stat.}$ the statistical error of the considered reflection.

b Patterson map

In X-ray scaterring, only the intensity of the reflections is measured : the phase is lost. This is the well-know phase problem which makes the refinement of the structure more difficult. However, information on the atomic structure can be obtained by use of the Patterson map. In surface X-ray diffraction, we use the plot of the two-dimensional Patterson function $P(x, y)$ given by :

$$P(x,y) = \sum_{h,k} |F_{hk0}|^2 \cos 2\pi(hx + ky) \qquad \text{(IV.1)}$$

As already mentioned our dataset only contains fractional-order reflections of the (6×6) structure so that the Patterson map only reveals the atomic order of the surface reconstruction. The Patterson obtained with our dataset is plotted in Figure IV.10 with its asymmetric unit highlighted in red. The contour plot reveals positive peaks corresponding to interatomic vectors of the real structure [Feidenhans'l, 1989].

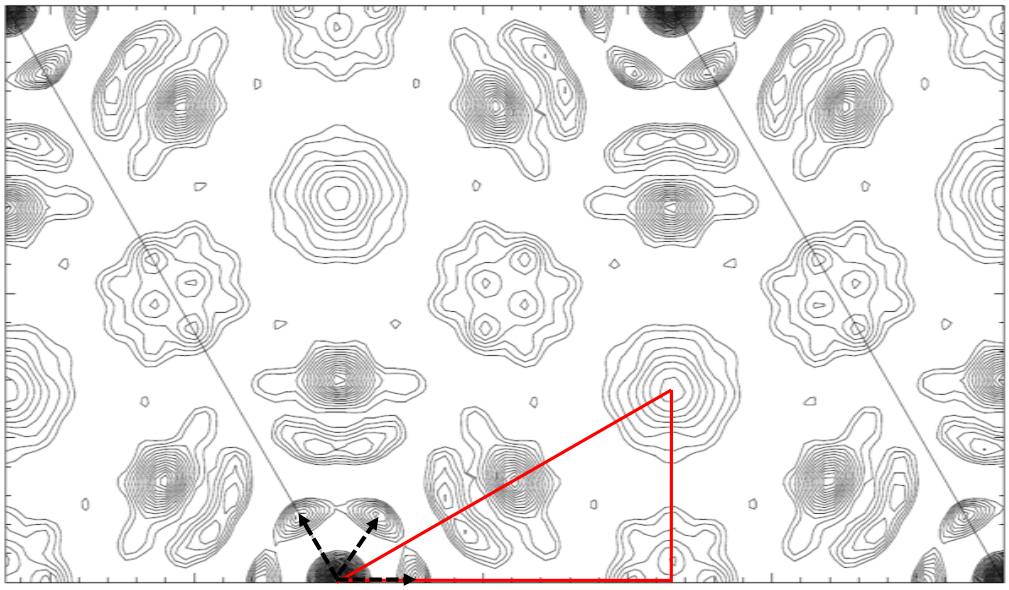

Figure IV.10 – Experimental fractional-order Patterson function plotted on the (6×6) unit cell. The three arrowed peaks are known to be due to trimer of Au.

In Table IV.1 are shown the relative weights in interatomic distance vectors in the AuSi system [Dornisch *et al.*, 1991] which indicates that the most intense peaks are due to distance between two gold atoms. From a Patterson map, one can therefore derive a set of interatomic vectors to build a trial model from which calculated structure factors can be obtained and compared to the experiment (see section II.2.2).

According to our Patterson map, the strongest peak in the irreducible unit corresponds to a Au-Au distance of about 2.8 Å. The three arrows point out three equivalent interatomic vectors of similar length. Dornisch *et al.* showed that they are due to Au trimers that are the

prominent structural elements of the Si(111)-Au($\sqrt{3}\times\sqrt{3}$)R30° and of the Si(111)-Au(6×6) structures [Dornisch *et al.*, 1991]. Indeed, Au trimers correspond to three interactomic vectors of same length rotated by 120°. Howes *et al.* also reported the formation of Au trimers being at the origin of the same contour plot in the Patterson map in the case of the formation of a Au-($\sqrt{3}\times\sqrt{3}$)R30° reconstruction on Ge(111).

However the refined model proposed by Dornisch *et al.* was still incomplete. Indeed, using classical methods to determine a specific structure, one requires to have a starting model close to the real one. This condition, which is by the way quite strong, ensures that the assumed phases (implicitly imposed by the trial model) are close to the real ones. A starting model can for example be extracted from STM measurements. Moreover, our Patterson map (see Figure IV.10) displays additional peaks which means that some other representative interatomic distances have to be considered in the model. Despite the apparent simplicity of the Patterson map and many efforts to propose a trial structure based on Au trimers completed with either Au or Si atoms to fit the other interatomic distances, no satisfactory model could be deduced.

If a proper model from a Patterson map can not be proposed, other approaches, called direct methods, can be applied. These direct methods are based on the calculation of physical properties helping to find the most plausible starting models. For example, with a method based on the calculation of entropy, Gilmore *et al.* were able to directly determine the Si-(7×7) reconstruction from a dataset of structure factors [Gilmore *et al.*, 1997]. Using the same method applied to the SXRD data of Dornisch *et al.* , Grozea *et al.* have been able to propose a model of the atomic structure of the Au-(6×6) reconstruction [Grozea *et al.*, 1998].

c Direct method refinement : Grozea's model

Briefly, their method consists in adjoining a set of phases to the measured set of intensities. The proposed phases are estimated to be self-consistent with a figure of merit corresponding to the most plausible structure, this latter being determined by a minimum relative entropy method [Gilmore *et al.*, 1997]. The resulting phasing maps, classified according to the agreement with the figure of merit, are the images of the charge density *i. e.* of the atomic structure. However, in practice, in the initial stage, only partial phasing maps (*i. e.* only

Table IV.1 – Relative weight of interatomic distance vectors in the Au-Si system [Dornisch *et al.*, 1991].

Distance vector	$Z_1 \times Z_2$	Rel. weight
Au-Au	6241	1
Au-Si	1106	0.18
Si-Si	196	0.03

partial structures) can be obtained and new atoms (*i. e.* charge density) are added in the structure through iterative processes controlled at each step. In the work of Grozea *et al.* , the best partial phasing map has a *p3* symmetry and reveals 20 Au atoms. The completion of the structure by their iterative method resulted in the hexagonal unit lattice represented in Figure IV.11.

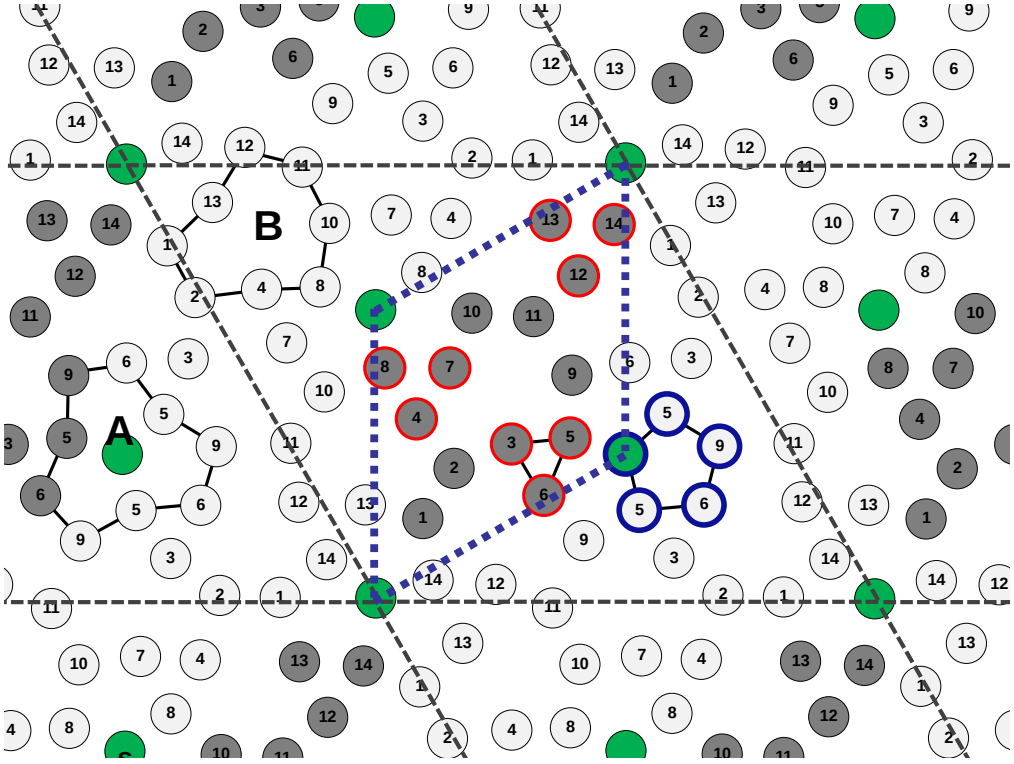

Figure IV.11 – Scheme of the Au-(6×6) hexagonal lattice (dashed-black line). It is composed of 45 atoms : 14 independent sites (grey atoms in dashed-blue hexagonal primitive lattice) from which the 28 others can be deduced by the *p3* symmetry (the equivalent atoms have the same number). The 3 other atoms (green) are the special sites partially occupied (see text). The structure is also completely described by tiling the plane with the highlighted A and B rings which are formed by sub-structural trimers (red) and pentagons (blue)

The resulting surface structure obtained by Grozea *et al.* therefore consists in a hexagonal structure with a *p3* symmetry (almost *p31m*). In Figure IV.11, the grey atoms are the 14 independent sites, the equivalent atoms related by *p3* symmetry have the same number. In green are highlighted the sites on the symmetry axis having a partial occupancy as revealed by their analysis. In addition, Grozea *et al.* mention the presence of twin domains. More interestingly this structure is composed of two kinds of ring sites : the sites A which are partially occupied, and the sites B which present two rotational variants. A combination of pure empty A rings and B rings corresponds to a structure with a $\sqrt{3}$ periodicity.

As mentioned by Grozea *et al.* , this reconstruction is "astonishingly simple, and at the same time complicated". Simple because it displays sub-structural units composed of gold tri-

mers in agreement with the structure proposed by Dornisch *et al.* and complicated because it forms incomplete and complete pentagons (Figure IV.11). If all the A sites would be filled, only complete pentagons would form. In addition to the positions of the gold atoms presented in Figure IV.11, Grozea *et al.* also proposed the refinement of the Si atomic structure in the first layers which were found to be necessary to improve the agreement between the model and their experiment. Their results pointed out that the Si positions in the first layer differ a lot from their positions in the bulk.

Indeed, with only the Au atoms taken into account, with two domains but without including special site atoms, the χ^2 value obtained by Grozea *et al.* is still 32, very far from the ideal value of 1. The addition of two double Si layers reduced this value to 8. Finally, they obtained their best agreement (χ^2 =3.8) by including the gold atoms with partial occupations (green atoms in Figure IV.11) and a strain field in the substrate which strongly displaces the Si atoms in the first layers.

The model of Grozea *et al.* is attractive because it offers a trial model for a standard structure refinement composed of Au trimers as well as other structural units that could not have been deduced from the Patterson function analysis. Indeed, the presence of the pentagon units can explain why it has been impossible for Dornisch *et al.* [Dornisch *et al.*, 1991] to determine the (6×6) structure with classical methods since any model taking into account only trimer units would be too far from the real structure and thus convicted to fail.

Even if the direct method is very powerful, several weak points have to be mentioned concerning their study. First, their experimental structure factors dataset contains much less reflections than our dataset (about a factor four , see Figure IV.8(d)). Second, their systematic uncertainty in their measurements ($\sim$10 % [Dornisch *et al.*, 1991]) is much higher than our and despite that, their χ^2 value remains rather high[i]. Moreover, the reduction of the χ^2 has been obtained only through strong assumptions. Finally, the experimental conditions imposed a transfert of the sample into a baby chamber, which could have influenced the results.

Therefore, in the following we present our structure refinement of the (6×6) reconstruction. With the help of Grozea's model as a starting structure, we confront this latter to our own set of X-ray data which contains more reflections (*i. e.* less uncertainties). An important point is that our data were collected under completely different experimental conditions, it is thus even more interesting to compare the two (6×6) structures.

i. The χ^2 value is inversely proportional to the uncertainty value so that a high uncertainty lowers the χ^2 .

d Determination of the structure of the (6×6) reconstruction

Without the Si substrate

In the first χ^2 minimization attempts, only the Au atoms were taken into account. The model used in the first evaluation simply consisted in the hexagonal lattice (dashed-black) presented in Figure IV.11 with 45 gold atoms. All atoms were assumed to have the same Debye-Waller (DW) as well as the same occupancy parameter (even for the special sites). Their displacements were allowed with respect to the *p3* symmetry which means that the special atoms were assumed to be immobile and that the different sets of three related atoms were constrained in directions respecting the imposed symmetry. The evaluation of this model gives a χ^2 value of 10.1 which is a very good value regarding the simplification imposed in our model. This agreement confirms that the structure proposed by Grozea *et al.* , which is quite surprising at first sight, is the real one and forms in our experiment.

Without giving many details, the paper of Grozea *et al.* mentions that the structure displays twin domains. The twin domain can be deduced by a mirror placed along the long diagonal of the primitive *p3* unit cell highlighted in Figure IV.11 by dashed-blue lines, which is the short diagonal of the (6×6) unit cell. Figure IV.12 shows domain 1 in white, which corresponds to the structure presented in Figure IV.11, and its twin domain 2 in yellow through the mirror m.

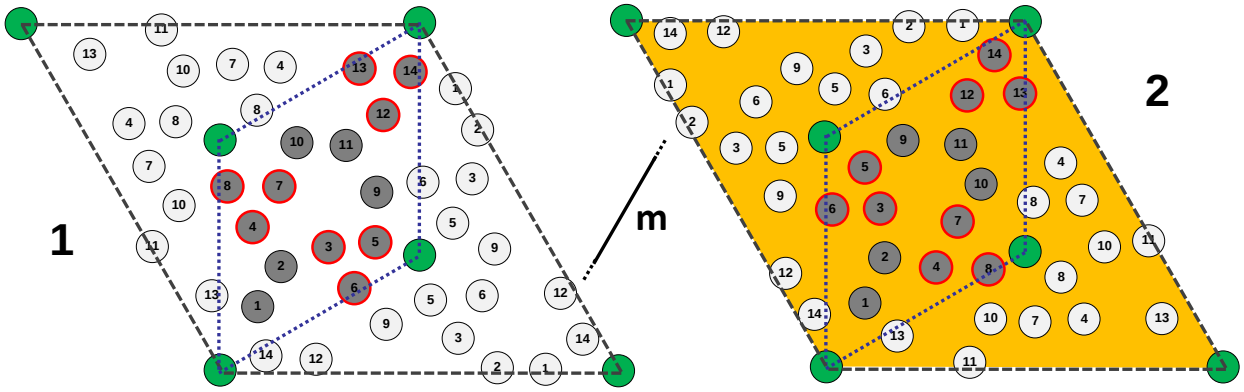

Figure IV.12 – Unit cell of domain 1 (in white) and the corresponding unit cell of the twin domain (2 in yellow) deduced through a mirror m placed along the long diagonal of the primitive unit cell. Other mirrors can be deduced from the *p3* symmetry and correspond to the edges of the unit lattice.

The other mirrors are deduced by the *p3* symmetry and correspond to the edges of the unit lattice. The addition of an incoherently scattering second domain in the fit procedure reduced the χ^2 to 5.8, confirming the results described by Grozea *et al.* . This result, already very good, can be improved by focusing on the special sites. Indeed, Grozea *et al.* pointed out that the gold atoms located on the symmetry axis display a partial occupancy of 0.504±0.004.

In our previous fit process, this effect has not been revealed as all the atoms in the model were assumed to have the same occupancy value. To take into account this potential difference, distinct occupancy as well as DW parameters were attributed to the special atoms. This led to a decrease of the χ^2 value down to 3.1, and the occupancy value of the special atoms droped to 0.49±0.015, whereas the occupancies of other atoms remained equal to 1.

These results demonstrate that with only gold atoms, the model proposed by Grozea *et al.* is already in very good agreement with our SXRD data. The χ^2 value is even much better in our case, despite the much lower uncertainties in our dataset. However, to improve their χ^2 value, Grozea *et al.* had to include several Si double layers subjected to a strain field that displaces the atoms far from their bulk positions, especially in the first layer. We will see below if the addition of Si atoms in our model can influence the χ^2 minimization.

With a Si substrate

By simply adding a silicon double layer below the gold reconstruction, at the bulk position, with an occupancy assumed to be equal to 1, the χ^2 value decreased to 1.85 with the Si atoms slightly displaced from their original positions. This result does not support Grozea *et al.* 's model as the Si atoms are not strongly displaced from their bulk ones. However the reduction of the χ^2 value shows that the Si atoms contribute to the diffracted signal, even if their contribution remains weak.

A last fit was performed with a Si double layer with the positions given by Grozea *et al.* , in this case, with the occupancies of the Au, special Au and Si atoms assumed to be 1, 0.49 and 1 respectively, the final χ^2 value is 1.3, with still very slight displacements with respect to Grozea's positions observed during the fitting. However, the small difference between the two χ^2 values (1.85 and 1.3) does not allow to definitely choose this last model which seems to be less physical because of the large displacements of the Si atoms with respect to their bulk values. Despite the fact that the Au atoms seem to have an influence on the position of the Si atoms in the first layer of the substrate, our experimental data would make us believe that the preferred solution is the one for which the Si bulk positions are conserved. The atomic positions obtained in the last two fits can be found in Table 2 and 3 in Annexe. The final in-plane DW value of non-special surface gold atoms was found to be 1.3±0.04 Å^2 which is twice its bulk value (0.6 Å^2 [Sears and Shelley, 1991]). Remarkably, the increase by a factor of two to three times of the bulk DW term for surface atoms has already been observed during the analysis of the Au-($\sqrt{3}\times\sqrt{3}$)R30° reconstruction [Plass and Marks, 1995]. It has been attributed to the lack of neighbours providing additional degrees of freedom to the atoms to vibrate. However, the DW term for special Au atoms and Si atoms could not be refined, presenting very low ($\sim$0 Å^2)[i] and very high ($\sim$2 Å^2) DW terms, respectively.

i. This very low value might be implied by the 3-fold symmetry axis onto which these atoms sit.

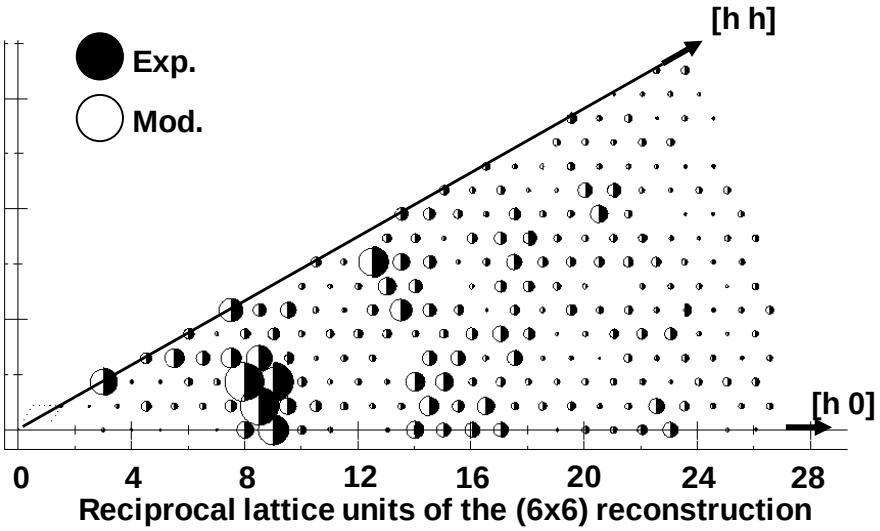

Figure IV.13 – Experimental structure factors (in black), together with the final model structure factors (in white). The circles are of same sizes (*i. e.* same intensity) for all reflection illustrating the final agreement χ^2 of 1.3.

Through this model evaluation we have thus shown that the structure proposed in the paper of Grozea *et al.* agrees very well with our measurement (see Figure IV.13). It is particularly interesting to note that partial occupancies of special atoms as well as twin domains are fully confirmed by our analysis. Moreover, it means that this particular structure also forms in our experimental conditions which consist in a thick deposit at RT annealed and then cooled down. Two specific features have however to be discussed here in more details. It concerns the positions of the Si atoms and the partial occupancy. As the experimental investigation have shown to reach their limits concerning these questions, they are discussed in the light of the simulation results which offer the possibility to go beyond.

Indeed, the simulations support the fact that the Si atoms of the first layer are strongly displaced in the presence of the (6×6) reconstruction. Moreover, whereas the OR were found to form in the case of a thick Au crystal in contact with a Si substrate terminated by a Si double layer, the (6×6) structure is found to form through deep re-arrangement of the first layer. This latter looses its surface bulk structure and form distorted trimers distributed in an organized manner within the (6×6) unit cell [Nogaret, to be published].

The partial occupancy ($\sim$0.5) of the special atoms requires more attention too. Indeed, this value needs to be related to a physical meaning and indicates that a Au atom can be present or not at this special position in equal proportion. This value is not attributed to the presence of a vacancy in one of the special site in the structure as a fit performed with this constrain results in the increase of the χ^2 value. It rather indicates the coexistence, in equi-proportion, of (6×6) cells with the special sites fully occupied, and (6×6) cells with special sites unoccupied. This assumption has been confirmed by the energetic study of the (6×6)

reconstruction performed by *ab-initio*. The calculations point out that the overall structure is a mix of an unfaulted structure with $\sim 0\%$ occupancy and a faulted structure with $\sim 100\%$ occupancy for special atoms, the surface energy of the faulted structure (0.406 J.m^{-2}) being higher by only 22 mJ.m^{-2} compared to the unfaulted one (0.384 J.m^{-2}) [Nogaret, to be published].

It is worthwhile to mention that the Au-(6×6) reconstruction, combining gold trimer and pentagon units, has been observed by STM during the study of the location of Pb absorption site on this structure [Jalochowski, 2003]. This study confirms all the main features described in the model presented above with a nuance concerning the special sites at the corner of the unit cell which are supposed to be absent of the structure. This is however surprising as the χ^2 increases by a factor three if their occupancy is fixed at 0 in our model evaluation. Nevertheless the energy of this unexpected structure which looks more like a two-dimensional pseudo-glass has been calculated in our *ab-initio* simulations and found to be energetically favorable with 0.41 J.m^{-2} compared to the 1.5 J.m^{-2} for the nominal Si(111) surface.

e Discussion on the (6×6) ↔($\sqrt{3}$×$\sqrt{3}$)R30° transition

Despite a wide literature covering the reconstructions in the Au-Si(111) system (see section IV.1) and the results presented in this chapter, there are still open questions concerning the potential relationships between the (6×6) and the ($\sqrt{3}$×$\sqrt{3}$)R30° reconstructions. We remind here that the transition between the (6×6) and the ($\sqrt{3}$×$\sqrt{3}$)R30° reconstruction is reversible and occurs around 700 K. However, below 700 K we can not conclude that the ($\sqrt{3}$×$\sqrt{3}$)R30° has disappeared because its reconstruction peaks are overlapped by those of the (6×6) . Moreover, the atomic processes governing the transition between the two structures are unknown. During our experiments, a peculiar scattering signal that seems to be related to both reconstructions has been recorded.

Figure IV.14 is a zoom on the low Q values of the solid map plotted in Figure IV.2. Two arrows highlight the presence of some kind of diffuse rings that surround the ($\sqrt{3}$×$\sqrt{3}$)R30° reconstruction peaks. Their radius is of the length of the (6×6) reciprocal unit cell and their intensity is orientated toward the origin of reciprocal space. This kind of rings have already been observed in LEED studies [Takahashi *et al.*, 1991; Higashiyama *et al.*, 1986a] but at high temperatures (around 600 K) so that they were attributed to a kind of disorder implied by the competition between the (6×6) and ($\sqrt{3}$×$\sqrt{3}$)R30° structures. However, in our case, they were recorded after the return at RT, the system was therefore already solidified and the atomic diffusion very low. Moreover, if one looks a bit closer, they are actually not rings of constant intensity but more composed of a diffuse intensity linking two (6×6) peaks with a maximum in between. At the moment, no clear structure can be proposed to explain this

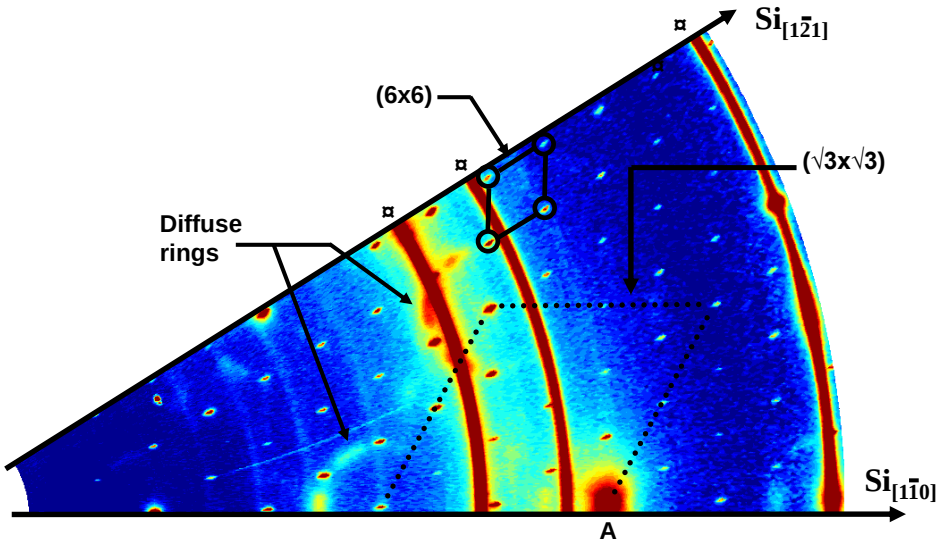

Figure IV.14 – Zoom on the map plotted on Figure IV.2 highlighting the orientated diffuse rings surrounding the common (6×6) and ($\sqrt{3}\times\sqrt{3}$)R30° reconstruction peaks.

kind of intensity distribution, however, it might be related to unexplained features already reported. Some studies report LEED diffraction patterns that do not correspond to STM images [Salvan *et al.*, 1985; Takami *et al.*, 1994] which implies that some area of the samples can locally present "frustrated" structures. In our case, it could correspond to domains composed of (6×6) unit cells turned by 30° with respect to the Si(1×1) structure,*i. e.* parallel to the ($\sqrt{3}\times\sqrt{3}$)R30° unit cell. Maybe some kind of domain walls between remaining ($\sqrt{3}\times\sqrt{3}$)R30° domains and (6×6) domains.

In this chapter are described the experimental results concerning the conditions of formation of the (6×6) reconstruction as well as its stability. It is found to form around 680 K upon cooling and its structure has been determined using quantitative SXRD with important precisions brought by the simulations. Interestingly the (6×6) reconstruction has been found to re-form at 600 K by surface diffusion of the Au atoms of the droplets. It means that the AuSi droplets can be supercooled at least down to 30 K below the eutectic temperature. The next chapter describes the different observations concerning the AuSi droplets and their tendency to supercooling depending on the substrate's structure.

Summary of Chapter IV

Experimental results :

- The (6×6) reconstruction is found to form during the cooling process around 680 K. The process is reversible : if the sample is heated again, the (6×6) disappears around 700 K.
- The higher the sample is annealed, the better the reconstruction is defined.
- After having been destroyed by ion bombardment in the supercooled regime (600 K), the (6×6) reconstruction reforms thanks to the diffusion of Au atoms from the droplets to the bare substrate.
- The recovering of the Si surface by annealing only to 600 K shows that the wetting layer of gold improves the mobility of the Si atoms.

Determination of the (6×6) structure :

- The collection of the data has been performed at RT and consists in 980 reflections integrated and corrected.
- The averaging of the data results in a systematic error of 3.9 % in the *p3m1* symmetry group reducing the number of independent reflection to 441.
- The study of several (6×6) rods shows that this reconstruction is 1 ML thick with domains of about 60 nm.
- The Patterson map shows the characteristic peaks related to the trimer units. The other peaks are impossible to address with a simple model.
- The determination of the structure is done with a starting model proposed by Grozea *et al.* who had a very high uncertainty on their data, a minimization of the χ^2 value thanks to strong assumptions and completely different experimental conditions.
- The resulting gold structure consists in two domains, composed of trimer and pentagonal units, related by a mirror. Some special sites present a partial occupancy of 0.5 implying that they are present in one domain but not in the other.
- Our experimental data do not provide enough details to choose between the two best models differing in the positions of the Si atoms (bulk position : χ^2 =1.8, position of Grozea *et al.* : χ^2 =1.3).
- The simulation results tend to confirm that the Si atoms of the first layer are strongly displaced from the bulk positions and form distorted trimers displaying a long range order.

Chapter V

Supercooling in AuSi droplets

Contents

Throughout the two previous chapters, we have seen that the dewetting of a thin gold film leads to the formation of islands and then to droplets when passing through T_e. In addition, the (6×6) reconstruction can form upon cooling if the system is annealed high enough. In our experiments, when cooling down the samples, different solidification temperatures were recorded depending on the experimental conditions. This chapter presents the different results concerning the supercooling effect measured for AuSi droplets on Si(001) (section V.1), Si(111)-(6×6)Au and Si(111)-($\sqrt{3}\times\sqrt{3}$)R30°Au surfaces (section V.2). Note here that in almost all the cases the solidification process is found to extend in a given range of temperature. The solidification is found to start at a given temperature (*i. e.* some of the droplets have solidified) and to be completed at lower temperatures. In each case, we describe the appearance of the first grains and the recorded complete solidification. For comparison between the different experiments the solidification temperature T_s is taken as the lowest one, for which all the droplets are solidified.

V.1 On Si(001) substrates

V.1.1 Si(001) substrate's structure

As it has been done for the Si(111) substrate, we present in Figure V.1 the Si(001) substrate. This orientation yields a four fold symmetry at the surface, with the surface unit vectors being [100] and [010]. Due to the definition of the reciprocal lattice, the determination of the reciprocal surface unit cell in the case of cubic symmetry is simple as it leaves all vectors unchanged through the transformation (but their length).

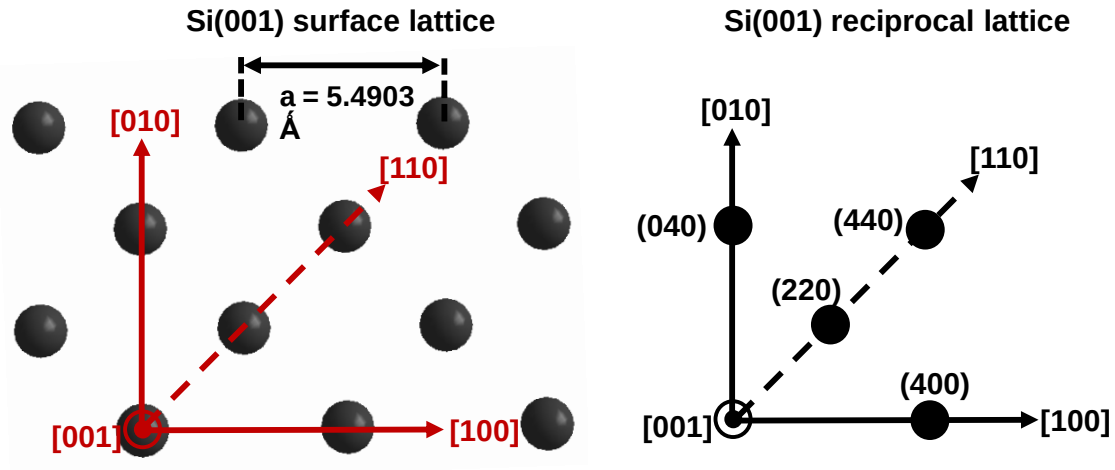

Figure V.1 – Scheme of the atomic arrangement in a the cubic symmetry of the Si(001) plane. The surface unit vectors are represented in red (plain).

Si(001) substrates thus differ at the atomic scale from the Si(111) leading to several

physical differences between the two orientations. For example, the atomic density is different between the two orientations, thus they do not present the same electronic density. As a consequence, the rearrangement of the surface atoms is only composed of dimers, leading to a (2×1) reconstruction on Si(001) instead of a (7×7) on Si(111). The surface energy of Si(001) is higher than that of Si(111) (see Chapter I), the growth of gold is therefore expected to be different as well as the wetting conditions [Ressel *et al.*, 2003]. Another difference lies in the absence of Au-induced surface reconstructions of Si(001). To compare with the extensively studied Au-Si(111) system presented later, we performed a typical experiment on the Si(001) substrate by a deposit at RT of about 8 ML and a subsequent annealing to form AuSi droplets through dewetting and melting at the eutectic temperature. The supercooling behaviour and the solidification structure have been investigated as presented hereafter.

V.1.2 Supercooling on the Si(001) surface

After the observation of the melting process by the formation of the AuSi eutectic liquid, the sample was annealed 40 K above T_e, *i. e.* at 670 K. It was then cooled down to record the temperature at which the solidification process takes place. The *radial-scans* performed along the Si[110] azimuth at 670 K, 580 K and 550 K are plotted on the graph in Figure V.2(a). At 670 K it displays a liquid structure with the appearance of the first grains of gold (the Au(220) peak starts to grow) at 580 K. The complete solidification process is then observed at 550 K, which is 80 K below T_e, with the appearance of the Au(111), Au(200) and Au(220) peaks supporting the creation of a polycrystal.

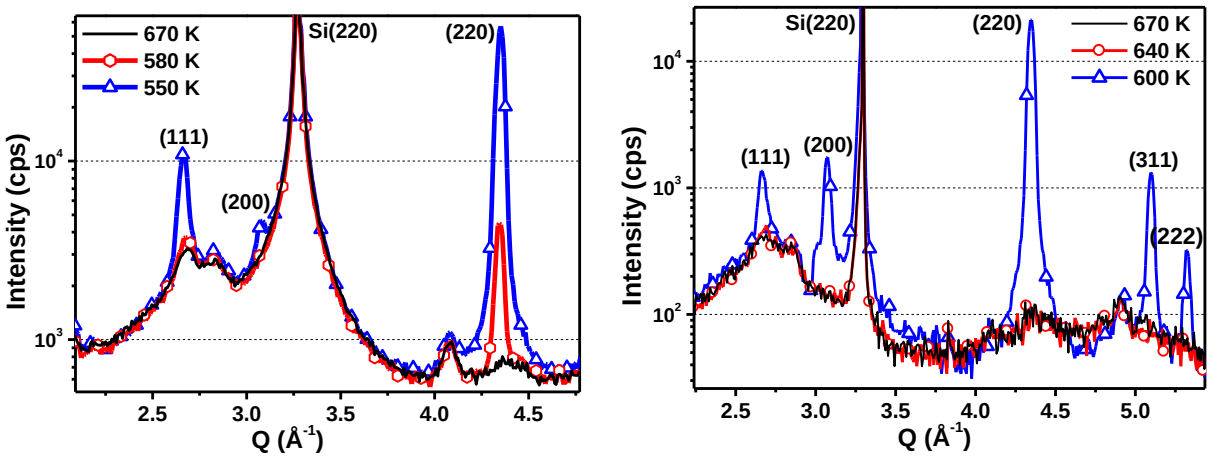

Figure V.2 – *Radial-scans* along the [110] azimuth (a) at 670 K, 580 K and 550 K, for a 8 ML deposit, annealed at 670 K and (b) at 670 K, 640 K and 600 K, for the same deposit annealed at 720 K.

Then the sample was heated again, but this time the maximum annealing temperature

was 720 K. Figure V.2(b) shows the *radial-scans* still performed along the Si[110] direction during cooling down of the sample from this temperature. Interestingly, in this case the solidification takes place at 600 K which is only 30 K below T_e.

V.1.3 Solid structure

After a return at RT, the system is in the solid state and a reciprocal space map was recorded. Due to the substrate symmetry, the map covers in this case 45° of reciprocal space and is plotted in Figure V.3. Compared to the solidification of AuSi alloy onto Si(111) substrate (see Figure IV.2), the solid gold is found to be very textured on the Si(001) with a clear "cube on cube" epitaxy : the Au(220) ring intensity is concentrated on the Si[110] direction while the majority of the Au(200) intensity (as well as the of Au(400)) is located on the Si[100] azimuth. Therefore the clearly preferred OR between the solidified Au and the Si(001) surface is : [100]Au(001)||[100]Si(001).

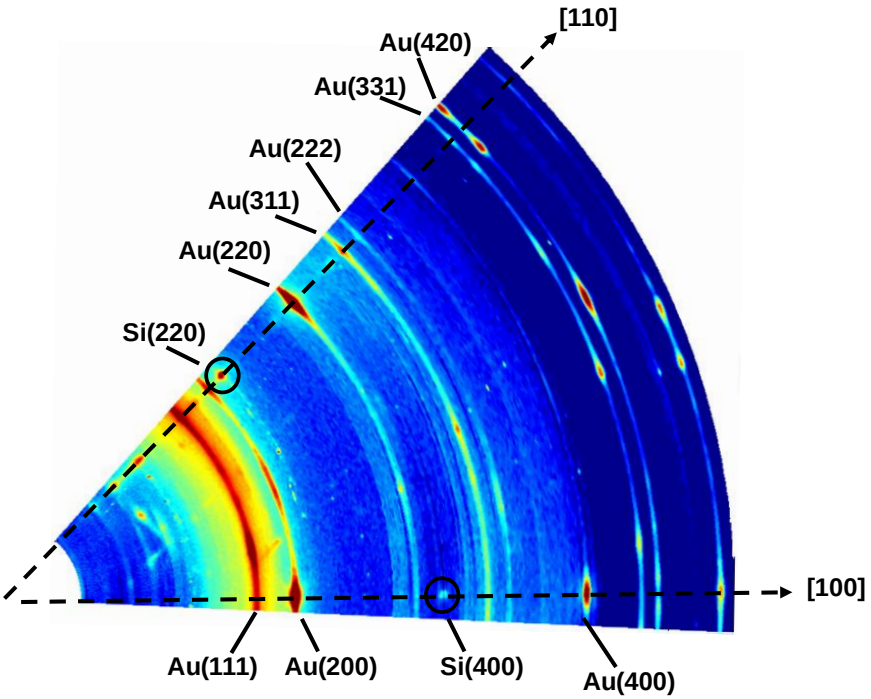

Figure V.3 – Reciprocal space map of solidified Au on Si(001) substrate.

These results show that in the case of the Si(001) substrate, the higher the annealing the lower the supercooling and the resulting solid islands are made of grains displaying a parallel in-plane epitaxial relationship with the surface. A higher annealing leads to concentration changes in the droplets as well as in their size. The influence of the annealing temperature related to the droplet size thus seems to be a parameter that has to be taken into account. It is discussed in the next section in the light of the results obtained on Si(111) substrates.

V.2 On Si(111) substrates

Figure V.4 is guide a to the eyes for a clear overview of the different signals encountered during the measurements. In the previous chapter (Chapter IV), the graphs were plotted as a function of the reciprocal lattice units to simplify the indexation of the reconstruction peaks that are located on fractional orders. In this chapter as well as in the next one, graphs are plotted as a function of the momentum transfer Q ($Å^{-1}$) which allows comparisons in more general cases.

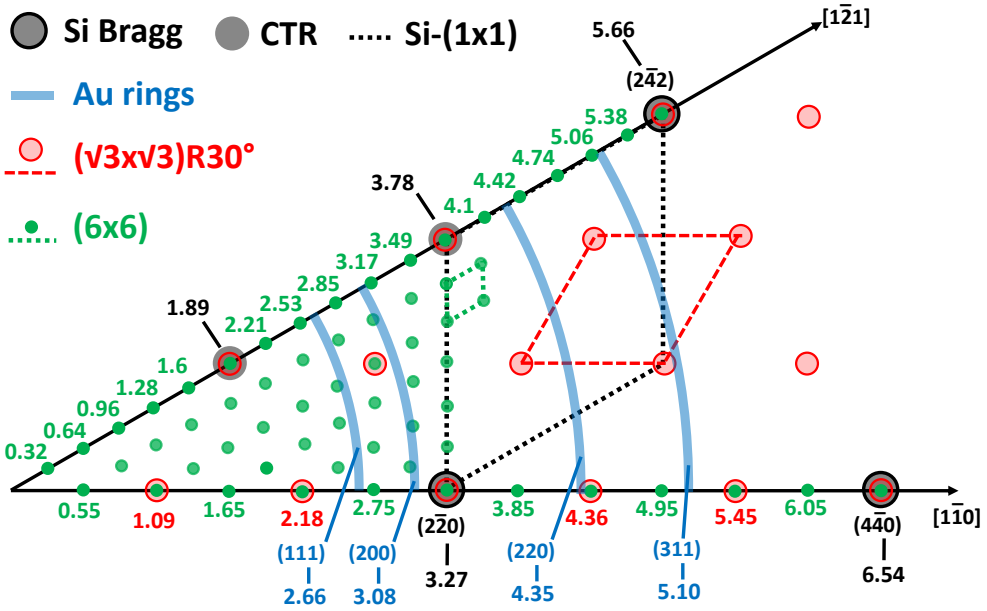

Figure V.4 – Scheme representing the 30° (between the Si[1$\bar{1}$0] and Si[1$\bar{2}$1] azimuth) of reciprocal space required to get a clear overview of the different signals encountered during the measurement (see Figure IV.2). The positions of Si Bragg peaks, CTRs, (6×6) or ($\sqrt{3}\times\sqrt{3}$)R30° reflections and Au Debye-Scherrer rings are given in the space of momentum transfer Q ($Å^{-1}$).

The map of Figure V.4 therefore allows to quickly visualize the different signals recorded in the scans, especially the numerous reconstruction peaks, along the Si[1$\bar{1}$0] and Si[1$\bar{2}$1] azimuths. This highlights, for example, that the ($\sqrt{3}\times\sqrt{3}$)R30° reconstruction peaks can only be recorded along the [1$\bar{1}$0] direction. Along the other directions, they overlap with the CTRs and the Bragg peaks.

V.2.1 Supercooling on Si(111)-($\sqrt{3}\times\sqrt{3}$)R30°Au reconstruction

In Chapter IV we have seen that on Si(111), AuSi droplets coexist with a wetting layer reconstructed either ($\sqrt{3}\times\sqrt{3}$)R30° or (6×6) . In the case of gold deposits of the order of 6 ML, we have seen that a necessary step to form the (6×6) reconstruction during the cooling down was a minimum annealing of about 60 K above T_e, otherwise only the ($\sqrt{3}\times\sqrt{3}$)R30°

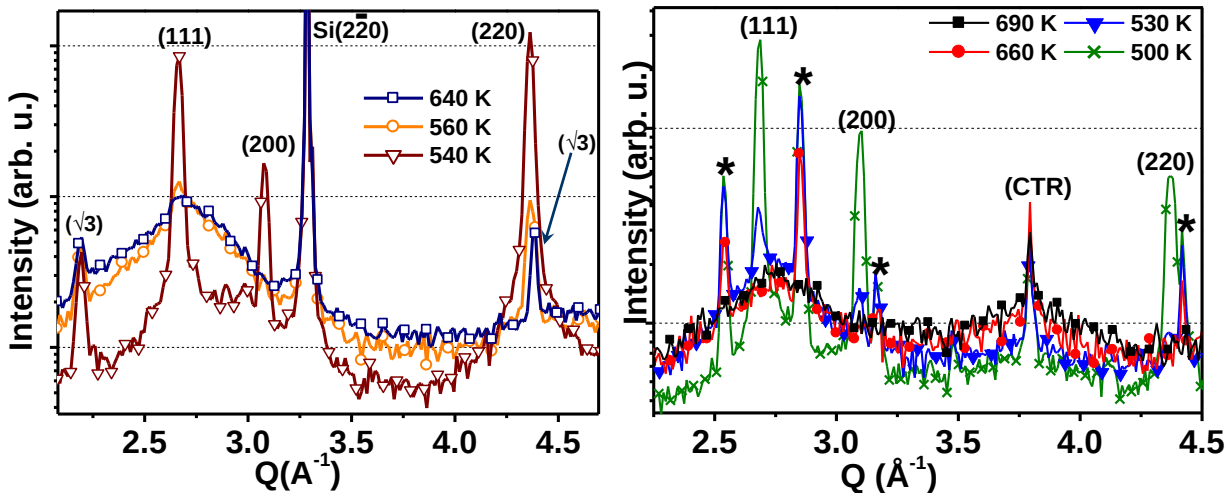

Figure V.5 – (a) *Radial-scans* performed along the [1$\bar{1}$0] azimuth (along which the ($\sqrt{3}\times\sqrt{3}$)R30° peaks can be observed) at 640 K, 560 K and 540 K, for a 5 ML deposit after annealing at 640 K. (b) *Radial-scans* along the [1$\bar{2}$1] azimuth at 690 K, 660 K, 530 K and 500 K for a 6 ML deposit. The (6×6) reconstruction peaks are marked by ∗.

reconstruction is obtained. In the following, we compare the supercooling behaviour of the AuSi droplets in presence of either a ($\sqrt{3}\times\sqrt{3}$)R30° or a (6×6) reconstruction. During the majority of the cooling experiments, the temperature was reduced by steps of 10 K and measurements, such as *radial-scans*, were recorded at each temperature. However, for clarity, the graphs display only specific temperatures which are believed to be essential for the description of the process.

In a first experiment, a deposit of 5 ML of gold was performed and annealed only 10 K above T_e to prevent the formation of the (6×6) upon cooling. Figure V.5(a) presents three *radial-scans* recorded along the [1$\bar{1}$0] azimuth at 640, 560 and 540 K during the cooling process. On each scan the ($\sqrt{3}\times\sqrt{3}$)R30° peaks are visible and no (6×6) peaks are observed. At 640 K, the system is in the liquid state and the first solid grains appear at 560 K. The complete liquid-solid transition of the droplet sets in at 540 K which is 90 K below T_e.

V.2.2 Supercooling on Si(111)-(6×6)Au reconstruction

In another experiment, 6 ML were deposited at RT and annealed at 690 K. This annealing temperature was chosen because it was found to be the lowest value to form the (6×6) upon cooling. This choice therefore reduces a potential effect due to the difference in the annealing and allows closer comparisons with the previous experiment. Figure V.5(b) gathers *radial-scans* recorded along the [1$\bar{2}$1] azimuth during the cooling process. This direction has been chosen in order to see the (6×6) peaks (marked with a star) and at the same time to avoid

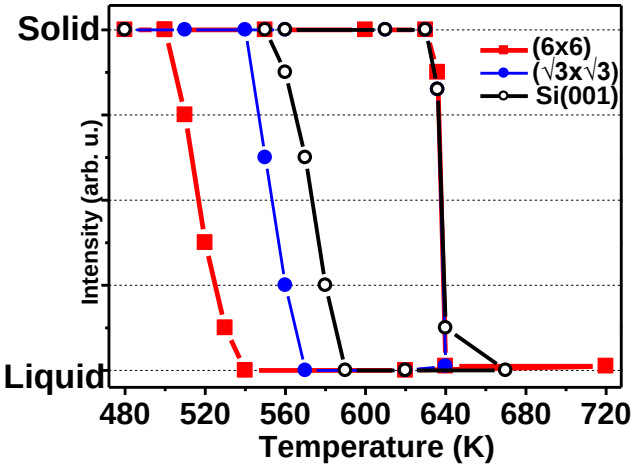

Figure V.6 – Schematic evolution of the Bragg intensity highlighting the solid-liquid-solid phase transition cycles for Si(001), Si(111)-($\sqrt{3}\times\sqrt{3}$)R30°Au and Au on Si(111)-(6×6)Au substrates.

the Si(2$\bar{2}$0) Bragg peak. At 690 K, all the droplets are in the liquid state as confirmed by the absence of gold peaks. At 660 K, the formation of the (6×6) reconstruction takes place and confirms the results presented in Chapter III. At 530 K, which is 10 K and 20 K below the solidification temperatures with the ($\sqrt{3}\times\sqrt{3}$)R30° reconstruction and the Si(001) surface, the appearance of the first grains happens. Moreover, the intensity of the (6×6) reconstruction peaks has also increased. Finally, the complete crystallization of the system was obtained only when it was cooled down to 500 K, *i. e.* 130 K below T_e

Interestingly, the overall process as well as the different remarkable temperature values were found to be reproducible when starting over a solid-liquid-solid transition cycle. It is therefore possible to represent these results by plotting the Au(220) reflection intensity as a function of temperature (see Figure V.6). The curves present an "hysteresis" shape, the width of the loop illustrating the supercooling capacity. Moreover, for the cases investigated so far, *i. e.* ∼6 ML annealed at different temperatures on different surfaces, the hysteresis curves show a liquid-solid transition that extend over a range of temperature of about 40 K. This point will be discussed in section V.4 in terms of droplets' size and reconstruction quality. However, Figure V.6 clearly indicates that the supercooling behaviour of the AuSi eutectic droplets is influenced by the substrate orientation and/or reconstruction type.

In addition to the supercooling measurements described above, some remarkable features were recorded during the cooling down of the samples. It has been presented if Chapter I that a AuSi 2D crystal has been reported to form at the surface of the AuSi eutectic liquid alloy [Shpyrko *et al.*, 2006; Mechler *et al.*, 2010]. Figure V.7(a) is a graph on which are superposed our liquid structure factor measurement in the undercooled regime (around 600 K) and the ones (at low and high temperature) performed in the work of Shpyrko *et al.* for low Q values [Shpyrko *et al.*, 2007]. Our scan in this case is recorded outside symmetry axis to

avoid reconstructions or Bragg peaks. Our recorded peaks are at the positions of the ones measured by Shpyrko *et al.* , corresponding to a low temperature 2D crystal phase floating at the surface of the AuSi eutectic liquid (see section I.7). It thus seems here that this two dimensional crystal is also present at the surface of the liquid droplets in our case. In addition, in the following graphs plotted in the next section the peak at 3.27 $Å^{-1}$, highlighted with a little triangle above it, should not be taken as a reconstruction peak. This peak is present even at high temperatures and also corresponds to a surface 2D crystal phase[i].

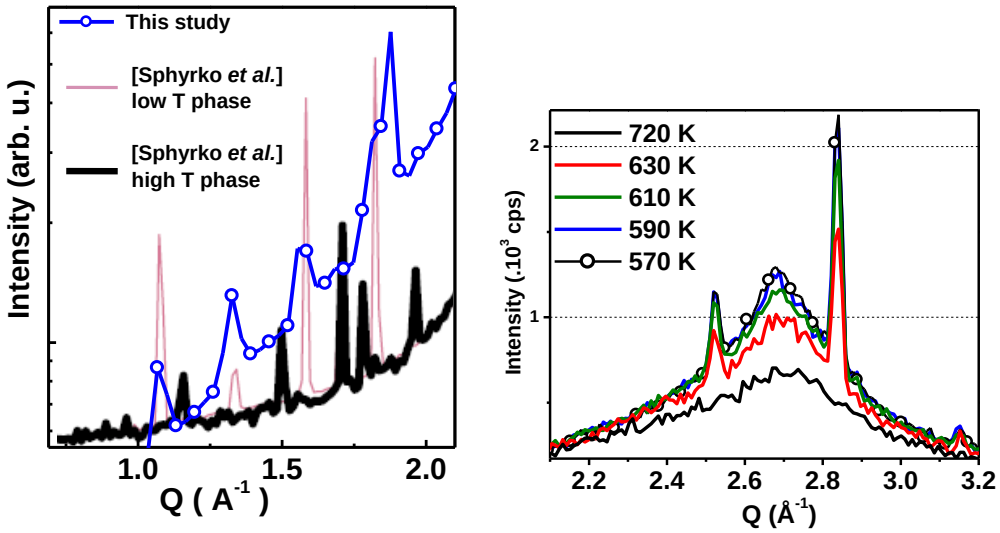

(a) (b)

Figure V.7 – (a) Superposition of our experimental liquid structure factor and the ones extracted from the paper of Shpyrko *et al.* [Shpyrko *et al.*, 2007] revealing the correspondence between peaks arising from a 2D AuSi crystal.(b) *Radial-scans* for several temperatures upon cooling, performed on the Si[1$\bar{2}$1] azimuth and focusing on the first order of the liquid structure. The narrowing of the peak indicates a decrease in the standard deviation of the mean inter-atomic distance in the liquid and thus illustrates the ordering of the liquid.

Another special feature concerns the evolution of the liquid and the (6×6) reconstruction signals with the decrease of the temperature. Figure V.7(b) shows scans performed on the first order of the liquid structure factor for different temperatures during cooling and before solidification (along the Si[1$\bar{2}$1] azimuth). It reveals that the liquid peak gets narrower and increases in intensity with decreasing temperature. The narrowing of the liquid is due to a less dispersed value of the mean distance between two first-neighbour atoms and thus underlines the ordering of the atoms in the liquid. At the same time, the (6×6) reconstruction peaks are also found to increase in intensity illustrating the improvement of the quality of the reconstruction.

i. It is however impossible to distinguish between the low T or the high T structure as in the work of Shpyrko, two peaks can be found at this position, each one corresponding to a different phase.

In this section, very important results were obtained. First, for a similar amount of gold deposited, the resulting AuSi liquid droplets are found to present a much larger supercooling behaviour in the presence of a (6×6) reconstruction (T_s=500 K) compared with the ($\sqrt{3}\times\sqrt{3}$)R30° reconstruction (T_s=540 K) or the Si(001) substrate[ii] (T_s=550 K). In addition, a two dimensional AuSi crystal is assumed to be floating on the surface of the liquid droplets. Finally, the ordering of the atoms in the liquid upon cooling is recorded in parallel with the improvement of the reconstruction quality. As the supercooling effect is larger in presence of the (6×6) reconstruction, we believe that it can influence the liquid behaviour and thus the solidification process. The next section is therefore devoted to the study of the liquid structure in the presence of the (6×6) reconstruction.

V.3 Study of the liquid structure

We have seen in Chapter I (section I.8.2) that a solid can influence a liquid's structure, at least in the first layers. The (6×6) reconstruction presents trimers of pentagons and is found to be very stable (see Chapter IV). As it has been shown that the supercooling behaviour of a liquid can be influence by the appearance of the icosahedral short range order (see section I.5.2), the underlying idea appearing here is that the reconstruction, due to its specific structure, can influence the formation of fivefold clusters into the AuSi droplets. The creation or the increase of this order would lead to the stabilization of the liquid phase. To see whether or not this idea is relevant, experimental measurements and simulations were performed to get more information on the inner structure of the liquid.

V.3.1 Experimental study

In Figure V.8 is plotted the reciprocal space map of the AuSi system in the liquid state in the supercooled regime after annealing at 720 K. It displays the Si Bragg peaks, the (6×6) reconstruction peaks and three rings that correspond to the first three accessible maxima of the accessible liquid structure factor. The radial structure factor of the liquid is extracted by performing the angular average of the experimental liquid intensity which is similar to the pair correlation function (see section I.4). A first step to know whether or not the liquid structure can be compared to the (6×6) structure is to derive the mean structure factor of this latter. To do so, the intensities of all measured (6×6) diffraction peaks contained in 0.05 Å^{-1} intervals of the reciprocal map were summed up. The result of this operation is represented by the black crosses in Figure V.9(a) in a way that each cross corresponds to

ii. onto which no gold reconstruction is reported.

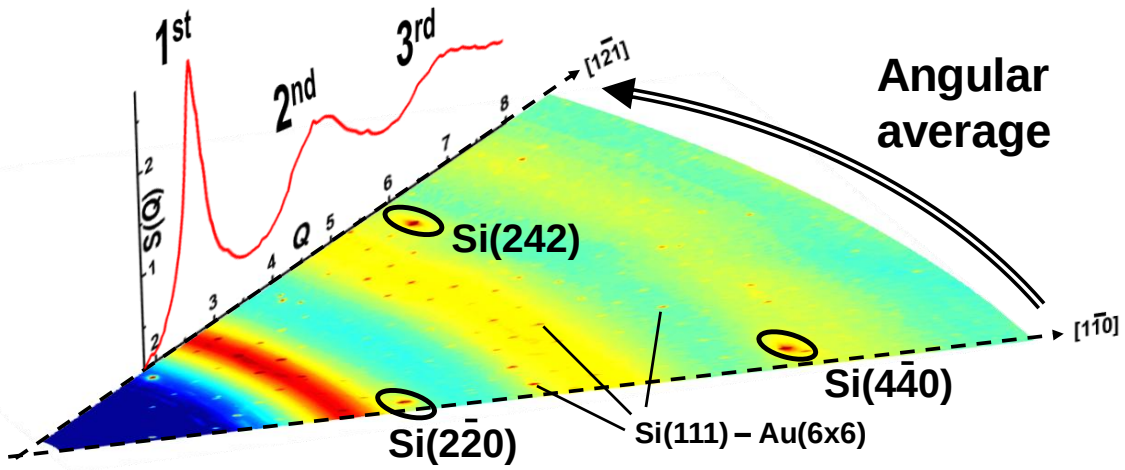

Figure V.8 – Reciprocal space map covering 30° of reciprocal space (between the silicon [1$\bar{1}$0] and [12$\bar{1}$] azimuth) recorded in the supercooled state. The red colors correspond to high intensities whereas blue correspond to low ones and yellow to intermediate ones. This map displays the Si monocrystal Bragg peaks and a mesh of thin peaks corresponding to the (6×6) reconstruction already observed in the previous chapter. The three intense rings correspond to first, second and third order of the liquid structure factor which can be extracted by an angular average of the intensity.

the total (6×6) intensity encountered in the chosen interval. The smoothening of the discrete characteristics of the signal is performed by a fast Fourier transform which lowers the high frequency components and results in a representative curve of the radial intensity distribution. The extended shoulder on the second order is characteristic of the pentagonal order present in the reconstruction [Sachdev and Nelson, 1984; Kelton *et al.*, 2006].

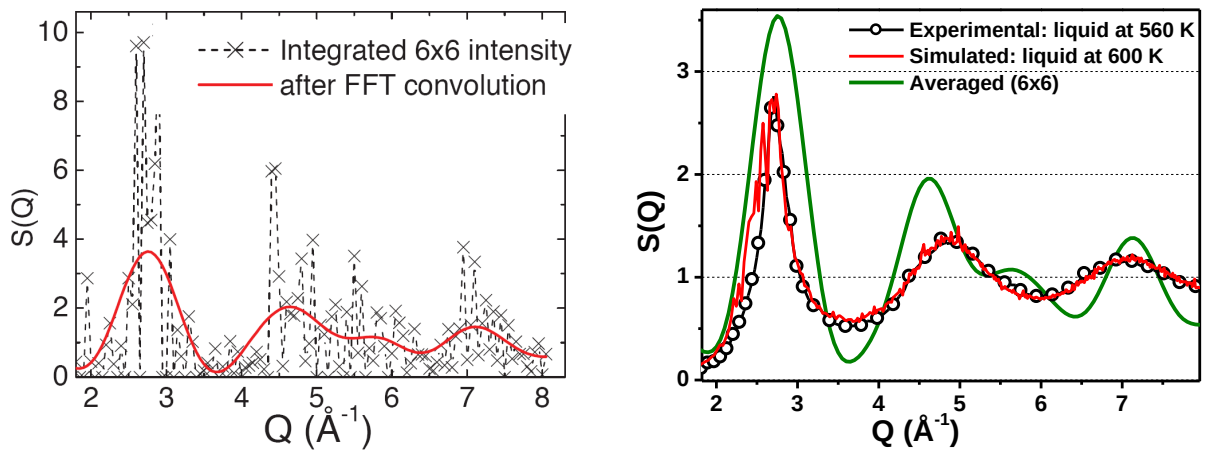

(a) (b)

Figure V.9 – (a) Summation of all the measured intensity arising from the (6×6) reconstruction (black crosses) and result of the Fourier transform illustrating its radial intensity distribution (red) (b)Plot of the structure factor of the experimental liquid, simulated liquid and a hypothetical structure factor by averaging the (6×6) reconstruction peaks.

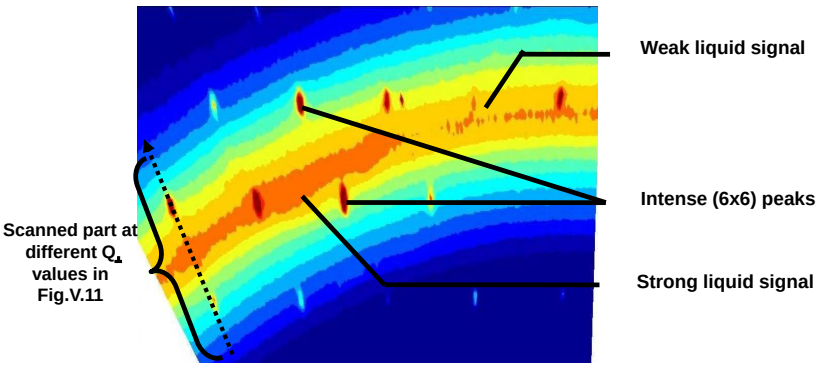

Figure V.10 – Zoom on the first order of the liquid structure factor. The intensity increases in the vicinity of intense (6×6) reconstruction peaks reflecting local similarities between the two structures.

The experimental liquid structure factor in its supercooled state is plotted on the graph in Figure V.9(b) together with the theoretical structure factor of the simulated liquid at 600 K provided by *ab-initio* calculations performed by A. Pasturel. The two liquid structure factors are in very good agreement which confirms the accuracy of the molecular dynamics simulations of this system. In addition is plotted the radial intensity distribution of the (6×6) reconstruction. It compares well to the experimental and theoretical structure factors pointing out the presence of similar interatomic distances in the (6×6) reconstruction and the liquid.

When looking closer at the first order of the liquid in the map of Figure V.8 we remark an in-plane anisotropy of the intensity distribution from the liquid (see Figure V.10). Even more interesting, the liquid signal is enhanced in the vicinity of the strongest (6×6) reconstruction peaks. This observation suggests that structural similarities between the reconstructed interface and the adjacent liquid layers may exist in a way that the liquid tends to adopt the structure of the reconstruction. The dashed arrow in Figure V.10 indicates the direction of the reciprocal space along which the scans presented in Figure V.11(a) and (b) are performed. More precisely, it corresponds to the scan noted **1**, performed along this direction and in the plane, *i. e.* at $Q_{\perp} \sim 0$ Å^{-1}. The scans **2** ,**3** and **4** are performed along the same in-plane azimuth but at different values of $Q_{\perp}$: 1.34, 2 and 2.68 Å^{-1}, respectively.

The (6×6) reconstruction is a 1 ML thick surface structure, its diffracted intensity thus corresponds to a mesh of rods perpendicular to the surface in the reciprocal space. The vertical dashed lines in Figure V.11(a) represents two intense rods existing on the direction onto which the scans are performed. Along each scan of Figure V.11(b), the intensity of the two (6×6) rods are therefore recorded.

As far as the liquid droplets are concerned, the resulting diffracted signal is different. In reciprocal space, the diffracted intensity of an isotropic liquid is distributed at the surface of a sphere having a radius inversely proportional to the mean distance between two nearest neighbour atoms. This spherical intensity distribution has a finite thickness due to the devia-

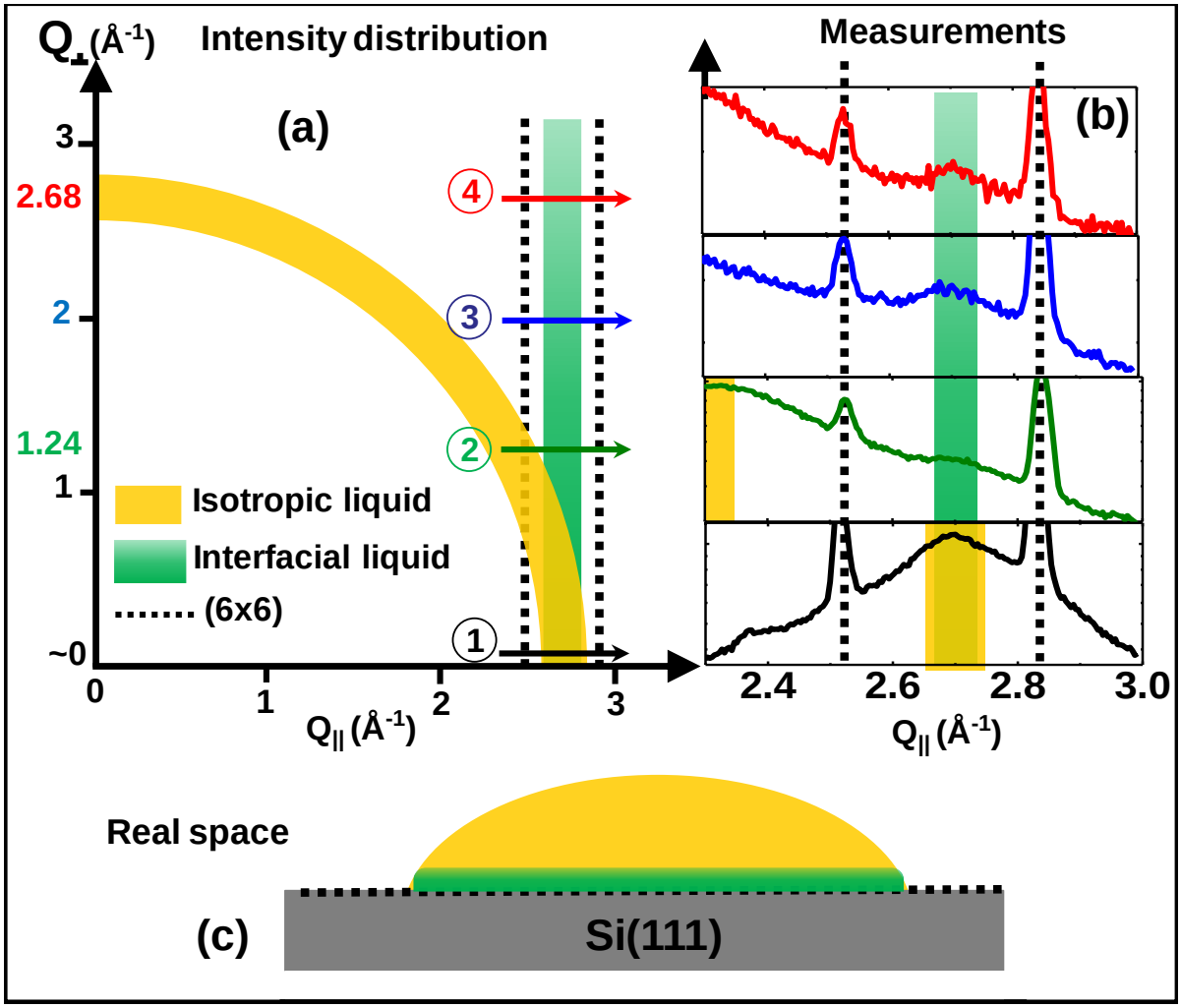

Figure V.11 – (a) Scheme of the distribution of the intensity in the ($Q_{\parallel}$,$Q_{\perp}$) plane in the direction of the dashed arrow in Figure V.10. (b) Scans corresponding to the arrows plotted in (a), performed in the plane (scan **1**) and parallel to it for several values of out-of-plane momentum transfer, $Q_{\perp}$ (scans **2**, **3** and **4**). (c) Representation of the system with equivalent colors between the diffracting structures and the corresponding intensities.

tion of the mean inter-atomic distance. It is represented in Figure V.11(a) by the yellow area which is the cut, in the studied plane, of one fourth of the liquid sphere. Scan **1**, performed in the plane, therefore displays the liquid signal in the middle of the two (6×6) reconstruction peaks. Scan **2**, recorded at $Q_{\perp} = 1.24$ Å^{-1}, also displays the (6×6) signal because of their rod shape distribution, but the liquid signal is shifted to the left in agreement with its spherical shape. In scans **3** and **4**, the (6×6) reconstruction signal is still measured whereas the maximum of the liquid intensity is no longer within the scanned range.

However, in scans **2**, **3** and **4**, an unexpected bump of intensity is still recorded between the two (6×6) reconstruction peaks, at the in-plane position of the first maximum of the liquid structure factor. A remaining intensity at this in-plane position that does not vanish along $Q_{\perp}$ highlights the presence of a rod at the position of the liquid. It therefore reveals

the presence of a structured interfacial liquid in the droplet ("liquid rod" in Figure V.11(a) and (b)) whose lateral short range order is influenced by the (6×6) reconstruction (see Figure V.10). In other words, the system seems to correspond to liquid droplets in the presence of a (6×6) reconstruction that can influence the structure of the liquid at the solid-liquid interface as represented in Figure V.11(c).

It has been shown in Chapter IV that the (6×6) reconstruction is composed of trimers of pentagons. We thus propose that the influence of this reconstruction on the structure of the liquid consists in helping the formation of -or stabilizing pre-existing- five-fold clusters that favor the liquid state and prevent the solidification process (see section I.8.2). Our measurements clearly revealed the existence of a structured liquid at the interface with the substrate in the presence of the (6×6) reconstruction. However, it was not possible to measure experimentally the creation of a five-fold ISRO in the supercooled droplets.

In order to confirm to what extend our proposed process can be validated, simulations on the liquid were performed.

V.3.2 Simulation results

The aim of these simulations is to explore the structure of the liquid at a temperature above T_e (at 700 K) and in the supercooled regime (600 and 500 K) to detect potential changes during the cooling process. To do so, 256 atoms with a proportion of Au and Si atoms corresponding to the eutectic composition are arranged in a cubic box with periodic boundary conditions. The side box length is 16.5 Å and the duration of the run is 30 ps with a time step of 3 fs.

In Figure V.12 is plotted the mean-square displacement $< r^2(t) >$ deduced from the simulations. The three temperatures display a similar evolution presenting distinctive regimes. The first one concerns the short times with a ballistic motion of the atoms with an amplitude evolving as t^2. It is then followed by a "crossover" region where the slope weakens. The slowing down of the motion arises when the atoms come across their first neighbours and arrange in coordination polyhedra such as those presented in Figure I.22. At longer time, the mean-square displacement grows linearly with time corresponding to the diffusive regime. The extraction of the self-diffusion coefficients yields 0.075, 0.046 and 0.020 $Å^2.ps^{-1}$ at 700, 600 and 500 K, respectively, and confirms the liquid behaviour for the three temperatures. For each temperature, a neighbor analysis of the simulated eutectic liquid was carried out. The detailed three-dimensional picture of the local structure was extracted and, using the Honeycutt-Andersen indices presented in section I.5.2, the percentage of clusters with five-fold symmetries (represented by 1551, 1451 and 1431 pairs) in the liquid could be calculated. On the graph in Figure V.13 is plotted the variation of the percentage of each considered

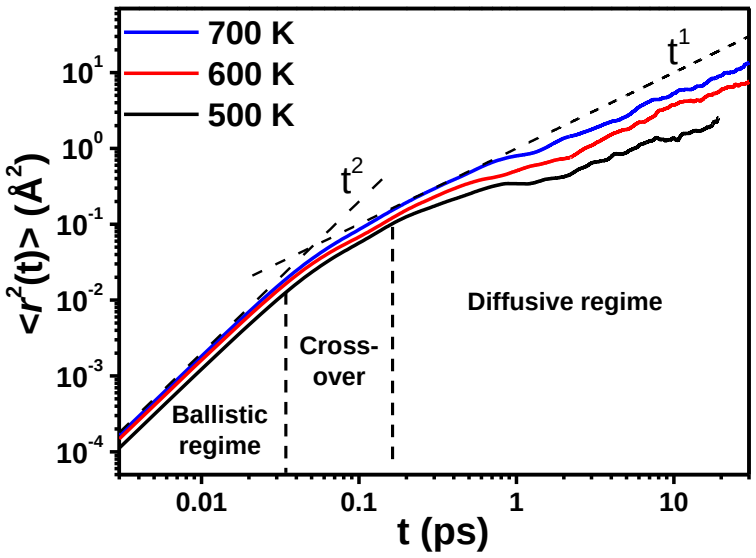

Figure V.12 – Mean-square displacement $< r^2(t) >$ deduced from the simulations at 700, 600 and 500 K.

pair as well as the one of the total five-fold symmetry pairs. The short-range order displays an appreciable proportion (46 %) of pairs in local five-fold arrangement at 700 K. During the cooling down to the supercooled regime, this proportion increases to reach 51 % and 54 % at 600 and 500 K, respectively. These results therefore reveal that, first, five-fold ISRO can develop in the AuSi eutectic liquid and second, that the supercooling process enhances its

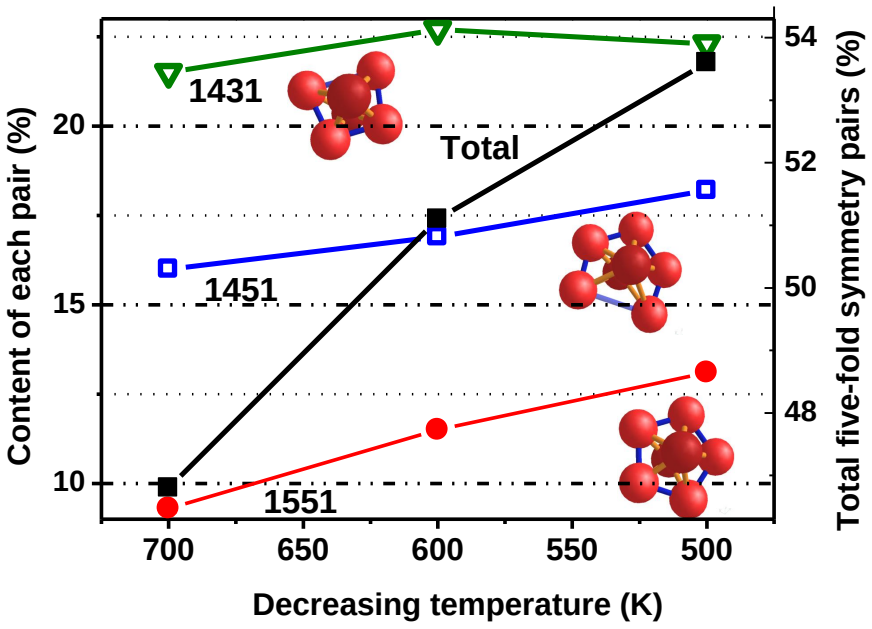

Figure V.13 – Percentage of the 1551, 1451, 1431 five-fold clusters present in the simulated liquid (referring to the left axis) and of the total five-fold symmetry pairs (referring to the right axis) as a function of decreasing temperature.

formation.

An interesting information consists in the comparison of the interatomic distances found in the different structures. This done in Figure V.14 showing the surface unit cell of the (6×6) reconstruction (with the extended trimers of pentagons surrounding it), the 1551 cluster found in the simulated liquid and the f.c.c. gold structure at 550 K. Remarkably, the nearest-neighbour distance in the pentagons is 2.86 Å at room temperature, denser than for gold in its bulk f.c.c. structure (2.90 Å at 550 K), but close to the interatomic distance (2.84 Å) in icosahedral Au clusters in the supercooled liquid, as deduced from the simulations. Moreover, the five-fold clusters found in the simulated liquid and the pentagons of the (6×6) reconstruction present very similar topology. Therefore, the (6×6) surface structure offers perfect sites to stabilize the five-fold clusters, which in turn stabilize the supercooled metal.

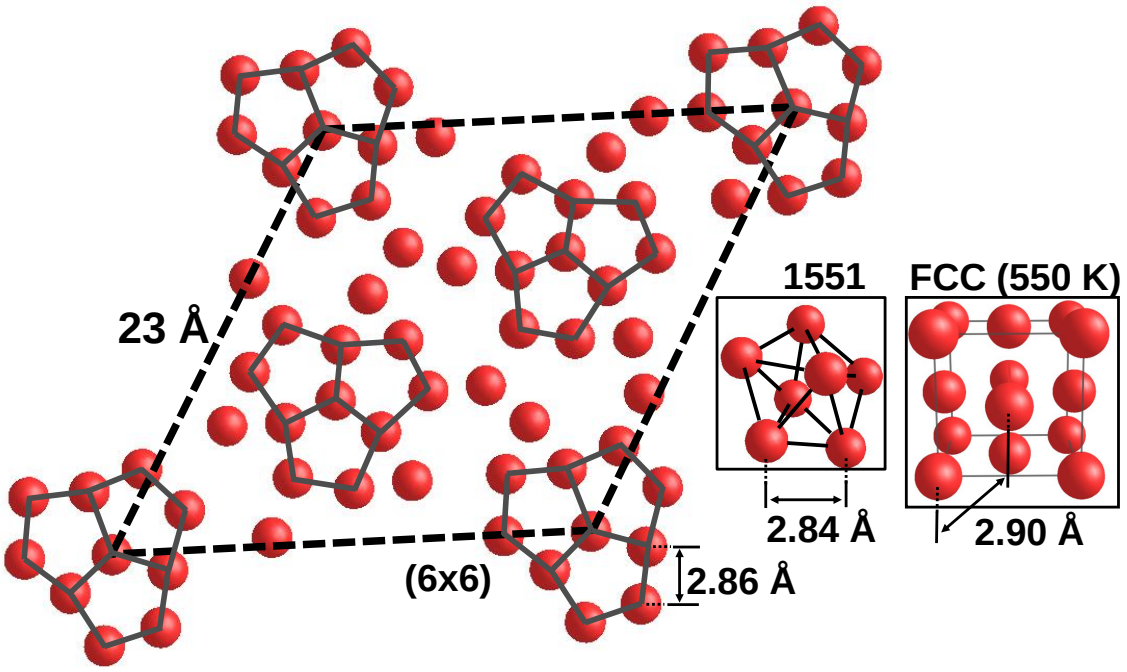

Figure V.14 – Image of the Si(111)-(6×6)Au reconstruction surface leading to enhanced supercooling with the unit cell highlighted by the black line (only the Au atoms are shown). Out of 45 atoms in the unit cell, 30 are in a pentagonal environment (green lines). In insets are shown a gold pentagonal cluster (1551) present in the simulated liquid and the fcc gold lattice at 550 K. The cluster has similar topology and bond length (2.84 Å) as the surface structure (2.86 Å), both denser than the Au fcc lattice at this temperature (2.90 Å).

Throughout the investigations presented above in this section, several key points have been highlighted and show that the (6×6) structure has an influence on the liquid and play a role in the enhancement of the supercooling effect observed in the AuSi liquid droplets :

- The ordering of the atoms in the liquid is recorded in parallel with the improvement of the quality of the (6×6) reconstruction.
- The average radial structure factors of the experimental and simulated (presenting

ISRO) liquids as well as that of the (6×6) reconstruction display similarities.

- The first maximum of the liquid structure factor presents an in-plane anisotropy of the intensity distribution : it is more intense in the direction of the strong (6×6) peaks reflecting the liquid lateral short range order influenced by the reconstruction.
- A rod of intensity is recorded along $Q_\perp$ at the in-plane position of the liquid revealing the ordering of the liquid close to the droplet/substrate interface.
- The analysis of the simulations performed on the liquid at different temperatures shows that the ISRO can develop in the AuSi liquid and is enhanced in the supercooling regime.
- The mean interatomic distance in the five-fold clusters is smaller than that in the f.c.c. gold structure and at the same time display pentagons of similar topology (and size) than those present in the (6×6) reconstruction.

In the light of all these results, it is therefore proposed that the Au-induced Si(111)-(6×6) reconstruction, which present very unusual pentagonal arrangement, promote and/or enhance the nucleation of five-fold clusters in the liquid. The creation of the ISRO in the AuSi droplets thus stabilize the liquid state and enhance the supercooling behaviour (see Figure V.15).

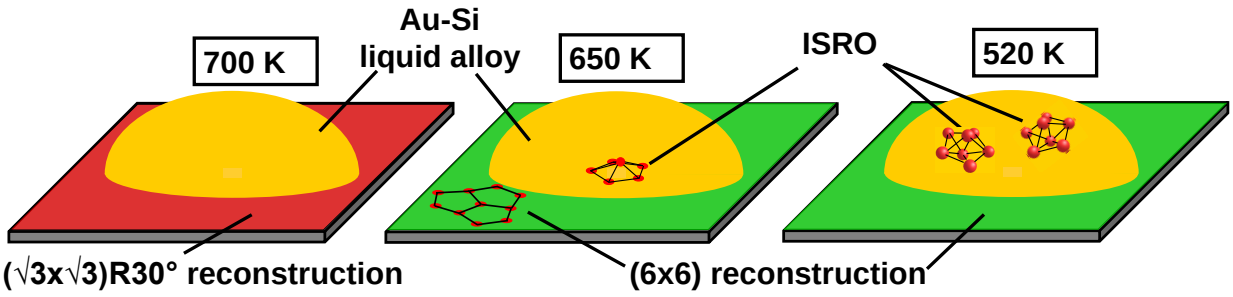

Figure V.15 – Schematic illustration of the proposed process. At 700 K the AuSi droplet forms on the Si(111)-($\sqrt{3}\times\sqrt{3}$)R30° surface. Upon cooling, at 650 K, the (6×6) reconstruction is formed and influences the liquid's structure. With still decreasing temperature, the ISRO develop in the droplet and stabilize the liquid down to 520 K.

In Figure V.15, the images suppose that the reconstructions extend all over the surface, even at the droplets/substrate interface. However, on the BM32 beamline, the wide size of the beam prevents a precise measure and only provides an average over a large surface of the sample. In addition, the islands cover a few percent of the total area so that it is not strictly possible to conclude the existence of a long-range ordered reconstruction at the substrate-droplet interface. As the (6×6) reconstruction is very stable and energetically favourable, it is however possible to think that a similar structure can form locally. The question of the interface's structure is discussed in Chapter VII.

The enhancement of the supercooling by the (6×6) reconstruction is however obtained

if the sample is annealed at least 60 K above T_e. Compared with the results obtained in the case of the Si(001) substrate for which higher annealing lead to lower supercooling, one would thus expect a solidification process that takes place at a higher temperature than the one measured with the $(\sqrt{3}\times\sqrt{3})$R30° reconstruction (annealed lower). It seems therefore unavoidable to focus on the effect of the annealing process that is responsible of three effects that could influence the solidification :

- Following the phase diagram of the AuSi system, a higher annealing leads to a larger Si content in the droplets.
- The higher the annealed temperature, the larger the droplets.
- The quality of the (6×6) reconstruction is improved with a large annealing.

Concerning the concentration of the droplets, it could not be determined experimentally in this work. It is thus reasonably assumed that it follows the equilibrium phase diagram as the droplet is in contact with the Si substrate reservoir and can adjust the Si content with the temperature variations. Therefore, whatever the maximum annealing temperature is, upon cooling to T_e, the concentration follows the liquidus line and has the eutectic value at T_e. The process governing the Si concentration adjustments is discussed in Chapter VII.

It is assumed in this work that the size of the droplets (even for deposits of 2 ML) are too large to induce surface effects and thus have an influence on the supercooling effect. Therefore, the presentation of the size effects does not aim to show potential features arising at the nanoscale but consists in the study of the influence of the (6×6) and $(\sqrt{3}\times\sqrt{3})$R30° reconstructions on droplets of different sizes. The underlying idea being the increase of the surface-to-volume ratio for which the influence of the surface (reconstruction) on the volume (liquid) is assumed to be enhanced. It is possible to influence the size of the droplets by changing the deposited amount and/or the annealing temperature (coarsening process), the formation of the reconstructions being at the same time dependent on the annealing temperature. Therefore, by performing several experiments with different amounts of gold and different annealing temperatures, it has been possible to study in parallel, the formation of the reconstructions (as well as its quality in the case of the (6×6) reconstruction) and their influence on liquid droplets of different sizes (*i. e.* of different surface/volume ratios).

V.4 Study of the size effect

In a first experiment, three different experiments with 2 ML, 10 ML and 30 ML of gold were performed by annealing at the same temperature of 720 K. A larger deposit leads to larger islands and then to larger droplets for equivalent annealing temperature which at the same time allows the formation of the (6×6) reconstruction upon cooling.

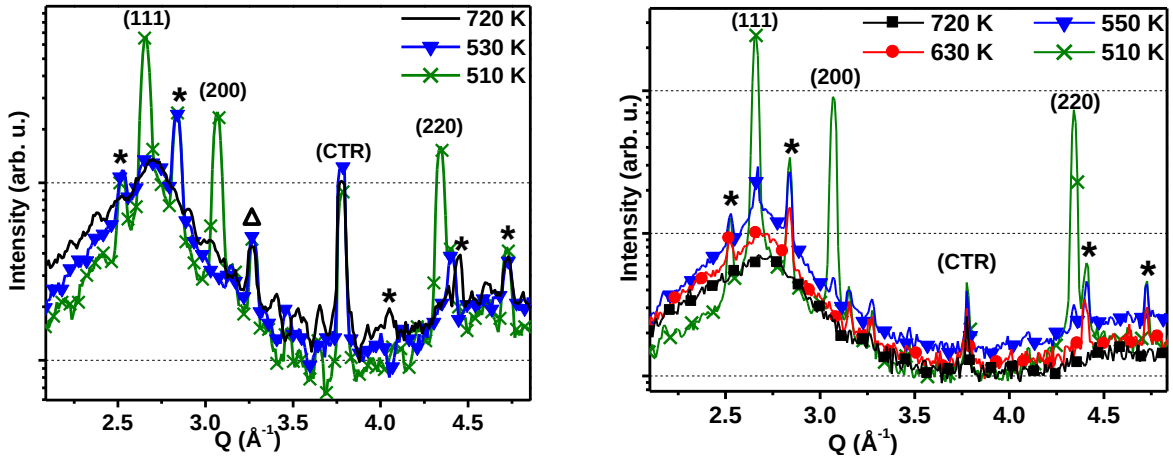

Figure V.16 – *Radial-scans* along the [1$\bar{2}$1] azimuth (a) at 720 K, 530 K and 510 K, for a 2 ML deposit and (b) at 720 K, 630 K, 550 K and 510 K, for the same sample onto which were added 8 ML to reach a total of 10 ML.

Figure V.16(a) shows the solidification scans for the 2 ML sample. At 530 K upon cooling, the scan only displays (6×6) reconstruction peaks, the crystal truncation rod and the 2D floating crystal peak. The droplets are thus still liquid at 530 K and display a sharp liquid-solid transition that takes place at 510 K. On the same sample was added 8 ML of gold to reach a total deposit of 10 ML and a second annealing at 720 K was performed. In this case, the solidification of the system arises at 510 K as for the 2 ML deposit, with the very first grains observed to appear at 550 K (see Figure V.16(b)). The major part of the droplets in this case thus turn into solid islands at a similar temperature than for 2 ML. Again,

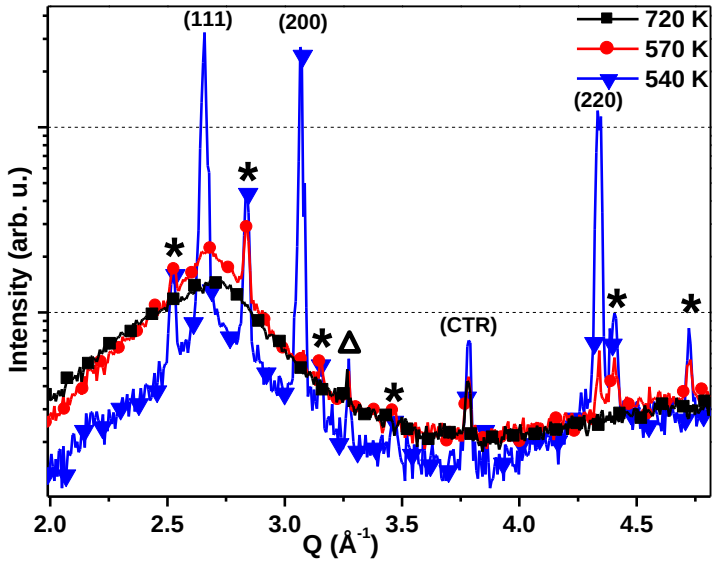

Figure V.17 – *Radial-scans* along the [1$\bar{2}$1] azimuth at 720 K, 570 K and 540 K, for a 30 ML deposit.

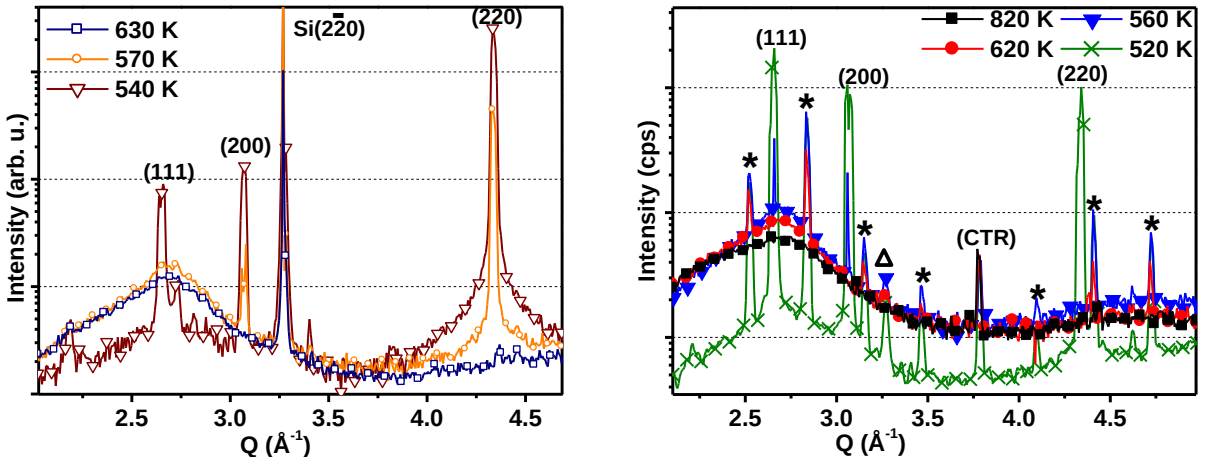

(a) (b)

Figure V.18 – *Radial-scans* for a 30 ML deposit (a) along the [1$\bar{1}$0] azimuth at 630 K, 570 K and 540 K and (b) along the [1$\bar{2}$1] azimuth at 820 K, 620 K, 560 K and 520 K, in this case the sample was previously annealed at 940 K

the procedure was performed for a 30 ML deposit. Figure V.17 shows that in this case the solidification process initiates at 570 K with the emergence of a very weak Au(220) peak. At 540 K, the liquid-solid transition sets in.

On the one hand, the 2 ML and 10 ML samples, both annealed at 720 K to get the creation of a (6×6) reconstruction, present the same order of supercooling compared to the 6 ML sample in the previous section (even annealed a bit lower, at 690 K, with a (6×6) reconstruction) : in these cases the solidification is recorded at 500∼510 K. This observation claims for a size-independent supercooling behaviour or more precisely that the difference in the surface/volume ratios between the two experiment does not influence the development of the ISRO. On the other hand, the 30 ML sample, also annealed at 720 K in presence of a (6×6) reconstruction, displays a lowered supercooling effect (T_s=540 K) : this claims for at least some size-dependence of the supercooling behaviour with the idea that a larger volume is less influenced by the surface structure.

In order to conclude whether or not the size effect is prominent and confirm the influence of the (6×6) reconstruction, a 30 ML deposit was annealed at the eutectic temperature whereas another one was annealed well above T_e, at 940 K [i]. The sample annealed at 940 K formed much larger droplets because of the coarsening process [Swiech *et al.*, 1991].

The cooling experiment shows that the 30 ML sample annealed at T_e (see Figure V.18(a)), only presents a partial $(\sqrt{3}\times\sqrt{3})$R30° reconstruction and that most of the grains are already formed at 570 K (very intense Au(220) peak) with a complete solidification that sets in when 540 K is reached. The 30 ML sample annealed at very high temperature (940 K) and therefore

i. We paid attention not to heat the sample higher in order to avoid gold evaporation.

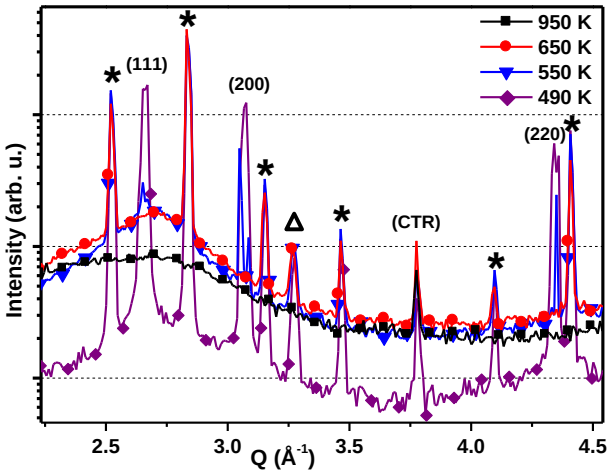

Figure V.19 – *Radial-scans* along the [1$\bar{2}$1] azimuth at 950 K, 750 K, 650 K and 490 K, for the 2+8 ML sample.

composed of larger droplets with a clear (6×6) reconstruction solidifies at lower temperature : 520 K (see Figure V.18(b)). From these comparisons, two key points can be expressed :

1. The 5 ML and 30 ML samples, both annealed only slightly above T_e with two different sizes of droplets and cooled down in the presence of the $(\sqrt{3}\times\sqrt{3})$R30° reconstruction display the same solidification temperature : 540 K.

2. The 30 ML sample annealed at 940 K and the 30 ML sample annealed at 720 K were both cooled down with the (6×6) reconstruction. However the former has larger droplets as well as a "better" (6×6) reconstruction and solidified at lower temperatures (T_s=520 K) than the latter (T_s=540 K). The same trend has also been observed for the 10 ML deposit after annealing at 950 K, which presented a nicer (6×6) reconstruction and a solidification temperature shifted by -10 K (T_s=490 K) (see Figure V.19).

Throughout these measurements carried out on different substrates and experimental conditions (deposited amounts, annealing temperatures, reconstructions), several assumptions were confirmed. Whatever the deposited amount is, the presence of the (6×6) reconstruction enhances the supercooling behaviour, the $(\sqrt{3}\times\sqrt{3})$R30° reconstruction always leading to lower supercooling. Moreover, if a large amount of gold is deposited (30 ML), the influence of the (6×6) reconstruction on the supercooling behaviour is weaker because the surface/volume ratio is smaller unless a sufficient annealing is applied to promote the creation of a (6×6) reconstruction of high quality.

The aim of this chapter was to present the different results concerning the supercooling phenomena arising in AuSi liquid droplet in contact with Si substrates. We have seen that a low supercooling is recorded on Si(001) substrates

whereas it is enhanced on Si(111) substrate. The maximum supercooling value has been observed in the case of the Si(111)-(6×6)Au surface for which a signal corresponding to an ordering of the liquid at the liquid-solid interface has been recorded. As the structure of the (6×6) reconstruction is locally formed with pentagonal units, we believe that this particular surface can favour the presence of clusters presenting five-fold symmetry and stabilize the liquid phase. The simulation results performed on the system tend to confirm this explanation. In the next chapter, we investigate other systems that are used to grow nanowires through the VLS process.

Summary of Chapter V

Supercooling in the Au-Si(001) system :

- For AuSi droplets solidifying on a Si(001) substrate, it is found that the higher the sample is annealed, the smaller the supercooling is.
- The in-plane orientation relationship between the solidified gold and the Si(001) substrate is strongly dominated by the "cube on cube" epitaxy.

Supercooling in the Au-Si(111) system :

- 6 ML of Au annealed 10 K above T_e followed by a cooling down results in the solidification of the AuSi droplets in the presence of a $(\sqrt{3}\times\sqrt{3})$R30° reconstruction 90 K below T_e.
- For a similar amount of gold annealed 60 K above T_e, the solidification takes place in the presence of the (6×6) reconstruction 120∼130 K below T_e.
- Upon cooling, the presence of the AuSi 2D crystal phase is observed as well as the ordering of the liquid in parallel to the ordering of the (6×6) reconstruction.

Investigation of the liquid's structure :

- The radial structure factors of the experimental and simulated liquids fit very well attesting the accuracy and reliability of the simulations for the liquid state in this system.
- The first order of the liquid signal is enhanced in the vicinity of the most intense (6×6) peaks indicating structural similarities between the two.
- A rod of intensity is recorded at the in-plane position of the liquid revealing the ordering of the liquid close to the droplet/substrate interface.
- The neighbor analysis of the simulated eutectic liquid shows an appreciable increase of the amount of five-fold clusters with the decrease of the temperature.
- The mean interatomic distance in the five-fold clusters is smaller than that in the f.c.c. gold structure and at the same time display pentagons of similar topology (and size) than those present in the (6×6) reconstruction.

Size effect :

- The comparison of several experiments carried out with different amounts of gold and different maximum annealing temperatures confirmed that the supercooling behaviour is influenced by the surface reconstruction : the (6×6) reconstruction tends to lower the solidification temperature.
- The (6×6) influence is reduced with the increase of the sizes of the droplets increasing the surface-to-volume ratio,*i. e.* for large droplets a part of the liquid do not "feel" the surface.
- The influence the (6×6) is again increased when this latter is of high quality.

Chapter VI

Case of other systems and inert substrates

Contents

In Chapter V, we have discussed the solidification processes of AuSi droplets on Si substrates. Many efforts were put in this system which revealed, depending on the substrate's structure, unexpected behaviour upon cooling. In order to attempt a comparison with the results obtained with Au-Si, similar experiments were performed on the Au-Ge and Al-Si which are supposed to have relatively close properties as they also combine a metal and a semi-conductor and can be used for VLS growth. In addition to the study of the solidification path, some results concerning growth and dewetting are presented and compared to the case of Au on Si(111). The AuSi and AuGe supercooling behaviour was also studied on "inert" substrates ; hence constituting closed systems as opposed to opened when on the SC substrastes.

VI.1 Au on Ge(111)

As it has been done in the case of the Au-Si system in Chapter V (see Figure V.4), a scheme of the reciprocal space is plotted in Figure VI.1, which allows to easily distinguish between the substrate, the solid islands, the liquid droplets and the reconstructions diffraction signals.

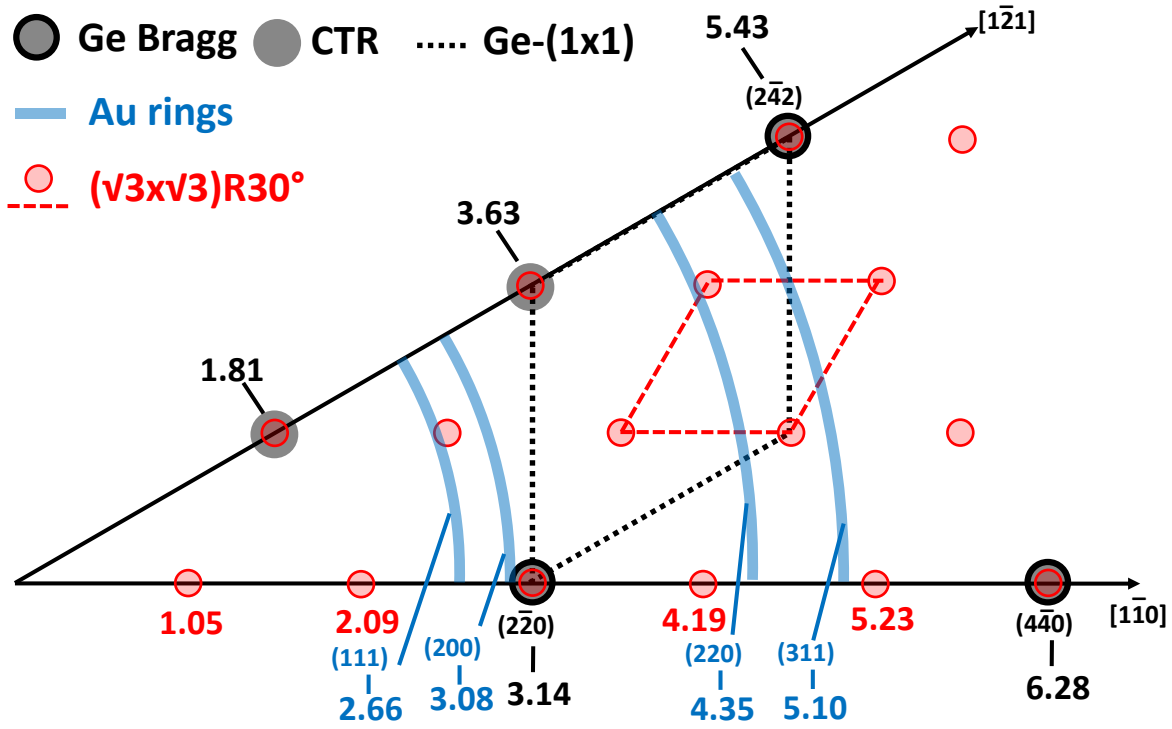

Figure VI.1 – Scheme representing the 30° (between the Ge[1$\bar{1}$0] and Ge[1$\bar{2}$1] azimuth) of the reciprocal space. The positions of the Ge Bragg peaks, CTR , $(\sqrt{3}\times\sqrt{3})$R30° reflections and Au rings are given in momentum transfer Q (Å^{-1}) values.

Layer by layer deposit

Figures VI.2 gathers the *radial-scans* performed during the deposition of several ML of Au on a Ge(111) substrate. At 0.5 ML, both scans only display the Ge substrate features (Bragg peaks and CTRs) without any gold crystalline signal. The scan along the $[1\bar{1}0]$ direction, however, reveals the presence of the $(\sqrt{3}\times\sqrt{3})$R30° reconstruction [Howes *et al.*, 1993]. When 1 ML is reached, the Au peaks appear, their intensity increases as long as the deposition process is maintained and depends on the in-plane orientation (*i. e.* on the azimuth). The Au(200) peak is already very intense for only 1 ML along the $[1\bar{1}0]$ direction whereas its signal along the $[1\bar{2}1]$ axis appears only at 3 ML and is very low. The Au(220) reflection appears on both axes at 1 ML and also increases with increasing deposition. The Au(111) peak remains quite low on both axes even for 3 ML. The presence of well defined Au Bragg peaks as well as $(\sqrt{3}\times\sqrt{3})$R30° reconstruction peaks for a 3 ML deposit seem to indicate that the RT growth of Au on Ge(111) is achieved by the formation of 3D crystalline structures together with a reconstructed wetting layer in this experiment. This result is a bit surprising as the surface energy of Ge(111) is smaller than the one of Si(111). As the uncertainty on the temperature below 450 K is large, we believe that we did not wait long enough before proceeding to the Au deposit so that it had been performed above RT.

In addition to the Au Bragg peaks, two reflections (at ~ 2.15 Å^{-1} and ~ 2.5 Å^{-1}) are present on both axes and do not correspond to any lattice spacing in gold. They are assumed to come from the formation of a AuGe crystalline phase and are discussed in details later.

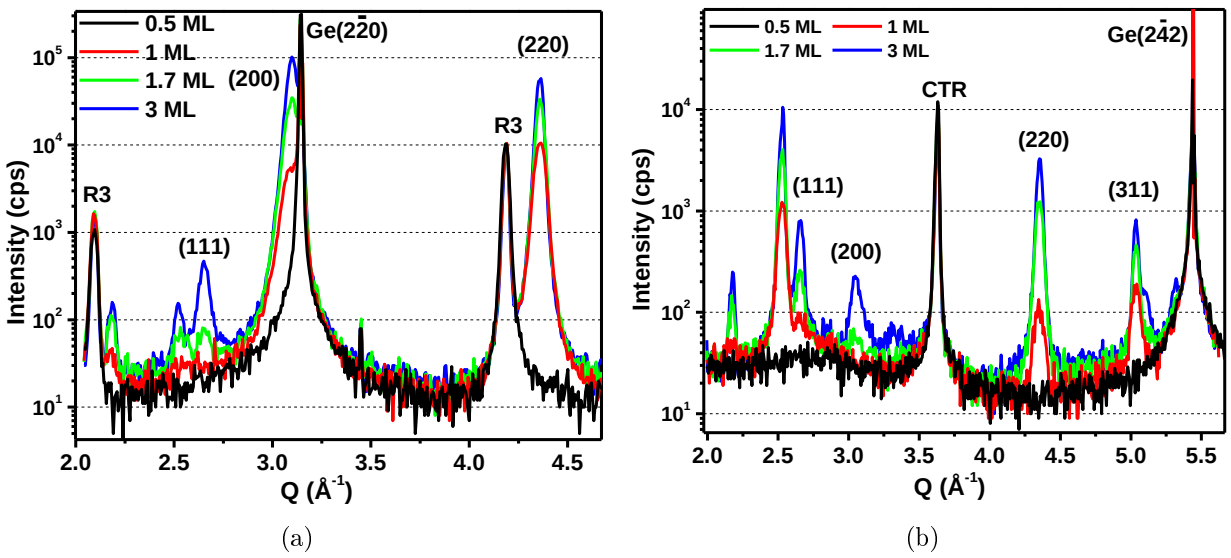

(a) (b)

Figure VI.2 – *Radial-scans* performed at RT for a total deposit of 0.5, 1, 1.7 and 3 ML of Au, along (a) the Ge$[1\bar{1}0]$ azimuth and (b) the Ge$[1\bar{2}1]$ azimuth. **R3** stands for $(\sqrt{3}\times\sqrt{3})$R30° reconstruction peaks.

Annealing and melting

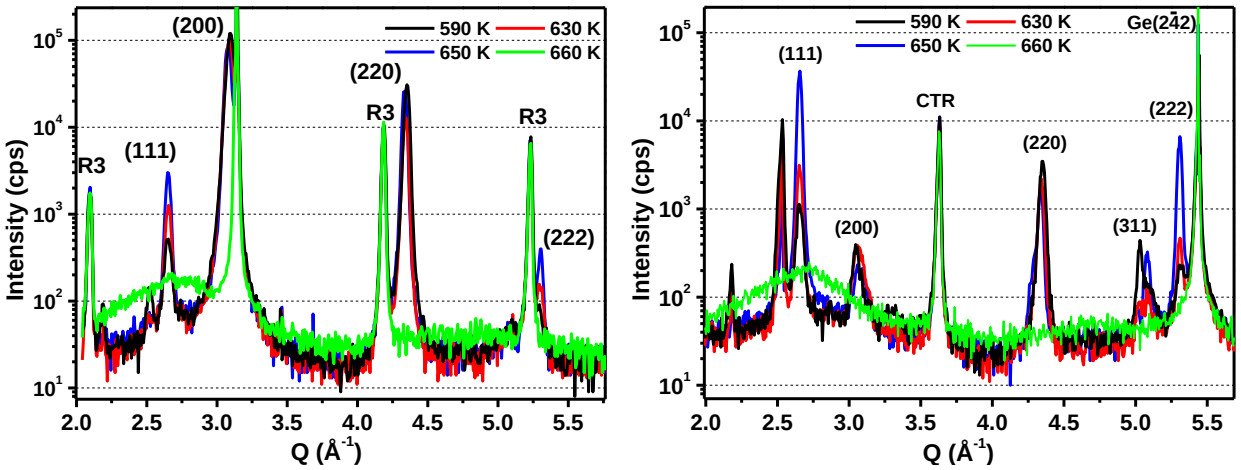

Figure VI.3 – *Radial-scans* performed upon annealing at 590 K, 630 K, 650 K, 660 K along (a) the Ge[1$\bar{1}$0] azimuth and (b) along the Ge[1$\bar{2}$1] azimuth.

Figures VI.3 shows the same *radial-scans* as in the previous Figure but for several temperature during annealing of the sample. Only the Au(111) reflections (and thus Au(222)) increase with T. At 660 K, all the gold reflections vanish confirming the solid-liquid transition. In addition, we note here that the two unassigned peaks mentioned above also disappear at T_e with the appearance of the liquid droplets whereas the $(\sqrt{3}\times\sqrt{3})$R30° reconstruction peaks remain. The sample was then annealed at a maximum of 710 K and a reciprocal space map of the liquid system was recorded (see Figure VI.3)

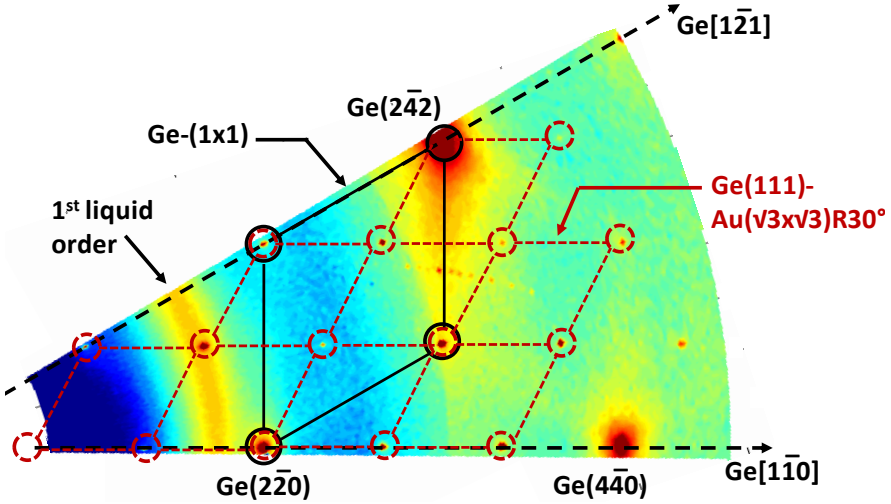

Figure VI.4 – Reciprocal space map of the Au-Ge system in the liquid state (at 670 K). The red, and blue colors refer to high and low intensity, respectively. The yellow colors represent intermediate intensities.

This map is rather simple, displaying the Ge Bragg peaks, the Ge(111)-($\sqrt{3}\times\sqrt{3}$)R30°Au reflections and the first order of the liquid signal. The second order of the liquid is almost invisible (as well as on the scans), which may be due to the low amount of Au deposited. Above T_e, the system is therefore composed of AuGe liquid droplets in the presence of a ($\sqrt{3}\times\sqrt{3}$)R30° reconstruction.

Cooling to T_s

As for the Au-Si system, we determine the solidification temperature by recording *radial-scans* upon cooling until the Au peaks reappear indicating the creation of crystal grains in the droplets. This is plotted for both axes upon cooling, at 710 K, 610 K, 590 K and 570 K in Figure VI.5. The very first traces of solid grains are recorded at 610 K, with the emergence

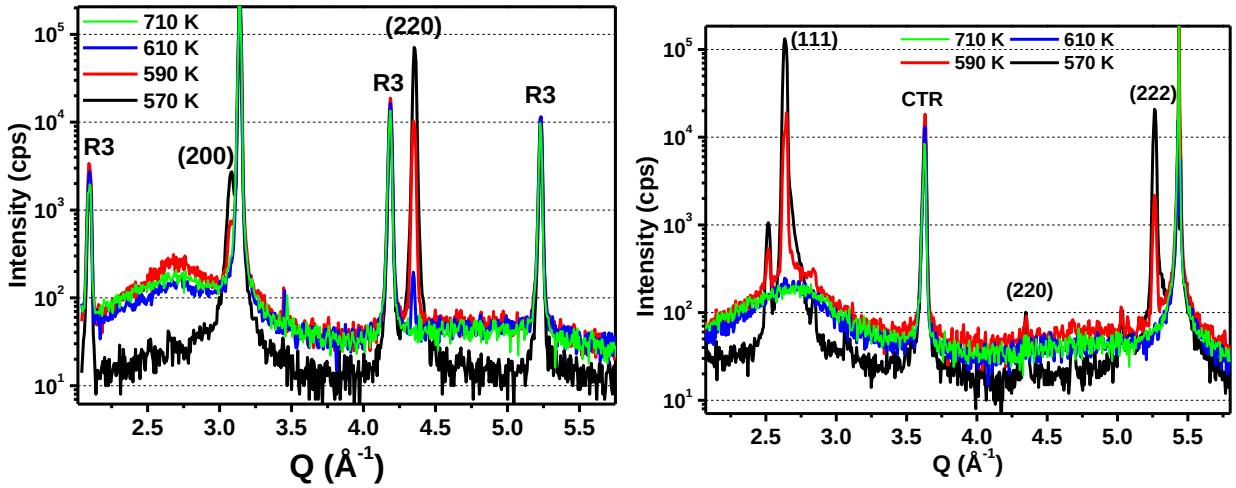

(a) (b)

Figure VI.5 – *Radial-scans* recorded upon cooling at 710 K, 610 K, 590 K and 570 K along (a) the Ge[1$\bar{1}$0] azimuth and (b) the Ge[1$\bar{2}$1] azimuth.

of the Au(220) reflection along the Ge[1$\bar{1}$0] azimuth but the majority of the droplets are still in the liquid state. The sample must be cooled down to 590 K to observe a substantial rise of the Au peaks intensity, the complete solidification of the system is obtained at 570 K, *i. e.* 90 K below T_e. Moreover, we note that the Au(111) peak is now very intense on the Ge[1$\bar{2}$1] axes but does not reappear along the [1$\bar{1}$0] direction. The Au(220) intensity, in the contrary, concentrates along the Ge[1$\bar{1}$0] azimuth. A reciprocal space map of the system in the solid state was thus recorded to visualize the intensity distribution of the gold structures (see Figure VI.6).

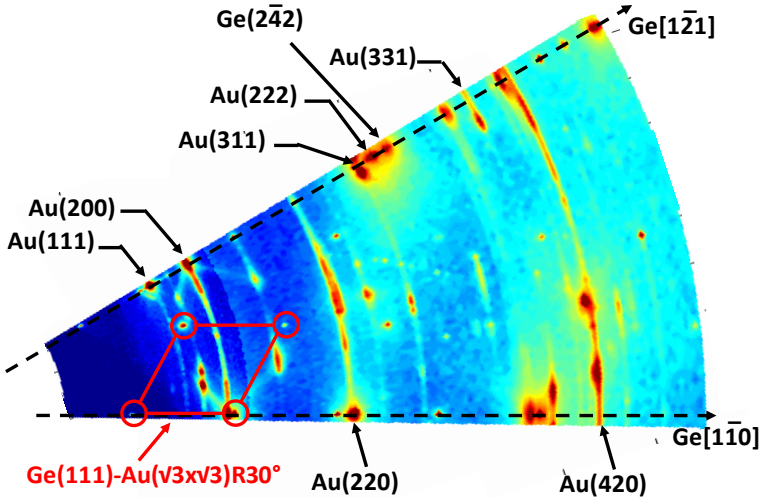

Figure VI.6 – Reciprocal space map of the Au-Ge system in the solid state (at RT) after melting and solidification. The red, and blue colors refer to high and low intensity, respectively. The yellow colors represents intermediate intensities

Epitaxies after melting and solidification

In the case of Au on Si(111), we have seen that the solid reciprocal space map presented gold rings (see Figure IV.2). This claimed for the solidification of gold grains in a quite random manner but with the predominant in-plane epitaxial relationships discussed in Chapter III which reappears after crystallization. Here, the solid map displays traces of gold rings but with a very inhomogeneous repartition of the intensity. It therefore reveals that the grains are very textured in the plane, depending on their epitaxial orientation perpendicular to the substrate. The Au(220) rings intensity concentrates on the Ge[1$\bar{1}$0] azimuth, which therefore

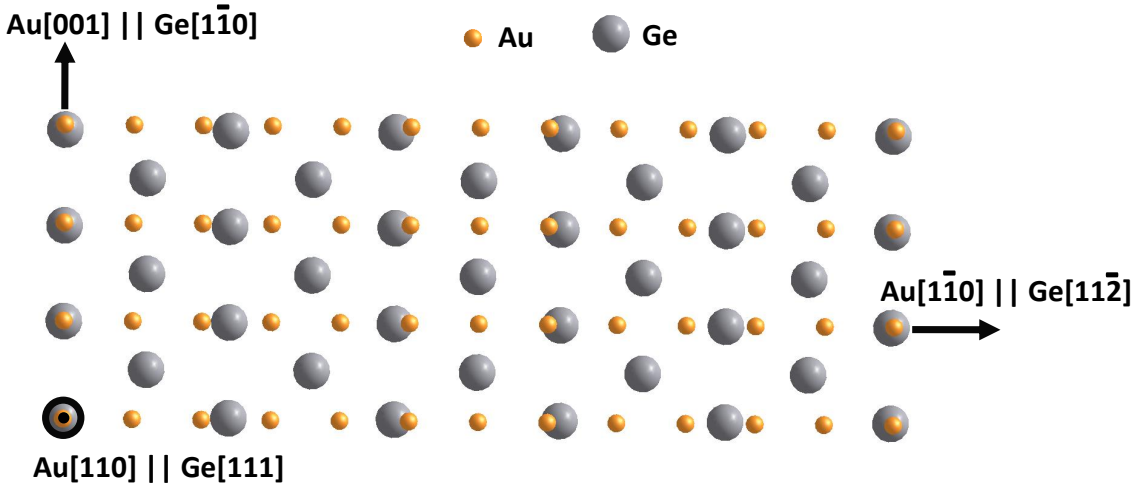

Figure VI.7 – Top view of the interface represented by the superposition of the Au(110) plane above the Ge(111) plane, the lattice parameters values are taken at 300 K. The Au(110) plane is rotated around the Ge[111] axis by 30° with respect to the parallel epitaxy.

corresponds to the OR1 presented in Chapter III : $[1\bar{1}0]$Au(111)$\|[1\bar{1}0]$Ge(111). Concerning the Au(111) intensity, which is concentrated on the Ge$[1\bar{2}1]$ direction, it corresponds to the [001]Au(110)$\|[1\bar{1}0]$Ge(111) epitaxial relationship. Figure VI.7 illustrates this configuration in the real space and shows the quite perfect matching between the atoms of the Ge$[1\bar{1}0]$ row and those of the Au[001] row, which explain this preferred orientation.

Discussion on AuGe crystalline phases.

During the deposit, we pointed out the existence of two unassigned peaks which are believed to arise from the presence of a metastable AuGe solid phase. The α domain present in the Au-Ge phase diagram corresponds to a stable AuGe fcc crystal with a lattice parameter equivalent to the one of pure gold. The difference only lies in substitutions of some Au atoms by Ge. The α phase can therefore not be distinguished from pure fcc <Au> by diffraction experiments. However, two AuGe metastable phases, with different crystal structures, can form depending on the experimental conditions [Okamoto and Massalski, 1984] :

- the hexagonal close packed β-AuGe phase ($a \simeq 2.9$ Å, $c \simeq 4.7$ Å)
- and the body-centered tetragonal γ-AuGe phase ($a \simeq 11.55$ Å, $c \simeq 22.33$ Å).

These two phases are known to arise under out-of-equilibrium conditions, by quenching an AuGe liquid alloy. The resulting phase depends on the alloy concentration [Anantharaman *et al.*, 1966; Manaila, 1999]. The β-AuGe can however not be at the origin of the peaks recorded here, its lattice parameters presenting no corresponding distance to their positions.

Concerning the γ-AuGe phase, its crystal structure and lattice parameters make it more suitable to fit the recorded peaks. Indeed, the distance $d_{(040)}$ and $d_{(044)}$ which are equal to 2.89 Å and 2.56 Å, respectively, give the closest corresponding Q values ($Q_{(040)}$=2.17 Å^{-1} and $Q_{(044)}$=2.45 Å^{-1}, respectively). The difference between the proposed reflections and the recorded ones can come from a slight difference in the value of the lattice parameters. We are however aware that the proposed structure is supposed to form here at RT during the growth of Au on Ge whereas it is more likely to form during quenching processes in literature.

Only one study reports its formation in the case of the elaboration of sputtered AuGe films on quartz substrate at RT [Ikegawa, 1988]. The γ-AuGe phase was found to quickly transform into α-AuGe and cubic Ge with soft annealing (below 370 K). This is not the case here as the two concerned peaks remain upon annealing, they only disappear at the solid-liquid transition temperature. More recently, the metastable γ-AuGe phase was observed to form in specific conditions during the strong undercooling of a AuGe liquid droplet at the tip of a Ge nanowire [Sutter and Sutter, 2011].

In our case, the metastable phase reappear but its signal after the solidification process is

very low compared to that recorded during the deposition process. It is thus believed here that these two peaks arise because of the formation of a AuGe crystalline alloy which is suppose to be the γ-AuGe phase. However the possibility that this phase corresponds to another unreported AuGe phase can not be excluded as our results and experimental conditions do not fully agree with published results.

VI.2 Al on Si(111)

Au is the historically used catalyst for the growth of Si nanowires [Wagner and Ellis, 1964]. However it is also at the origin of potential contamination problems lowering the performances of the nanowires. Al seems to be a promising metal to avoid contamination and replace gold, the most important problem being however its high reactivity with oxygen and thus the formation of an Al-oxide that strongly lowers the efficiency of the VLS process. It is however interesting to study its behaviour under experimental conditions similar to those used for the Au catalyst.

The experiment on the Al-Si(111) system was carried out on the ID03 beamline. For a given material, the scattering of X-ray is proportional to the square of its atomic number Z. With $Z_{Al} = 13$ and $Z_{Au} = 79$, the Al X-ray scattering is almost 40 times weaker compared to Au. ID03 offers the possibility to perform surface characterizations under UHV with a more brilliant beam and is therefore more suitable to study the Al-Si system. The two experiments consisted in annealing, melting and cooling 10 ML and 30 ML of Al deposited at RT on Si(111) substrates.

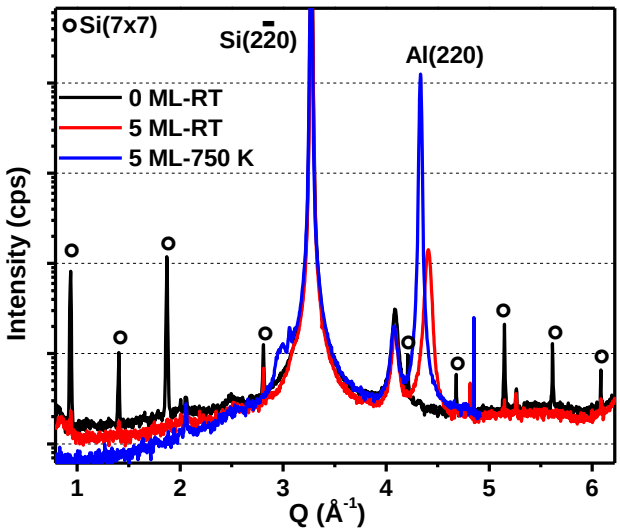

Figure VI.8 – *Radial-scans* along the Si[1$\bar{1}$0] azimuth, recorded before any deposit of Al at RT and after a deposit of 5 ML of Al at RT and 750 K. The peaks marked with a circle are Si-(7×7) reconstruction peaks.

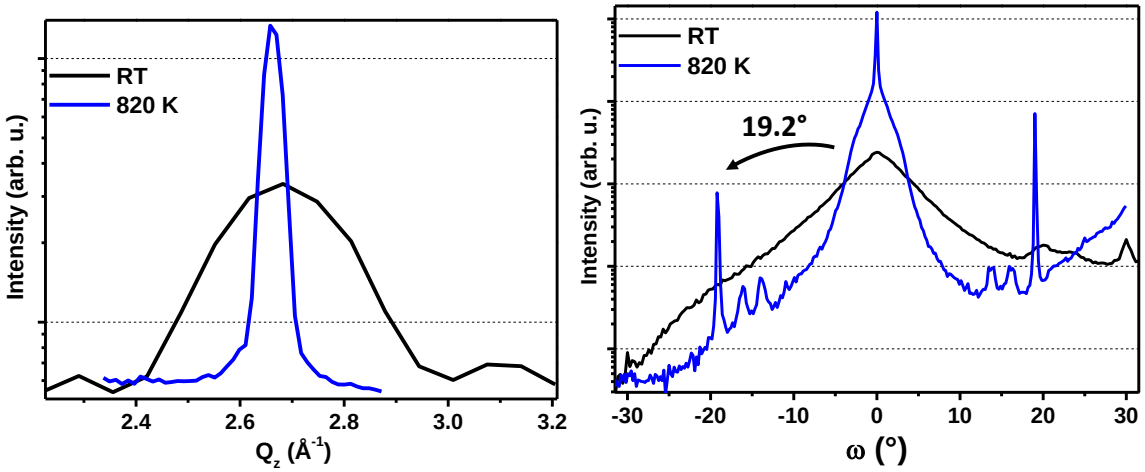

(a) (b)

Figure VI.9 – (a) *l-scans* (along $\boldsymbol{Q}_\perp$) crossing the Al(3$\bar{1}$1) Bragg peak at RT and 820 K and (b) *Rocking-scans* on the Al(220) ring at RT and 820 K.

Figure VI.8 shows that as soon as 10 ML are deposited, the strong Si-(7×7) peaks disappear and the Al diffraction peaks appear. Along the Si[1$\bar{1}$0] , only the Al(220) peak is present which is quite similar to the Au-Si in similar conditions (see Chapter III).

Figure VI.9(a) compares two *l-scans* performed on the Au(220) reflection at RT and after annealing of the sample. The result is comparable to what has been observed for the Au-Si system (Figure III.10(b)) : the peak narrows with annealing which corresponds to the dewetting of the film. The value of the FWHM at RT yields an estimation of the film thickness of 2.4 nm corresponding to $\sim$10 ML in agreement with the deposited amount. At 820 K, the height of the structures is about 16.5 nm.

At the same time, similar measurements on in-plane orientation relationship as in the Au-

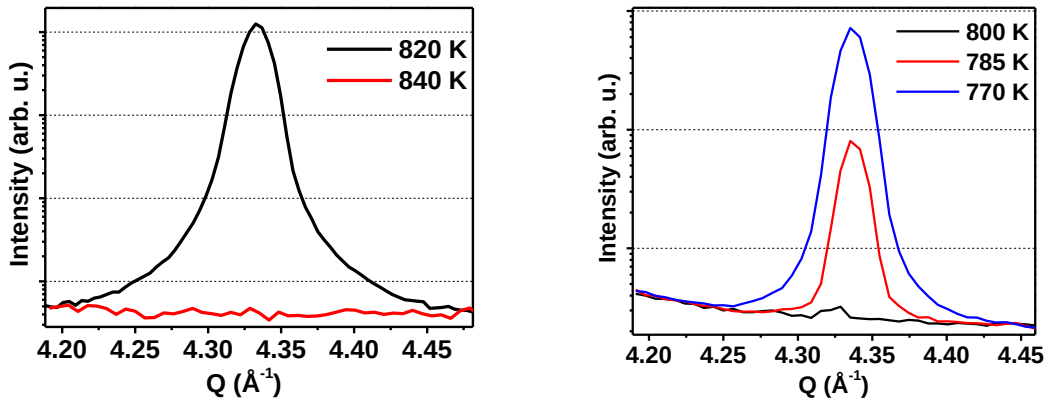

(a) (b)

Figure VI.10 – *Radial-scans* on the Al(220) peak (along the Si[1$\bar{1}$0] azimuth) (a) upon annealing at 820 K and 840 K and (b) upon cooling at 800 K, 785 K and 770 K .

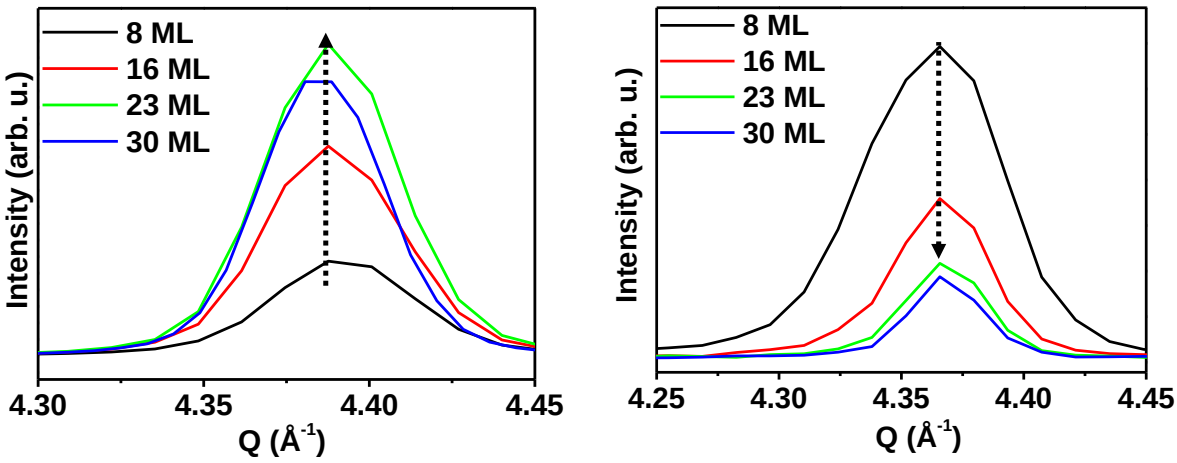

Figure VI.11 – *Radial-scans* performed during the deposit of Al on the Si substrate for 8, 16, 23 and 30 ML on the Al(220) peak (a) along the Si[1$\bar{1}$0] azimuth and (b) along the Si[1$\bar{2}$1] azimuth.

Si system were performed (see Figure VI.9(b)). At low temperature, a *rocking-scan* on the Al(220) ring displays a very broad peak centered on Si[1$\bar{1}$0] and changes into a narrower peak with the appearance of a second one (at 19°) with annealing. The Al-Si system thus presents a similar dewetting process, as described in Chapter III for Au-Si, which is accompanied by epitaxial reorganization upon annealing. We can however notice here that the central peak displays a "double-width" shape. This can arise from a bimodal distribution of the sizes of the structures.

When the sample is annealed at increasing temperature, the Al(220) peak vanishes around the Al-Si eutectic temperature at 840 K for which the solid-liquid transition takes place (Figure VI.10(a)). The sample can not be annealed higher otherwise Al evaporation can happen. Upon cooling the first solid grains appear at 785 K and the solidification sets in at 770 K(Figure VI.10(b)).

For this sample the deposited amount of Al was too low to extract a clear liquid signal. Another experiment was thus performed on a new sample with a 30 ML deposit. During the deposition, *radial-scans* were performed on the Al(220) signal along the Si[1$\bar{1}$0] and Si[1$\bar{2}$1] azimuths (see Figure VI.11). The intensities vary in opposite ways : they increase along the [1$\bar{1}$0] axis whereas they decrease along the [1$\bar{2}$1] direction, highlighting a coverage dependence of the in-plane orientation of the Al(111)-Si(111) interface at RT.

The sample was then annealed and *radial-scans* were acquired at 780, 795 and 835 K showing a progressive transition between solid Al Bragg peaks and a clear liquid signal by approaching the eutectic temperature (Figure VI.12). Upon cooling, the liquid signal transformed back into gold peaks when the liquid-solid transition takes place at 780 K which is 50 K below T_e.

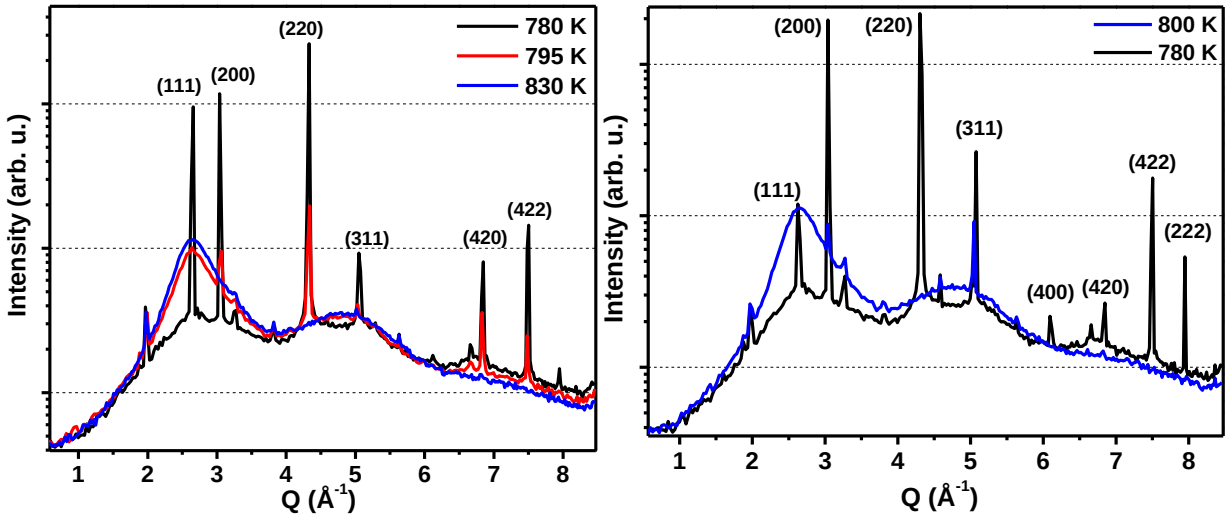

Figure VI.12 – *Radial-scans* performed between the [1$\bar{1}$0] and [1$\bar{2}$1] Si azimuth upon annealing a 30 ML Al deposit on Si(111) at 780 K, 795 K and 830 K.

Compared to the Au-Si system (or Au-Ge), the supercooling behaviour recorded in these experiments on Al-Si are not very surprising. It has already been reported in literature that large degree of supercooling (more than 100 K) can be achieved even for bulk studies [Das *et al.*, 2001]. However, the degree of supercooling and the solidification pathways are numerous, very complex and depend on many parameters such as the concentration, the thermal history, the cooling rate or the formation of metastable phases. In the case presented here, in the presence of a Si substrate and a very small cooling rate, it is reasonably assumed that a simple segregation process takes place resulting in the solidification of separated primary

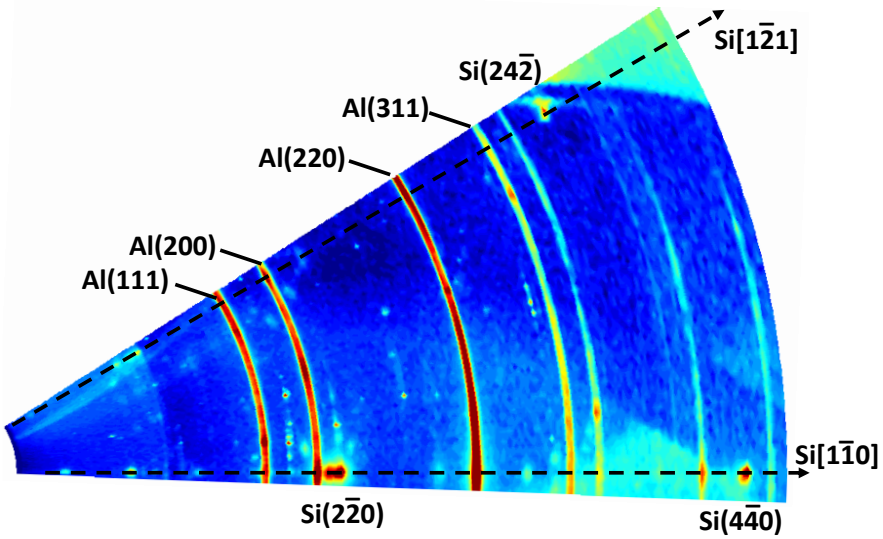

Figure VI.13 – Reciprocal space map of the Al-Si system in the solid state (at RT). The red, and blue colors refer to high and low intensity, respectively. The yellow colors represents intermediate intensities

phases of Al and Si.

After solidification, the sample was cooled down to 300 K and a reciprocal space map was recorded (Figure VI.13). This map reveals solid crystalline Al Debye-Scherrer rings that are quite homogeneous. Contrary to the Au-Ge system, the melting-solidification cycle results in an untextured solid in the case of Al on Si(111).

Complementary results obtained with the Al catalyst

In addition to the understanding of the fundamental aspects described throughout this manuscript, the challenge is to control them. During one experiment, we tried to use the large difference in the eutectic temperatures between the Al-Si ($T_e = 850\ K$) and the Al-Ge ($T_e = 700\ K$) systems to grow Ge NWs on a Si(111) substrate through an Al catalyst.

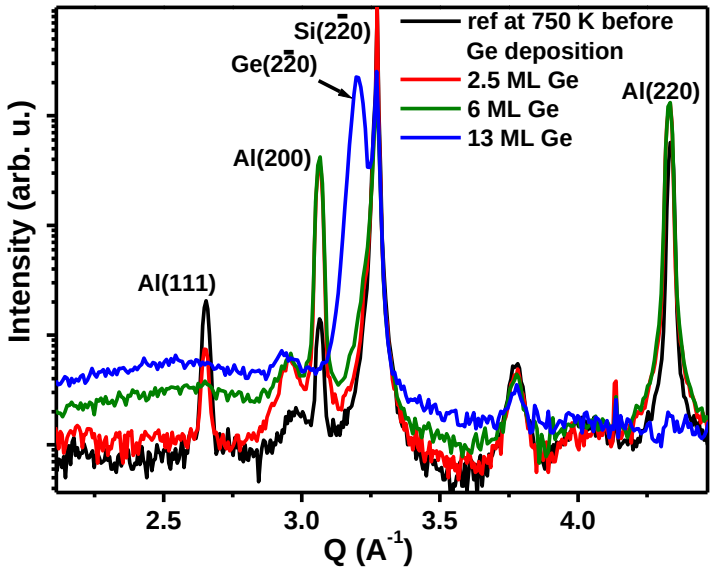

Figure VI.14 – *Radial-scan* performed along the Si[1$\bar{1}$0] azimuth in the case of a Si(111) sample onto which 6ML of Al were deposited, annealed and cooled down to 750 K (black). Same *radial-scan* after the addition of 2.5 (red), 6 (green) and 13 ML (blue) of Ge at a constant temperature of 750 K.

To do so, we have annealed a deposit of 6 ML of Al on a Si(111) surface at 870 K in order to form the AlSi droplets. Then the system was cooled down to 750 K and a *radial-scan* along the Si[1$\bar{1}$0] azimuth was recorded (see Figure VI.14). It displays the Al Bragg peaks and confirms the solidification of the sample[i]. Then, we recorded the same scan during the addition of Ge at 750 K, *i. e.* 50 K above the Al-Ge eutectic temperature. Remarkably, after the addition of 2.5 ML of Ge the intensity of the Al(111) peak decreased whereas those of the Al(200) and Al(220) increased. After the addition of a total of 6 ML, the Al(111) peaks has disappeared leaving a very weak liquid signal. For 13 ML of Ge added on the sample,

i. The wide peak at 3.75 Å corresponds to the formation of small crystals of SiC.

no more Al Bragg peaks were recorded reflecting the melting of the system. In addition, the Ge(220) Bragg peak appeared which means that some Ge structures (film, islands, NWs...) have formed in epitaxy with the Si(111) surface. Sadly, it has been impossible to perform *ex-situ* characterization on this sample to see if nanowires had been grown with success. These measurements reveal that the addition of Ge onto the surface composed of AlSi solid islands above the eutectic temperature of Al-Ge allows the melting of the system and the potential growth of Ge NWs.

The presentation of this experiment, which is not very conclusive, aims however to show why the knowledge of the physic of the eutectic liquid droplets studied in this work is important as it could lead to a better control of the growth parameters and should provide a wide range of tools to design new nano-objects.

In addition to the investigations of the Au-Si(111), Au-Si(001), Au-Ge(111) and Al-Si(111), some attempts to get more information on the behaviour of those metal-SC liquids were carried out on substrates that are supposed to be inert, at least chemically. To do so we have performed similar experiments as presented above and in Chapter V for AuSi on a SiO_2 substrate and AuGe on SiO_2 and Al_2O_3 substrates.

VI.3 Case of "inert" substrates

VI.3.1 AuSi on SiO_2

In this experiment, a MBE co-deposit of Au and Si was performed in required proportions to reach a total of 6 ML of a AuSi alloy at the eutectic composition. Following the same experimental procedure as in all the previous experiments, the sample was heated and *radial-scans* were recorded until the disappearance of the crystalline peaks vanish at the eutectic temperature (see Figures VI.15(a) and (b)). We can note here that the melting process starts at 610 K, the complete melting of the system arises at 630 K. The sample is then annealed at 720 K and cooled down. During the cooling process, *radial-scans* are also recorded to measure the temperature at which the liquid-solid transition takes place (see Figures VI.15(c) and (d)). This allows the observation of the first solid grains at 570 K (presence of the Au(220) peak in Figure VI.15(d)) and a very progressive solidification process that ends when a temperature of 510 K is reached. However, at 530 K, the transition is already almost complete. Surprisingly, one can remark a peak at 2.52 $Å^{-1}$ arising at 530 K in Figure VI.15(c), which does not correspond to any fcc gold interplanar distance. A comparison that can easily be made concerns the metastable γ-AuGe phase which was supposed to be responsible of a

peak at the same position in section VI.1. It can also be attributed to an Au-Si metastable phase reported in section III.2 as the peak corresponds to the $Au_7Si(400)$ interplanar distance (see Table III.2). The formation of metastable phases in these systems however clearly requires deeper investigations.

Interestingly, compared to the Au-Si(111) samples, several differences can be observed. The melting process is found to start 20 K below T_e, the solidification begins at 570 K and ends around 520 K with the potential formation of AuSi metastable phases. The supercooling value (with T_e taken as the reference point) is difficult to measure but can be roughly estimated to be 100 K with a solidification process differing from the case of the "open" system. These results will be discussed in more details in the next chapter.

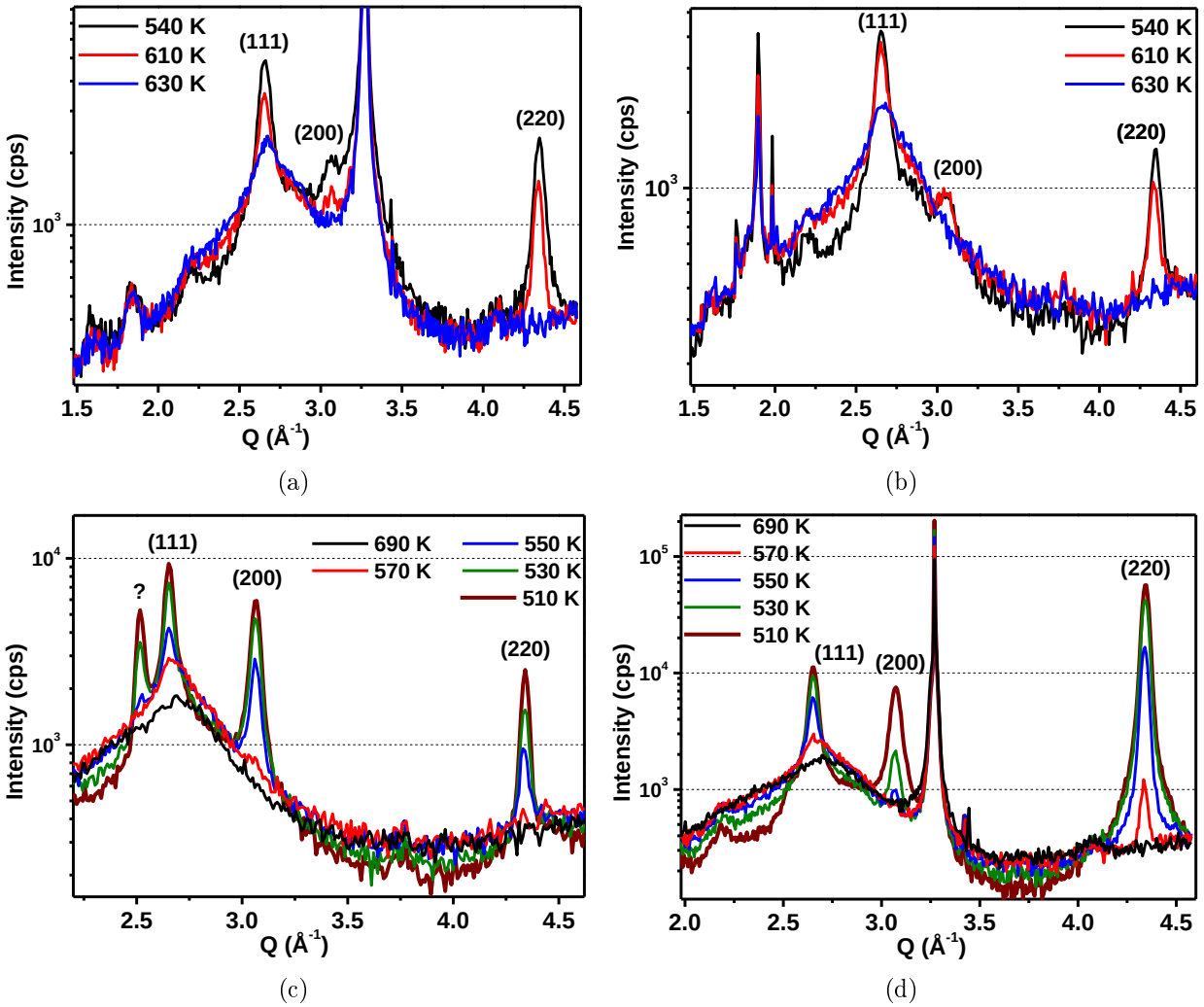

Figure VI.15 – (a)-(b) *Radial-scans* performed on the two substrate's axes upon heating, at 540, 610 and 630 K. (c)-(d) *Radial-scans* performed on the two substrate's axes upon cooling, at 690, 570, 550, 530 and 510 K. For a eutectic AuSi deposit of 7 ML.

VI.3.2 AuGe on SiO_2

The same experiment was performed but this time with a co-deposit of 6 ML of a AuGe eutectic alloy on a SiO_2 substrate. However, no solid-liquid transition was observed passing through the eutectic temperature. At 690 K, the Au(220) peak was still present in the scans, confirming the presence of gold grains. This observation was assumed to arise because of a concentration gap between the eutectic concentration and the real one with a lack of Ge in some islands. To overcome this issue, additional Ge was deposited at 690 K and, at the same time, fast *radial-scans* were recorded on the Au(220) peak to follow the melting process (see Figure VI.16(a)). The sample was then cooled down, the Au(220) peak appeared at 560 K, its intensity progressively increased with cooling and reached its maximum at 490 K whereas

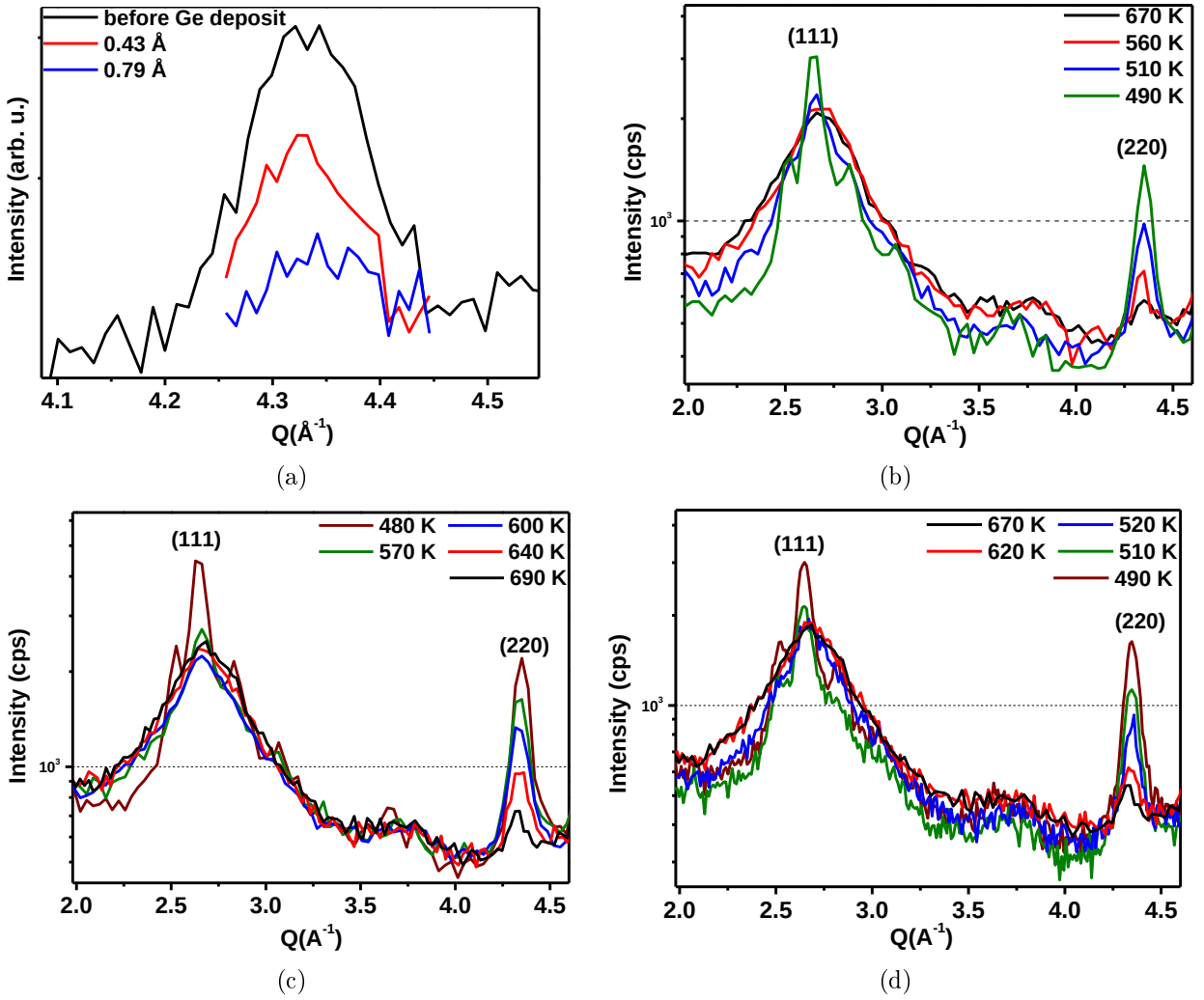

Figure VI.16 – (a) *Radial-scan* on the Au(220) peak during the deposition of additional Ge at 690 K until the disappearance of the peak due to the melting of the system. (b) *Radial-scans* performed at 670, 560, 510 and 490 K upon cooling from 690 K after the deposition of additional Ge. (c) *Radial-scans* performed at 480, 570, 600, 640 and 690 K upon heating. (d) *Radial-scans* performed at 670, 620, 520, 510 and 490 K upon a second cooling process from 690 K.

the Au(111) peak only appeared at 510 K and slightly increased when the temperature was decreased again by 20 K. To get a clear measure of the melting temperature of the system, the sample was heated again (see Figure VI.16(c)). Surprisingly, at 570 K the Au(111) peak has already disappeared and the Au(220) intensity starts to decrease. This latter still presents a weak intensity at 690 K suggesting that some parts of the system remain solid even 60 K above the eutectic temperature. A subsequent cooling of the system displays quite the same solidification process as in the first cycle (see Figure VI.16(d)) with a progressive increase of the Au(220) peak and a late appearance of the Au(111) peak around 500 K.

For this experiment the phase transitions were found to take place over a wide temperature range with even some islands that could not be melted. It reflects a potential heterogeneities that will be described later.

VI.3.3 AuGe on Al_2O_3

Similarly to the previous experiment, a co-deposit of 6 ML of Au and Ge at a supposed eutectic composition was carried out on an Al_2O_3. This substrate is of particular interest as it has been reported to induce ordering in liquid Al in contact with it [Oh *et al.*, 2005]. Again, during the first heating process of the sample, the Au(220) peak could not be removed even at 820 K (see Figure VI.17(a)), suggesting, as in the previous experiment, that the composition was far from the eutectic one. To compensate, the Ge deposit was continued (at 820 K) until the Au(220) peak vanishes and the sample was subsequently cooled down (see Figure VI.17(b)). As for AuGe deposited on SiO_2, the Au(220) peak progressively increased with the decreasing temperature whereas the Au(111) peak as well as two other peaks attributed to the γ phase appeared. More interestingly, it was the first time that SC Bragg peaks, others than the bulk substrate peaks, were recorded. Here, at 500 K, the Ge(111) and Ge(311) Bragg peaks appeared and revealed that, as predicted by the phase diagram, a segregation process takes place leaving Au and Ge in separated solid phases.

Again, it was necessary to confirm the melting temperature of the present system so that the sample was heated again (see Figure VI.17(c)). At 590 K, all peaks (from Au, γ and Ge) were still present but their intensities had already started to decrease. This trend was confirmed at 650 K for which a major part of the diffraction signal is due to the liquid. At 670 K, only the Au(220) peak remained and is attributed to islands with compositions still far from the eutectic one, *i. e.* presenting an excess in gold so that only partial melting was observed even above the eutectic temperature. Upon subsequent cooling, the Au(220) peak reappeared progressively, the Au(111) and γ peaks appeared at 500 K and increased in intensity when the temperature was reduced to 480 K, for which the Ge Bragg peaks arised.

The investigation of the Au-Ge system on the Al_2O_3 surface displays similar results to

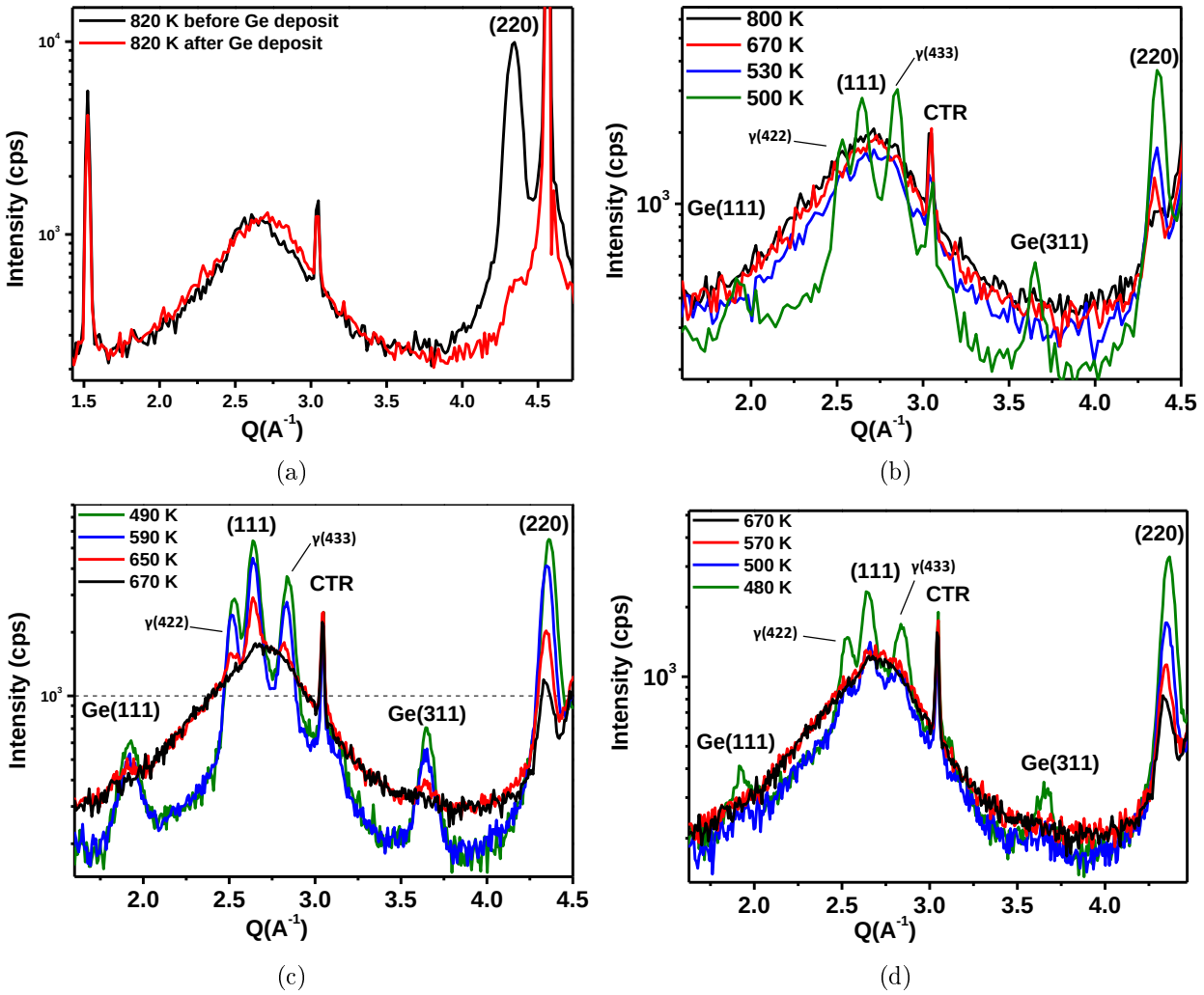

Figure VI.17 – (a) *Radial-scans* performed at 820 K before (black) and after (red) additional Ge deposition. (b) *Radial-scans* performed during the first cooling from 820 K, at 800, 670, 530 and 500 K. (c) *Radial-scans* performed during the second annealing of the sample at 490 K, 590 K, 650 K and 670 K. (d) *Radial-scans* performed during the second cooling sequence at 670, 570, 500 and 480 K

those obtained for AuGe on SiO_2. The liquid-solid transition is very progressive and metastable phases are found to form. In addition, the formation of very small crystallites of pure Ge are observed.

The results presented in this chapter as well as in the previous one, show that the supercooling behaviour of the metal-SC droplets can strongly differ from an experiment to another. At this point of this manuscript we have described our measurements and have begun to propose potential explanations to these kind of effects. However, the complexity of studying the behaviour of liquids, at the nanoscale, seems to require deeper discussion to bring a clearer point of view on what has been observed. The next chapter is dedicated to such discussion.

Summary of Chapter VI

Au-Ge(111) :

- The growth of Au on Ge(111) is found to follow a Stranski-Krastanow mode in presence of a $(\sqrt{3}\times\sqrt{3})$R30° reconstruction. The uncertainty on the temperature below 450 K makes hard to know if the deposit has been carried out at RT.
- The reciprocal space map recorded in the liquid state does not display anisotropic variation of the intensity of the liquid signal in the first ring of scattering.
- Upon cooling, the solidification process takes place 90 K below the recorded melting temperature and results in the formation of very textured grains.
- During the experiment, some unassigned peaks are recorded and are attributed to the γ-AuGe metastable phase even if we are aware that our experimental conditions are far from those required to form this phase.

Al-Si(111) :

- The Al-Si(111) system presents similar behaviour compared to the Au-Si(111) system : the dewetting of the film is accompanied by a rearrangement of the orientation relationships.
- Two samples have been investigated, one with 5 ML and the other one with 30 ML, both showed a liquid-solid transition occurring about 60 K below T_e.
- The reciprocal space map recorded at RT after solidification displays relatively homogeneous Al Debye-Scherrer rings revealing the weak texture of the grains.

Case of inert substrates :

- **AuSi on SiO_2 :** For this experiment, it was more complicated to determine the phase transitions. The islands start to melt at 610 K and are completely melted at 630 K. Upon cooling a very progressive liquid-solid transition is observed with the apparition of the first grains at 570 K and a complete solidification at 510 K (∼100 K below T_e). A peak not corresponding to any gold Bragg peak is also recorded.
- **AuGe on SiO_2 and Al_2O_3 :** In both cases, the uncertainty on the composition is very high and we did not observe the complete melting. The solidification is extremely progressive but continues down to very low temperature with the appearance of the γ phase peaks. In both cases, the liquid-solid and solid-liquid transition temperatures are very difficult to determine. In the case of the Al_2O_3 substrate we observe the apparition of the Ge Bragg peaks.

Chapter VII

Discussion and synthesis

In Chapter III, experimental results have been presented concerning the dewetting process, which has been found to be accompanied by changes in the in-plane orientation relationships. In Chapter IV we have studied the formation, the stability and the atomic structure of the Si(111)-(6×6)Au reconstruction which can coexist with either droplets or solid islands. In these two chapters, even if complementary experiments can be imagined to obtain more precise information on critical points, the global understanding of the results allows to provide satisfactory explanations. In Chapter V and VI, we strove to characterize in more details the catalyst liquid phase which revealed unexpected supercooling effects in the Au-Si(111) system. Similar experiments have been performed in other systems for comparison. The behaviour of the liquid phase in interaction with a solid surface at the nanoscale is a fundamental feature in the current research concerning the growth of nanowires. This section therefore aims to discuss the experimental results described in the last two chapters (V and VI) and presents an overview of the different physical concepts.

Problematics

The supercooling behaviour of a given system is not easy to understand. Indeed, the general thermodynamical concepts briefly exposed in Chapter I to explain the liquid-solid phase transition, mostly due to the early work of Turnbull, were at the beginning only derived for the case of pure elements. Moreover, the supercooling phenomena in pure elements are still not completely elucidated [Vinet *et al.*, 2002; Kim and Kelton, 2007] and new concepts on nucleation processes are proposed [Quested and Greer, 2005]. In addition, based on the assumption of Frank [Frank, 1952], the internal structure of liquids is thought to be locally ordered in a pentagonal symmetry but, despite new means of characterization and a constant increase of simulation capacities, it remains hard to bring evidences for this effect.

It becomes even more complex to study supercooling effects when dealing with alloys. From a liquid alloy, numerous solid phases can form depending on the cooling parameter, their study requires a lot of attention and well-defined experimental conditions. The obtained phase diagram can display many domain boundaries increasing the complexity of the study of the phase transitions. Moreover, in experiments that take place far from equilibrium conditions, it is not rare to observe the formation of metastable phases.

Paradoxically, the solidification of eutectic liquids is wrongly thought to be quite easy to understand as it is supposed to consist in the segregation of the two components, resulting in two separated solid phases. Moreover, the existence of liquid eutectics is quite intriguing as the liquid phase is found at very low temperature for a given composition and can transform in glass through rapid solidification. Eutectic liquids are also assumed to have a poor tendency to supercooling [Takeda *et al.*, 2007; Itami *et al.*, 2010]. The mystery of their structure

remains challenging but recent studies, both experimental and theoretical, have made evident breakthroughs [Ikeda *et al.*, 2002; Takeda *et al.*, 2007; Itami *et al.*, 2007; Pasturel *et al.*, 2010; Tasci *et al.*, 2010; Chirawatkul *et al.*, 2011]. The complexity of supercooling phenomena is further increased when a liquid is in contact with a solid. Often, heterogeneous nucleation is triggered and promote solidification. However, in some cases, specific surfaces are no good nucleants for specific liquids [Greer, 2006].

The complexity of the present work therefore lies in the study of a metal-SC eutectic liquid (mostly AuSi) in interaction with its respective SC solid substrate (Si), under the form of nanometric droplets. Therefore, it is very hard to use thermodynamical models, merely due to the fact, for instance, that interface energies are difficult to measure. Moreover, a slight difference in one of the parameters of the system can lead to big changes in its solidification process. In section I.7.1, we have presented how the equilibrium is modified between a droplet at the tip of a nanowire and one on a flat substrate. A very recent study has revealed that it can strongly influence the solidification process. Indeed, Sutter *et al.* reported the formation of the metastable γ-AuGe phase when cooling down a AuGe droplet at the tip of a nanowire [Sutter and Sutter, 2011]. In the same study, in the light of our results published one year before [Schülli *et al.*, 2010], they decided to perform the same experiment in the Au-Si system. During their cooling procedure, they reported that no metastable AuSi phase forms, however they obtained an amorphous AuSi solid. This is therefore a completely different result compared to ours. In our experiments, the X-ray measurements clearly highlight that the solidified gold is crystalline as gold Bragg peaks are recorded when the solid-liquid transition takes place. Through this simple example, one can see that there is still a lot to be explained in the solidification process of these particular liquids.

The experimental conditions are thus believed to strongly influence the numerous processes involved in the interaction between the droplets/islands and the underlying substrate. Figure VII.1 illustrates this statement by gathering the different features that have been raised through the present study. It shows that the VLS process, which seems rather simple at first sight and is widely used to grow nanowires, encompass many atomic processes that have to be understood to improve our control on the growth conditions and more generally to enlarge our knowledge of the physics at the nanoscale.

In the following we compare our findings to published results and make a synthesis on the knowledge we have so far on the systems studied in this work.

Structure of the interface and of the solidified droplets

The knowledge of the structure of the interface is of prime importance because its effect on the liquid's structure and the resulting islands is assumed to be very strong. However, in the

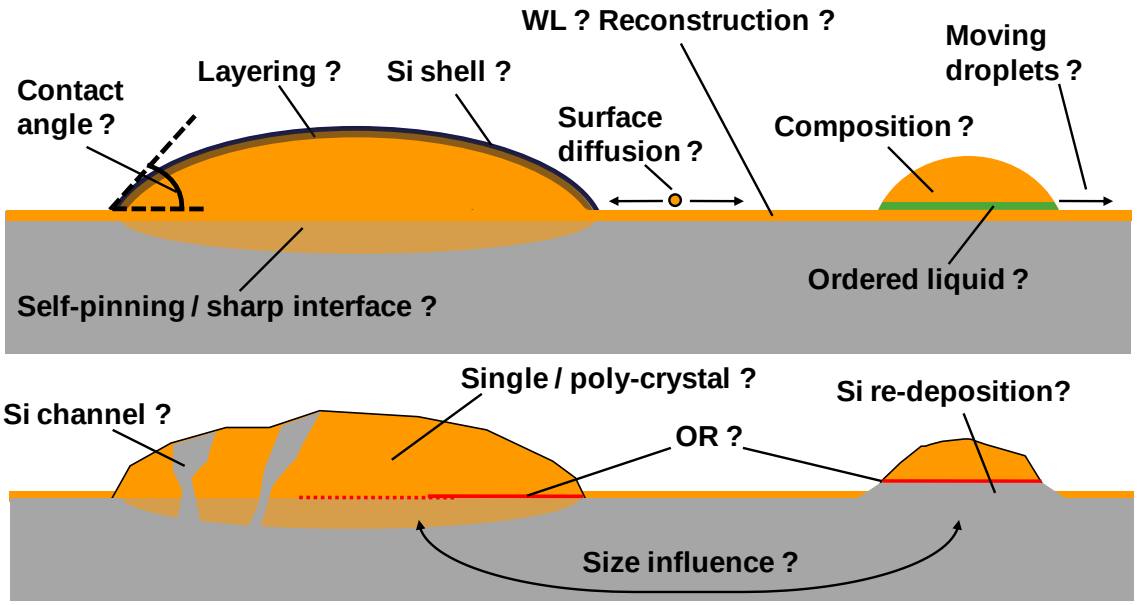

Figure VII.1 – Scheme of the different features that raise questions concerning the first stages of the VLS process. Some aspects concern the droplets (composition, layering, Si shell...), some others the free surface (surface diffusion, WL, reconstruction...) or the interface with the substrate (interface structure, ordered liquid...). The solidification process is also concerned (phase separation, creation of Si channel, Si redeposition at the interface and amount of supercooling) as well as the resulting structure (OR, crystalline structure). The overall process being maybe dependent on the size which itself depends on the deposited amount of material as well as on the annealing temperature (and on time).

literature, this aspect is controverted as flat interfaces and pinned droplets are both reported.

An ellipsometrical study has been performed on the Au/Si(111) system by Mümmler *et al.* who claimed that a 60 nm thick gold deposit forms a homogeneous single crystal film at RT [Mümmler and Wissmann, 1998]. With increasing temperatures, the film dewets and turns into droplets at 590 K (40 K below T_e). The mean sizes of the droplets/islands is about 5 μm and upon cooling, the solidification is recorded at 540 K. This study is, to our knowledge, the only one that reports such supercooling behaviour (ΔT =50 K) in the Au-Si(111) system. The amount of supercooling is equal to the one observed in our case for the Au-Si(001) system (section V.1.2), which is assumed to be a "classical" value as it has already been reported by Chen *et al.* in 1967 [Chen and Turnbull, 1967]. However this study does not give any information on the interface structure which is supposed to be one of the most relevant parameters to understand the supercooling effect, as stated in Chapter V.

Wakayama *et al.* carried out a gold deposit in UHV at 670 K on Si(111) substrates, resulting in direct formation of droplets. The TEM images revealed a sharp interface after deposition [Wakayama and Tanaka, 1997]. Then, one sample was exposed to air and put back in UHV whereas the other one was maintained in UHV. Both were then annealed at 1070 K for 30 min. After the cooling down to RT, the former sample displays gold islands embedded

in the Si substrate whereas the latter displays gold islands sitting at the tip of a Si base. The authors explain this effect by assuming that the Si equilibrium concentration in the droplets is adjusted by two different processes, depending on the nature of the free surface (between the droplets). In the sample not exposed to air, they supposed that the Si concentration is ensured by the diffusion of the Si surface atoms. Therefore the interface remains sharp and upon cooling, the Si atoms in excess are expelled below the droplet and form a little Si whisker. In the contrary, the sample exposed to air presents a polluted free surface which is assumed to prevent the surface diffusion of Si atoms. Thus, the Si concentration equilibrium is due to Si diffusion under the droplets and the islands are pinned.

A similar study has been performed by Ferralis *et al.* who reported a self-pinning process that takes place under the AuSi droplets [Ferralis *et al.*, 2008]. Although the AuSi droplets annealed only at T_e displayed a sharp interface, the ones annealed at higher temperatures (1100 K) showed deep depressions once the gold islands had been removed after solidification. The assumed process is also the readjustment of the chemical composition which has been measured to follow the liquidus line. The solidification process is obtained by quenching, which prevents any observation of the supercooling behaviour. However, the authors also performed an experiment during which the sample was slowly cooled down. They obtain similar results with no Si atoms refilling the depression and they do not mention any supercooling effect. In both cases the authors claim for phase separation with Si channels (as represented in Figure VII.1), which seem to be enhanced in the case of big droplets. These results are in contradiction with earlier observations of Swiech *et al.* who recorded the displacement of AuSi droplets at high temperatures (950 K) [Swiech *et al.*, 1991]. The displacement of the AuSi droplets has also been observed by Ressel *et al.* more recently [Ressel *et al.*, 2003]. This study focuses on the variation of the contact angle of the AuSi droplets as a function of temperature on either Si(001) or Si(111). In addition are reported displacements of the droplets by incorporation or dissolution of the Si atoms at the surface. The SEM images reveal that the droplets leave flat Si(111) terraces behind them, which claims for very flat interfaces. Another significant result is the observation of a constant contact angle ($43°$ [i]) between the droplets and the Si(111) surface for temperatures ranging from 670 K to 920 K and its sudden decrease when the sample is heated higher. In comparison, it decreases linearly with increasing temperature on Si(001). The authors conclude that this peculiar behaviour on Si(111) is more consistent with droplets presenting a flat interface. The abrupt change in the contact angle as well as in the shape of the droplet is discussed in terms of interface energies : at the edges of the droplets, a reconstruction transition takes place, which locally modifies the equilibrium. This explanation is supported by the fact that the contact angle

i. measured in the liquid phase.

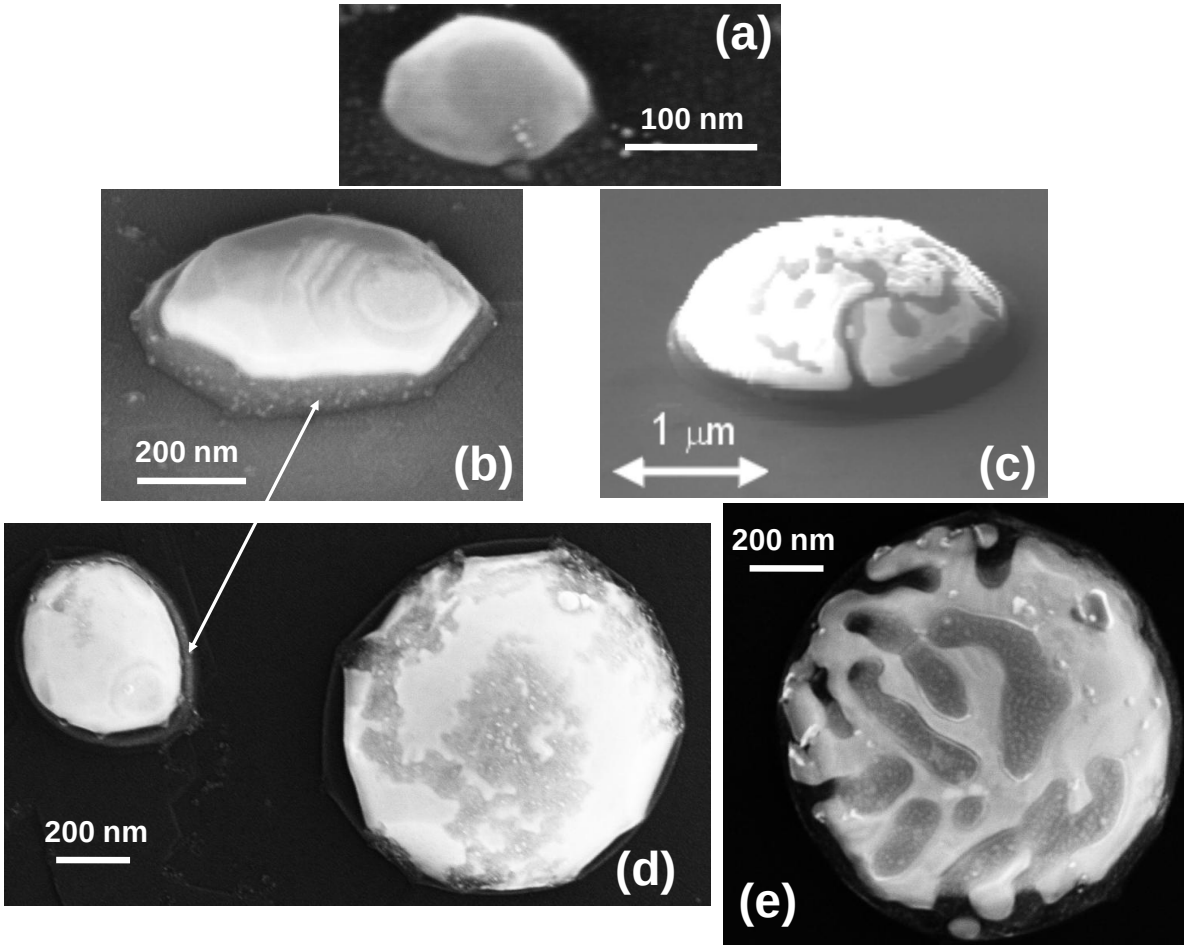

Figure VII.2 – SEM images of a typical island present on the Si(111) substrate after a deposit of (a) 5 ML of Au annealed at 670 K (b) 6 ML AuSi eutectic annealed at 720 K (c) 10 ML annealed at 1055 K (d) 30 ML of Au annealed at 940 K and (e) 10 ML [ii] of Au annealed at 940 K.

decreases linearly with temperature on the Si(001) surfaces for which no surface reconstruction is known to form. Figure VII.2 compares different SEM images obtained in this work in different experimental conditions ((a), (b), (d) and (e)) to the SEM images of an island reported by Ressel *et al.* ((c)) [Ressel *et al.*, 2003]. For each island a Si block is present at its base [iii]. For the sample in image (b), the idea was to reduce the potential formation of the depression under the droplet by co-depositing Au and Si in eutectic proportion. In this experiment, very similar results have been recorded compared to a pure gold deposit (in terms of surface reconstruction and supercooling effect). The resulting island displays a large Si base with what is supposed to be pure solid gold on top of it. In comparison, the island in image (c) obtained by Ressel *et al.* , which is by far the largest one, also displays a Si base but the upper part is composed of two phases. In bright is the Au phase whereas the Si forms dark channels. This kind of marbling solid structure has also been reported by Ferralis *et al.*

iii. Except for image (a), which corresponds to the smallest deposit and the lowest annealing temperature, onto which it is rather hard to distinguish.

[Ferralis *et al.*, 2008]. This seems to be also the case in our experiments when large islands are formed (image (d) right and image (e)). Therefore there might be a critical size value separating two solidification processes. If the droplet is smaller than the critical size, all the Si atoms solidify at the base, if it is larger, some of the Si atoms remain trapped in the liquid and solidify in channels.

Concerning the structure of the interface, our experiments support the idea of a flat interface between the islands and the substrate as presented by Ressel *et al.* instead of pinned islands as reported by Ferralis *et al.* . This is shown in the SEM images but it is also supported by X-ray diffraction results. Indeed, during the dewetting of the film we showed the change in the in-plane orientation relationship which has been explained using the CSL theory (see section III.2.2). This theory which seems to be relevant in the Au-Si case as well as in the Au-Ge and Al-Si systems can however be applied only if the two crystal lattices are assumed to be parallel, *i. e.* the interface is flat. In Chapter III, the Figure III.11 shows a *rocking-scan* on the Au(220) ring at RT after a melting-cooling cycle which displays the two characteristic peaks of the two principal ORs confirming the flatness of the interface after solidification.

The diverging results obtained in literature concerning the interface geometry are assumed to arise because of differences in the preparation of the surface. In the present work, the surface preparation is similar to that of Ressel *et al.* whereas Ferralis *et al.* deposit gold on a H-Si(111) surface [Ferralis *et al.*, 2007]. Consequently, despite the fact that Ferralis *et al.* suppose no difference between the two processes, we can legitimately think that the presence of H atoms at the surface can prevent the islands from moving or at least prevent the Si atoms of the surface from diffusing, as stated by Wakayama *et al.* [Wakayama and Tanaka, 1997]. The Si atoms are thus taken from under the droplets upon annealing resulting in the cavity and the pinned droplet. Moreover, Ferralis *et al.* use this property to study the surface diffusion of the gold atoms [Ferralis *et al.*, 2009]. The removal of the H atoms present between the droplets can be done by annealing the sample at 780 K. The measure of the gold spreading on Si(111) is achieved by recording the formation time of the $(\sqrt{3}\times\sqrt{3})$R30°Au that occurs by diffusion of Au atoms from the droplets to the newly bare surface similarly to what has been presented in the re-formation of the (6×6) reconstruction (see section IV.2.2). Another study confirms our assumption : Piscopiello *et al.* reported gold islands embedded in the Si(001) surface when annealing a thin gold film under a flux of N_2 and in the presence of residual O_2 [Piscopiello *et al.*, 2008]. The resulting in-plane epitaxial relationships are totally different than those found in the present study (see section V.1.3) which gives evidence of "cube on cube" epitaxy. This also explains why in one of our experiment, carried out on the ID01 beamline and for which UHV conditions could not be achieved, the surface did not display neither gold reconstruction nor supercooling effects.

The flatness of the interface implies that upon cooling, the Si atoms in excess are expelled out of the droplets leaving some flat terraces onto which the (6×6) is more likely to form [Ressel *et al.*, 2003; Swiech *et al.*, 1991]. Even if it is impossible to conclude that the (6×6) reconstruction can form below the droplets, we believe that the flat interface is more favourable to allow, at least locally, some similar structures that promote the ISRO in the liquid.

As we have seen that polluted surfaces suppress the surface diffusion of gold, it seems relevant to see if the (6×6) gold reconstruction, consisting in a thin adsorbed film spread all over the substrate, can also have an impact on the diffusion processes of the Si atoms.

Surfactant properties of the (6×6) reconstruction

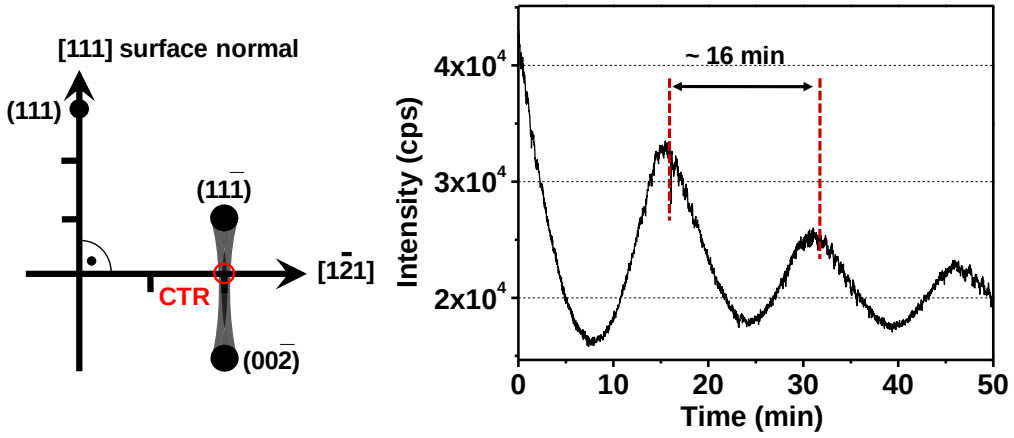

Figure VII.3 – left : Representation of the CTR, the red circle indicates where the intensity has been recorded. right : Variation of the CTR intensity as a function of time during the Si deposition.

Actually, the question was to know whether or not the (6×6) reconstruction could block, in some way, the Si atoms diffusion which would thus have an impact on the solidification process. To answer this, AuSi droplets were formed together with a (6×6) reconstruction as described in previous sections and cooled down to the supercooling regime at 600 K. The experiment consisted in recording the variation of intensity of a CTR as a function of time while Si atoms are added by MBE (see Figure VII.3). The recorded intensity displays periodic oscillations and the elapsed time between two maxima (∼16 min) corresponds to the completion of one Si monolayer [Feidenhans'l, 1989]. Figure VII.4 shows two *radial-scans* performed along the Si[1$\bar{1}$0] direction before and after the Si deposit. The two scans are identical reflecting that the layer-by-layer growth of the Si is possible even in the presence of the gold (6×6) reconstruction. This result is however not really surprising as it confirms that Au is an effective surfactant for Si (see section IV.2.2).

Thus, the liquid presents a sharp interface at the substrates' surface and can exchange Si

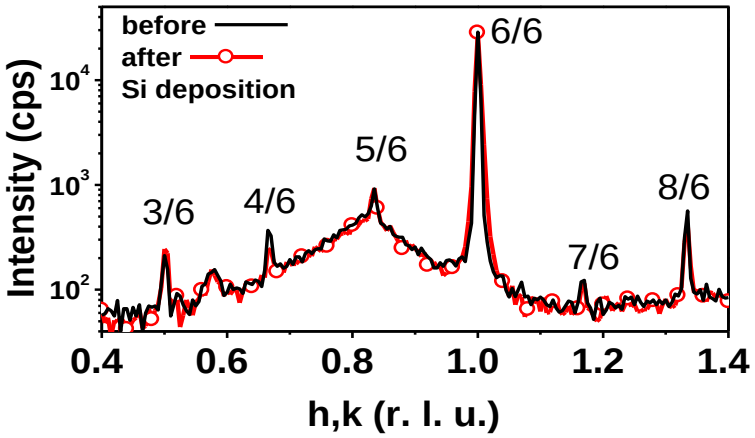

Figure VII.4 – *Radial-scans* performed along the Si[1$\bar{1}$0] azimuth before (black) and after the addition of Si in the presence of gold droplets together with a (6×6) reconstruction at 600 K.

atoms which are assumed to come from the surface. In addition, it is important to remind here that is has been shown in literature as well as in the present study that 2D Au-Si crystals can form at the liquid-vapour interface, either on (001) [Pinardi *et al.*, 2009] or (111) [Ressel *et al.*, 2000; Shpyrko *et al.*, 2006] surfaces. Moreover, we report in Figure V.11 the presence of a "liquid-rod" indicating the ordering of the liquid atoms at the liquid-substrate interface. This ordering revealed similarities in its structure with the (6×6) reconstruction layer which coexists with the AuSi droplets (see Figure V.10). With this description, one easily understands that the liquid state, through these experiments, is brought in very unusual conditions and thus reveals unexpected behaviour. The formation of the AuSi shell observed at the surface of the droplets can be legitimately supposed to be linked to the potential formation of silicides in this system prior to melting (see section III.1.2(c) and [Agnus, 2007]). The formation of islands with a silicide structure can not be ruled out even if no specific metastable AuSi phase can be distinguished in the light of our experiments. In addition to what has been presented above, the question concerning the size-dependence of the different processes makes the study even more complex.

Size of gold islands on Si(111) bare substrates

As already pointed out in the case of the resulting structures of the droplets after solidification, it seems that size can influence the different physical processes. Indeed, in our study of the epitaxial relationships, the dependence of the size of the grains toward the selected OR has been discussed (see section III.2.3(d)). In addition, the single or poly-crystalline structure of the islands as a function of their size has been reported in the PhD work of Agnus [Agnus, 2007] in good agreement with our comparison between GISAXS, GIXS and SEM results. Finally, in section V.4, we have pointed out that the influence of the (6×6) reconstruction is

enhanced when the surface/volume ratio is increased, *i. e.* when the droplets are small.

The control of the sizes of the catalytic droplets is a challenge as it controls the diameter of the NWs and therefore their properties. The present work did not aim to study quantitatively the parameters that control the size of the droplets. However, several experiments using different amounts of Au and different maximum annealing temperatures allowed us to compare, for example, the supercooling effect as function of the relative sizes of the droplets (see section V.4). Figure VII.5 shows the SEM images and the respective size distribution at RT for a 6 ML gold deposit annealed at a maximum of T_e ((a) and (c)) and for a 30 ML gold deposit annealed at a maximum of 940 K ((b) and (d)) on Si(111) surfaces.

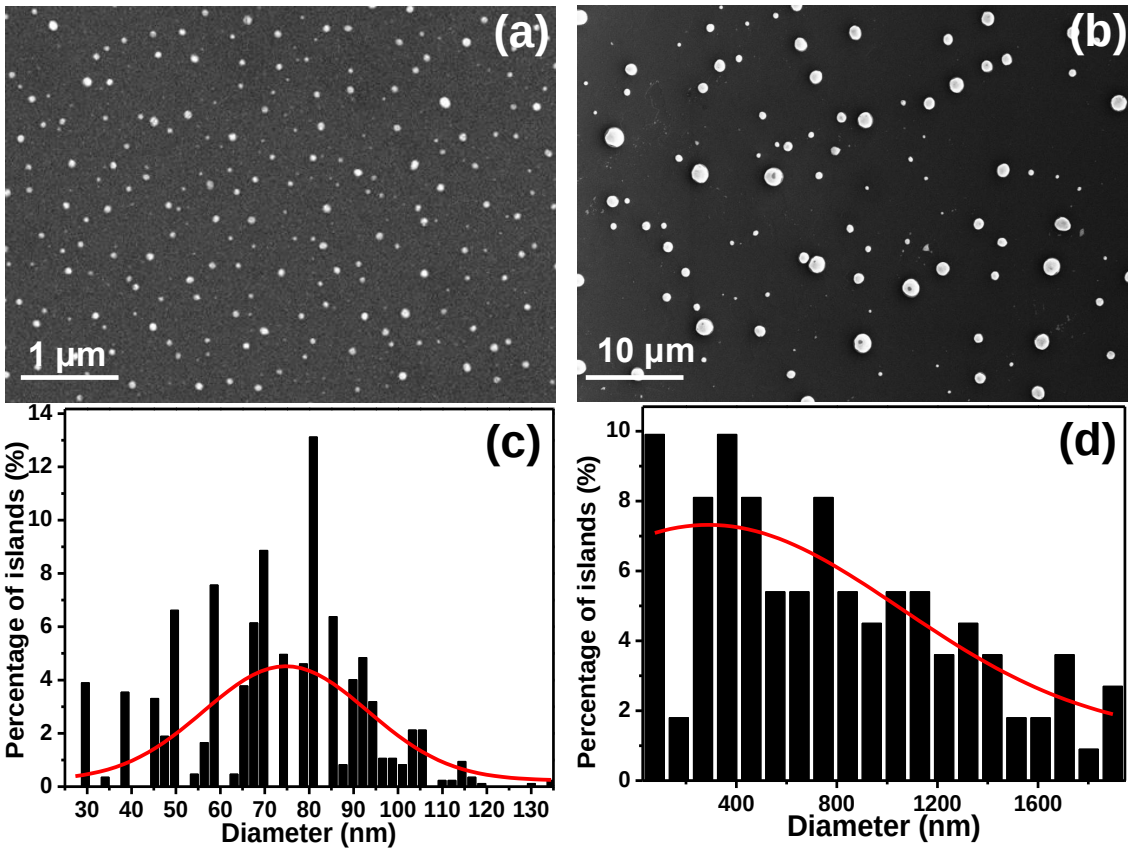

Figure VII.5 – SEM images of the resulting islands at RT after the deposition on Si(111) substrates of (a) 6 ML of Au annealed at T_e (b) 30 ML annealed at 940 K. (c) and (d) Respective size distributions.

The comparison between this two extreme cases shows a large difference of the mean size of about one order of magnitude. Despite a wide literature covering AuSi, it is only recently that quantitative studies on the details of the process of kinetics growth have been carried out [Ruffino and Grimaldi, 2010; Agnus, 2007]. In their study, Ruffino *et al.* performed measurement on the size of the Au islands as a function of the deposit and the annealing time at 873 K on Si(111). The authors conclude that at 873 K the growth process is governed by

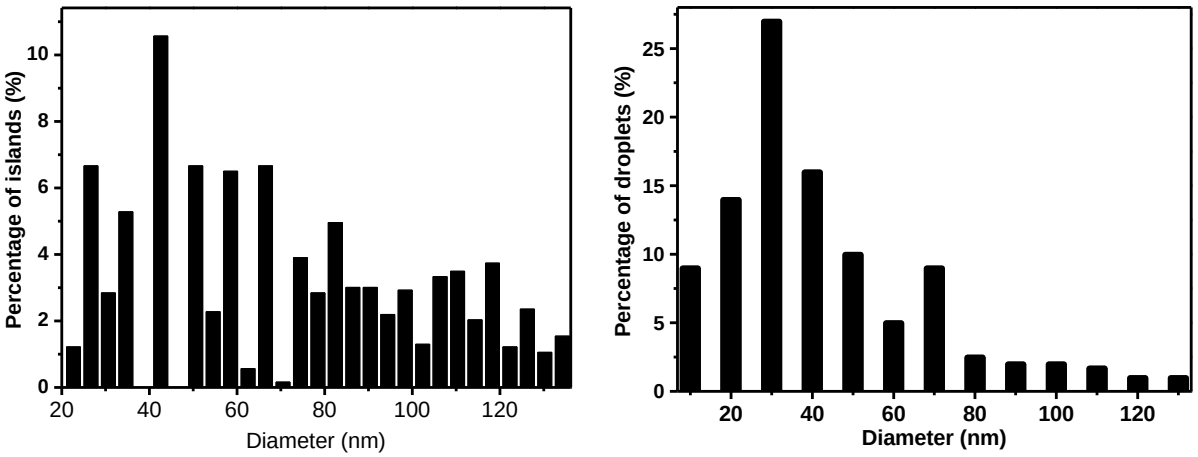

(a) (b)

Figure VII.6 – Size distribution of gold islands performed by the annealing at 670 K of (a) 5 ML on Si(111) and (b) 4 ML on Ge(111) [Porret *et al.*, 2011]

surface diffusion limited ripening with a surface diffusion coefficient of $8.2 \cdot 10^{-16}$ $m^{-2}.s^{-1}$ in good agreement with the measures of Ferralis *et al.* at this temperature [Ferralis *et al.*, 2009]. It is however worth to mention that the sizes and the formation processes can be strongly modified on vicinal surfaces as the atomic steps offer nucleation sites to the islands [Kirakosian *et al.*, 2001; Hibino and Watanabe, 2005; Agnus, 2007] .

Due to the fact that Si and Ge are very similar elements, the Au-Si and Au-Ge systems are often thought to be similar as well. Interestingly, gold islands obtained by the dewetting of a thin film deposited on Ge(111) display sizes similar to those obtained on a Si(111) surface. This can be seen in Figure VII.6 which compares the size distributions of gold islands obtained on Si(111) in this work and of gold islands obtained on Ge(111) in similar experimental conditions [Porret *et al.*, 2011]. This simple observation is not insignificant as several recent results give signs of large differences between the two eutectic systems as described below.

Cases of Au-Ge and Al-Si systems

As already presented in Figure I.25, the AuGe liquid alloy displays smaller concentration fluctuations than the AuSi liquid. Therefore a weaker tendency of the AuGe alloy to unmixing could be expected so that larger supercooling values should be observed. In this work, the largest measured supercooling in the case of Au-Ge(111) is 90 K (see section VI.1) whereas it is 130 K in the case of Au-Si(111) (see section V.2.2) for similar experimental conditions. Furthermore a mean supercooling value of 50 K (see section V.1.2) was found in the case of the Au-Si(001) system. These comparisons clearly highlight that the stabilization of the AuSi liquid on a specific Si(111) surface down to very low temperatures is surprising.

Contrary to the Au-Si system, unexpected supercooling and solidification behaviour of

the AuGe alloy has been reported in literature but the reasons of such behaviour still remain controversial [Adhikari *et al.*, 2006; Kodambaka *et al.*, 2007]. However, in these studies, the droplets are studied in the case of nanowires growth, *i. e.* under a flux of GeH_4 or Ge_2H_6 gas, the stabilization of the liquid state seems to be due to the growth flux itself that changes the equilibrium conditions. Therefore direct comparison with our experiments has to be done very carefully. Some other differences in physical properties between the two alloys were also pointed out in a recent study of Pershan *et al.* [Pershan *et al.*, 2009a]. Their study concerned the absence of a 2D crystal floating at the surface of the respective liquid (in contrary to the AuSi liquid). The authors discuss this feature by investigating the influence of the difference in enthalpy of mixing of the two alloys (-30 kJ.mol^{-1} for AuSi and -21.5 kJ.mol^{-1} for AuGe) but can not conclude with a satisfactory explanation. In addition the AuSi eutectic liquid is known to form amorphous structures by quenching [Klement *et al.*, 1960] whereas the AuGe liquid rather forms metastable structures [Okamoto and Massalski, 1984] reflecting quite different solidification processes. Therefore, even if it seems attractive at first glance, the comparison between the two systems remains quite risky and requires further experiments.

The study of the Al-Si system has been motivated by its potential substitution to Au as a catalyst. The report of the growth of Si nanowires with Al under the eutectic temperature has been reported to be VSS process [Wang *et al.*, 2006]. However, more recent studies report that Si nanowires can be grown through a VLS process down to 790 K but specific thermal history ("pregrowth" annealing) as well as specific growth flux have to be respected [Wacaser *et al.*, 2009; Choi *et al.*, 2011]. In the present work, the experiments performed on the Al-Si(111) system, compared to Au-Si(111), led to similar results in terms of dewetting but the recorded supercooling value is of 60 K for this system. Although it has been reported that the interface between the AlSi liquid and a Si(111) surface exhibits an atomically flat transition layer [Arai *et al.*, 2000], such ordering can not be said to occur in our experiments. The AlSi eutectic liquid can thus be significantly supercooled, however to compare to the AuSi system, it is rather relevant to use a normalized supercooling value : $\Delta T_n = \Delta T/T_e$. For AlSi $\Delta T_n = 0.11$ whereas it comes $\Delta T_n = 0.21$ for AuSi. Comparatively, the supercooling effect is therefore much larger in the AuSi system.

In the this manuscript we have presented the supercooling effect by giving the solidification temperature T_s. For comparisons within several experiments on the same system, we have used the eutectic temperature T_e as a reference temperature and in extension, expressed in certain cases the supercooling value as $\Delta T = T_e - T_s$. The normalized value given just above was also expressed using the eutectic point as the reference. However, even if the absolute value of the lowest recorded solidification temperature (500 K) is very low and unexpected for the Au-Si system, a ΔT_n of 0.21 is important but not extraordinary [Vinet *et al.*, 2002].

Therefore, if one really wants to realize in what extend the supercooling amount recorded in this work in the Au-Si system is important, a study of the sub-eutectic region is necessary.

The sub-eutectic region and the "real" supercooling value

In Figure VII.7 is plotted an extract from the bulk Au-Si phase diagram with representations of the melting and solidification cycles of the AuSi islands in the case of a Si(111)-(6×6)Au reconstructed sample.

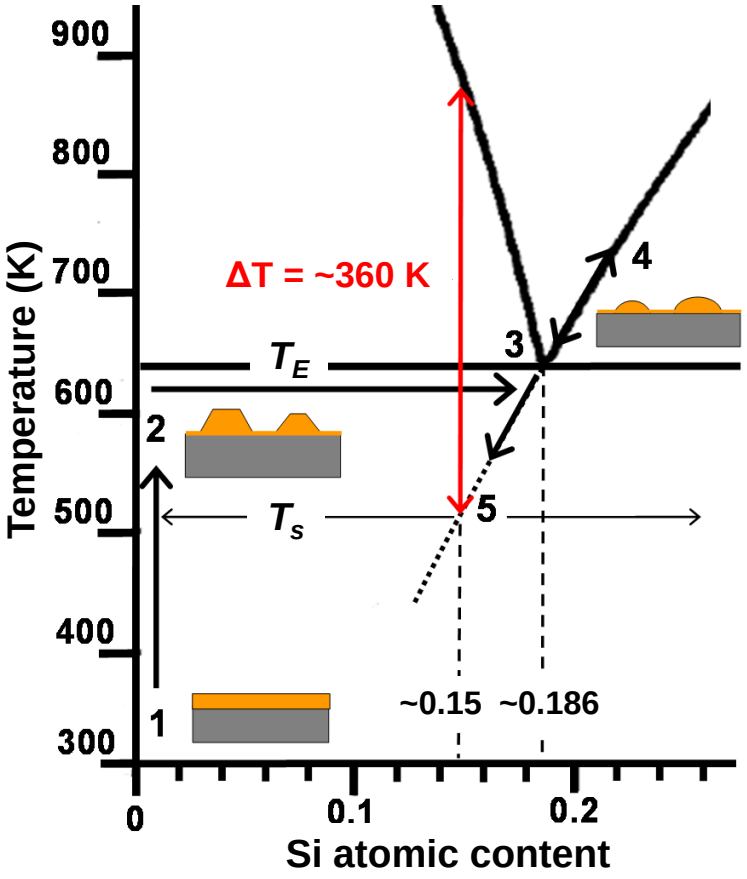

Figure VII.7 – Extract from the bulk Au-Si phase diagram together with representations of the melting and solidification cycles of AuSi islands on an Si(111)-(6×6)Au reconstructed surface. The numbers 1 to 5 refer to successive experimental steps, and the large black arrows indicate the pathways followed by the islands during heating/cooling cycles.

The numbers 1 to 5 refer to the successive experimental steps studied throughout this work [iv]. Above T_e, either on heating or cooling, the liquid is expected to follow the Si liquidus line. If the sample is annealed at 720 K for instance, the maximum Si content in the droplets reaches 22 at.%. Upon cooling, the Si atoms are expelled from the droplets and at T_e, the concentration reaches the eutectic one. Below T_e, the concentration is assumed to follow the metastable Si liquidus represented by the extrapolated dotted line. Therefore, at the lowest

iv. Deposit, dewetting, melting, cooling down, solidification.

recorded solidification temperature (T_s 510 K), the composition of the droplet corresponds to ∼15 at.% Si and the degree of supercooling represented by the red arrow has to be measured between the solidification point and the Au liquidus above T_e. The supercooling value is therefore ∼360 K and corresponds to a ΔT_n of 0.42 which is a very large value highlighting once again the particular behaviour of the AuSi eutectic liquid in this work.

Complementary information provided by "closed" systems

In the major part of this work, the experiments on Au-Si, Au-Ge and Al-Si alloys have been performed in what can be called "open" systems, *i. e.* in contact with a SC reservoir. It underlines the fact that the amount of the SC phase (Si or Ge) in the droplets can evolve with temperature (and time) and also modify the equilibrium conditions such as the structure and the energy of the surfaces/interfaces. Naively, we decided to perform the same kind of experiments on "inert" substrates to suppress these effects by working with "closed" system.

In the case of AuSi on a SiO_2 surface, the most interesting result concerns the very wide temperature range into which the solidification or the melting process take place (see section VI.3.1). Indeed, depending on the Au peak under consideration, the supercooling value varies from 60 K to 120 K. In addition, unassigned peaks are recorded after the solidification process which might correspond to the appearance of silicide phases.

For AuGe on either SiO_2 or Al_2O_3, we had to face a problem of concentration which can not be ensured to be the eutectic one. In both experiments we had to proceed to the addition of Ge at a temperature higher than the eutectic one and record the disappearance of the Au peaks at the same time. In the case of Al_2O_3 it even seems that not all the islands have been melted. However on the SiO_2 substrates, the appearance and the disappearance of the Au(220) peak are recorded over a wide temperature range whereas the Au(111) peak (as well as the γ peaks) appears at a very low temperature of 500 K but also disappears well below T_e (at 570 K) upon heating. On Al_2O_3, the Au(220) intensity varies with temperature but is still present even when heating the sample 60 K above T_e, the study of the other peaks (Au(111) and γ) could make us conclude to a supercooling value of 220 K, with a segregation process.

Clearly these experiments display supercooling and solidification processes that are not fully understood. The important problem seems to be the control of the concentration which can lead to different behaviour for the different droplets on the same substrate. A strong temperature gradient over the Al_2O_3 surface can also not be excluded as this particular sample had to be mounted in a specific way. In addition, the calibration technique of the pyrometer on this surface can be at the origin of larger uncertainties on the temperature values.

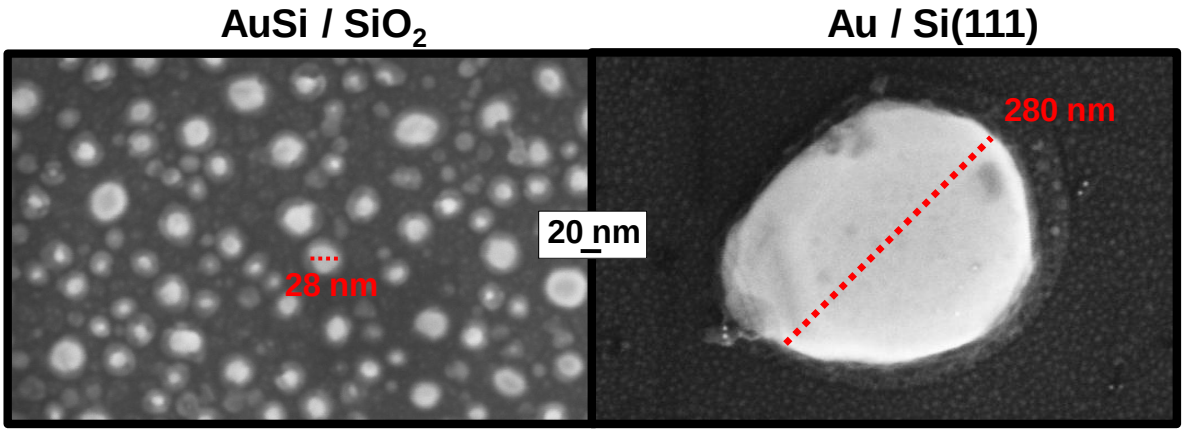

Figure VII.8 – Left : SEM picture of the resulting islands that formed during the experiment presented in section VI.3.1 concerning the 6 ML AuSi deposit on SiO_2 substrates annealed at 690 K. Right : SEM picture of the resulting islands that formed during a typical experiment with a deposit of 6 ML of Au on a Si(111) surface annealed at 720 K. The scale bar is the same for the two images to highlight the size difference between the two experiments.

The left hand side of Figure VII.8 shows a SEM picture of the resulting islands formed during the experiment of AuSi on SiO_2. The mean size of the islands is 20 nm. Surprisingly it is about ten times smaller than a typical island that forms on a Si(111) substrate in similar conditions (right hand side of Figure VII.8). The sizes are of the same order for AuGe islands on SiO_2 and even smaller on Al_2O_3 (around 10 nm). As the diffusion length is assumed to be larger on perfectly clean oxide surfaces, this result may arise because of not properly prepared surfaces : there must be defects such as CO or HO adsorbed species preventing the surface diffusion. The difference in size observed between the "open" and "closed" system might explain the difference in supercooling behaviour as it can modify the contact angle (see section III.1.2) and thus the solidification process (see Figure I.19) [v]. It can also be at the origin of the melting the AuSi islands below T_e (see Figure VI.15(a)). Indeed, very small crystallites are known to melt below their theoretical melting point. This effect could not be studied in more details here but further experiment following this idea would be interesting to complete the study of these intriguing eutectic liquids. However the important aspects of this work remain the liquid and surface/interface structures that are believed to be the key parameters.

Indeed, the relevant question is not to know whether or not the structure of the substrate has an influence on the liquid state and the solidification but rather *how* it influences them. Figure VII.9 is the reciprocal space map of the AuGe liquid on the Al_2O_3 substrate recorded at 600 K, in the supercooled state.

v. The alumina substrates were historically used to increase the contact angle and get closer to homogeneous nucleation conditions [Turnbull and Cech, 1950; Perepezko and Paik, 1984].

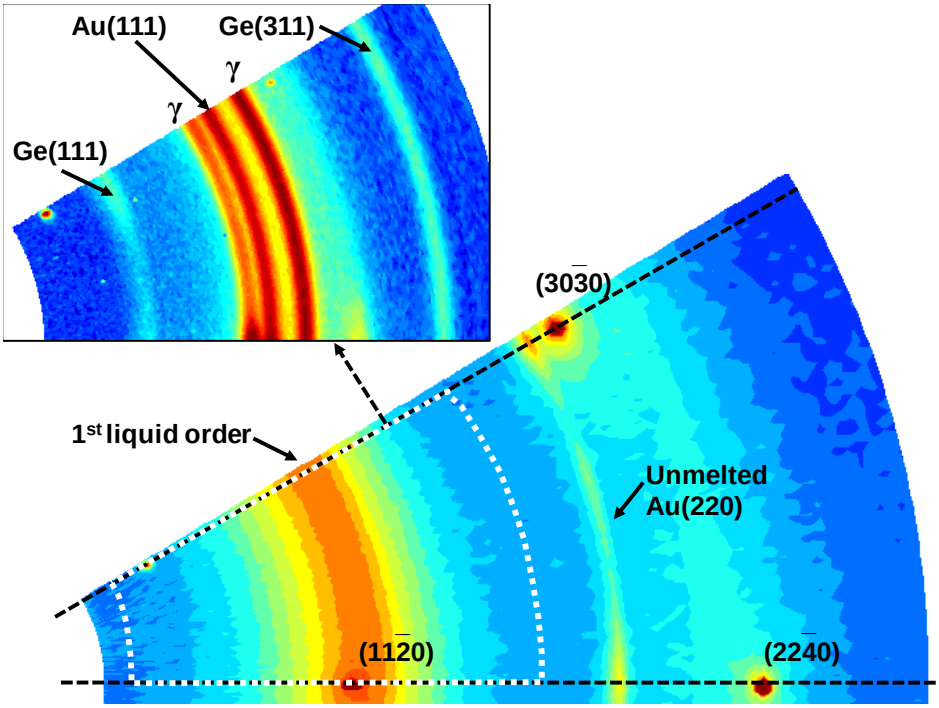

Figure VII.9 – Reciprocal space map covering 30° of reciprocal space recorded for AuGe on Al_2O_3 at 600 K. The red colors correspond to high intensities whereas blue correspond to low ones and yellow to intermediate ones. This map displays the Al_2O_3 monocrystal Bragg peaks and CTRs. The intense ring corresponds to the first order of the liquid structure factor. The inset represents the sector surrounded with the white-dashed line in the solid state after solidification.

For this liquid, no lateral variation of the intensity is recorded which indicates a normal isotropic structure of the liquid. In inset is plotted the part of the map surrounded by the white-dashed line but at RT, after solidification of the system. Compared to the solid map recorded in the case of Au on Ge(111) (see Figure VI.6), the Debye-Scherrer rings display a perfectly constant distribution of the intensity (both for Au and Ge). This reveals that the resulting solid Au (and Ge) consists in untextured polycrystalline grains (*i. e.* a powder). In other words, the solidification of AuGe on an Al_2O_3 surface which seems to undergo very large supercooling, results in a solid structure that does not share strong epitaxial relationship with the substrate. In comparison, the weaker supercooling behaviour of the same liquid recorded on Ge(111) was followed by a solid structure that displayed strong in-plane orientation relationships.

In the light of these numerous experiments, there is no doubt that the liquid structure and the supercooling behaviour strongly depends on the structure of the substrate's surface. A surface can act as a nucleant while another do not help solidification.

For the Au-Si system, it is even more relevant when comparing the two different "open" systems that are Au on Si(001) and Au on Si(111). The Si(001) substrate, onto which very low

supercooling was recorded, presents a clear parallel in-plane epitaxy after solidification of the droplets (see Figure V.3). It reveals that the Si(001) substrate is a good nucleation surface for both Si (which is not surprising) and Au, the AuSi alloyed droplets undergoing unmixing due to concentration fluctuations. On the Si(111) substrate, the supercooling effect is enhanced and the study of the in-plane orientation relationships between the solidified islands and the Si surface shows that it is less easy for the two crystals to match their respective structures. Moreover, the supercooling effect is even more enhanced in the presence of the (6×6) surface reconstruction, and at the same time, the ordering of the liquid close to the interface is observed. The parallel studies of this Si(111)-(6×6)Au reconstruction which locally displays pentagonal arrangement, the ordering of the liquid and the simulation results make us believe that the flat interface between the liquid and the Si(111) surface promote icosahedral short range order that would be at the origin of the lowering of the concentration fluctuations and the stabilization of the liquid phase.

Conclusion and Perspectives

The aim of this PhD was to characterize the behaviour of the AuSi eutectic liquid droplets in interaction with Si(111) substrates. The problem has been tackled by studying, *in-situ* and using the synchrotron radiation mostly in the GIXS geometry, the different steps composing the overall process : the deposit, the dewetting, the melting, the annealing, the formation of surface structures and the solidification.

We have shown that at RT, the deposition of several monolayers (∼7 ML) results in the formation of a flat polycrystalline gold film, with a majority of the grains displaying however an epitaxial relationship with Au and Si lattices being parallel. The very few experiments carried out with small deposits (∼2 ML) showed that at RT the gold can be assumed to be alloyed to the substrate with the possibility of forming some AuSi phases. With further deposition, the film grows with the appearance of crystalline gold grains forming a sharp interface with the Si substrate. If the deposit is carried out at higher temperatures, typically 570 K, the equilibrium conditions are modified and the growth follows a Stranski-Krastanow mode.

With the increase of the temperature, the film is subjected to small amplitude fluctuations roughening its surface. The dewetting process is found to take place when the temperature of 560 K is reached : the film transforms into islands. At the same time, due to differing thermal expansions of the two materials with the annealing, the mismatch values between the two lattices evolve and the epitaxial relationships are found to change. This effect has been explained using the CSL theory. The most stable configuration experimentally measured around 600 K corresponds to the Au(111) planes parallel to the Si(111) substrate turned by 19° with respect to the parallel epitaxy. This configuration is recovered after melting and solidification of the droplets. When the temperature equals the eutectic temperature T_e we observe the melting of the islands attesting of the diffusion of the Si atoms to adjust the concentration with respect to the eutectic one.

In our experiments, the Si atoms needed to adjust the droplets' concentration are believed to be provided by surface diffusion. Indeed, several measurements show that the surface diffusion of Si is enhanced due to the surfactant properties of the wetting layer of gold. Moreover, this wetting layer is found to induce two surface reconstructions : the Si(111)-(6×6)Au and the Si(111)-($\sqrt{3}\times\sqrt{3}$)R30°Au . The transition between the two is reversible and takes place around 700 K. The quantitative analysis of the (6×6) reconstruction has revealed that this latter presents a very specific structure which is composed of two domains and contains trimers and pentagons.

In addition to the formation of a AuSi 2D crystal at the surface of the droplets, the cooling experiments have revealed that the supercooling behaviour is influenced by the orientation of the substrates as well as by the surface reconstructions. The largest supercooling value has

been measured with a Si(111)-(6×6)Au reconstructed sample, the smallest on the Si(001) substrate, the Si(111)-($\sqrt{3}\times\sqrt{3}$)R30°Au being intermediate. In addition, in the case of the Si(111)-(6×6)Au reconstructed surface, the AuSi liquid revealed an ordering at the interface with the substrate. This liquid also seems to present structural similarities with the (6×6) reconstruction, the pentagonal arrangement, that could stabilize the liquid state down to very low temperatures.

The Au-Ge(111) and Al-Si(111) systems have also been studied. Although the temperature control below 450 K is quite uneasy, it seems that the growth of Au on Ge(111) follows a Stranski-Krastanow mode with the wetting layer inducing a ($\sqrt{3}\times\sqrt{3}$)R30° reconstruction. The in-plane orientation relationships differ from those measured in the Au-Si(111) system but can also be explained using the CSL theory. The Al-Si(111) case is more similar to the Au-Si(111) in terms of dewetting process and epitaxial relationships but no surface reconstruction has been recorded. Concerning the supercooling behaviour of both systems, the measured values are not as surprising as in the Au-Si(111) system. Moreover, it is believed that the comparison between the different systems concerning the liquid behaviour is still premature and requires further experiments as well as some simulation investigations. The role of simulations is supposed to be a key point in our understanding of these eutectic alloys in the future.

This investigation of the Au-Si system and more generally of metal-SC systems, even if it is restrained to the case of nanometric droplets, has brought answers to several questions concerning the structure and the behaviour of liquid catalysts. There are however still some aspects that are believed to require further studies to go beyond the current knowledge. The most important one seems to be by far the question concerning the existence or not of a long-range ordered reconstruction at the substrate-droplet interface. The best way to answer this question would be the investigation of a single island. This could be done using a nano-sized beam. Indeed, with a beam of the order of the island's size, by placing the detector on a (6×6) reflection and at the same time scanning the sample, one could record the intensity variation as a function of the position of the beam on the surface. The position of the islands at the surface could also be determined using similar idea by placing the detector on a gold Bragg peak or by using the fluorescence signal. With still the same idea, it would be possible to study the epitaxial relationships or the crystalline structures of the islands as a function of their sizes.

However, the will of characterizing the influence of the size on the structural/morphological features comes from the fact that the dewetting of a thin gold film on a nominal Si substrate results in particles with characteristics presenting a large distribution. Ideally, a solution is

to find a way to form very identical particles homogeneously spread over the substrate. In this way, the characterization of a specific feature can be done using a wide spot that lights several particles which are assumed to behave in the same way. A nice sample to do so is the use of patterned substrates that allows to choose the size as well as the position of the particles on the substrate. The use of patterned substrates combined to *in-situ* studies of the growth of nanowires (through CVD) is the next step to go further in the understanding of such systems. A nice experiment would be the study of the supercooling in AuSi droplets at the tip of nanowires grown on a patterned substrate. In the one hand, these kinds of experiments are performed in a constrained environment but in the other hand, they ensure a better reproducibility as well as a stronger control of the parameters.

In addition to all this, a very important aspect still remains our incapacity to measure the concentration in the droplets. Above T_e, it is reasonably assumed to follow the Si liquidus line, however the question remains open when cooling down below T_e in the supercooling regime into which the formation of metastable solid phases can not be excluded.

Beyond the improvement of our knowledge on the behaviour of supercooled liquids, the understanding of the physical processes arising in eutectic liquid is very important to have a better control on the catalytic reactions. The improvement of the control of the growth parameters would lead to the possibility of creating more complex objects. Moreover, as the characteristics of the SC nanowires strongly depend on the experimental conditions such as the temperature, the composition and the deposition flux, the possibility of growing nanowires well below the eutectic temperature thus allows to imagine the growth of nanowires with new morphologies and structures and therefore, new properties.

Annexe : Structure factors dataset and model

Table 1 – List of the experimental structure factors of the reflections (using the Miller indexes in the reciprocal unit cell of the (6×6) reconstruction), the total error σ, the corresponding calculated structure factor values and the partial χ^2 .

h	k	l	F_{data}	σ	F_{model}	χ^2
1	1	0.096	22.49	1.11	21.24	1.26
2	1	-0.096	12.39	1.06	12.07	0.09
2	1	0.096	13.82	1.11	12.07	2.48
2	2	0.07	167.74	7.46	169.76	0.07
2	2	0.096	185.62	8.43	169.75	3.54
3	0	-0.096	21.95	1.12	20.96	0.78
3	0	0.096	22.60	1.31	20.96	1.57
3	1	-0.096	30.02	1.53	29.68	0.05
3	1	0.096	29.52	1.61	29.68	0.01
3	2	-0.096	25.71	1.58	24.53	0.56
3	2	0.096	24.72	1.57	24.53	0.02
3	3	0.096	73.46	3.49	74.31	0.06
4	0	-0.096	12.91	1.74	13.65	0.18
4	0	0.096	14.03	1.66	13.65	0.05
4	1	-0.096	69.23	3.44	66.27	0.74
4	1	0.096	67.27	3.35	66.27	0.09
4	2	-0.096	17.66	2.07	22.28	4.99
4	2	0.096	19.07	2.07	22.28	2.41
4	3	-0.096	121.37	6.01	131.13	2.64
4	3	0.096	123.30	6.10	131.13	1.65
4	4	0.096	72.80	3.54	66.42	3.25
5	0	-0.096	16.35	2.02	17.79	0.51
5	0	0.096	17.76	2.11	17.79	0.00
5	1	-0.096	46.58	2.36	45.58	0.18
5	1	0.096	46.34	2.50	45.58	0.09
5	2	-0.096	48.41	2.63	51.87	1.73
5	2	0.096	48.57	2.87	51.87	1.32
5	3	-0.096	92.95	4.66	87.85	1.20
5	3	0.096	91.78	5.01	87.85	0.62
5	4	-0.096	24.17	3.61	26.45	0.40
5	4	0.096	23.67	3.90	26.45	0.51
5	5	0.096	152.17	7.55	154.97	0.14
6	1	-0.096	46.55	2.62	43.75	1.14
6	1	0.096	47.24	2.88	43.75	1.47
6	2	-0.096	47.13	2.83	41.81	3.54
6	2	0.096	45.92	3.05	41.81	1.82
6	3	-0.096	129.66	6.44	134.13	0.48
6	3	0.096	130.89	7.05	134.13	0.21
6	4	-0.096	69.83	4.09	69.29	0.02
6	4	0.096	68.13	4.39	69.29	0.07
6	5	-0.096	90.98	5.29	84.16	1.66
6	5	0.096	90.01	5.23	84.16	1.25
7	0	-0.096	15.59	5.04	13.56	0.16
7	0	0.096	13.06	5.68	13.56	0.01
7	1	-0.096	73.45	3.83	78.85	1.99
7	1	0.096	72.71	4.12	78.85	2.22
7	2	-0.096	239.07	11.76	269.82	6.84
7	2	0.096	246.57	13.13	269.82	3.14
7	3	-0.096	170.73	8.44	175.29	0.29
7	3	0.096	169.45	9.09	175.29	0.41
7	4	-0.096	79.50	5.25	75.35	0.62
7	4	0.096	71.11	5.58	75.35	0.58
7	5	-0.096	107.89	6.07	99.96	1.71
7	5	0.096	107.91	6.09	99.96	1.71
7	6	-0.096	41.84	4.36	33.63	3.54
7	6	0.096	42.77	4.25	33.63	4.62
7	7	0.096	66.72	3.82	64.32	0.40
8	0	-0.096	113.77	5.71	115.41	0.08
8	0	0.096	111.09	6.08	115.41	0.50
8	1	-0.096	242.16	12.16	252.27	0.69
8	1	0.096	252.36	13.68	252.27	0.00
8	2	-0.096	252.16	12.39	191.91	23.64
8	2	0.096	255.23	13.59	191.91	21.71
8	3	-0.096	78.65	8.95	37.56	21.08

h	k	l	F_{data}	σ	F_{model}	χ^2	h	k	l	F_{data}	σ	F_{model}	χ^2
8	3	0.096	68.64	7.47	37.56	17.31	10	2	-0.096	30.08	4.21	35.49	1.65
8	4	-0.096	37.84	3.88	42.52	1.45	10	2	0.096	32.57	4.17	35.49	0.49
8	4	0.096	37.22	4.33	42.52	1.50	10	3	-0.096	46.83	3.50	44.18	0.58
8	5	-0.096	39.75	4.07	39.82	0.00	10	3	0.096	42.64	3.82	44.18	0.16
8	5	0.096	37.65	4.12	39.82	0.28	10	4	-0.096	58.06	4.06	59.03	0.06
8	6	-0.096	30.06	4.87	28.48	0.11	10	4	0.096	61.79	4.13	59.03	0.45
8	6	0.096	29.99	4.92	28.48	0.09	10	5	-0.096	69.33	4.59	73.71	0.91
8	7	-0.096	34.00	5.63	43.17	2.65	10	5	0.096	71.50	4.64	73.71	0.23
8	7	0.096	38.88	5.06	43.17	0.72	10	6	-0.096	116.25	6.80	115.97	0.00
9	0	-0.096	198.74	9.79	198.79	0.00	10	6	0.096	115.76	6.77	115.97	0.00
9	0	-0.07	178.59	8.81	198.80	5.26	10	7	-0.096	108.08	6.21	110.07	0.10
9	0	0.07	178.45	8.81	198.80	5.33	10	7	0.096	110.67	6.34	110.07	0.01
9	0	0.096	196.82	10.52	198.79	0.04	10	8	-0.096	57.31	4.82	56.86	0.01
9	1	-0.096	109.44	5.57	113.26	0.47	10	8	0.096	57.39	4.71	56.86	0.01
9	1	0.096	108.84	6.03	113.26	0.54	10	9	-0.096	76.57	5.31	80.66	0.59
9	2	-0.096	62.75	3.71	60.72	0.30	10	9	0.096	75.52	5.23	80.66	0.97
9	2	0.096	63.86	4.05	60.72	0.60	10	10	0.096	67.49	4.26	55.72	7.63
9	3	-0.096	26.69	4.67	26.93	0.00	11	0	-0.096	34.69	3.58	31.84	0.63
9	3	0.096	22.38	6.23	26.93	0.53	11	0	0.096	35.10	3.87	31.84	0.71
9	4	-0.096	54.19	3.89	53.54	0.03	11	1	-0.096	55.00	3.50	53.82	0.11
9	4	0.096	48.48	3.84	53.54	1.73	11	1	0.096	52.82	3.81	53.82	0.07
9	5	-0.096	27.06	5.09	30.07	0.35	11	2	-0.096	40.50	3.89	44.57	1.10
9	5	0.096	28.95	4.79	30.07	0.05	11	2	0.096	40.80	3.90	44.57	0.93
9	6	-0.096	42.47	4.46	44.92	0.30	11	3	-0.096	43.83	4.07	41.90	0.23
9	6	0.096	44.69	4.32	44.92	0.00	11	3	0.096	43.04	4.14	41.90	0.08
9	7	-0.096	198.48	11.46	182.99	1.83	11	4	-0.096	58.12	4.61	56.81	0.08
9	7	0.096	203.89	11.63	182.99	3.23	11	4	0.096	60.54	4.58	56.81	0.66
9	8	-0.096	59.63	4.70	56.77	0.37	11	5	-0.096	139.02	7.71	150.14	2.08
9	8	0.096	58.67	4.66	56.77	0.17	11	5	0.096	141.64	7.84	150.14	1.18
9	9	0.07	80.06	3.93	81.99	0.24	11	6	-0.096	88.53	5.43	85.62	0.29
9	9	0.096	88.24	4.86	81.98	1.66	11	6	0.096	89.66	5.51	85.62	0.54
10	0	-0.096	60.58	3.74	62.46	0.25	11	7	-0.096	83.70	5.34	82.38	0.06
10	0	0.096	59.12	4.03	62.46	0.69	11	7	0.096	85.08	5.32	82.38	0.26
10	1	-0.096	73.34	4.02	75.73	0.35	11	8	-0.096	31.48	7.50	31.39	0.00
10	1	0.096	72.38	4.32	75.73	0.60	11	8	0.096	31.19	7.11	31.39	0.00

h	k	l	F_{data}	σ	F_{model}	χ^2	h	k	l	F_{data}	σ	F_{model}	χ^2
11	9	-0.096	61.10	4.90	61.82	0.02	13	6	0.096	32.96	9.54	34.03	0.01
11	9	0.096	61.60	4.77	61.82	0.00	13	7	-0.096	47.14	5.35	40.13	1.72
11	10	-0.096	42.54	5.46	39.06	0.41	13	7	0.096	51.16	5.01	40.13	4.85
11	10	0.096	41.27	5.48	39.06	0.16	13	8	-0.096	78.80	5.34	77.04	0.11
11	11	0.096	55.06	4.52	51.58	0.59	13	8	0.096	77.47	5.23	77.04	0.01
12	1	-0.096	38.23	4.12	38.18	0.00	13	9	-0.096	84.11	5.55	73.41	3.72
12	1	0.096	37.55	4.20	38.18	0.02	13	9	0.096	82.24	5.44	73.41	2.64
12	2	-0.096	28.04	5.69	33.55	0.94	13	10	-0.096	15.60	11.09	25.65	0.82
12	2	0.096	31.34	5.12	33.55	0.19	13	10	0.096	23.20	12.40	25.65	0.04
12	4	-0.096	46.90	4.86	48.76	0.15	13	11	-0.096	4.11	15.62	39.36	5.09
12	4	0.096	46.35	4.83	48.76	0.25	13	12	-0.096	47.36	7.75	48.27	0.01
12	5	-0.096	88.06	5.44	85.35	0.25	13	12	0.096	37.95	9.22	48.27	1.25
12	5	0.096	86.87	5.33	85.35	0.08	13	13	0.096	74.87	4.89	61.01	8.03
12	7	-0.096	23.04	11.93	31.55	0.51	14	0	-0.096	110.61	6.47	117.99	1.30
12	7	0.096	26.16	8.88	31.55	0.37	14	0	0.096	109.53	5.80	117.99	2.13
12	8	-0.096	63.97	4.98	68.85	0.96	14	1	-0.096	121.19	6.80	130.98	2.07
12	8	0.096	63.30	4.82	68.85	1.32	14	1	0.096	121.71	6.82	130.98	1.85
12	9	-0.096	36.39	6.27	37.72	0.04	14	2	-0.096	128.19	7.17	111.58	5.37
12	9	0.096	35.64	6.09	37.72	0.12	14	2	-0.07	115.12	5.95	111.58	0.35
12	10	-0.096	59.34	5.29	52.43	1.71	14	2	0.07	109.02	5.69	111.58	0.20
12	10	0.096	59.13	5.22	52.43	1.65	14	2	0.096	119.76	6.73	111.58	1.48
12	11	-0.096	33.76	9.71	32.03	0.03	14	3	-0.096	93.50	5.70	95.38	0.11
12	11	0.096	24.12	11.64	32.03	0.46	14	3	0.096	90.73	5.55	95.38	0.70
13	0	-0.096	30.95	5.04	26.06	0.94	14	4	-0.096	75.65	5.61	80.59	0.77
13	0	0.096	30.68	5.07	26.06	0.83	14	4	0.096	76.70	5.46	80.59	0.51
13	1	-0.096	37.68	5.20	45.09	2.03	14	5	0.096	19.92	16.64	9.93	0.36
13	1	0.096	40.89	4.91	45.09	0.73	14	6	-0.096	79.03	5.27	73.15	1.24
13	2	-0.096	123.74	6.97	126.22	0.13	14	6	0.096	80.04	5.22	73.15	1.74
13	2	0.096	124.16	7.00	126.22	0.09	14	7	-0.096	91.78	5.76	101.65	2.93
13	3	-0.096	94.73	5.64	93.71	0.03	14	7	0.096	93.71	5.77	101.65	1.89
13	3	0.096	94.69	5.63	93.71	0.03	14	8	-0.096	94.79	5.88	76.53	9.64
13	4	-0.096	55.36	4.85	56.44	0.05	14	8	0.096	100.39	6.07	76.53	15.45
13	4	0.096	56.43	4.71	56.44	0.00	14	9	-0.096	45.49	6.16	46.75	0.04
13	5	-0.096	58.48	15.79	53.34	0.11	14	9	0.096	44.35	6.16	46.75	0.15
13	5	0.096	77.22	10.19	53.34	5.49	14	10	-0.096	14.49	11.40	23.21	0.58

h	k	l	F_{data}	σ	F_{model}	χ^2	h	k	l	F_{data}	σ	F_{model}	χ^2
14	10	0.096	18.47	12.03	23.21	0.16	15	13	0.096	53.61	5.56	49.24	0.62
14	11	-0.096	47.94	7.41	54.72	0.84	15	14	-0.096	25.91	11.37	26.21	0.00
14	11	0.096	50.58	6.98	54.72	0.35	15	14	0.096	28.76	8.74	26.21	0.09
14	12	-0.096	43.22	6.85	38.84	0.41	15	15	0.096	43.66	4.93	41.76	0.15
14	12	0.096	46.08	6.25	38.84	1.34	16	0	-0.096	101.38	6.28	95.67	0.83
14	13	-0.096	32.25	8.19	35.27	0.14	16	0	0.096	99.85	6.15	95.67	0.46
14	13	0.096	35.48	7.20	35.27	0.00	16	1	-0.096	111.16	6.56	113.22	0.10
14	14	0.096	20.39	9.48	7.48	1.85	16	1	0.096	109.73	6.45	113.22	0.29
15	0	-0.096	87.36	5.37	95.57	2.34	16	2	-0.096	64.81	5.71	62.72	0.13
15	0	0.096	85.10	5.27	95.57	3.95	16	2	0.096	64.43	5.51	62.72	0.10
15	1	-0.096	81.51	5.25	74.29	1.89	16	3	-0.096	102.10	6.17	98.26	0.39
15	1	0.096	80.22	5.16	74.29	1.32	16	3	0.096	105.32	6.24	98.26	1.28
15	2	-0.096	50.13	15.87	43.13	0.19	16	4	-0.096	70.07	5.12	67.21	0.31
15	2	0.096	56.85	9.70	43.13	2.00	16	4	0.096	82.82	5.37	67.21	8.45
15	3	-0.096	31.73	9.08	44.93	2.11	16	5	-0.096	31.04	7.48	36.09	0.46
15	3	0.096	28.96	10.21	44.93	2.45	16	5	0.096	25.08	10.12	36.09	1.18
15	4	-0.096	101.72	6.16	105.48	0.37	16	6	-0.096	49.72	5.62	51.80	0.14
15	4	0.096	102.70	6.12	105.48	0.21	16	6	0.096	49.57	5.59	51.80	0.16
15	5	-0.096	63.17	5.05	63.16	0.00	16	7	-0.096	59.76	5.34	68.74	2.83
15	5	0.096	66.12	4.94	63.16	0.36	16	7	0.096	61.84	5.29	68.74	1.70
15	6	-0.096	70.37	5.13	74.80	0.75	16	8	-0.096	44.85	13.28	43.12	0.02
15	6	0.096	71.29	5.07	74.80	0.48	16	9	-0.096	112.04	7.65	121.39	1.50
15	7	-0.096	62.77	6.50	69.33	1.02	16	9	0.096	112.30	7.63	121.39	1.42
15	7	0.096	69.89	6.14	69.33	0.01	16	10	-0.096	96.53	6.17	84.46	3.82
15	8	-0.096	52.15	5.65	42.84	2.72	16	10	0.096	89.42	5.88	84.46	0.71
15	8	0.096	51.44	5.60	42.84	2.36	16	11	-0.096	33.90	8.19	29.70	0.26
15	9	-0.096	45.48	7.14	53.24	1.18	16	11	0.096	25.67	10.44	29.70	0.15
15	9	0.096	46.54	7.05	53.24	0.90	16	12	-0.096	52.03	5.74	48.77	0.32
15	10	-0.096	93.72	7.79	94.94	0.02	16	12	0.096	50.48	5.83	48.77	0.09
15	10	0.096	85.06	7.96	94.94	1.54	16	13	-0.096	12.34	10.15	15.91	0.12
15	11	-0.096	33.04	8.46	37.07	0.23	16	13	0.096	18.65	11.15	15.91	0.06
15	11	0.096	36.42	7.52	37.07	0.01	16	14	-0.096	32.38	7.67	35.10	0.13
15	12	-0.096	37.39	7.37	32.90	0.37	16	14	0.096	28.13	8.79	35.10	0.63
15	12	0.096	38.47	6.89	32.90	0.65	16	15	-0.096	56.24	5.41	54.77	0.07
15	13	-0.096	54.93	5.65	49.24	1.01	16	15	0.096	55.17	5.38	54.77	0.01

h	k	l	F_{data}	σ	F_{model}	χ^2	h	k	l	F_{data}	σ	F_{model}	χ^2
17	0	-0.096	93.86	7.84	89.12	0.37	18	3	0.096	29.04	9.85	28.49	0.00
17	0	0.096	105.00	7.41	89.12	4.59	18	4	-0.096	34.75	7.06	35.27	0.01
17	1	-0.096	50.39	7.29	44.10	0.74	18	4	0.096	37.27	6.44	35.27	0.10
17	1	0.096	41.69	7.59	44.10	0.10	18	5	-0.096	44.36	6.32	42.33	0.10
17	2	-0.096	33.71	8.06	43.65	1.52	18	5	0.096	50.38	5.78	42.33	1.94
17	2	0.096	34.99	7.36	43.65	1.38	18	7	-0.096	62.26	5.66	63.51	0.05
17	3	-0.096	27.14	9.44	29.76	0.08	18	7	0.096	63.22	5.62	63.51	0.00
17	3	0.096	25.49	10.32	29.76	0.17	18	8	-0.096	59.55	5.59	51.27	2.20
17	4	-0.096	16.61	10.46	21.95	0.26	18	8	0.096	56.89	5.65	51.27	0.99
17	4	0.096	20.02	11.16	21.95	0.03	18	10	-0.096	26.16	11.96	27.00	0.00
17	5	-0.096	69.88	5.24	68.53	0.07	18	10	0.096	24.97	12.69	27.00	0.03
17	5	0.096	70.53	5.21	68.53	0.15	18	11	-0.096	27.52	16.81	18.39	0.29
17	6	-0.096	30.99	8.54	37.95	0.66	18	11	0.096	19.76	15.15	18.39	0.01
17	6	0.096	22.32	12.06	37.95	1.68	18	13	-0.096	20.82	11.61	14.20	0.33
17	7	-0.096	60.94	10.12	63.35	0.06	18	13	0.096	22.58	11.86	14.20	0.50
17	7	0.096	66.15	9.27	63.35	0.09	19	0	-0.096	17.87	11.22	15.44	0.05
17	8	-0.096	53.48	6.05	51.18	0.15	19	0	0.096	24.68	9.62	15.44	0.92
17	8	0.096	53.32	6.07	51.18	0.12	19	1	-0.096	52.82	7.80	50.38	0.10
17	9	-0.096	45.55	6.33	53.08	1.41	19	1	0.096	56.17	7.32	50.38	0.63
17	9	0.096	49.74	5.88	53.08	0.32	19	2	-0.096	43.81	5.88	45.83	0.12
17	10	-0.096	29.57	9.98	44.83	2.34	19	2	0.096	44.35	5.69	45.83	0.07
17	10	0.096	26.76	11.45	44.83	2.49	19	3	-0.096	17.73	10.99	15.04	0.06
17	11	-0.096	25.44	11.64	32.60	0.38	19	3	0.096	17.74	10.91	15.04	0.06
17	11	0.096	30.14	8.57	32.60	0.08	19	4	-0.096	38.80	17.17	49.95	0.42
17	12	-0.096	53.25	5.97	53.67	0.01	19	4	0.096	67.65	10.05	49.95	3.10
17	12	0.096	52.79	5.89	53.67	0.02	19	5	-0.096	57.43	9.18	53.72	0.16
17	13	-0.096	33.76	7.44	34.23	0.00	19	5	0.096	60.58	8.87	53.72	0.60
17	13	0.096	32.97	7.41	34.23	0.03	19	6	-0.096	30.69	9.18	38.19	0.67
17	14	-0.096	20.28	11.28	21.71	0.02	19	6	0.096	35.03	7.45	38.19	0.18
17	14	0.096	15.16	10.28	21.71	0.41	19	7	-0.096	59.81	5.58	66.96	1.64
18	1	-0.096	51.70	6.68	56.39	0.49	19	7	0.096	60.40	5.56	66.96	1.39
18	1	0.096	41.96	7.90	56.39	3.34	19	8	-0.096	25.76	15.46	25.78	0.00
18	2	-0.096	38.75	6.99	32.04	0.92	19	8	0.096	33.66	13.89	25.78	0.32
18	2	0.096	40.39	6.63	32.04	1.59	19	9	-0.096	13.95	10.37	17.71	0.13
18	3	-0.096	28.56	11.02	28.49	0.00	19	9	0.096	24.85	11.69	17.71	0.37

h	k	l	F_{data}	σ	F_{model}	χ^2
19	10	-0.096	43.15	7.23	42.20	0.02
19	10	0.096	46.53	6.63	42.20	0.43
19	11	-0.096	28.11	10.02	21.52	0.43
19	11	0.096	27.67	9.75	21.52	0.40
20	0	-0.096	49.59	5.44	43.26	1.36
20	0	0.096	47.91	5.48	43.26	0.72
20	1	-0.096	38.98	6.42	31.14	1.49
20	1	0.096	37.79	6.35	31.14	1.10
20	2	-0.096	41.72	6.59	41.84	0.00
20	2	0.096	36.97	7.20	41.84	0.46
20	3	-0.096	51.07	6.09	56.30	0.74
20	3	0.096	47.98	6.31	56.30	1.74
20	4	-0.096	65.86	5.48	69.35	0.41
20	4	0.096	69.01	5.42	69.35	0.00
20	5	-0.096	33.26	7.83	39.34	0.60
20	5	0.096	30.58	8.77	39.34	1.00
20	6	-0.096	38.00	7.35	33.96	0.30
20	6	0.096	38.77	7.19	33.96	0.45
20	7	-0.096	35.59	7.72	48.12	2.63
20	7	0.096	32.46	8.55	48.12	3.35
20	8	-0.096	18.82	11.39	24.10	0.22
20	8	0.096	18.26	11.11	24.10	0.28
20	9	-0.096	21.60	12.09	17.59	0.11
20	9	0.096	24.69	10.82	17.59	0.43
20	10	-0.096	41.76	6.79	51.64	2.12
20	10	0.096	43.47	6.27	51.64	1.70
21	0	-0.096	43.02	6.41	43.27	0.00
21	0	0.096	41.27	6.65	43.27	0.09
21	1	-0.096	41.91	7.06	43.29	0.04
21	1	0.096	39.13	7.38	43.29	0.32
21	2	-0.096	41.35	6.67	38.89	0.14
21	2	0.096	35.00	7.76	38.89	0.25
21	3	-0.096	33.31	7.72	29.12	0.29
21	3	0.096	36.95	6.77	29.12	1.34
21	4	-0.096	81.96	5.68	84.45	0.19
21	4	0.096	81.37	5.61	84.45	0.30
21	5	-0.096	88.88	16.88	23.42	15.04
21	6	-0.096	36.27	7.25	36.47	0.00
21	6	0.096	39.63	6.54	36.47	0.23
21	7	-0.096	16.95	11.35	25.38	0.55
21	7	0.096	29.94	9.91	25.38	0.21
21	8	-0.096	45.14	6.27	33.27	3.58
21	8	0.096	43.97	6.27	33.27	2.91
21	9	-0.096	37.21	7.79	42.97	0.55
21	9	0.096	33.50	8.41	42.97	1.27
22	0	-0.096	63.57	6.04	68.05	0.55
22	0	0.096	62.85	5.92	68.05	0.77
22	1	-0.096	105.95	6.45	102.50	0.29
22	1	-0.07	95.42	5.37	102.51	1.74
22	1	0.07	94.62	5.35	102.51	2.17
22	1	0.096	104.88	6.40	102.50	0.14
22	2	-0.096	29.17	9.14	24.52	0.26
22	2	0.096	31.83	8.11	24.52	0.81
22	3	-0.096	51.86	5.84	41.86	2.93
22	3	0.096	52.89	5.66	41.86	3.80
22	4	-0.096	30.78	9.24	28.72	0.05
22	4	0.096	26.02	10.49	28.72	0.07
22	5	-0.096	31.57	8.27	21.10	1.60
22	5	0.096	23.22	12.20	21.10	0.03
22	6	-0.096	9.88	10.14	20.52	1.10
22	6	0.096	15.33	10.82	20.52	0.23
22	7	-0.096	43.71	6.67	30.74	3.78
22	7	0.096	42.58	6.57	30.74	3.25
22	8	-0.096	41.23	7.80	40.71	0.00
22	8	0.096	45.35	6.74	40.71	0.47
23	0	-0.096	94.59	6.12	100.43	0.91
23	0	0.096	94.68	6.08	100.43	0.89
23	1	-0.096	58.54	5.74	64.87	1.22
23	1	0.096	60.99	5.57	64.87	0.48
23	2	-0.096	44.10	8.49	50.64	0.59

h	k	l	F_{data}	σ	F_{model}	χ^2
23	2	0.096	47.67	7.88	50.64	0.14
23	3	-0.096	35.82	7.46	33.90	0.07
23	3	0.096	33.76	7.75	33.90	0.00
23	4	-0.096	20.51	12.04	20.59	0.00
23	4	0.096	17.29	11.27	20.59	0.09
23	5	-0.096	40.19	6.88	39.11	0.02
23	5	0.096	38.99	6.81	39.11	0.00
23	6	-0.096	44.96	6.88	42.42	0.14
23	6	0.096	43.10	6.90	42.42	0.01
24	1	-0.096	36.03	7.91	36.70	0.01
24	1	0.096	36.29	7.55	36.70	0.00
24	2	-0.096	54.71	5.91	59.38	0.63
24	2	0.096	54.19	5.75	59.38	0.82
24	3	-0.096	26.40	13.06	24.68	0.02
24	3	0.096	31.71	8.87	24.68	0.63
24	4	-0.096	34.34	8.67	39.57	0.36
24	4	0.096	33.90	8.33	39.57	0.46
24	5	-0.096	54.40	7.01	49.10	0.57
24	5	0.096	51.29	6.82	49.10	0.10
25	0	-0.096	25.30	12.96	25.01	0.00
25	0	0.096	13.99	10.49	25.01	1.10
25	1	-0.096	31.49	10.46	34.53	0.08
25	1	0.096	33.26	10.21	34.53	0.02
25	2	-0.096	53.32	5.87	50.11	0.30
25	2	0.096	51.92	5.72	50.11	0.10
25	3	-0.096	35.52	7.60	35.51	0.00
25	3	0.096	34.05	7.64	35.51	0.04
26	0	-0.096	13.62	14.16	18.43	0.12
26	0	0.096	18.87	15.48	18.43	0.00
26	1	-0.096	47.30	5.90	43.19	0.48

Table 2 – In-plane average atomic positions of the 14 independent gold sites and two Si layers (12 atoms per layer) in the positions of the bulk. The other atomic positions can be deduced by *p3* symmetry. Values for the errors on the positions (δx, δy) as well as the displacements from the starting positions (Δx, Δy in Å) are given. Gold Debye-Waller factor : 1.1±0.04 Å^2. Occupancy of special sites : 0.49±0.015. Agreement factor χ^2 : 1.8

x	Δx	δx	y	Δy	δy
Gold sites					
0	-	-	0	-	-
0.33333	-	-	0.66667	-	-
0.66667	-	-	0.33333	-	-
0.309	-0.0004	0.00048	0.3018	-0.0012	0.00049
0.1852	0.0012	0.00053	0.1804	0.0024	0.00057
0.2545	0.0028	0.00051	0.0315	0.002	0.00054
0.447	0.0011	0.00048	0.3553	-0.0007	0.00048
0.0089	-0.0018	0.0005	0.3582	-0.0004	0.00049
0.4523	0.0019	0.00063	0.2356	0.0012	0.0006
0.133	0.0029	0.00046	0.4765	0.0019	0.00051
0.2836	-0.0003	0.00058	0.5337	-0.0017	0.00058
0.4841	0.0001	0.00048	0.1353	-0.0005	0.00052
0.1366	0.0002	0.00049	0.044	0.001	0.00062
0.5772	-0.0019	0.00052	0.3724	-0.0016	0.00053
0.4128	-0.0022	0.00052	0.5288	-0.0015	0.00052
0.0855	0.0017	0.00055	0.2168	0.0003	0.00054
0.2845	0.0027	0.00052	0.412	0.0017	0.00057

x	Δx	δx	y	Δy	δy
Silicon layer 1					
0.0556	0.0076	0.0036	0.1111	-0.004	0.0032
0.2222	-0.0129	0.0032	0.1111	-0.0062	0.0032
0.3889	-0.0116	0.0029	0.1111	-0.003	0.003
0.0556	0.0042	0.0029	0.2778	0.0132	0.0031
0.2222	-0.01	0.0033	0.2778	0.0068	0.0033
0.3889	-0.0037	0.0035	0.2778	-0.0093	0.0031
0.5556	0.0061	0.0034	0.2778	-0.0168	0.0037
0.0556	-0.0048	0.0032	0.4444	0.011	0.0031
0.2222	-0.0089	0.0032	0.4444	-0.001	0.0037
0.3889	0.0073	0.0032	0.4444	-0.0125	0.0032
0.5556	-0.0052	0.0029	0.1111	-0.0168	0.0033
0.2222	-0.0031	0.0037	0.6111	-0.0091	0.0037

x	Δx	δx	y	Δy	δy
Silicon layer 2					
0.1111	0.0059	0.0036	0.0556	0.0059	0.0036
0.1111	-0.0022	0.0017	0.2222	-0.0022	0.0017
0.4444	0.0003	0.0041	0.2222	0.0003	0.0041
0.6111	-0.0011	0.0017	0.3889	-0.0011	0.0017
0.2778	-0.0021	0.0021	0.5556	-0.0021	0.0021
0.4444	-0.0008	0.0017	0.5556	-0.0008	0.0017
0.2778	-0.0027	0.0024	0.2222	0.0044	0.0029
0.2778	0.0046	0.0021	0.3889	0.0009	0.0021
0.4444	-0.0051	0.0022	0.3889	-0.0004	0.002
0.9444	0.0059	0.0036	0.0556	0.0059	0.0036
0.7778	-0.0022	0.0017	0.8889	-0.0022	0.0017
0.7778	0.0003	0.0041	0.2222	0.0003	0.0041

Table 3 – In-plane average atomic positions of the 14 independent gold sites and two Si layers (12 atoms per layer) in the positions given by Grozea *et al.* . The other atomic positions can be deduced by *p3* symmetry. Values for the errors on the positions (δx, δy) as well as the displacements from the starting positions (Δx, Δy in Å) are given. Gold Debye-Waller factor : 1.3±0.04 Å^2. Occupancy of special sites : 0.49±0.015. Agreement factor χ^2 : 1.3

x	Δx	δx	y	Δy	δy
Gold sites					
0	-	-	0	-	-
0.33333	-	-	0.66667	-	-
0.66667	-	-	0.33333	-	-
0.309	0.001	0.00052	0.3018	0.0002	0.00057
0.1852	0.0008	0.00055	0.1804	0.0029	0.00057
0.2545	0.0028	0.0005	0.0315	0.0018	0.00055
0.447	-0.0001	0.00051	0.3553	-0.0013	0.00052
0.0089	-0.002	0.0051	0.3582	-0.0005	0.00051
0.4523	0.0014	0.00057	0.2356	0.0008	0.00061
0.133	0.0022	0.00051	0.4765	0.0026	0.00057
0.2836	0.0006	0.00053	0.5337	-0.0005	0.00057
0.4841	0.001	0.00049	0.1353	0.0001	0.00058
0.1366	0.0003	0.00053	0.044	0.0026	0.00064
0.5772	-0.0019	0.00052	0.3724	-0.0017	0.00058
0.4128	-0.003	0.00054	0.5288	-0.0021	0.00055
0.0855	0.0009	0.00058	0.2168	0.0007	0.00051
0.2845	0.0024	0.00054	0.412	0.0017	0.00057

x	Δx	δx	y	Δy	δy
Silicon layer 1					
0.3681	0.0039	0.0048	0.1072	0.0052	0.0064
0.3577	0.0093	0.0045	0.235	0.0082	0.0044
0.2369	0.0088	0.0043	0.139	0.0053	0.0042
0.196	0.0035	0.0054	0.3002	-0.0072	0.0053
0.1738	0.0101	0.0041	0.397	-0.0062	0.0037
0.0908	-0.001	0.0042	0.3398	-0.0087	0.0046
0.5261	0.0094	0.0051	0.4502	0.0025	0.0058
0.3955	-0.0044	0.0101	0.4152	0.0061	0.007
0.068	-0.0031	0.0103	0.0989	0.0059	0.013
0.4335	-0.0026	0.0042	0.0133	-0.0045	0.0041
0.2121	-0.0028	0.0053	0.5884	0.0053	0.0057
0.5702	-0.0072	0.0074	0.2555	0.0029	0.0077

x	Δx	δx	y	Δy	δy
Silicon layer 2					
0.0582	0.0006	0.0099	0.1099	-0.0061	0.0138
0.222	-0.0003	0.0057	0.609	-0.0053	0.0064
0.2249	-0.0093	0.0043	0.1144	-0.0103	0.0046
0.3882	-0.0026	0.0054	0.1113	0.0031	0.0067
0.387	0.0058	0.0045	0.2756	-0.0045	0.0042
0.057	-0.0013	0.0042	0.2832	-0.0048	0.0049
0.2211	-0.0092	0.0054	0.2794	0.0038	0.0057
0.2189	-0.0008	0.0043	0.4392	-0.0057	0.0051
0.3926	-0.0009	0.0097	0.4408	-0.0112	0.0074
0.5547	0.0042	0.0079	0.2745	-0.0092	0.0078
0.5531	-0.0023	0.0054	0.1076	-0.0061	0.0056
0.0495	-0.0058	0.0047	0.4409	0.0144	0.047

References

[Adhikari *et al.*, 2006] H Adhikari, AF Marshall, CED Chidsey, and PC McIntyre. Germanium nanowire epitaxy : Shape and orientation control. *Nano Letters*, 6(2) :318–323, February 2006.

[Adhikari *et al.*, 2007] Hemant Adhikari, Ann F. Marshall, Irene A. Goldthorpe, Christopher E. D. Chidsey, and Paul C. McIntyre. Metastability of Au-Ge liquid nanocatalysts : Ge Vapor-Liquid-Solid nanowire growth far below the bulk eutectic temperature. *ACS Nano*, 1(5) :415–422, December 2007.

[Agnus, 2007] G Agnus. Texturation de surfaces et applications : Croissance auto-organisée de nanostructures. *PhD Thesis ; www.tel.archives-ouvertes.fr*, (00270692), 2007.

[Allen and Kasper, 1988] F. Allen and E. Kasper. *Silicon-Molecular Beam Epitaxy*, volume 1. E. Kasper and J. Bean, chemical rubber, boca raton, FL edition, 1988.

[Als-Nielsen *et al.*,] J. Als-Nielsen, M. Altarelli, J. Baruchel, R. Currat, A. Fontaine, V.T. Forsyth, A. Freund, G. Krill, M. Lambert, G. McIntyre, F. Mezei, J. Morse, J. Pannetier, D. Raoux, R. Sherm, B. Fak, M. Schlenker, G. Schmahl, C. Williams, and H. Zabel. *Neutron and Synchrotron radiation for condensed matter studies Volume 1 : Theory, Instruments and methods.* J. Baruchel, J.L. Hodeau, M.S. Lehmann, J.R. Regnard, C. Schlenker, Verlag Berlin Heidelberg, springer edition.

[Anantharaman *et al.*, 1966] T. R. Anantharaman, H. L. Luo, and W. Element. Formation of new intermetallic phases in binary eutectic systems by drastic undercooling of the melt. *Nature*, 210(5040) :1040–1041, 1966.

[Andersen *et al.*, 1971] G.A. Andersen, J.L. Bestel, A.A. Johnson, and B. Post. Eutectic decomposition in the gold—silicon system. *Materials Science and Engineering*, 7(2) :83–90, February 1971.

[Aoki *et al.*, 2002] Hirokatsu Aoki, Koichi Hotoduka, and Toshio Itami. The hidden structure in liquid IIIB-VB alloys. *Journal of Non-Crystalline Solids*, 312-314 :222–226, October 2002.

[Arai *et al.*, 2000] Arai, Tsukimoto, Muto, and Saka. Direct observation of the atomic structure in a Solid-Liquid interface. *Microscopy and Microanalysis : The Official Journal of Microscopy Society of America, Microbeam Analysis Society, Microscopical Society of Canada*, 6(4) :358–361, July 2000. PMID : 10898820.

[Ascencio *et al.*, 1998] J. A. Ascencio, C. Gutiérrez-Wing, M. E. Espinosa, M. Marín, S. Tehuacanero, C. Zorrilla, and M. José-Yacamán. Structure determination of small particles by HREM imaging : theory and experiment. *Surface Science*, 396(1-3) :349–368, January 1998.

[Bauer and Poppa, 1972] E. Bauer and H. Poppa. Recent advances in epitaxy. *Thin Solid Films*, 12(1) :167–185, September 1972.

[Becker and Doring, 1935] R. Becker and W. Doring. Kinetic treatment of germ formation in supersaturated vapour. *Annalen der Physik*, 24(8) :719–752, 1935.

[Becker *et al.*, 1989] R. S. Becker, B. S. Swartzentruber, J. S. Vickers, and T. Klitsner. Dimer-adatom-stacking-fault (DAS) and non-DAS (111) semiconductor surfaces : A comparison of Ge(111)-c(2×8) to Si(111)-(2×2), -(5×5), -(7×7), and -(9×9) with scanning tunneling microscopy. *Physical Review B*, 39(3) :1633, 1989.

[Becker, 1938] R. Becker. Nucleation during precipitation of metallic mixed crystals. *Annalen der Physik*, 32(1/2) :128–140, 1938.

[Binnig *et al.*, 1983] G. Binnig, H. Rohrer, Ch. Gerber, and E. Weibel. (7×7) reconstruction on Si(111) resolved in real space. *Physical Review Letters*, 50(2) :120, January 1983.

[Boisselier and Astruc, 2009] Elodie Boisselier and Didier Astruc. Gold nanoparticles in nanomedicine : preparations, imaging, diagnostics, therapies and toxicity. *Chemical Society Reviews*, 38 :1759, 2009.

[Bollmann and Nissen, 1968] W. Bollmann and H.-U. Nissen. A study of optimal phase boundaries : the case of exsolved alkali feldspars. *Acta Crystallographica Section A*, 24(5) :546–557, September 1968.

[Calliari *et al.*, 1984] L. Calliari, M. Sancrotti, and L. Braicovich. Agglomeration at Si/Au interfaces : A study with spatially resolved Auger line-shape spectroscopy. *Physical Review B*, 30 :4885, 1984.

[Castanet *et al.*, 1978] R. Castanet, R. Chastel, and C. Bergman. Etude thermodynamique du systême Au-Si. *Materials Science and Engineering*, 32(1) :93–98, January 1978.

[Celino *et al.*, 2007] Massimo Celino, Vittorio Rosato, Andrea Di Cicco, Angela Trapananti, and Carlo Massobrio. Role of defective icosahedra in undercooled copper. *Physical Review B*, 75(17) :174210, May 2007.

[Chen and Chen, 1996] C. R. Chen and L. J. Chen. Structural evolution and atomic structure of ultrahigh vacuum deposited Au thin films on silicon at low temperatures. *Applied Surface Science*, 92 :507–512, February 1996.

[Chen and Turnbull, 1967] H. S. Chen and D. Turnbull. Thermal properties of gold-silicon binary alloy near the eutectic composition. *Journal of Applied Physics*, 38(9) :3646–3650, 1967.

[Chirawatkul *et al.*, 2011] Prae Chirawatkul, Anita Zeidler, Philip S. Salmon, Shin'ichi Takeda, Yukinobu Kawakita, Takeshi Usuki, and Henry E. Fischer. Structure of eutectic liquids in the Au-Si,

Au-Ge, and Ag-Ge binary systems by neutron diffraction. *Physical Review B*, 83(1) :014203, January 2011.

[Choi *et al.*, 2011] S.Y. Choi, W. Y. Fung, and W. Lu. Growth and electrical properties of al-catalyzed si nanowires. *Applied Physics Letters*, 98(033108), 2011.

[Curtin, 1987] W. A. Curtin. Density-functional theory of the solid-liquid interface. *Physical Review Letters*, 59(11) :1228, 1987.

[Dahmen, 1982] U. Dahmen. Orientation relationships in precipitation systems. *Acta Metallurgica*, 30(1) :63–73, January 1982.

[Das *et al.*, 2001] SK Das, JH Perepezko, RI Wu, and G Wilde. Undercooling and glass formation in Al-based alloys. *Materials Science and Engineering A-Structural Materials Properties*, 304 :159–165, May 2001.

[David *et al.*, 2008] Thomas David, Denis Buttard, Tobias Schülli, Florian Dallhuin, and Pascal Gentile. Structural investigation of silicon nanowires using GIXD and GISAXS : evidence of complex saw-tooth faceting. *Surface Science*, 602(15) :2675–2680, August 2008.

[D'Evelyn and Rice, 1981] Mark P. D'Evelyn and Stuart A. Rice. Structure in the density profile at the Liquid-Metal-Vapor interface. *Physical Review Letters*, 47(25) :1844, December 1981.

[Dornisch *et al.*, 1991] D. Dornisch, W. Moritz, H. Schulz, R. Feidenhans'l, M. Nielsen, F. Grey, and R. L. Johnson. Au/Si(111) : Analysis of the $(\sqrt{3}\times\sqrt{3})$R30° and (6×6) structures by in-plane x-ray diffraction. *Physical Review B*, 44(20) :11221, November 1991.

[Egry *et al.*, 1995] Ivan Egry, Georg Lohoefer, and Gerd Jacobs. Surface tension of liquid metals : Results from measurements on ground and in space. *Physical Review Letters*, 75(22) :4043, 1995.

[Eswaramoorthy *et al.*, 2007] Santhana K. Eswaramoorthy, James M. Howe, and Govindarajan Muralidharan. In situ determination of the nanoscale chemistry and behavior of Solid-Liquid systems. *Science*, 318(5855) :1437 –1440, November 2007.

[Fahrenheit, 1724] D. G. Fahrenheit. Experimenta & observationes de congelatione aquae in vacuo factae. *Philosophical Transaction Royal Society of London*, 33 :78, 1724.

[Feidenhans'l, 1989] R Feidenhans'l. Surface structure determination by X-ray diffraction. *Surface Science Reports*, 10(3), 1989.

[Ferralis *et al.*, 2007] N. Ferralis, R. Maboudian, and C. Carraro. Structure and morphology of annealed gold films galvanically displaced on the si(111) surface. *Journal of Physical Chemistry C*, 111(20) :7508–7513, May 2007.

[Ferralis *et al.*, 2008] Nicola Ferralis, Roya Maboudian, and Carlo Carraro. Temperature-Induced Self-Pinning and nanolayering of AuSi eutectic droplets. *Journal of the American Chemical Society*, 130(8) :2681–2685, February 2008.

[Ferralis *et al.*, 2009] Nicola Ferralis, Farid El Gabaly, Andreas K. Schmid, Roya Maboudian, and Carlo Carraro. Real-Time observation of reactive spreading of gold on silicon. *Physical Review Letters*, 103(25), December 2009.

[Frank, 1952] F.C Frank. Supercooling of liquids. *Proceeding of the Royal Society of London Series A*, 215 :43–46, 1952.

[Frenken and van der Veen, 1985] Joost W. M. Frenken and J. F. van der Veen. Observation of surface melting. *Physical Review Letters*, 54(2) :134, January 1985.

[Fuchigami and Ichimiya, 1996] Kenji Fuchigami and Ayahiko Ichimiya. Gold deposition on a surface. *Surface Science*, 357-358 :937–942, June 1996.

[Gaskell, 2011] Philip H. Gaskell. NCM – looking back – moving forward. *Journal of Non-Crystalline Solids*, 357(14) :2769–2774, July 2011.

[Gilmore *et al.*, 1997] C. J. Gilmore, L. D. Marks, D. Grozea, C. Collazo, E. Landree, and R. D. Twesten. Direct solutions of the Si(111)-(7×7) structure. *Surface Science*, 381(2-3) :77–91, June 1997.

[Gossmann *et al.*, 1985] H. -J. Gossmann, J. C. Bean, L. C. Feldman, E. G. McRae, and I. K. Robinson. (7×7) reconstruction of Ge(111) surfaces under compressive strain. *Physical Review Letters*, 55(10) :1106, 1985.

[Greer, 2006] AL Greer. Liquid metals : Supercool order. *Nature Materials*, 5(1) :13–14, January 2006.

[Grozea *et al.*, 1998] D Grozea, E Landree, L.D Marks, R Feidenhans'l, M Nielsen, and R.L Johnson. Direct methods determination of the Si(111)-(6×6)Au surface structure. *Surface Science*, 418(1) :32–45, November 1998.

[Grozea *et al.*, 2000] D. Grozea, E. Bengu, and L. D. Marks. Surface phase diagrams for the Ag-Ge(111) and Au-Si(111) systems. *Surface Science*, 461(1-3) :23–30, August 2000.

[han, 2010] *Handbook of CHEMISTRY and PHYSICS 91st Edition,*. 2010.

[Hannon *et al.*, 2006] JB Hannon, S Kodambaka, FM Ross, and RM Tromp. The influence of the surface migration of gold on the growth of silicon nanowires. *Nature*, 440(7080) :69–71, March 2006.

[Heni and Lowen, 2002] M Heni and H Lowen. Do liquids exhibit local fivefold symmetry at interfaces ? *Physical Review E*, 65(2), February 2002.

[Hibino and Watanabe, 2005] H. Hibino and Y. Watanabe. Arrangement of Au-Si alloy islands at atomic steps. *Surface Science*, 588(1-3) :L233–L238, August 2005.

[Higashiyama *et al.*, 1986a] K. Higashiyama, S. Kono, and T. Sagawa. Study of the Si(111)-Ga surface by x-ray photoelectron and Auger electron diffraction. *Surface Science*, 175(3) :L794–L800, October 1986.

[Higashiyama *et al.*, 1986b] Kazuyuki Higashiyama, Shozo Kono, and Takasi Sagawa. Structural disorder of Si(111)-($\sqrt{3}\times\sqrt{3}$)-Au surface studied by LEED. *Japanese Journal of Applied Physics*, 25(Part 2, No. 2) :L117–L120, February 1986.

[Higashiyama *et al.*, 2001] Kazuyuki Higashiyama, Akihiro Egami, Shinya Hosoi, and Kazushi Suzuki. Partial disorder of the Si(111)-(6×6)-Au surface studied by scanning tunneling microscopy. *Japanese Journal of Applied Physics*, 40(Part 1, No. 12) :6985–6992, December 2001.

[Honeycutt and Andersen, 1987] J.D Honeycutt and H.C Andersen. Molecular-dynamics study of melting and freezing of small Lennard-Jones clusters. *Journal of Physical Chemistry*, 91(19) :4950–4963, September 1987.

[Horio, 1999] Y. Horio. Different growth modes of Al on Si(111)-(7×7) and Si(111)-($\sqrt{3}$×$\sqrt{3}$)-Al surfaces. *Japanese Journal of Applied Physics*, 38 :4881–4886, 1999.

[Hoshino *et al.*, 2008] Y. Hoshino, Y. Kitsudo, M. Iwami, and Y. Kido. The structure and growth process of Au/Si(111) analyzed by high-resolution ion scattering coupled with photoelectron spectroscopy. *Surface Science*, 602(12) :2089–2095, June 2008.

[Howes *et al.*, 1993] P. B. Howes, C. Norris, M. S. Finney, E. Vlieg, and R. G. van Silfhout. Structure of Ge(111)-($\sqrt{3}$×$\sqrt{3}$)R30°-Au determined by surface X-ray diffraction. *Physical Review B*, 48(3) :1632, 1993.

[Huang and Williams, 1988] Judy H. Huang and R. Stanley Williams. Surface-structure analysis of Au overlayers on Si by impact-collision ion-scattering spectroscopy : ($\sqrt{3}$ × $\sqrt{3}$ and (6×6) Si(111)/Au. *Physical Review B*, 38(6) :4022, 1988.

[Huang *et al.*, 1990] H. Huang, S. Y. Tong, W. S. Yang, H. D. Shih, and F. Jona. Atomic structure of Si(111)-($\sqrt{3}$×$\sqrt{3}$)-Al studied by dynamical low-energy electron diffraction. *Physical Review B*, 42(12) :7483, 1990.

[Huisman *et al.*, 1997] Willem Jan Huisman, Joost F. Peters, Michel J. Zwanenburg, Steven A. de Vries, Trevor E. Derry, Douglas Abernathy, and J. Friso van der Veen. Layering of a liquid metal in contact with a hard wall. *Nature*, 390(6658) :379–381, November 1997.

[Hume-Rothery and Anderson, 1960] W. Hume-Rothery and E. Anderson. Eutectic compositions and liquid immiscibility in certain binary alloys. *Philosophical Magazine*, 5 :383, 1960.

[Ikeda *et al.*, 2002] Motoshige Ikeda, Takeru Shibata, Hirokatsu Aoki, and Toshio Itami. The large concentration fluctuations in the liquid eutectic systems with deep eutectic points. *Journal of Non-Crystalline Solids*, 312-314 :217–221, October 2002.

[Ikegawa, 1988] S. Ikegawa. Reversible change between metastable crystalline phases by laser beam irradiation in sputtered Au-Ge alloy films. *Journal of Vacuum Science and Technology A : Vacuum, Surfaces, and Films*, 6 :1855, 1988.

[Ikuhara and Pirouz, 1996] Yuichi Ikuhara and P. Pirouz. Orientation relationship in large mismatched bicrystals and coincidence of reciprocal lattice points (CRLP). *Materials Science Forum*, 207-209 :121–124, 1996.

[Itami *et al.*, 2007] T Itami, H Aoki, T Shibata, M Ikeda, and K Hotozuka. The estimation of concentration fluctuations in liquid Ag-Si and Au-Si alloys. *Journal of Non-Crystalline Solids*, 353(32-40) :3011–3016, October 2007.

[Itami *et al.*, 2010] T. Itami, j. Okada, Y. Watanabe, T. Ishikawa, and S. Yoda. Supercooling of homogeneous liquid phase of liquid metals and alloys - Poor supercooling around the eutectic composition of liquid system. *Materials Transactions*, 51(9) :1510–1515, 2010.

[Jaccodine, 1963] R. J. Jaccodine. Surface energy of germanium and silicon. *Journal of The Electrochemical Society*, 110(6) :524–527, 1963.

[Jakse and Pasturel, 2003] N Jakse and A Pasturel. Local order of liquid and supercooled zirconium by ab initio molecular dynamics. *Physical Review Letters*, 91(19), November 2003.

[Jakse and Pasturel, 2008] N. Jakse and A. Pasturel. Glass forming ability and short-range order in a binary bulk metallic glass by ab initio molecular dynamics. *Applied Physics Letters*, 93(11) :113104, 2008.

[Jalochowski and Bauer, 1988] M. Jalochowski and E. Bauer. Title ? *Physical Review B*, 37 :8622, 1988.

[Jalochowski, 2003] M. Jalochowski. Si(111)-(6×6)Au surface morphology and nucleation of Pb at low temperature. *Progress in Surface Science*, 74, 2003.

[James, 1982] R.W. James. *The Optical Principles of the Diffraction of X-rays*. Ox Bow, Connecticut, 1982.

[Jiran and Thompson, 1992] E. Jiran and C.V. Thompson. Capillary instabilities in thin, continuous films. *Thin Solid Films*, 208(1) :23–28, February 1992.

[Jónsson and Andersen, 1988] Hannes Jónsson and Hans C. Andersen. Icosahedral ordering in the Lennard-Jones liquid and glass. *Physical Review Letters*, 60(22) :2295, May 1988.

[Karayiannis *et al.*, 2011] Nikos Karayiannis, Rohit Malshe, Juan de Pablo, and Manuel Laso. Fivefold symmetry as an inhibitor to hard-sphere crystallization. *Physical Review E*, 83(6), June 2011.

[Kato, 1989] Hiroshi Kato. Eutectic reactions and textures of Au-Si alloy films on single-crystal silicon. *Japanese Journal of Applied Physics*, 28 :953–956, 1989.

[Katzel and Meinel, 1989] D. Katzel and K. Meinel. Growth modes of Au on Si(111) and the mechanism of the silicide formation. *Journal of Crystal Growth*, 98 :690–696, July 1989.

[Kelton *et al.*, 2003] K. Kelton, G. Lee, A. Gangopadhyay, R. Hyers, T. Rathz, J. Rogers, M. Robinson, and D. Robinson. First X-Ray scattering studies on electrostatically levitated metallic liquids : Demonstrated influence of local icosahedral order on the nucleation barrier. *Physical Review Letters*, 90(19), May 2003.

[Kelton *et al.*, 2006] K.F. Kelton, A.K. Gangopadhyay, T.H. Kim, and G.W. Lee. A case for local icosahedral order in undercooled metallic liquids and the influence on the nucleation barrier. *Journal of Non-Crystalline Solids*, 352(50-51) :5318–5324, December 2006.

[Köhler *et al.*, 1991] U. Köhler, O. Jusko, G. Pietsch, B. Müller, and M. Henzler. Strained-layer growth and islanding of germanium on Si(111)-(7×7) studied with STM. *Surface Science*, 248(3) :321–331, 1991.

[Khramtsova and Ichimiya, 1998] Elena A. Khramtsova and Ayahiko Ichimiya. Comparative study of room- and high-temperature Si(111)-($\sqrt{3} \times \sqrt{3}$)R30°-Au structures using one-beam RHEED intensity rocking-curve analysis. *Physical Review B*, 57(16) :10049, April 1998.

[Khramtsova *et al.*, 1999] Elena A. Khramtsova, Hiroto Sakai, Kazuhiko Hayashi, and Ayahiko Ichimiya. One monolayer of gold on an Si(111) surface : surface phases and phase transitions. *Surface Science*, 433-435 :405–409, August 1999.

[Kim and Kelton, 2007] T. H. Kim and K. F. Kelton. Structural study of supercooled liquid transition metals. *The Journal of Chemical Physics*, 126(5) :054513, 2007.

[Kim *et al.*, 1996] K. S. Kim, Y. W. Kim, N. G. Park, W. S. Cho, D. S. Choi, S. S. Kim, and C. N. Whang. Growth mode of Au layer on Si(001). *Nuclear Instruments and Methods in Physics Research Section B : Beam Interactions with Materials and Atoms*, 117(3) :289–294, September 1996.

[Kim *et al.*, 2008] BJ Kim, J Tersoff, S Kodambaka, MC Reuter, EA Stach, and FM Ross. Kinetics of individual nucleation events observed in nanoscale vapor-liquid-solid growth. *Science*, 322(5904) :1070–1073, November 2008.

[Kim *et al.*, 2009] Donghyun Kim, Amanda L. Giermann, and Carl V. Thompson. Solid-state dewetting of patterned thin films. *Applied Physics Letters*, 95(25) :251903, 2009.

[Kirakosian *et al.*, 2001] A. Kirakosian, J.-L. Lin, D. Y. Petrovykh, J. N. Crain, and F. J. Himpsel. Functionalization of silicon step arrays i : Au passivation of stepped si(111) templates. *Journal of Applied Physics*, 90(7) :3286, 2001.

[Klement *et al.*, 1960] W. Klement, R. H. Willens, and Pol Duwez. Non-crystalline structure in solidified Gold-Silicon alloys. *Nature*, 187(4740) :869–870, September 1960.

[Kodambaka *et al.*, 2006] S. Kodambaka, J. Tersoff, M. C. Reuter, and F. M. Ross. Diameter-Independent Kinetics in the Vapor-Liquid-Solid Growth of Si Nanowires. *Physical Review Letters*, 96(9) :096105, March 2006.

[Kodambaka *et al.*, 2007] S Kodambaka, J Tersoff, MC Reuter, and FM Ross. Germanium nanowire growth below the eutectic temperature. *Science*, 316(5825) :729–732, May 2007.

[Kresse and Furthmuller, 1996] G Kresse and J Furthmuller. *Physical Review B*, 54 :11169, 1996.

[Kresse and Furthmullers, 1996] G Kresse and J Furthmullers. Efficiency of *ab-initio* total energy calculations for metals and semiconductors using a plane-wave basis set. *Computational Materials Science*, 6 :15–50, 1996.

[Kresse and Joubert, 1999] G Kresse and D Joubert. *Physical Review B*, 59 :1758, 1999.

[Kurz and Fisher, 1998] W. Kurz and D.J. Fisher. *Fundamentals of solidification, fourth revised edition.* Trans Tech. Publications. 1998.

[Lander and Morrison, 1964] J.J Lander and J Morrison. Surface reactions of silicon with aluminum and with indium. *Surface Science*, 2 :553–565, 1964.

[Lander, 1964] J.J. Lander. Chemisorption and ordered surface structures. *Surface Science*, 1(2) :125–164, April 1964.

[Lazzari, 2002] Rémi Lazzari. IsGISAXS : a program for grazing-incidence small-angle x-ray scattering analysis of supported islands. *Journal of Applied Crystallography*, 35(4) :406–421, July 2002.

[Li, 1996] Dongqing Li. Drop size dependence of contact angles and line tensions of solid-liquid systems. *Colloids and Surfaces A : Physicochemical and Engineering Aspects*, 116(1-2) :1–23, September 1996.

[Liu *et al.*, 2003] X.R. Liu, C.D. Cao, and B.B. Wei. Rapid eutectic growth in undercooled Al-Ge alloy under free fall condition. *Chinese Physics*, 12(11) :1266–1271, November 2003.

[Liu *et al.*, 2004] RP Liu, DM Herlach, M Vandyoussefi, and AL Greer. Undercooling and solidification of Al-50 at.% Si alloy by electromagnetic levitation. *Metallurgical and Materials Transactions A-Physical Metallurgy*, 35A(2) :607–612, February 2004.

[Lojkowski and Fecht, 2000] Witold Lojkowski and Hans-Jörg Fecht. The structure of intercrystalline interfaces. *Progress in Materials Science*, 45(5-6) :339–568, September 2000.

[Mackay, 1962] A. L. Mackay. A dense non-crystallographic packing of equal spheres. *Acta Crystallographica*, 15(9) :916–918, September 1962.

[Magnussen *et al.*, 1995] O. M. Magnussen, B. M. Ocko, M. J. Regan, K. Penanen, P. S. Pershan, and M. Deutsch. X-Ray reflectivity measurements of surface layering in liquid mercury. *Physical Review Letters*, 74(22) :4444, May 1995.

[Manaila, 1999] R. Manaila. Metastable metallic alloys. *Physica status solidi a*, 176(2) :801–834, 1999.

[Mark *et al.*, 1977] Peter Mark, J. D. Levine, and S. H. McFarlane. Atomic structure of the Si(111)-(7×7) surface. *Physical Review Letters*, 38(24) :1408, June 1977.

[Marks *et al.*, 1998] L. D. Marks, E. Bengu, C. Collazo-Davila, D. Grozea, E. Landree, C. Leslie, and W. Sinkler. Direct methods for surfaces. *Surface review and Letters*, 5 :1087–1106, 1998.

[Mechler *et al.*, 2010] S. Mechler, P. Pershan, E. Yahel, S. Stoltz, O. Shpyrko, B. Lin, M. Meron, and S. Sellner. Self-consistent interpretation of the 2D structure of the liquid $Au_{82}Si_{18}$ surface : Bending rigidity and the Debye-Waller effect. *Physical Review Letters*, 105(18), October 2010.

[Mehl and Papaconstantopoulos, 1996] J. Michael J. Mehl and Dimitrios A. Papaconstantopoulos. Applications of a tight-binding total-energy method for transition and noble metals : Elastic constants, vacancies, and surfaces of monatomic metals. *Physical Review B*, 54(7) :4521, 1996.

[Mezey and Giber, 1982] L. Z. Mezey and J. Giber. The surface free energies of solid chemical elements : Calculation from internal free enthalpies of atomization. *Japanese Journal of Applied Physics*, 21(11) :1569–1571, 1982.

[Minoda *et al.*, 1992] H. Minoda, Y. Tanishiro, N. Yamamoto, and K. Yagi. Growth of Si on Au deposited Si(111) surfaces studied by UHV-REM. *Applied Surface Science*, 60-61 :107–111, 1992.

[Mümmler and Wissmann, 1998] K. Mümmler and P. Wissmann. Spectroscopic ellipsometry on gold clusters embedded in a Si(111) surface. *Thin Solid Films*, 313-314 :522–526, 1998.

[Mullins, 1957] W. W. Mullins. Theory of thermal grooving. *Journal of Applied Physics*, 28(3) :333, 1957.

[Nagao *et al.*, 1998] T. Nagao, S. Hasegawa, K. Tsuchie, S. Ino, C. Voges, G. Klos, H. Pfnür, and M. Henzler. Structural phase transitions of Si(111)-($\sqrt{3} \times \sqrt{3}$)R30°-Au : phase transitions in domain-wall configurations. *Physical Review B*, 57(16) :10100, April 1998.

[Naidich *et al.*, 1975] Y. V. Naidich, V. M. Perevertailo, and L. P. Obushchak. Surface properties of binary melts of gold with germanium and silicon. *Zhurnal Fizicheskoi Khimii*, 49 :1554, 1975.

[Nakajima *et al.*, 1997] Y. Nakajima, C. Voges, T. Nagao, S. Hasegawa, G. Klos, and H. PfnÃ$\frac{1}{4}$r. Critical scattering at the order-disorder phase transition of Si(111)-($\sqrt{3} \times \sqrt{3}$) surface : A phase transition with particle exchange. *Physical Review B*, 55(13) :8129, April 1997.

[Nebolsin and Shchetinin, 2003] V. A. Nebolsin and A. A. Shchetinin. Role of surface energy in the Vapour-Liquid-Solid growth of silicon. *Inorganic Materials*, 39 :899, 2003.

[Needs and Mansfield, 1989] R J Needs and M Mansfield. Calculations of the surface stress tensor and surface energy of the (111) surfaces of iridium, platinum and gold. *Journal of Physics : Condensed Matter*, 1(41) :7555–7563, 1989.

[Nelson, 1983] David R. Nelson. Order, frustration, and defects in liquids and glasses. *Physical Review B*, 28(10) :5515, November 1983.

[Nix and MacNair, 1941] F. C. Nix and D. MacNair. The thermal expansion of pure metals : Copper, gold, aluminum, nickel, and iron. *Physical Review*, 60(8) :597, October 1941.

[Nogami *et al.*, 1990] J. Nogami, A. A. Baski, and C. F. Quate. ($\sqrt{3}\times\sqrt{3}$)→(6×6) phase transition on the Au/Si(111) surface. *Physical Review Letters*, 65(13) :1611, 1990.

[Nogaret, to be published] T. Nogaret. Epitaxial thin foil and the (6×6) surface reconstruction in Au-Si(111). to be published.

[Northrup, 1984] John E. Northrup. Si(111)-($\sqrt{3}\times\sqrt{3}$)-Al : an Adatom-Induced reconstruction. *Physical Review Letters*, 53(7) :683, 1984.

[Oh *et al.*, 2005] S.H. Oh, Y Kauffmann, C Scheu, WD Kaplan, and M Ruhle. Ordered liquid aluminum at the interface with sapphire. *Science*, 310(5748) :661–663, October 2005.

[Okamoto and Massalski, 1984] H. Okamoto and T. B. Massalski. The Au-Ge (Gold-Germanium) system. *Bulletin of Alloy Phase Diagrams*, 5 :601–610, 1984.

[Okuda *et al.*, 1996] Taichi Okuda, Hiroshi Daimon, Hiroaki Shigeoka, Shigemasa Suga, Toyohiko Kinoshita, and Akito Kakizaki. Surface core level shifts of the Au adsorbed Si(111) reconstructed surfaces. *Journal of Electron Spectroscopy and Related Phenomena*, 80 :229–232, May 1996.

[Oura *et al.*, 1985] K. Oura, M. Katayama, F. Shoji, and T. Hanawa. Real-Space determination of atomic structure of the si(111)-($\sqrt{3} \times \sqrt{3}$)R30°-Au surface by Low-Energy Alkali-Ion scattering. *Physical Review Letters*, 55(14) :1486, 1985.

[Pasturel *et al.*, 2010] A. Pasturel, Emre S. Tasci, Marcel H. F. Sluiter, and N. Jakse. Structural and dynamic evolution in liquid Au-Si eutectic alloy by ab initio molecular dynamics. *Physical Review B*, 81(14), April 2010.

[Perepezko and Paik, 1984] J.H. Perepezko and J.S. Paik. Thermodynamic properties of undercooled liquid metals. *Journal of Non-Crystalline Solids*, 61-62(Part 1) :113–118, January 1984.

[Pershan *et al.*, 2009a] P. S. Pershan, S. E. Stoltz, S. Mechler, O. G. Shpyrko, A. Y. Grigoriev, V. S. K. Balagurusamy, B. H. Lin, and M. Meron. Surface structure of the liquid $Au_{72}Ge_{28}$ eutectic phase : X-ray reflectivity. *Physical Review B*, 80(12) :125414, 2009.

[Pershan *et al.*, 2009b] P. S. Pershan, S. E. Stoltz, Oleg G. Shpyrko, Moshe Deutsch, Venkatachalapathy S. K. Balagurusamy, Mati Meron, Binhua Lin, and Reinhard Streitel. Surface structure of liquid Bi and Sn : An x-ray reflectivity study. *Physical Review B*, 79(11) :115417, March 2009.

[Pierre-Louis *et al.*, 2009] O. Pierre-Louis, A. Chame, and Y. Saito. Dewetting of ultrathin solid films. *Physical Review Letters*, 103(19) :195501, November 2009.

[Pinardi *et al.*, 2009] A.L. Pinardi, S.J. Leake, R Felici, and IK Robinson. Formation of an Au-Si eutectic on a clean silicon surface. *Physical Review B*, 79(4), January 2009.

[Piscopiello *et al.*, 2008] Emanuela Piscopiello, Leander Tapfer, Marco Antisari, Pasquale Paiano, Paola Prete, and Nicola Lovergine. Formation of epitaxial gold nanoislands on (100) silicon. *Physical Review B*, 78(3), July 2008.

[Plass and Marks, 1995] Richard Plass and Laurence D. Marks. UHV transmission electron microscopy structure determination of the Si(111)-($\sqrt{3} \times \sqrt{3}$)R30° surface. *Surface Science*, 342(1-3) :233–249, November 1995.

[Plass and Marks, 1997] Richard Plass and Laurence D. Marks. Submonolayer Au on Si(111) phase diagram. *Surface Science*, 380(2-3) :497–506, May 1997.

[Pollack, 1988] H. W. Pollack. *Materials Science and Metallurgy*, volume 4th ed. Prentice-Hall edition, 1988.

[Porret *et al.*, 2011] C Porret, T. Devilliers, A. Jain, R. Dujardin, and A. Barski. Importance of kinetics effects in the growth of germanium nanowires by vapour-liquid-solid Molecular Beam Epitaxy. *Journal of Crystal Growth*, 323 :334–339, 2011.

[Quested and Greer, 2005] T.E. Quested and A.L. Greer. Athermal heterogeneous nucleation of solidification. *Acta Materialia*, 53(9) :2683–2692, May 2005.

[Rauscher *et al.*, 1999] Markus Rauscher, Rogerio Paniago, Hartmut Metzger, Zoltan Kovats, Jan Domke, Johann Peisl, Hans-Dieter Pfannes, Jörg Schulze, and Ignaz Eisele. Grazing incidence small angle x-ray scattering from free-standing nanostructures. *Journal of Applied Physics*, 86(12) :6763, 1999.

[Rayleigh, 1878] L. Rayleigh. On the instability of jets. *Proceedings of the London Mathematical Society*, s1-10(1) :4–13, November 1878.

[Regan *et al.*, 1995] M. J. Regan, E. H. Kawamoto, S. Lee, P. S. Pershan, N. Maskil, M. Deutsch, O. M. Magnussen, B. M. Ocko, and L. E. Berman. Surface layering in liquid gallium : An X-Ray reflectivity study. *Physical Review Letters*, 75(13) :2498, 1995.

[Reichert *et al.*, 2000] H Reichert, O Klein, H Dosch, M Denk, V Honkimaki, T Lippmann, and G Reiter. Observation of five-fold local symmetry in liquid lead. *Nature*, 408(6814) :839–841, December 2000.

[Renaud *et al.*, 2004] G. Renaud, M. Ducruet, O. Ulrich, and R. Lazzari. Apparatus for real time *in-situ* quantitative studies of growing nanoparticles by grazing incidence small angle x-ray scattering and surface differential reflectance spectroscopy. *Nuclear Instruments and Methods in Physics Research Section B : Beam Interactions with Materials and Atoms*, 222(3-4) :667–680, August 2004.

[Renaud *et al.*, 2009] Gilles Renaud, Rémi Lazzari, and Frédéric Leroy. Probing surface and interface morphology with Grazing Incidence Small Angle X-Ray Scattering. *Surface Science Reports*, 64(8) :255–380, August 2009.

[Renaud, 1998] G. Renaud. Oxide surfaces and metal/oxide interfaces studied by grazing incidence X-ray scattering. *Surface Science Reports*, 32(1/2), 1998.

[Ressel *et al.*, 2000] B. Ressel, S. Heun, T. Schmidt, and K.C. Prince. XPEEM study of liquid Au-Si droplets on Si(111) near to the eutectic point. *Defect and Diffusion Forum*, 183-185 :181–188, 2000.

[Ressel *et al.*, 2003] B. Ressel, K. C. Prince, S. Heun, and Y. Homma. Wetting of Si surfaces by Au-Si liquid alloys. *Journal of Applied Physics*, 93(7) :3886, 2003.

[Robach *et al.*, 2000] O. Robach, Y. Garreau, K. Aïd, and M. B. Véron-Jolliot. Corrections for surface x-ray diffraction measurements using the z-axis geometry : finite size effects in direct and reciprocal space. *Journal of Applied Crystallography*, 33 :1006–1018, 2000.

[Roper *et al.*, 2007] Steven M. Roper, Stephen H. Davis, Scott A. Norris, Alexander A. Golovin, Peter W. Voorhees, and Mark Weiss. Steady growth of nanowires via the vapor-liquid-solid method. *Journal of Applied Physics*, 102(3) :034304, 2007.

[Ross *et al.*, 2005] F. M. Ross, J. Tersoff, and M. C. Reuter. Sawtooth faceting in silicon nanowires. *Physical Review Letters*, 95(14) :146104, 2005.

[Ross, 2010] Frances M Ross. Controlling nanowire structures through real time growth studies. *Reports on Progress in Physics*, 73(11) :114501, November 2010.

[Rota *et al.*, 2006] A Rota, A Martinezgil, G Agnus, E Moyen, T Maroutian, B Bartenlian, R Megy, M Hanbucken, and P Beauvillain. Au island growth on a Si(111) vicinal surface. *Surface Science*, 600(6) :1207–1212, March 2006.

[Ruffino and Grimaldi, 2010] F Ruffino and MG Grimaldi. Atomic force microscopy study of the growth mechanisms of nanostructured sputtered au film on si(111) : Evolution with film thickness and annealing time. *Journal of Applied Physics*, 107(10), May 2010.

[Sachdev and Nelson, 1984] Subir Sachdev and D.R. Nelson. Theory of the structure factor of metallic glasses. *Physical Review Letters*, 53 :1947, 1984.

[Sakai *et al.*, 1998] Hiroto Sakai, Elena A. Khramtsova, and Ayahiko Ichimiya. Metastable ordering of domain walls into Si(111)($2\sqrt{21}\times2\sqrt{21}$)R($\pm10.9°$)-au structure studied by reflection high energy electron diffraction and scanning tunneling microscopy. *Japanese Journal of Applied Physics*, 37(Part 2, No. 6B) :L755–L757, June 1998.

[Salvan *et al.*, 1985] F. Salvan, H. Fuchs, A. Baratoff, and G. Binnig. Au/Si(111) overlayer : Characterization by tunneling microscopy and spectroscopy. *Surface Science*, 162(1-3) :634–639, October 1985.

[Schenk *et al.*, 2002] T Schenk, D Holland-Moritz, V Simonet, R Bellissent, and D.M. Herlach. Icosahedral short-range order in deeply undercooled metallic melts. *Physical Review Letters*, 89(7), August 2002.

[Schülli *et al.*, 2010] T. U. Schülli, R. Daudin, G. Renaud, A. Vaysset, O. Geaymond, and A. Pasturel. Substrate-enhanced supercooling in AuSi eutectic droplets. *Nature*, 464(7292) :1174–1177, April 2010.

[Schmidt *et al.*, 2010] V. Schmidt, J. V. Wittemann, and U. Gösele. Growth, thermodynamics, and electrical properties of silicon nanowires. *Chemical Reviews*, 110(1) :361–388, January 2010.

[Schwalbach and Voorhees, 2008] Edwin J. Schwalbach and Peter W. Voorhees. Phase equilibrium and nucleation in VLS-Grown nanowires. *Nano Letters*, 8(11) :3739–3745, November 2008.

[Sears and Shelley, 1991] V.F. Sears and S.A. Shelley. Debye-Waller factor for elemental crystals. *Acta Crystallographica Section A*, 47 :441–446, 1991.

[Seifert *et al.*, 2001] C. Seifert, R. Hild, M. Horn-von Hoegen, R. A. Zhachuk, and B. Z. Olshanetsky. Au induced reconstructions on Si(111). *Surface Science*, 488(1-2) :233–238, August 2001.

[Shaffir *et al.*, 2009] E. Shaffir, I. Riess, and W.D. Kaplan. The mechanism of initial de-wetting and detachment of thin au films on YSZ. *Acta Materialia*, 57(1) :248–256, January 2009.

[Shechtman *et al.*, 1984] D. Shechtman, I. Blech, D. Gratias, and J. Cahn. Metallic phase with Long-Range orientational order and no translational symmetry. *Physical Review Letters*, 53(20) :1951–1953, November 1984.

[Sheng *et al.*, 2006] H.W. Sheng, W.K. Luo, F.M. Alamgir, J.M. Bai, and E Ma. Atomic packing and short-to-medium-range order in metallic glasses. *Nature*, 439(7075) :419–425, January 2006.

[Shibata *et al.*, 1992] A. Shibata, Y. Kimura, and K. Takayanagi. Si(111)-($\sqrt{3}\times\sqrt{3}$)-Au growing on a (7×7) surface. *Surface Science*, 273(1-2) :L430–L434, June 1992.

[Shpyrko *et al.*, 2005] Oleg G. Shpyrko, Alexei Yu. Grigoriev, Reinhard Streitel, Diego Pontoni, Peter S. Pershan, Moshe Deutsch, Ben Ocko, Mati Meron, and Binhua Lin. Atomic-Scale surface demixing in a eutectic liquid BiSn alloy. *Physical Review Letters*, 95(10) :106103, 2005.

[Shpyrko *et al.*, 2006] OG Shpyrko, R Streitel, VSK Balagurusamy, AY Grigoriev, M Deutsch, BM Ocko, M Meron, BH Lin, and PS Pershan. Surface crystallization in a liquid ausi alloy. *Science*, 313(5783) :77–80, July 2006.

[Shpyrko *et al.*, 2007] OG Shpyrko, R Streitel, VSK Balagurusamy, AY Grigoriev, M Deutsch, BM Ocko, M Meron, BH Lin, and PS Pershan. Crystalline surface phases of the liquid Au-Si eutectic alloy. *Physical Review B*, 76(24), December 2007.

[Skriver and Rosengaard, 1992] H. L. Skriver and N. M. Rosengaard. Surface energy and work function of elemental metals. *Physical Review B*, 46(11) :7157, 1992.

[Spaepen, 1975] F Spaepen. Structural model for solid-liquid interface in monoatomic systems. *Acta Metallurgica*, 23(6) :729–743, 1975.

[Srolovitz and Safran, 1986a] D. J. Srolovitz and S. A. Safran. Capillary instabilities in thin films. I. Energetics. *Journal of Applied Physics*, 60(1) :247, 1986.

[Srolovitz and Safran, 1986b] D. J. Srolovitz and S. A. Safran. Capillary instabilities in thin films. II. Kinetics. *Journal of Applied Physics*, 60(1) :255, 1986.

[Steinhardt *et al.*, 1981] P.J. Steinhardt, D.R. Nelson, and M Ronchetti. Icosahedral bond orientational order in supercooled liquids. *Physical Review Letters*, 47(18) :1297–1300, 1981.

[Steinhardt *et al.*, 1983] P.J. Steinhardt, D.R. Nelson, and M Ronchetti. Bond-orientational order in liquids and glasses. *Physical Review B*, 28(2) :784, 1983.

[Stich *et al.*, 1992] I. Stich, M. C. Payne, R. D. King-Smith, J-S. Lin, and L. J. Clarke. Ab-initio total-energy calculations for extremely large systems : Application to the takayanagi reconstruction of Si(111). *Physical Review Letters*, 68(9) :1351, 1992.

[Sutter and Sutter, 2008] E Sutter and P Sutter. Phase diagram of nanoscale alloy particles used for vapor-liquid-solid growth of semiconductor nanowires. *Nano Letters*, 8(2) :411–414, February 2008.

[Sutter and Sutter, 2011] E Sutter and P Sutter. Formation and stabilization of single-crystalline metastable AuGe phases in Ge nanowires. *Nanotechnology*, 22 :295605, 2011.

[Swiech *et al.*, 1991] W. Swiech, E. Bauer, and M. Mundschau. A low-energy electron microscopy study of the system Si(111)—Au. *Surface Science*, 253(1-3) :283–296, August 1991.

[Takahashi *et al.*, 1991] S. Takahashi, Y. Tanishiro, and K. Takayanagi. Short range orders of an adsorbed layer : gold on the Si(111)-(7×7) surface. *Surface Science*, 242(1-3) :73–80, February 1991.

[Takami *et al.*, 1994] Tomohide Takami, Daiji Fukushi, Tomonobu Nakayama, Masayuki Uda, and Masakazu Aono. Structural correlation among different phases in the initial stage of epitaxial growth of Au on Si(111). *Japanese Journal of Applied Physics*, 33(Part 1, No. 6B) :3688–3695, June 1994.

[Takayanagi *et al.*, 1985] Kunio Takayanagi, Yasumasa Tanishiro, Shigeki Takahashi, and Masaetsu Takahashi. Structure analysis of Si(111)-(7×7) reconstructed surface by transmission electron diffraction. *Surface Science*, 164(2-3) :367–392, December 1985.

[Takeda *et al.*, 2007] S. Takeda, H. Fujii, Y. Kawakita, Y. Kato, S. Fujita, Y. Yokota, and S. Kohara. Structure of liquid Au-Si alloys around the eutectic region. *Materials Science and Engineering : A*, 449-451 :590–593, March 2007.

[Tanaka *et al.*, 2006] M. Tanaka, K. Higashida, H. Nakashima, H. Takagi, and M. Fujiwara. Orientation dependence of fracture toughness measured by indentation methods and its relation to surface energy in single crystal silicon. *International Journal of Fracture*, 139(3-4) :383–394, June 2006.

[Tasci *et al.*, 2010] Emre S. Tasci, Marcel H.F. Sluiter, Alain Pasturel, and Pierre Villars. Liquid structure as a guide for phase stability in the solid state : Discovery of a stable compound in the Au-Si alloy system. *Acta Materialia*, 58(2) :449–456, January 2010.

[Tostmann *et al.*, 1999] H. Tostmann, E. DiMasi, P. S. Pershan, B. M. Ocko, O. G. Shpyrko, and M. Deutsch. Surface structure of liquid metals and the effect of capillary waves : X-ray studies on liquid indium. *Physical Review B*, 59(2) :783, January 1999.

[Turnbull and Cech, 1950] D. Turnbull and R. E. Cech. Microscopic observation of the solidification of small metal droplets. *Journal of Applied Physics*, 21(8) :804, 1950.

[Turnbull and Fisher, 1949] D. Turnbull and J. C. Fisher. Rate of nucleation in condensed systems. *The Journal of Chemical Physics*, 17(1) :71, 1949.

[Turnbull, 1950a] D. Turnbull. Correlation of Liquid-Solid interfacial energies calculated from supercooling of small droplets. *The Journal of Chemical Physics*, 18 :769, 1950.

[Turnbull, 1950b] D. Turnbull. Formation of crystal nuclei in liquid metals. *Journal of Applied Physics*, 21(10) :1022, 1950.

[Turnbull, 1950c] D. Turnbull. Kinetics of heterogenous nucleation. *The Journal of Chemical Physics*, 18(2) :198, 1950.

[Turnbull, 1950d] D. Turnbull. The supercooling of aggregates of small metal particles. *Journal of Metals*, 2(9) :1144–1148, 1950.

[Turnbull, 1952] David Turnbull. Kinetics of solidification of supercooled liquid mercury droplets. *The Journal of Chemical Physics*, 20(3) :411, 1952.

[Tyson and Miller, 1977] W.R. Tyson and W.A. Miller. Surface free energies of solid metals : Estimation from liquid surface tension measurements. *Surface Science*, 62(1) :267–276, 1977.

[Vinet *et al.*, 2002] Bernard Vinet, Lena Magnusson, Hasse Fredriksson, and Pierre Jean Desré. Correlations between surface and interface energies with respect to crystal nucleation. *Journal of Colloid and Interface Science*, 255(2) :363–374, November 2002.

[Vitos *et al.*, 1998] L. Vitos, A. V. Ruban, H. L. Skriver, and J. Kollar. The surface energy of metals. *Surface Science*, 411 :186–202, 1998.

[Vlieg, 1997] E. Vlieg. Integrated intensities using a Six-Circle surface X-ray diffractometer. *Journal of Applied Crystallography*, 30(5) :532–543, 1997.

[Vlieg, 2000] E Vlieg. ROD : a program for surface x-ray crystallography. *Journal of Applied Crystallography*, 33 :401–405, April 2000.

[Voigtländer, 2001] Bert Voigtländer. Fundamental processes in Si/Si and Ge/Si epitaxy studied by scanning tunneling microscopy during growth. *Surface Science Reports*, 43(5-8) :127–254, September 2001.

[Wacaser *et al.*, 2009] B. A. Wacaser, M. C. Reuter, M. M. Khayyat, CY Wen, R Haight, S. Guha, and F. M. Ross. Growth system, structure, and doping of Aluminum-Seeded epitaxial silicon nanowires. *Nano Letters*, 9(9) :3296–3301, 2009.

[Waghorne *et al.*, 1976] R.M. Waghorne, V.G. Rivlin, and G.I. Williams. Structure of liquid alloys of the Au-Si and Au-Ge systems. *Journal of physics F : Metal Physics*, 6(2) :147, 1976.

[Wagner and Ellis, 1964] R.S. Wagner and W.C Ellis. Vapor-Liquid-Solid mechanism of single crystal growth. *Applied Physics Letters*, 4(5) :89–&, 1964.

[Wakayama and Tanaka, 1997] Yutaka Wakayama and Shun-ichiro Tanaka. Nanometer-scale Si/Au bilayer dots fabricated by self-assembly process through liquid phase epitaxy. *Nanostructured Materials*, 8(8) :1033–1039, December 1997.

[Wang and Perdew, 1991] Y. Wang and J.P. Perdew. *Physical Review B*, 44 :13298, 1991.

[Wang and Schaaf, 2011] Dong Wang and Peter Schaaf. Thermal dewetting of thin au films deposited onto line-patterned substrates. *Journal of Materials Science*, June 2011.

[Wang *et al.*, 2004] Y. Wang, S. Teitel, and C. Dellago. Melting of icosahedral gold nanoclusters from molecular dynamics simulations. *Journal of Chemical Physics*, 122, 2004.

[Wang *et al.*, 2006] Yewu Wang, Volker Schmidt, Stephan Senz, and Ulrich Gosele. Epitaxial growth of silicon nanowires using an aluminium catalyst. *Nature Nanotechnology*, 1(3) :186–189, December 2006.

[Wang *et al.*, 2008] N. Wang, Y. Cai, and R.Q Zhang. Growth of nanowires. *Materials Science and Engineering R*, 60 :1–51, 2008.

[Warren, 1969] B.E. Warren. *X-Ray Diffraction.* Addison-Wesley, Reading, MA, 1969.

[Wen *et al.*, 2009] CY Wen, MC Reuter, J Bruley, J Tersoff, S Kodambaka, EA Stach, and FM Ross. Formation of compositionally abrupt axial heterojunctions in Silicon-Germanium nanowires. *Science*, 326(5957) :1247–1250, November 2009.

[Wilk *et al.*, 1994] G. D. Wilk, R. E. Martinez, John F. Chervinsky, Frans Spaepen, and J. A. Golovchenko. Low-temperature homoepitaxial growth on Si(111) mediated by thin overlayers of Au. 10.1063/1.112185, 1994.

[Wu *et al.*, 2010] Yaping Wu, Yinghui Zhou, Changjie Zhou, Huahan Zhan, and Junyong Kang. Atomic structure and formation mechanism of identically sized Au clusters grown on Si(111)-(7×7) surface. *The Journal of Chemical Physics*, 133(12) :124706, 2010.

[Yamada *et al.*, 1984] I. Yamada, H. Inokawa, and T. Takagi. Epitaxial growth of Al on Si(111) and Si(100) by ionized-cluster beam. *Journal of Applied Physics*, 56 :2746, 1984.

[Yeh *et al.*, 1993] J.-J. Yeh, J. Hwang, K. Bertness, D. J. Friedman, R. Cao, and I. Lindau. Growth of the room temperature Au/Si(111)-(7×7) interface. *Physical Review Letters*, 70(24) :3768, June 1993.

[Young, 1805] Thomas Young. An essay on the cohesion of fluids. *Philosophical Transactions of the Royal Society of London*, 95 :65–87, 1805.

[Zhang *et al.*, 2003] Jian-Min Zhang, Fei Ma, Ke-Wei Xu, and Xiao-Tian Xin. Anisotropy analysis of the surface energy of diamond cubic crystals. *Surface and Interface Analysis*, 35(10) :805–809, October 2003.

[Zhou *et al.*, 2011] T. Zhou, G. Renaud, C. Revenant, J. Issartel, T. U. Schülli, R. Felici, and A. Malachias. Atomic structure and composition of the (2×n) reconstruction of the Ge wetting layer on Si(001) investigated by surface x-ray diffraction. *Physical Review B*, 83(19) :195426, May 2011.

[Zhou, 2011] Tao Zhou. PhD work, SP2M/Inac-CEA Grenoble, 2011.

Résumé:

Les nanofils (NFs) de semi-conducteur (SC) sont des objets possédant des propriétés très intéressantes pour la fabrication de futurs composants électroniques à l'échelle nanométrique. Ils sont élaborés grâce à l'utilisation d'un catalyseur métallique (Au) formant un point eutectique profond en s'alliant à la phase SC (Si) permettant la germination et la croissance du NF à basses températures. Ce travail a pour but l'étude de la formation, de la structure et du comportement de ces gouttes d'alliage eutectique en interaction avec le substrat dont les propriétés futures du NF vont dépendre. L'étude a été menée *in-situ,* par utilisation du rayonnement synchrotron qui est un outil parfaitement dédié à la caractérisation de structures à l'échelle atomistique. Les gouttes d'eutectique ont été obtenues par démouillage du film d'or. L'étude de ce procédé a révélé des changements dans les relations d'épitaxies entre l'or et le silicium. Les gouttes ainsi formées sont accompagnées d'une couche de mouillage, se révélant être une reconstruction de surface, dont les conditions de formation ainsi que la structure atomique ont été déterminées. Lors du refroidissement, une augmentation des effets de surfusion a été observée en présence de cette reconstruction et a été expliquée par la structure même de cette dernière qui semble stabiliser l'état liquide. Des expériences similaires ont été faites sur d'autres systèmes (Au-Ge, Al-Si) et une synthèse a été réalisée pour comparer les connaissances actuelles sur le sujet avec les résultats de ce travail.

Mots clés
Nanofils, croissance, or, silicium, epitaxie par jet moléculaire, reconstruction de surface, eutectique, surfusion, solidification, transitions de phase, diffraction de rayon X

Abstract:

Semiconductor (SC) nanowires (NMs) have been identified as important components for future electronic and sensor nanodevices. They are produced using a metal catalyst (Au) that forms a low eutectic point with the SC phase (Si) and enables their nucleation and their growth at low temperatures. The aim of this study is to investigate the formation, the structure as well as the behaviour of such liquid eutectic droplets in interaction with the substrates on which the futur NMs properties will later depend. This work has been performed *in-situ*, using synchrotron radiation which is the perfect tool to characterize this mechanism at the atomistic scale. The eutectic droplets have been obtained through the dewetting of thin gold films. This process has been found to modify the epitaxial relationships between the gold and the silicon substrate. The obtained droplets are accompanied by a wetting layer (WL) whose conditions of formation as well as atomic structure, which turned to be a surface reconstruction, have been determined. During the cooling process, the supercooling effects in such AuSi eutectic droplets have been found to be enhanced in the presence of this reconstruction. It has been explained by its specific atomic structure which is likely to stabilize the liquid phase. Similar experiments on other systems (Au-Ge or Al-Si) were performed and a synthesis has been made in order to present the current knowledge on this topic in comparison with the results of this work.

Keywords
Nanowires growth, gold, silicon, molecular beam epitaxy, surface reconstruction, eutectic, supercooling, solidification, phase transition, X-ray diffraction